THOMAS A. MELLAN

DFT SIMULATIONS OF SELECTED STRONGLY CORRELATED FUNCTIONAL MATERIALS

SUPERVISED BY

DR RICARDO GRAU-CRESPO & DR FURIO CORÀ

A DISSERTATION SUBMITTED FOR THE DEGREE

DOCTOR OF PHILOSOPHY

OF THE

UNIVERSITY COLLEGE LONDON

DFT SIMULATIONS OF SELECTED STRONGLY CORRELATED FUNCTIONAL MATERIALS

THOMAS A. MELLAN

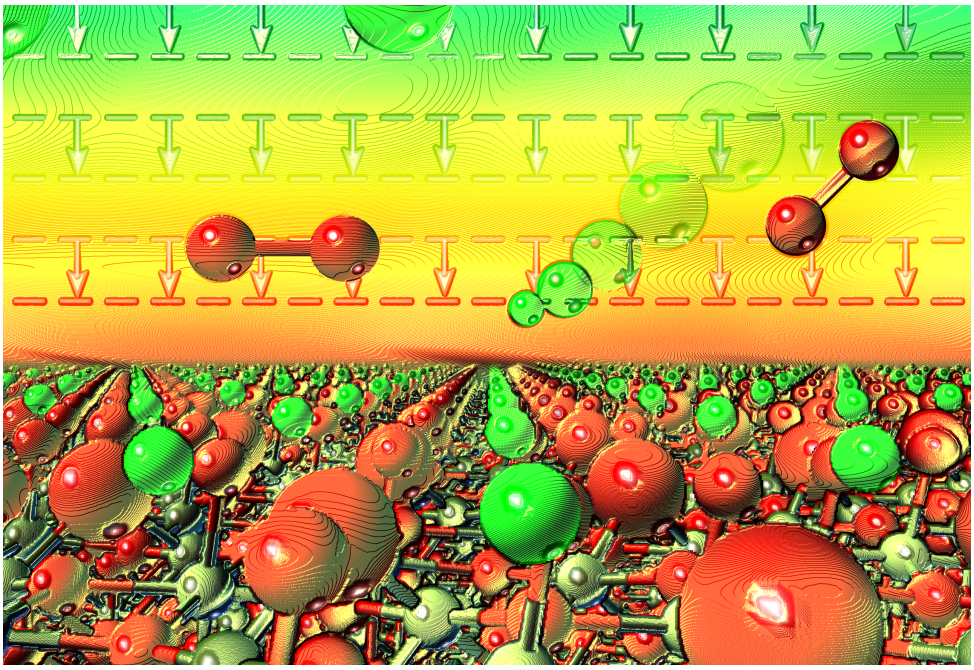

Electronic and redox properties of vanadium and manganese oxides

Mathematical and Physical Sciences
UCL

August 2015

Thomas A. Mellan

DFT simulations of selected strongly correlated functional materials: Electronic and redox properties of vanadium and manganese oxides.

SUPERVISORS:
Dr Ricardo Grau-Crespo
Dr Furio Corà

DEGREE:
PhD

LOCATION:
UCL, London

SUBMISSION DATE:
August 2015

DECLARATION

I, Thomas Mellan, confirm that the work presented in this thesis is my own. Where information has been derived from other sources, I confirm that this has been indicated in the thesis.

All work here was conceived jointly with my supervisors. Primary supervision was provided by Dr Ricardo Grau-Crespo (University of Reading, formerly at UCL), and by Dr Furio Corà (UCL). Prof. Phuti Ngoepe acted as supervisor during my month as Visiting Researcher at the Materials Modelling Centre, University of Limpopo (RSA). Prof. Sohrab Ismail-Beigi provided supervision for several months while visiting as a Research Associate at the Department of Applied Physics, University of Yale (USA).

Collaboration with other PhD students included the Heyd-Scuseria-Ernzerhof (HSE) calculations in Chapter 6.3.3 and dopant calculations Chapter 7.3.2, carried out in conjunction with Hao Wang (KAUST), and the surface calculations in Chapter 9, worked out in tandem with Khomotso Maenetja (University of Limpopo).

London, August 2015

Thomas A. Mellan

ABSTRACT

A theoretical investigation is presented on three correlated transition metal oxide systems - one oxide of vanadium, a manganate and a manganite. Beyond theoretical interest in the strongly interacting electronic structures, each system is relevant to materials design and developing new technologies. For each material in the thesis, vanadium dioxide (VO_2), manganese dioxide (β-MnO_2) and lanthanum manganite ($LaMnO_3$), reports are presented on the electronic, structural and thermodynamic properties calculated using density functional theory (DFT).

Strongly interacting electrons are a major challenge to modelling techniques, so to begin we examine the capacity of DFT to describe VO_2. Analysis is presented on the effect of on-site direct and exchange Coulomb corrections, and the exchange mixing parameter in hybrid functional calculations.

VO_2 phase transition potential energy surfaces are presented in terms of electronic and structural transition parameters. To access transition thermodynamics, zero temperature imaginary phonon modes are transformed to their transition temperature energies. The phonon and electron contributions to the total transition entropy are calculated, which allows us to discuss the nature of the VO_2 phase transition.

Surface thermodynamics are presented for VO_2. Results predict the energetically favoured surfaces, particle morphologies, and surface terminations as a function of temperature and pressure.

The Li and O adsorption thermodynamics of β-MnO_2 surfaces are explored from the perspective of reducing cathode over-potentials in the Li-air cell. The surface redox chemistry and electronic structure are studied with and without Li adatoms, leading to predictions on the operation of β-MnO_2 as a battery cathode material.

For $LaMnO_3$ it is found that intra-orbital exchange corrections to DFT reproduce electronic, magnetic and structural observables simultaneously. The importance of Hund's coupling to the $LaMnO_3$ ground state is explored in detail.

PUBLICATIONS

Many of the tables, figures and ideas presented in this thesis have already been published, or are under review or in preparation as journal articles:

- TA Mellan, F Corà, R Grau-Crespo, and S Ismail-Beigi. Importance of anisotropic Coulomb interaction in $LaMnO_3$. Physical Review B, 92, 085151, 2015.[1]
- TA Mellan and R Grau-Crespo. Density functional theory study of rutile VO_2 surfaces. The Journal of Chemical Physics, 137, 154706, 2012.[2]
- TA Mellan, KP Maenetja, PE Ngoepe, SM Woodley, CRA Catlow, and R Grau-Crespo. Lithium and oxygen adsorption at the β-MnO_2 (110) surface. Journal of Materials Chemistry A, 1(47):14879, 2013.[3]
- H Wang, TA Mellan, R Grau-Crespo, and U Schwingenschlögl. Spin polarisation, orbital occupation and band gap opening in vanadium dioxide: The effect of screened Hartree-Fock exchange. Chemical Physics Letters, 608:126–129, 2014.[4]
- TA Mellan, H Wang, U Schwingenschlögl, and R Grau-Crespo. Potential energy surfaces and the origin of the VO_2 phase transition entropy. *Under review.*
- TA Mellan and R Grau-Crespo. Computer modelling studies of VO_2 phases (review). *Book chapter in preparation.*

ACKNOWLEDGMENTS

I am hugely grateful to Ricardo for his help throughout, and to Furio, Sohrab and Phuti for their support at different stages.

CONTENTS

LIST OF FIGURES

Figure 57 The occupation of states is represented in the model Mn^{3+} d^4 manifold (majority spin only). The schematic qualitatively shows how orbital degeneracy is broken by octahedral crystal field (CF), Coulomb repulsion U_{eff} (U in the figure) and exchange J following Equation 77. Each vertical bar represents one unit of electron occupation, while the energy scale is qualitative. $\pi^{e_g\sigma}$ is defined in Equation 74 for which three limits are examined: $\pi^{e_g\sigma} = 0$ ($f_{x^2-y^2\sigma} = f_{3z^2-r^2\sigma} = 0.5$), $\pi^{e_g\sigma} = +1$ ($f_{x^2-y^2\sigma} = f_{3z^2-r^2\sigma} + 1 = 1$), and $\pi^{e_g\sigma} = -1$ ($f_{x^2-y^2\sigma} + 1 = f_{3z^2-r^2\sigma} = 1$). 201

Figure 58 Orbitals in the $LaMnO_3$ unit cell from a $U|J = 8|2$ eV calculation. a) MnO_6 octahedron with Jahn-Teller distorted plane and local basis vectors labelled. b) Visualisation of the occupation of the $3z^2 - r^2$ and $x^2 - y^2$ states in the rotated basis of the density matrix as well as their superposition for the total local e_g occupancy (plotting the occupation times the orbital expressed in spherical harmonics). c) The ordering of the occupied e_g shell ($1.97z^2 - 0.58x^2 - 1.4y^2$) in the (010) Jahn-Teller distorted FM coupled plane. d) The ordering of the occupied e_g shell in the (001) plane with AFM coupling along b. Note x, y, z is the local octahedron basis, and a, b, c lattice vectors correspond to x', y', z' global (pre-rotation) calculation basis. 203

Figure 59 *Top*: Mn d and O p density of states (states/eV) for both spin channels in a single $LaMnO_3$ formula unit, from $U|J = 8|2$ eV and $U|J = 8|3$ eV calculations. *Bottom*: Occupation ($f_{i\sigma}$) for $U|J = 8|0, 1, 2, 3$ eV, showing the spin/occupation polarisation cross-over for e_g occupation at $J \approx 2.4$ eV. 207

Figure 60 Local magnetic moment and oxidation state within the Bader volumes centred on single Mn cations (*top*) and O anions (*bottom*). Basal O within Jahn-Teller (JT) active (010) *ac* plane, and apical O in the non-JT $[010]$ *b* direction. Calculations from DFT+U_{eff} and DFT+$U|J$ methods, where notation $U_6|J$ and $U_8|J$ indicates U is fixed to 6 eV and 8 eV respectively, while J is varied. The experimental reference local magnetic moment is 3.7 μ_B.[17] Note, the Mn-O-Mn AFM coupling along the 'non-JT' out-of-plane direction does not generate a local magnetic moment for the apical O. 208

Figure 61 Simplified cubic single formula unit *Pm-3m* $La_1Mn_1O_3$ structure and dispersion compared for HSE,[18] $U_{\text{eff}} = 0$ eV and $U_{\text{eff}} = 8$ eV, and $U|J = 8|2$ eV and $U|J = 8|3$ eV calculations. Minority spin bands given by dotted blue line. 209

Figure 62 $LaMnO_3$ magnetic coupling constants J_1 and J_2 versus $U|J$ schema Hund's exchange parameter J, for $U = 6$ eV (white squares), $U = 7$ eV (white circles), $U = 8$ eV (black squares). J_1 and J_2 are defined in Equation 84. 210

Figure 63 *Left top panel:* Band gap of $LaMnO_3$ versus $U - J$ within the U_{eff} approach for fully relaxed structures where both electron-lattice and electron-electron interactions are active (dashed line, *e-l* and *e-e*) and for structures with the Jahn-Teller distortion frozen out so only electron-electron interactions are active (solid line, *e-e* only). *Left bottom and middle panels:* Jahn-Teller normal modes versus $U - J$ within the U_{eff} (white circles) and $U|J$ (black circles) approaches. *Right panels:* Orbitally ordered and strongly Jahn-Teller active *ac* plane, the local basis convention, and $\mathbf{Q}^{\text{Ortho}}$ and $\mathbf{Q}^{\text{Tetra}}$ modes. 214

LIST OF TABLES

CUSTOM CODES

ACRONYMS AND ABBREVIATIONS

AFM anti-ferromagnetic

AMF around mean-field

A-AFM A-type anti-ferromagnetic

b bridging O coordination

bb bridging-bridging O coordination

bbi bridging-bridging-inplane O coordination

bii bridging-inplane-inplane O coordination

CBM conduction band maximum

CI configuration interaction

DFT density functional theory

DMFT dynamical mean-field theory

DOS density of states

DM density matrix

e-e electron-electron

e-l electron-lattice

FLL fully localised limit

FM ferromagnetic

GGA generalised gradient approximation

GW Green's function screened Coulomb interaction calculation

G-AFM G-type anti-ferromagnetic

HEG homogenous electron gas

HF Hartree-Fock

HK Höhenberg-Kohn

HSE Heyd-Scuseria-Ernzerhof

IR infra-red

JT Jahn-Teller

KS Kohn-Sham

LDA local density approximation

LMO lanthanum manganite

M1 monoclinic

MIT metal-insulator transition

ML mono-layer

nn nearest neighbour

nnn next-nearest neighbour

NM non-magnetic

PAW projected augmented wave

PBE Perdew-Burke-Erzenhof

PBEsol Perdew-Burke-Erzenhof for solids

PES potential energy surface

PM paramagnetic

PZ81 Perdew-Zunger 81

QMC quantum Monte Carlo

R rutile

TF Thomas-Fermi

TMO transition metal oxide

VBM valence band maximum

VASP Vienna Ab Initio Simulation Program

XC exchange-correlation

XPS x-ray photoelectron spectroscopy

Part I

Introduction

1

STRONGLY CORRELATED AND FUNCTIONAL MATERIALS

1.1 INTRODUCTION

Functional materials are characterised by some usefulness inherent in design and local structure. Over the past several decades trends toward the nanoscale have placed increased emphasis on the understanding and control of local atomic structure and electronic behaviour. This has hugely opened the field of materials science, which now exhibits engineered function in materials such as colloids, artificial bone, superconductors, thin-films, and magnetic materials amongst others.

In this thesis we study a selected group of transition metal oxides, each endowed with an array of potentially useful properties. In each metal oxide the functional properties are innately drawn from the behaviour of localised electrons, for example, in terms of thermodynamics, ordering, or symmetry-breaking effects.

The materials in this thesis are vanadium dioxide (VO_2), manganese dioxide (MnO_2) and lanthanum manganite ($LaMnO_3$), which have materials design applications ranging from *smart windows*,[8,15,24,25,26,27,28,29,30] to next-generation *battery technology*[3,31] and non-volatile *data storage device*s.[32,33,34,35,36] Here we attempt to understand the chemical and physical properties of these materials using *ab initio* techniques. Typically, this means density functional theory calculations, with *post hoc* analysis of relaxed geometries, optimised electronic structures, and thermodynamic properties.

The layout of this thesis is given in the Contents on page 13, but in summary the main body is divided into six parts: Introduction from the current page, Methods on page 57, Results on page 107, Conclusion on page 219, Appendix on page 227 and Bibliography on page 245. The Introduction, Methods, and Results parts are separated by topic into chapters.

Beginning Chapter 1 on the preceding page, a lay introduction is provided to the thesis, strong correlation and functional materials. The introduction is developed in Chapter 2 on page 39, with the materials in the thesis discussed in reference to the literature.

The methodology is split into theoretical background, technical details and calculation of properties, which are given in turn in Chapters 3-5 from pages 57-95.

The results begin in Chapter 6 on page 107, on the density functional theory (DFT) description of VO_2, with analysis on the role of exchange interactions and on-site corrections. Chapter 7 on page 129 examines VO_2 potential energy surfaces and contributions to the transition entropy. Chapter 8 on page 149 gives thermodynamic analyses of the redox properties of VO_2 surfaces. Chapter 9 on page 167 concerns the redox thermodynamics of MnO_2 surfaces under Li doping, with particular reference to the Li-air battery. Finally Chapter 10 on page 187 deals with the nature of anisotropic exchange interactions in $LaMnO_3$, and reproduction thereof *via* DFT.

1.2 FUNCTION

Along with strong correlation, potential function and application are the recurring themes for the materials throughout this work. In general functional materials are considered to exhibit native electronic, structural or thermodynamic characteristics that can inherently serve a specific use, or can be exploited in the design of a technological application. In correlated materials in particular,[37] the interplay between kinetic and on-site potential interactions across different microscopic parameters provide a fertile basis for materials design.[38]

An important example in this thesis is the material VO_2, in which electronic, magnetic and structural phase transitions take place simultaneously in temperature.[9] As a result VO_2 has recently been subject to concerted efforts towards the design of switchable materials, most notably smart windows,[28,30,39] which exploit the modulation of optical constants across the phase transition.[15]

Another transition metal oxide (TMO) material of interest is β-MnO_2, which is structurally isomorphic to VO_2. Electrons in the partially occupied Mn *d*-band are localised, and experience strong on-

site direct and exchange Coulomb effects.[40] In particular anisotropic Coulomb interaction results in the characteristic non-collinear helical anti-ferromagnetic (AFM) spin structure and large fundamental band gap of 0.8 eV.[40,41,42] The redox thermodynamics of MnO_2 surfaces can be modified by the adsorption of Li, with the transfer of charge from Li adatoms and localisation onto surface Mn sites. The Li doping of MnO_2 is of consequently of interest to the development of the novel Li-air cell, reducing over-potentials at the cathode associated with Li_2O_2 formation.[43]

The final strongly correlated material of interest in this thesis is $LaMnO_3$, in which orbital-order, magnetic and structural degrees of freedom couple through strong on-site Coulomb repulsion.[44,45] This leads naturally to a complex phase diagram in temperature and pressure that makes $LaMnO_3$ an important parent doping material.[36,46,47,48] Potential manganite perovskite applications are numerous, but include for example low energy data storage devices, which exploit switchable spin-polarisation and colossal-magneto resistance.[37,49,50]

1.3 STRONG CORRELATION

In the manganese and vanadium oxides in this thesis, Coulomb repulsion affects striking broken symmetry and ordering effects, switchable characteristics and electron localisation. The strong interaction physics and chemistry that couples spin, charge, orbital and lattice degrees of freedom, can also often be key to materials science applications. Strongly correlated phenomena are now introduced, in the context of functional materials, before discussing the strong interactions between electrons in the manganese and vanadium oxides in this work specifically.

Many TMO systems with partially filled d (or f) shells can exhibit a range of strong correlation phenomena anomalous to band theory. An important example especially relevant to this work is the Mott insulating state, which typically occurs upon transition from a metal in a high structural symmetry phase, to a low symmetry AFM phase that is 'anomolously' insulating in respect of partial band filling.[51] This insulating energy gap is central to paradigms of 'Mottness', where a single half-occupied band at the Fermi level (E_F) is split into two bands

separated by 'U', due to the strong interaction between electrons with an atomic spatially-confined character. Late period examples include CoO, NiO, and $CaCuO_2$, where each despite having partial filling to d^7, d^8 and d^9 respectively on the $+2$ valence cation site, is a wide gap AFM insulator.[51] In addition to opening a gap through Mott-type localisation effects, such as occupancy/symmetry dependent on-site Coulomb and exchange, a range of fascinating ordering effects are also possible.[52,53]

In the example of the AB_2O_3 spinel Fe_3O_4, the material has cubic symmetry above the transition temperature (T_c= 120 K), and monoclinic symmetry below. Fine detail in the electronic structure is supplied by charge-ordered iron sites and a ferrimagnetic spin structure. Above the T_c the single 'A' site iron is occupied up to d^5 (*i.e.* $+3$ valence), while the two 'B' sites mix filling to d^5 and d^6 with equal weight to form a non-integer $+2.5$ valence.[51] Below the transition temperature the lowering of symmetry to the monoclinic structure is accompanied by a Verwey transition, breaking B site occupancy symmetry in favour of an alternating $+2/+3$ charge ordering.[54]

The role of orbital physics and chemistry in correlated electron systems is exemplified by $KCuF_3$,[52] which was one of the first materials to provide insight into relative roles of electron-phonon and super-exchange/localisation effects, which can compete or cooperate in the origin of lattice and orbital ordering.[55,56] In perovskite $KCuF_3$, O_h group symmetry is reduced to pseudo-cubic tetragonal by Jahn-Teller distorted CuF_6 units.[57] It is now known that the origin of the distortion however is not the usual electron-lattice (e-l) Jahn-Teller, but electron-electron (e-e) interactions which order the d^9-shell. The underlying Kugel-Khomskii[58] superexchange mechanism polarises orbital occupancy[59] ordering the single d-shell hole to alternate between $y^2 - z^2$ and $x^2 - z^2$ states.[51]

Beyond these simple examples, perovskites such as $Pr_{0.5}Ca_{0.5}MnO_3$ exhibit spin, charge *and* orbital ordering,[51] while a rich variety of phenomena exist with entirely different effects. A sample of other dramatic effects includes large volume variation in phase-change actinides and lanthanides, high-T_c layered copper oxide superconductors, heavy fermion materials, colossal magnetoresistors and thermoelectrics.[60] Note that VO_2 and $LaMnO_3$, as prototypical phase-transition[61,62,63]

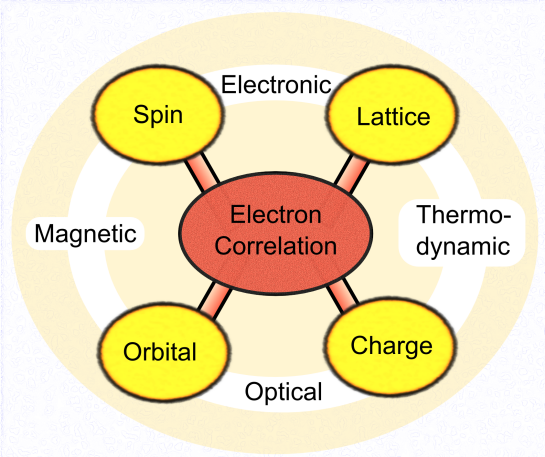

Figure 1: Charge, spin, orbital and lattice degrees of freedom, coupled through strong electron interaction.

and orbitally-ordered[44,45,53,54,64] correlated metal oxides, each will be covered in detail, with their introduction and discussion saved for the following chapter.

Strongly correlated (or strongly interacting) effects manifest to minimise the Coulomb repulsion felt between on-site electrons.[65] To study the effects of strong correlation, two broad methodology-types exist. *Particle models,* such as that of Hubbard (or Kanamori, *etc.*),[66,67,68,69] can focus on a rigorous description of electron correlations, but usually at the expense of excluding details such as the lattice. In the *ab initio* or *first principles* approach, calculations do account for structure and chemical composition, but compromise on the different approximations developed to treat e-e interactions. In DFT the approximations take several forms, but in essence all approaches implement a form of mean-field Coulomb treatment. The approximations reduce computational cost to an acceptable level, but also reduce the suitability of the technique to investigate materials with strongly interacting electrons.

To improve the poor DFT description of the strongly correlated materials in this work, we apply on-site Coulomb corrections using the DFT+U methodology. The DFT+U class of functionals provide means to break symmetry in band filling beyond typical homogenous electron gas exchange and crystal field effects. The additional polarisation of orbital occupation allows orbital ordering and a Mott-type gap that plain DFT approaches usually miss. By favouring polarised orbital occupation, DFT+U stabilises spin polarised solutions, providing

qualitative improvement in the description of magnetically ordered insulators.[70]

As the $+U$ correction is based on the static mean-field approximation,[70] opposed to the dynamical corrections employed in state-of-the-art methods such as DFT+dynamical mean-field theory (DMFT),[60,71] the approach naturally has limitations. For example, $+U$ is often treated as a parameter and if increased enough, symmetry breaking will always occur, irrespective of whether it physically exists. 'High-order' correlation is also inherently beyond the scope of $+U$ methods, but the methodology can correct zeroth (direct) and first (exchange) order Coulomb interactions in DFT. This can improve properties dependent on strong Coulomb interactions, including band gaps, magnetic ordering, orbital ordering and Jahn-Teller distortion, as well as improved treatment of the lattice and thermodynamics generally.

2

MATERIALS

2.1 VANADIUM DIOXIDE

2.1.1 *Introduction*

VO_2 exhibits several different structural polymorphs,[5,6,9,72,73,74,75,76,77,78,79] including for example VO_2 (A), (B), (BCC), (D), (M2), (M3), (N), (T). In this thesis we concentrate on monoclinic (M1) and rutile (R) VO_2, which are the commonest and two most important polymorphs. VO_2 (R) is nominally Rutile-like, as the structure is isomorphic to the neighbouring TMO TiO_2, with a tetragonal unit cell composed of orthorhombically distorted octahedra. Transition to the low symmetry M1 phase occurs with edge-sharing VO_6 units distorting to break translation symmetry and produce dimerised V-V pairs - the M1 and R phase local geometry is discussed further and in relation to the electronic structure in Chapter 2.1.2.

The M1-R phase transition occurs reversibly on heating and cooling, but as highlighted in Figure 2 also couples to stress[5] and doping,[6,80,81] amongst other parameters such as electric field.[82] Complex phase diagrams across numerous different order parameters hint at rich underlying physics and chemistry. Although ostensibly a simple *d*

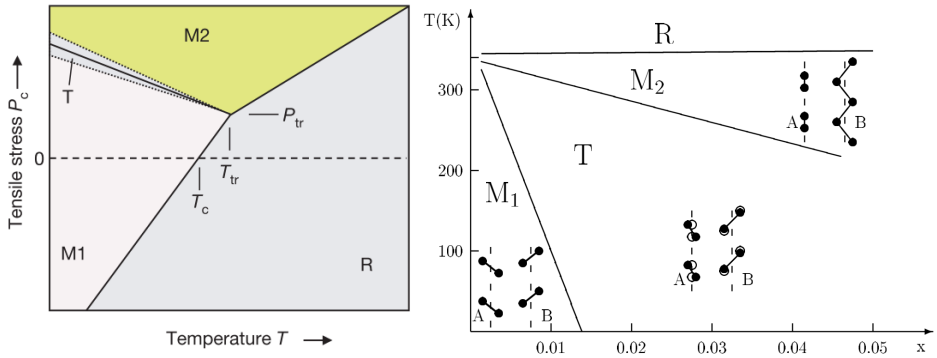

Figure 2: VO_2 phase diagrams in tensile stress,[5] and in dopant concentration,[6] against temperature.

band binary dioxide, research has established VO_2 as a prototype correlated metal oxide that has consistently and widely attracted attention. This includes interest from fundamental condensed matter theory research,[62,71,83,84,85,86,87] state-of-the-art first principles methods,[4,63,88,89,90,91,92,93] inorganic and physical chemistry[26,80,81,94,95,96] and materials design.[8,15,28,29,30,39]

Theoretical intrigue temporarily aside, VO_2 is especially important to materials science, due in large part to the first-order metal-insulator transition (MIT) which occurs at $T_c \approx 340$ K under ambient pressure. Although *vanadic oxide of Berzelius* (as VO_2 was first known) had been synthesised since the late nineteenth century,[97,98,99] several decades of investigation and characterisation passed before the first-order transition in VO_2 was exposed by Archer *et al.*[100], and Morin in the 1950's.[9] The discovery of a phase transition with an abrupt change in properties at T_c, sometimes referred to as the *Janus-faced* character of VO_2, began focused and intense experimental investigation. Some early and fundamental results are reproduced in Figure 3.

Figure 3 includes reports from Verleur *et al.*,[7] which show the qualitative variation in optical transmission. The results of Berglund and Guggenheim,[12] show a discontinuity in magnetic susceptibility, which changes by almost an order of magnitude. Striking reports of electrical conductivity as a function of temperature in Figure 3, show changes over several orders of magnitude (by factors of $\sim 10^{4-6}$), from measurements by Morin,[9] MacChesney *et al.*,[11] Brückner *et al.*,[10] and Babulaman *et al.*.[8]

Underlying the changes in the macroscopic observables at T_c, we can consider variation in local geometry and electronic structure. In Figure 4, metal cations pair in a quasi-one-dimensional chain (V-V dimerisation) redistributing inter-dimer charge on R-to-M1-phase cooling. Figure 4 also shows how the density of electronic states at E_F changes qualitatively as d band degeneracy is lifted on the transition from metal to insulator.

2.1.2 *Lattice and electrons*

The R phase of VO_2, shown in Figure 5, is isomorphic to several centre-table binary metal dioxides. This includes $3d$ transition oxides such

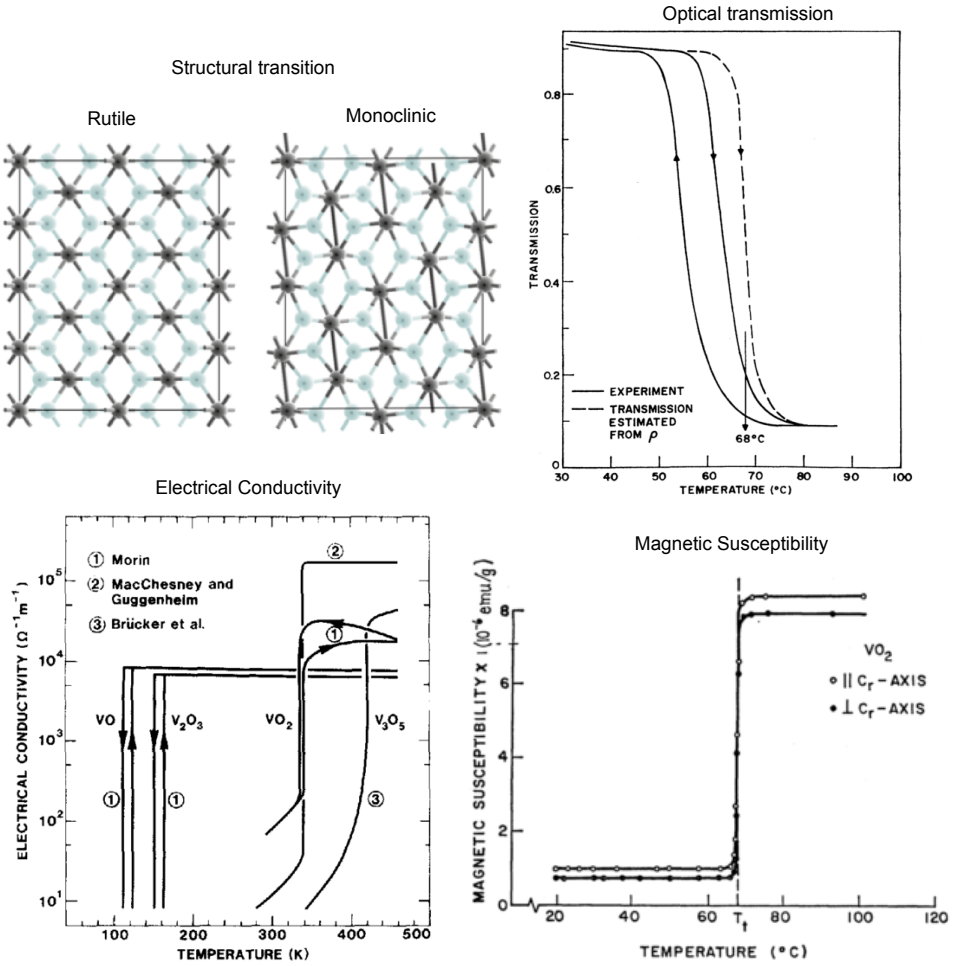

Figure 3: Ball and stick model showing structural transition from high symmetry rutile to monoclinic with dimerised V-V pairs. Experimental characterisation of the VO_2 phase transition: optical transmission[7] through a ~1000 Å thin film; electrical conductivity[8] in single crystals (Morin[9] & Brücker[10]) and a ~7000 Å thin film (MacChesney[11]); magnetic susceptibility[12] in a single crystal.

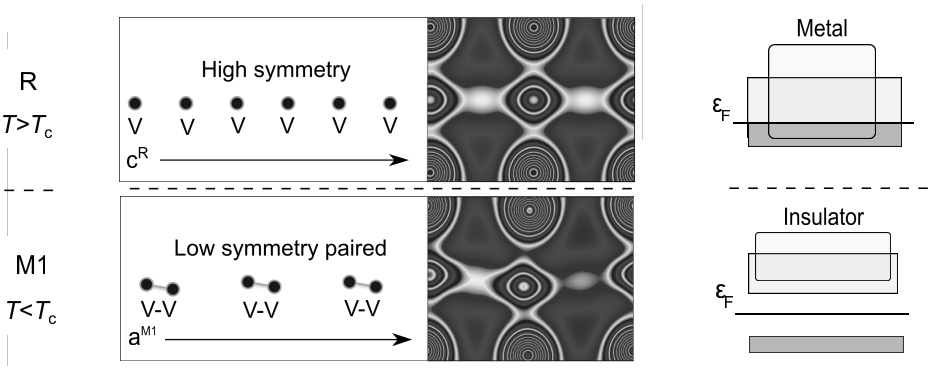

Figure 4: Qualitative features of the VO_2 phase transition: schematics of transition dimerisation in 1-dimensions, charge density in 2-dimensions, and electronic band gap from metal to insulator.

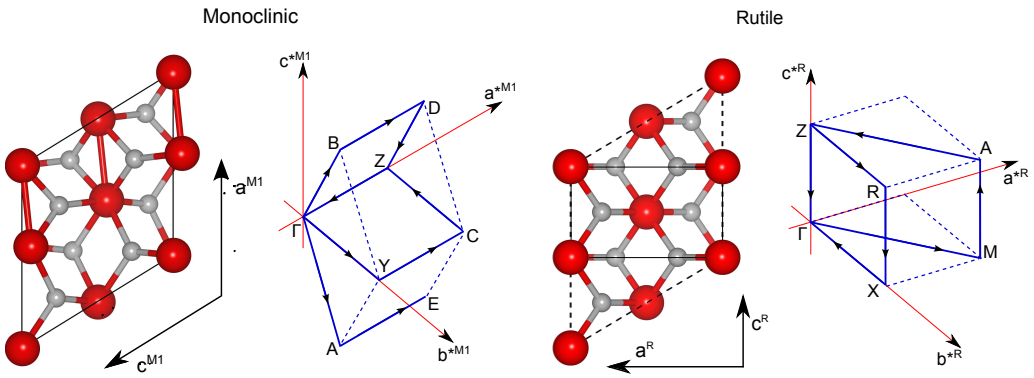

Figure 5: Unit cell and reciprocal space representations of the $P2_1/c$ (No. 14) symmetry VO_2 (M1), and $P4_2/mnm$ (No. 136) symmetry VO_2 (R) with M1 unit cell overlay.

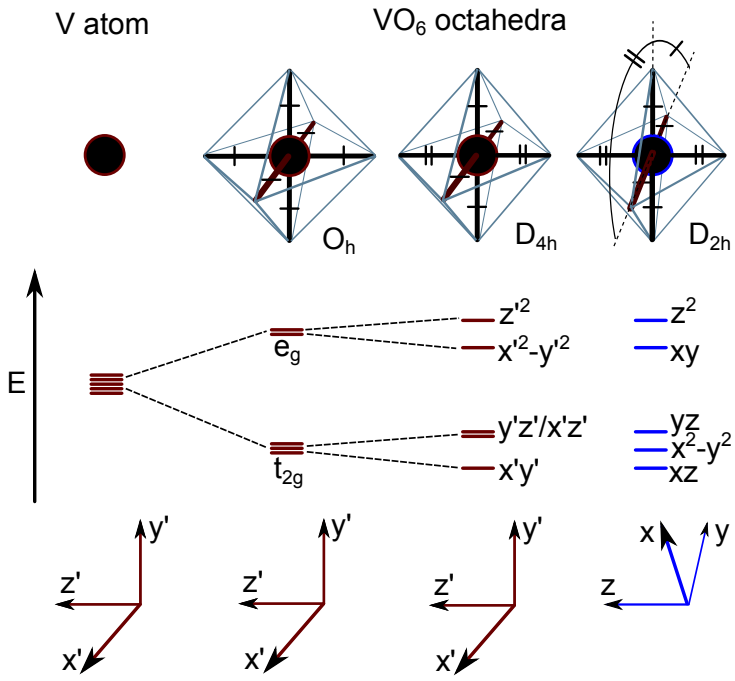

Figure 6: Qualitative schematic of energy level splitting in piecewise point group symmetry breaking, from spherical atomic to perfect O_h cubic, D_{4h} tetragonal and finally the D_{2h} orthorhombic VO_6 units found in VO_2 (R). Orthorhombic distortions in VO_2 (R) octahedra are described within a local basis (unprimed, blue) related to the VO_6 bond axial basis (primed, maroon) by a $\frac{\pi}{4}$ rotation. This switches d_{xy} and $d_{x^2-y^2}$ orbital labels, such that 'e_g' states are $d_{3z^2-r^2}$ and d_{xy}, and the 't_{2g}' states are d_{yz}, $d_{x^2-y^2}$ and d_{xz}.

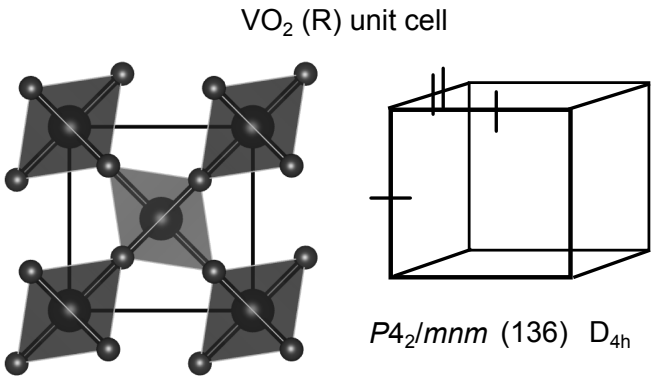

Figure 7: D_{2h} point group symmetry octahedra with orthorhombic distortions in VO_2 (R) combine to lift the space group symmetry to D_{4h} tetragonal.

as TiO_2 (*i.e.*, Rutile), CrO_2 and MnO_2, and from the $4d$ period, NbO_2, MoO_2, TcO_2, RuO_2 and RhO_2.

The Rutile-like VO_2 (R) has tetragonal symmetry with $P4_2/mnm$ (No. 136, D_{4h}) space group,[82] and a lattice defined by the two parameters $a^{\mathrm{R}} = 4.554$ Å and $c^{\mathrm{R}} = 2.856$ Å.[39]

The six atom VO_2 (R) unit cell comprises contributions from two VO_6 units. Perfect cubic O_h symmetry in each VO_6 is broken by contracting two V-O bonds to create two apical oxygen with $d(\text{V-O}) = 1.86$ Å and four basal oxygen with $d(\text{V-O}) = 1.97$ Å. Tetragonal D_{4h} symmetry is broken when the basal O-V-O angle deviates from $\frac{\pi}{2}$ by ± 0.029, lowering octahedral symmetry to the D_{2h} point group. A piecewise schematic of the point group symmetry breaking is shown in Figure 6, along with the unit cell with lifted space group symmetry in Figure 7.

The two octahedral units in the R unit cell are equivalent up to a $\frac{\pi}{2}$ rotation about c^{R}, which lifts the D_{2h} octahedral point group symmetry to D_{4h} space group symmetry in the unit cell. Repetition of the VO_2 (R) unit cell forms chains of edge sharing VO_6 octahedra in c^{R}, which are interlinked by corners.

In the VO_2 (R) electronic structure, the crystal field splits degenerate d bands into an 'e_{g}' band comprising $d_{3z^2\text{-}r^2}$ and d_{xy} states, and a 't_{2g}' band made up of $d_{x^2\text{-}y^2}$, d_{xz} and d_{xz}, as shown in Figure 6. This designation is atypical because the VO_6 octahedra in VO_2 (R) have orthorhombic distortions, so a natural local basis cannot be chosen

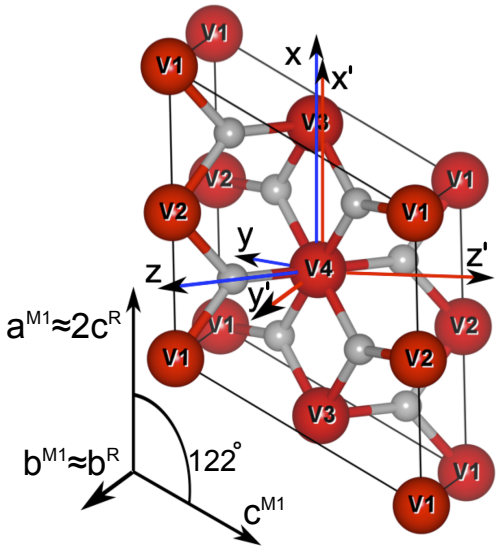

Figure 8: R phase in a $P2_1/c$ M1-like unit cell. Global axial Cartesian coordinates are denoted $x'y'z'$, local basis choice xyz, and lattice vectors abc.

with octahedral xyz axes pointing towards O ligands. To accommodate the non-orthogonal distortions a new local basis is chosen that bisects octahedral V-O bond axial directions, through a $\frac{\pi}{4}$ rotation about the z (apical V-O) axis. Since the d_{xy} and $d_{x^2-y^2}$ are equivalent up to a $\frac{\pi}{4}$ rotation about z, these orbital states are flipped with respect to the e_g and t_{2g} cubic group terms.

For each octahedral frame, a local basis is specified to diagonalise the d shell density matrix eigenvectors (for diagonalisation matrix, see Chapter 6). The rutile local octahedral basis is shown in Figure 8 with respect to an M1-type unit cell basis. The VO_2 (R) octahedra in Figure 8, *i.e.* 'V3' & 'V4', and 'V1' & 'V2', are related by a $\frac{\pi}{2}$ rotation about c^R (x).

The conventional $d_{||}$ and π^* symmetry VO_2 orbitals[6,83,85,101] are related to the canonical atomic-type states by Equation 1, and VO_2 σ^* states by Equation 2

$$t_{2g}\begin{cases} "d_{||}" = x^2 - y^2 & (Y_{22}) \\ "\pi^*" = yz + xz & (Y_{2-1} + Y_{2+1}) \end{cases} \tag{1}$$

$$e_g\begin{cases} "\sigma^*" = 3z^2 - r^2 + xy & (Y_{20} + Y_{2-2})\ . \end{cases} \tag{2}$$

The Y_{lm} angular terms are real spherical harmonics, where each Y_{lm} is a linear combination of Y_l^m complex harmonics:

$$Y_{lm} = \begin{cases} \frac{i}{\sqrt{2}}(Y_l^m - (-1)^m Y_l^{-m}) & \text{if } m < 0 \\ Y_l^0 & \text{if } m = 0 \\ \frac{1}{\sqrt{2}}(Y_l^{-m} + (-1)^m Y_l^m) & \text{if } m > 0\,. \end{cases}$$

While the $d_{||}$ state has lobes pointing along local x and y axes to octahedron edge centres (see Figure 8), π^* states are formed from xy and xz orbitals, so have lobes pointing toward octahedron faces. The z^2 part of σ^* states point along the apical V-O bonds in the local z axes. The xy part of σ^* is confined to the basal plane and has lobes pointing along the basal V-O bonds to octahedron corners.

The twelve atom VO_2 (M1) unit cell, shown in Figure 5, has the symmetry group $P2_1/c$ (No. 14, C_{2h}), with a lattice defined by the parameters $a^{M1} = 5.752$ Å, $b^{M1} = 4.538$ Å, and $c^{M1} = 5.383$ Å, and $\beta = 122.6^o$.[102]

The most prominent structural feature of the M1 phase is the quasi-one-dimensional chain of dimerised V-V units along the a^{M1} ($\sim c^R$) axis. The metal-metal pairing produces a 2.6 Å to 3.2 Å alternating V-V bond length, for intra and inter-dimer V distances respectively.[6]

In addition to the metal pairing, apical V-O distances form an alternating long-short pattern, producing the zig-zag tilting of the V-V dimers in a^{M1} ($\sim c^R$).

The crystallographic transition (from R to M1) can expressed as a basis transformation of the lattice vectors. The transformation matrix is not unique due to degeneracy in **a** and **b** R phase lattice vectors[78,103,104] - here we assume the convention

$$\begin{pmatrix} \mathbf{a} \\ \mathbf{b} \\ \mathbf{c} \end{pmatrix}_{\mathrm{M1}} = \begin{pmatrix} 0 & 0 & 2 \\ 0 & 1 & 0 \\ -1 & 0 & 1 \end{pmatrix} \begin{pmatrix} \mathbf{a} \\ \mathbf{b} \\ \mathbf{c} \end{pmatrix}_{\mathrm{R}},$$

where $\mathbf{a} = a_1\hat{\mathbf{e}}_x + a_2\hat{\mathbf{e}}_y + a_3\hat{\mathbf{e}}_z$, $\mathbf{b} = b_1\hat{\mathbf{e}}_x + b_2\hat{\mathbf{e}}_y + b_3\hat{\mathbf{e}}_z$ and $\mathbf{c} = c_1\hat{\mathbf{e}}_x + c_2\hat{\mathbf{e}}_y + c_3\hat{\mathbf{e}}_z$. Lattice transformation from $P4_2/mnm$ to $P2_1/c$ occurs on cooling due to soft modes at special point $\mathbf{R}$ $(0, \frac{1}{2}, \frac{1}{2})$[78,82] on the reciprocal lattice in Figure 5. The Mott-Hubbard or Peierls paradigmatic origin of imaginary transition phonon modes, and even how much entropy the phonons contribute as a fraction of the total transition latent heat, are matters of much debate, and will be discussed in detail in following chapters.

2.1.3 *Technological applications*

Research into the switchable material characteristics of VO_2 is driven by hope to develop novel technology, such as energy saving applications. Ideas being explored for commercial potential include microelectronics applications, such as the VO_2 Mott field-effect transistor (MFET),[13,105] which is a three pin switch for use in logic circuits (see Figure 9).[13] Electrostatic fields[13,82,105] or photo excitation,[106,107,108] can induce a MIT in VO_2 that is much faster than the usual transition, removing the dependence on lattice modes. This can be exploited to engineer an ultra-fast three terminal switch that lacks the speed limitations in usual field-effect transistors.[13] As electrostatic fields permeate metals and insulators differently, this provides means to modify the transition temperature T_c of the thermally activated transition, in addition to switch between phases about T_c electrostatically.[13]

VO_2 can also be employed as a micro-scale actuator, based on the large transformational strain (~ 1 % in c^R) from M1 to R phase.[14,109] Conventional bilayer thermal actuators rely on the differences in material's thermal expansion coefficients that are usually linear. In VO_2-based bimorph cantilevers, the actuation amplitudes measured close to T_c can be *much* larger, indeed several orders of magnitude larger than conventional bilayer materials. In addition VO_2 strain actuators have the advantage of coupling to several order parameters (electric

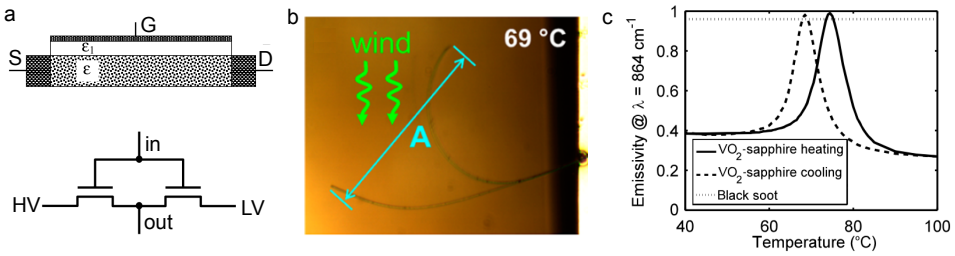

Figure 9: a) *Top*: VO_2 Mott field-effect transistor (MFET) with 'gate', 'source' and 'drain', showing the dielectric (ε_1) and the VO_2 (ε) thin-films. *Bottom*: two gate MFET logic circuit.[13] b) VO_2/Cr bimorph cantilever showing large amplitude actuation on 'wind' cooling about T_c.[14] c) VO_2 blackbody emissivity at T_c, compared to soot.

field, temperature, photon fluence, *etc.*), and due to drastic abrupt strain variation, produce actuation with a very high work-capacity to size ratio.[109]

Recent research by Kats *et al*. touts VO_2 as a 'perfect' blackbody emitter with potential for applications in infra-red (IR) camouflage, thermal regulation and IR tagging.[110] In thin-film VO_2, emissivity increases gradually in temperature, with a steep maximum centred around T_c which occurs due to the formation of regional nanoscale islands of M1 and R. The domains of disordered phase constitute a *metamaterial*, with IR losses comparatively greater than a 'black suit' reference at T_c, but strongly tuned by temperature variation.

Under the general heading of chromogenic activity, which is displayed by many TMO such as TiO_2 and MoO_2 photochromism and NiO and WO_3 electrochromism, VO_2 is *thermochromic* in that the optical properties change significantly with temperature. This provides perhaps the most discussed application of the VO_2 phase transition, in thermochromic coatings for *smart windows*.[8,15,24,25,26,27,28,29,30]

Thermochromic coatings of VO_2 work on the basis that IR solar through-put can be modulated as a function of temperature, as shown in Figure 10. For solar radiation, the IR component is partially blocked when a thin-film coating made of VO_2 increases in temperature above T_c. This acts to minimise excessive indoor warming on a hot day, while the opposite process can occur to retain heat upon cooling below T_c.

Thermochromic VO_2 coatings for windows have yet to find commercial success. Since their inception,[8] progress has stalled for several reasons:

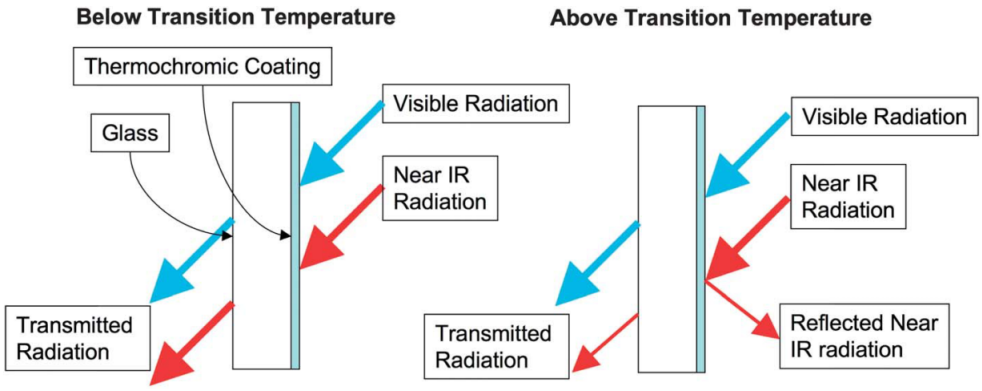

Figure 10: Schematic of the temperature dependent optical response exploited in thermochromic applications such as VO_2 smart windows.[15]

- The MIT in defect-free single-crystal VO_2 has a T_c of $\approx$ 340 K, far in excess of the ideal ambient room temperature.
- The spectral position (wavelength) of the peak transmission change is broad, and not confined to the IR region ideal for smart windows.
- The transition is asymmetric due to a wide hysteresis band.
- Absorption in the 400 - 700 nm optical band degrades transparency.
- The peak modulation in energy through-put is not large enough to be cost effective.

Many problems can be rectified by incorporating dopant atoms. For example, T_c can be tuned to near room temperature by doping with tungsten (at $\approx$ 20 K/1 at. % W).[94] Fluorine doping on anion sites also strongly reduces the T_c ($\approx$ 20 K/1.2 at. % F), but fluorine usefulness is tempered by an increase in the hysteresis width.[111,112]

Reduction in the transition hysteresis width is possible by titanium doping on cation sites.[113,114] The hysteresis width of 30 K in pristine nanoparticles, was reduced to 5 K for titanium doped particles with composition $V_{0.91}Ti_{0.09}O_2$.[113] Further developments include increased luminosity on magnesium doping and fluorine doping. In particular recently, co-doping has received much attention for promise of further improvements.[115,116,117]

On the side of theory, *ab initio* methodologies to treat VO_2 and advances in computing power have made possible demanding calculations of $V_{1-x}M_xO_2$ at low metal dopant concentration. Theoretical methods are now capable of investigating selective optical, structural and thermodynamic aspects of doped VO_2.[90,118,119,120] As a stepping stone to investigation of material properties relevant to applications, we present a study of the VO_2 (R) surface thermodynamics, predicting surface oxidation states in temperature and pressure - see Chapter 8.

2.1.4 *Phase transition origin*

Despite strong credentials for materials design, progress in real-life technological applications of VO_2 has been largely hampered by an incomplete theoretical understanding. One of the oldest but still actively debated topics concerns the relative role of electrons *vs* the lattice in the phase transition mechanism. This question in particular concerns whether the transition is driven by effects described best within the Peierls paradigm, or more appropriately by the alternative Mott-Hubbard physics and chemistry.

Since focused research into the VO_2 phase transition began in the 1950's,[9,100,121] much of the debate has been polarised. Many claim the transition occurs by Peierls transition *i.e.*, due to e-l interactions,[122] where perturbation of the quasi-one-dimensional V-V chain produces strong temperature dependent phonon softening and homopolar metal-metal bonding.[85] Others claim a Mott-Hubbard (e-e interaction) mechanism,[83,84,123] where strong intra-orbital Coulomb repulsion between localised valence electrons is critical. To reconcile the very different theoretical arguments and convincing experimental evidence on both sides, modern consensus appears to be moving against an exclusive e-e correlation or e-l Peierls transition, in favour of a joint Mott-Hubbard-Peierls paradigm.[63,71,124]

The relative influence of Mott-Hubbard or Peierls interactions in the transition is difficult to estimate quantitatively, however it possible to calculate the transition entropy from electronic and lattice contributions. The total latent heat of transition is experimentally known to be 44 meV/VO_2,[125] but the origin of the entropic contributions that drive the transition and produce this heat at T_c are less well under-

stood. Precisely, the origin of the transition entropy has historically been widely disagreed upon.[12,83,125,126,127,128] Suggestions range from a lattice to electron entropy ratio of 2 : 3 according to Pintchovski *et al.*,[125] to a ratio of 100 : 1 according to Hearn.[127] The transition entropy question is explored and answered in Chapter 7.

2.2 MANGANESE DIOXIDE AND THE LI-AIR BATTERY

Manganese dioxide (MnO_2) has been widely investigated as a cathode material in lithium-ion batteries, due to their Li intercalation capacity (forming Li_xMnO_2 phases), low toxicity, and relative low cost compared to oxides of other metals like Co or Ni.[129,130,131,132] Several MnO_2 polymorphs have been investigated in the context of Li-ion cells, including α-MnO_2 (hollandite), β-MnO_2 (pyrolusite), γ-MnO_2 (nsutite) and R-MnO_2 (ramsdellite).[129] Contrasting with other polymorphs, the rutile-structured phase (β-MnO_2) does not seem to be able to intercalate Li in the bulk, while mesoporous samples of the same polymorph do exhibit high Li uptake.[43] A recent computer simulation study by Tompsett *et al.*[40] has shown that there is an energy barrier (> 0.6 eV) for diffusion of Li from the surface to the bulk of β-MnO_2, which they demonstrate to be due to the much higher electrostatic potential (and therefore higher insertion energy) within the bulk. It thus seems plausible that most of the Li incorporated in β-MnO_2 lies at the surface (that is, in the walls of the pores), which would explain why mesoporous samples are able to accommodate much more Li than highly crystalline samples.

The Li–air system is a novel battery technology which promises higher specific energy than Li-ion batteries. In this battery the cathode reaction is not the formation of an intercalation compound but the reduction of oxygen gas in the presence of Li^+ ions forming lithium peroxide Li_2O_2 (or LiOH in the aqueous version).[16,133,134,135,136] Manganese oxides may also play an important role here: it has been shown that nanostructured MnO_2 in different polymorphic states are able to catalyse the formation and decomposition of Li_2O_2 in the cathode, thus decreasing the over-potentials required for the operation of the Li–air cell.[137] In this case it is the surface rather than the bulk of the manganese oxide which controls its function in the cathode, and there-

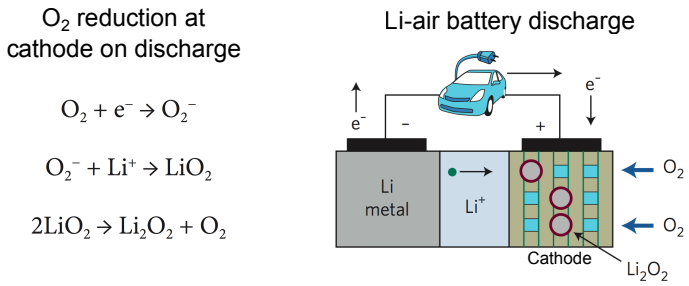

Figure 11: Li-air battery operation by reduction of O_2 at the cathode,[16] which can be composed of porous carbon with a β-MnO_2 catalyst.

fore the lack of Li intercalation in bulk β-MnO_2 should not limit its utilisation. Understanding the behaviour of the cathode catalysts is the key for improving the function of Li–air batteries.[31]

To gain insight of the molecular processes occurring at the Li–air battery cathode reaction in the presence of β-MnO_2, we investigate the simultaneous adsorption of lithium and oxygen at the most stable (110) surface of β-MnO_2. For a details on Li and O adsorption thermodynamics and charge transfer at the β-MnO_2 surfaces - see Chapter 9.

2.3 LANTHANUM MANGANITE

$LaMnO_3$ or lanthanum manganite (LMO) is characteristic of the ABO_3 family of strongly correlated TMO perovskites, which exhibit particularly rich and multi-faceted phase diagrams, usually in terms of several parameters.[138] Bulk, thin film, and interfacial $LaMnO_3$ are subject to a multitude of symmetry breaking, from crystal field,[138] octahedral distortion,[139] orbital ordering and Jahn-Teller (JT) distortion,[45,53,55,140,141] Mott-type strong d electron Coulomb interactions (direct and exchange),[142,143] and charge-transfer ordered (Verwey) states.[46,144,145] In LMO all of these mechanisms are believed to exist and compete in varying degrees. In particular the characteristic ordering and symmetry breaking *via* superexchange, JT distortion and orbital splitting from on-site Coulomb interaction, which are illustrated in Figures 12 & 13, are investigated in this thesis.

The complex phase diagram of LMO, in temperature, pressure[141] and dopant concentration,[36,37] make it the single most examined metal oxide in the La$M$$O_3$ class (where M is a transition metal atom).[146]

Doping on the ABO_3 A site leads to notable experimentally observable phenomena - for example Na and Ca doped $La_xA_{1-x}MnO_3$ can exhibit colossal magneto resistance (CMR)[47,147] and a Seebeck coefficient that can exhibit positive or negative values which may lead to potential thermopower applications.[48]

Pure bulk $LaMnO_3$ is spin polarised and not polar (see Figure 12), but recent theoretical work shows that the magnetic state in Sr doped $La_xSr_{1-x}MnO_3$ may be controlled through variation in the electric polarisation state.[36] Recent multi-ferroic theory predicts novel magnetic properties due to t_{2g} ferromagnetic superexchange in Ti-doped $LaMnO_3$ interfaces.[148] Finally, the interface between $La_xSr_{1-x}MnO_3$ and $BaTiO_3$ shows a polar state that also has a reversible orbital polarisation.[149] The coupling between magnetic state and ferroelectric polarisation at manganite interfaces is far from understood and a major interest to fundamental science, but also holds great potential to non-volatile data storage and memory device development.[32,33,34,35,36]

The fascinating basic physics and chemistry of LMO, even in the relatively simple undoped LMO bulk form, is evident from Figures 12 & 13. Results presented in Chapter 10, concern both details on the physical and chemical nature of LMO, and how to achieve a low computational cost and reliable *ab initio* description relevant to materials science.

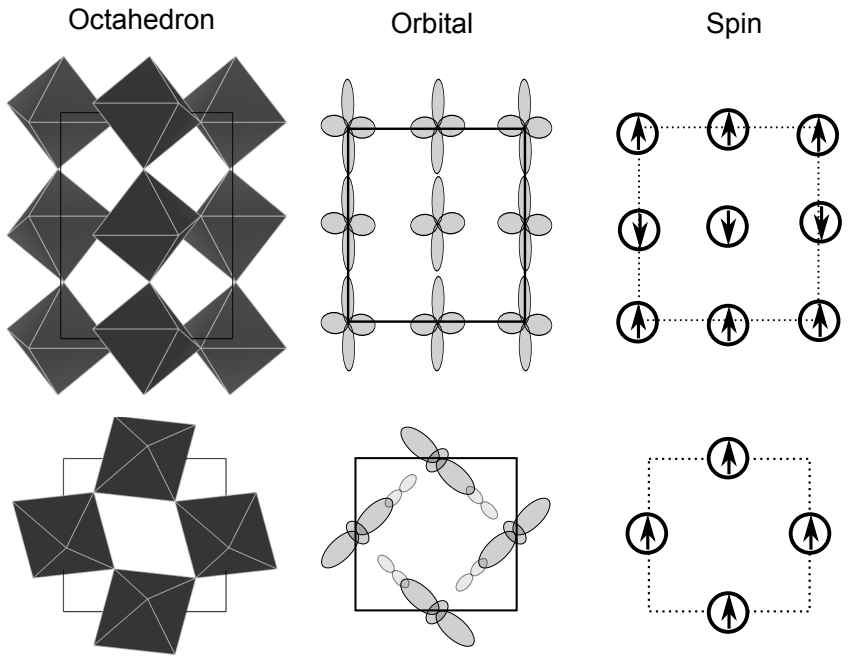

Figure 12: Bulk $LaMnO_3$ unit cell showing ordering in the local geometry of tilted MnO_6 octahedron, and in the orbital and spin structures.

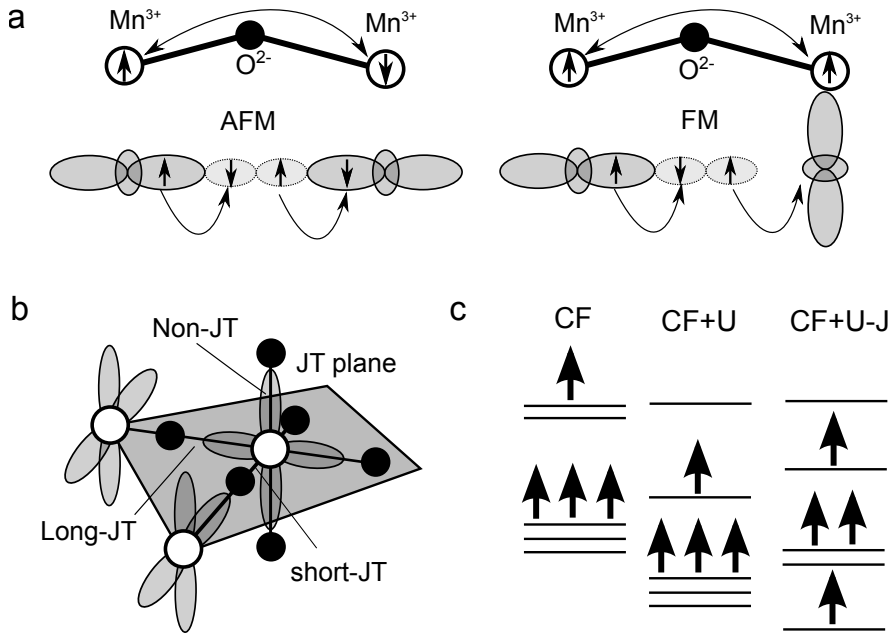

Figure 13: a) Exchange coupling of Mn sites through a diamagnetic O centre. Goodenough-Kanamori rules suggest AFM or FM Mn-Mn coupling, depending on the orbital ordering which differs in-plane and out-of-plane. b) Jahn-Teller distortion in the orbitally ordered FM coupled plane. c) Qualitative model schematic of piecewise occupancy symmetry breaking in energy levels, due to crystal-field (CF), on-site Coulomb (U), and on-site anisotropic exchange (J).

Part II

Methods

3

THEORETICAL BACKGROUND

In this first of three methodology sections we give a short introduction to the electronic structure theory relevant to the materials in this thesis. This is mainly an introduction to the basic *ab initio* techniques, but some theoretical background relevant to *strongly correlated oxides* in materials science is also included. Natural atomic units, $e^2 = \hbar = m_e = 1$, are assumed throughout unless noted otherwise. For brevity and readability of expressions, coordinate dependence is often implied, for example, charge density may be given as $\rho = \rho(\mathbf{r})$.

3.1 INTRODUCTION

In analogy to Hamilton's formulation of classical mechanics[150,151], many theoretical approaches to describe the electronic properties of physical systems begin posing a Hamiltonian $\hat{H}$ for a system of electrons and nuclei

$$\hat{H} = \hat{T} + \hat{V}\,. \tag{3}$$

In the Hamiltonian, $\hat{T}$ is the kinetic energy operator, and $\hat{V}$ is the operator corresponding to the potential energy of interactions. The ground state energy E, is given by variational principle[152]

$$E = \min_{\Psi} \langle \Psi | \, \hat{H} \, | \Psi \rangle \,, \tag{4}$$

with minimisation over all antisymmetric N-particle wave functions.

In 1926 Schrödinger used the above general form to describe electron-nucleus systems,[153] such as atoms and molecules. The non-relativistic time-independent† Schrödinger equation[153] is

$$\mathscr{H} \; \Psi(\{\mathbf{R}\}, \{\mathbf{r}\}) = E \, \Psi(\{\mathbf{R}\}, \{\mathbf{r}\}) \,, \tag{5}$$

where $\{\mathbf{X}\}$ is the set of coordinates for nuclei and for electrons. The Schrödinger Hamiltonian $\hat{\mathscr{H}}$ operates in the Hilbert space of the electronic-ionic system with wave function $\Psi(\{\mathbf{R}\},\{\mathbf{r}\})$. In *electronic structure theory*, which permeates all aspects of chemistry, much effort has been devoted to finding the 'best' approximate methods to solve the Schrödinger equation.

The Born-Oppenheimer approximation[154] allows Equation 5 to be reduced to a more soluble form by decoupling the motion of the heavy ions, the $\{\mathbf{R}\}$ coordinates, and the light electrons, the $\{\mathbf{r}\}$ coordinates. This approximation is based on the orders of magnitude difference in mass, and therefore velocity, of the nuclei and the electrons. Adiabatic separation of the $\{\mathbf{R}\}$ nuclear coordinates from the $\{\mathbf{r}\}$ electronic coordinates reduces the degrees of freedom considerably, with the approximation holding to a high degree except for in cases with strong electron-nucleus coupling, such as superconductors.

Treating the motion of electrons in a static ionic potential, the Schrödinger equation in the Born-Oppenheimer approximation is

$$\hat{\mathcal{H}}\,\Phi(\{\mathbf{r}\}) = E\,\Phi(\{\mathbf{r}\})\,. \tag{6}$$

$\hat{\mathcal{H}}$ takes the usual Hamiltonian form

$$\{\hat{T}+\hat{V}\}\Phi(\{\mathbf{r}\}) = E\Phi(\{\mathbf{r}\})\,,$$

and expanding the terms, $\hat{T}$ is a sum over the Laplacian ($\triangle = \nabla\cdot\nabla$), and $\hat{V}$ is a sum over electrostatic terms for e-e and e-l Coulomb interactions

$$\frac{1}{2}\sum_i\left(-\triangle_i + \sum_j \frac{1}{|\mathbf{r}_i-\mathbf{r}_j|} + 2U_{\text{ion}}(\mathbf{r}_i)\right)\;\Phi(\{\mathbf{r}\}) = E\,\Phi(\{\mathbf{r}\})\,. \tag{7}$$

Unfortunately, even this non-relativistic and time-independent Schrödinger equation in the Born-Oppenheimer approximation is still much too tricky to solve for ordinary materials and all but the simplest atoms. Fortunately, many non-exact solution techniques have been developed, often based on the reasoning that an approximate reduced form of $\Phi(\{\mathbf{r}\})$ can be used. This assumption works because often much of the wave function is either sparse or duplicated - not much happens

and when it does it happens again. This statement is closely related to what Kohn called the *near-sighted nature of quantum mechanic*s, and is much discussed by Bader (see margin note ⋆).[155]

One of the most important techniques that employs an approximate wave function is called Hartree-Fock (HF).[158] HF has a built-in exchange-correct mean-field Coulomb interaction as a result of the approximate 'single-electron' or independent-particle state function used.[65,159,160] In HF the state function for fermions, in our case the set of all electrons, is expressed as a single antisymmetrised product of one-body spin-orbitals called a Slater determinant[161]

$$\begin{aligned}\Phi_{\text{Slater}}(\{\mathbf{r}\}) &= \frac{1}{\sqrt{N!}}\sum_{P}(-1)^{P}[\varphi_{P(1)}(\mathbf{r}_1)\varphi_{P(2)}(\mathbf{r}_2)\dots\varphi_{P(N)}(\mathbf{r}_N)] \\ &= \frac{1}{\sqrt{N!}}\begin{vmatrix}\varphi_1(\mathbf{r}_1) & \dots & \varphi_1(\mathbf{r}_N)\\ \vdots & \ddots & \\ \varphi_N(\mathbf{r}_1) & & \varphi_N(\mathbf{r}_N)\end{vmatrix}.\end{aligned}$$

Φ_{Slater} has the advantage of naturally enforcing the Pauli exclusion principle for degenerate quantum numbers, but if the one-electron orbitals were chosen arbitrarily, the single Slater determinant approximation could be poor. To avoid this HF employs the variational principle introduced in Equation 4. The HF wave function is the Slater determinant that minimises variations in the expectation of the Hamiltonian ($\hat{\mathcal{H}}$ in Equation 6) with respect to single-particle states, $\delta E = \delta\left\langle \Phi \middle| \hat{\mathcal{H}} \middle| \Phi \right\rangle = 0$. The total energy expectation is expressed most transparently in bra-ket notation which highlights cancellation in the direct-exchange Coulomb mean-field (in square brackets) for δ_{ij},[160]

$$E_{\text{HF}} = \sum_{i}^{N}\left\langle i \middle| \hat{T} + \hat{V}_{\text{ext}} \middle| i \right\rangle + \frac{1}{2}\sum_{i,j}[\left\langle ij \middle| \hat{U} \middle| ij \right\rangle - \left\langle ij \middle| \hat{U} \middle| ji \right\rangle].$$

The HF equations are solved iteratively, in the sense that an initial Slater wave function is used to form the direct-exchange Coulomb mean-field which in turn determines a new Slater determinant.

Other more complicated approaches to a wave function such as configuration interaction (CI),[162] expand the number of Slater determinants, whereas sampling based methods such as quantum Monte

⋆ *Every element of the wave function is not coupled equally to every other. 'Near-sighted quantum mechanics' permits for example the single-particle approximation, and is central to linear scaling ab initio methods.*[156,157]

Carlo (QMC) increase variational freedom even further.[163] In QMC a sum of determinant products is multiplied by a correlation function called a Jastrow factor,[164] producing a very open and complicated wave function that is trialled using weighted random sampling.

One of the most successful approximate solutions to the Schrödinger equation is provided by a method called DFT, which was developed by Kohn and Sham (KS) based on the theorems of Höhenberg and Kohn (HK). The DFT paradigm maps an interacting wave function problem to a non-interacting density problem. Observable expectation values calculated from electron density $\rho(x, y, z)$ opposed to a wave function $\Phi(\{x_i, y_i, z_i\})$, have the advantage of reduced complexity, lowering the number of dimensions by at least $3N_e - 3$.

In DFT the biggest energy terms, which are single-body interactions such as kinetic and Hartree, are used in exact form.[160] The smaller energy contributions, which are also the more complicated higher-order terms responsible for quantum many-body effects (exchange and correlation), are usually approximated.[160] As in HF, the DFT problem is solved variationally by iteration to self-consistency. Kohn-Sham (KS) DFT minimises density functional Euler-Lagrange equations with respect to density. This yields an exact ground state density $\rho = \rho_0$ that satisfies

$$\frac{\delta}{\delta\rho}\{T_s[\rho] + V_{ee}[\rho]\} + \frac{\partial V_{\text{ext}}(\rho)}{\partial\rho} = 0\,.$$

The ground state total energy E is given by the sum of the density functional terms when $\rho = \rho_0$,

$$E[\rho] = T_s[\rho] + V_{ee}[\rho] + V_{\text{ext}}(\rho)\,.$$

$T_s[\rho]$ is kinetic energy (differing from $T[\rho]$ by the single-particle approximation), $V_{\text{ext}}[\rho]$ and $V_{ee}[\rho]$ are the ionic (external) and electronic potential interaction energies. In terms of computation the e-e term $V_{ee}[\rho]$ is most challenging. The characteristic DFT approach to overcome this problem is to calculate a density-density Hartree interaction and collect higher-order interactions, such as exchange and correlation into the so-called exchange-correlation (XC) term.

3.2.1 *Höhenberg-Kohn theorems*

The Höhenberg-Kohn (HK) theorems prove an equivalence that uniquely maps the ground state density $\rho_0(\mathbf{r})$ to the much more complicated many-body electronic wave function $\Phi(\{\mathbf{r}\})$.[165] The one-to-one mapping is set on sure and useful footing by three main points (two theorems and a corollary), which are discussed next.

- HK THEOREM 1: Two different external potentials, $v_{\text{ext}}(\mathbf{r})$ and $v'_{\text{ext}}(\mathbf{r})$, cannot give rise to the same ground state density $\rho_0(\mathbf{r})$.

Proof by contradiction - assume two external potentials $v_{\text{ext}}(\mathbf{r})$ and $v'_{\text{ext}}(\mathbf{r})$ differing by more than an additive constant can give the same ground state $\rho_0(\mathbf{r})$. Two different potentials produce two different Hamiltonians, $\hat{H}$ and $\hat{H}'$. Solving for the associated ground state-functions,

$$E = \langle \phi | \hat{H} | \phi \rangle$$

and

$$E' = \langle \phi' | \hat{H}' | \phi' \rangle .$$

By the variational principle

$$E = \langle \phi | \hat{H} | \phi \rangle < \langle \phi' | \hat{H} | \phi' \rangle ,$$

where adding and subtracting $\langle \phi' | \hat{H}' | \phi' \rangle$ leads to

$$E < \langle \phi' | \hat{H}' | \phi' \rangle - \langle \phi' | \hat{H} - \hat{H}' | \phi' \rangle .$$

Therefore,

$$E < E' + \int dr \; \rho_0(\mathbf{r}) \, (v_{\text{ext}}(\mathbf{r}) - v'_{\text{ext}}(\mathbf{r})). \tag{8}$$

Repeating the steps but swapping the primes leads to

$$E' < E + \int dr \; \rho_0(\mathbf{r}) \, (v'_{\text{ext}}(\mathbf{r}) - v_{\text{ext}}(\mathbf{r})). \tag{9}$$

Equations 8 & 9 together imply

$$E + E' < E' + E.$$

This contradiction implies a unique, one-to-one mapping between the ground state density and potential.

- Corollary: $\rho_0(\mathbf{r})$ uniquely determines the external potential $v_{\text{ext}}(\mathbf{r})$ and therefore the state-function $\phi(\mathbf{r})$.

This addendum which rigorously and uniquely maps $\rho_0(\mathbf{r})$ to $\phi(\mathbf{r})$ was a seminal advance in electronic structure theory, particularly considering the historical context. Formalisms based on electron density, such as the classical electron fluid described in the 1927 Thomas-Fermi theory,[166] were thought extremely crude in comparison to electron wave function provided by the familial D.R. Hartree and W. Hartree in 1935.[167]

- HK theorem 2: The ground state of a system, for a fixed external potential $v_{\text{ext}}(\mathbf{r})$, is given by minimising $E[\rho(\mathbf{r})]$ with respect to $\rho(\mathbf{r})$.

Proof by variational principle. It follows variationally that any $\rho(\mathbf{r})$ that isn't the ground state density, $(\rho(\mathbf{r}) \neq \rho_0(\mathbf{r}))$, necessarily produces an energy higher than the ground state energy.

In short, the first HK theorem provides theoretical rigour for an $\rho(\mathbf{r})$ based approach to electronic structure theory. This is complemented by the second HK theorem, which broadly provides a basis to find the ground state energy, and to do DFT by variational minimisation.

3.2.2 *Kohn-Sham DFT*

The original predecessor of KS DFT was Thomas-Fermi (TF) theory. TF theory treats charge density classically, neglecting exchange and correlation, while borrowing certain quantum concepts such as Fermi statistics and the $\hbar^3$ volume of phase space per two electrons. TF theory modulo amendments by Dirac does provide a treatment of exchange interactions, $\epsilon_x(\rho) \propto -\rho^{4/3}$,[168] and is a close analogue of modern KS DFT. Following historical precedence, we introduce the original TF DFT as a brief prelude to describing KS DFT.

3.2.2.1 *Thomas-Fermi DFT*

In TF theory *every* term is a functional of density $f[\rho]$, with electron density $\rho = \rho(\mathbf{r})$ specified as a continuous function of finding an electron in a d^3r volume element at $\mathbf{r}$. The kinetic functional has the form of homogenous electron gas (HEG) kinetic energy,[168] at the particular electron density of the material

$$T_{\mathrm{TF}} = \frac{3(3\pi^2)^{2/3}}{10} \int d^3r \; \rho^{5/3}(\mathbf{r}) \, .$$

Quantum mechanical Coulomb interaction is approximated with classical interaction between densities in the Hartree term

$$V_{\mathrm{Har}} = \frac{1}{2} \int d^3r \int d^3r' \; \frac{\rho(\mathbf{r})\rho(\mathbf{r}')}{|\mathbf{r} - \mathbf{r}'|} \, . \tag{10}$$

The ionic or external energy is given by

$$V_{\mathrm{ext}} = \int d^3r \; \rho(\mathbf{r}) \, v_{\mathrm{ext}}(\mathbf{r}) \, . \tag{11}$$

This set of density functional equations is solved by variational minimisation, subject to the physical constraints that $\rho(\mathbf{r}) \geq 0$ and $\int d^3r \; \rho(\mathbf{r}) = N$.[168]

The modern DFT of Kohn, Sham and Höhenberg, is based on the same idea of disposing with the complicated wave function in favour of density. Whereas the plain TF theory has only a simple Hartree interaction and neglects quantum many-body effects, KS DFT employs the Hartree interaction and a correcting XC term to account for many-body Coulomb effects.

3.2.2.2 *Kohn-Sham DFT*

KS DFT can be formulated in terms of either *Euler-Lagrange* or *one-electron Schrödinger equation* paradigms. Here we generate the KS DFT as an Euler-Lagrange equation with action minimised in density, and work towards showing the equivalence to a one-electron Schrödinger equation formulation.

The essence of modern DFT can be shown in two steps related to the two HK theorems introduced in Section 3.2.2. The many-body electronic wave function problem is mapped to density, and by the

variational principle, an Euler-Lagrange KS functional equation can be solved iteratively.

In the first step, kinetic and electron-electron terms are considered together in the *universal functional*,[168]

$$F[\rho] = \min_{\Psi \to \rho} \langle \Psi | \, \hat{T} + \hat{V}_{ee} \, | \Psi \rangle = T_s[\rho] + V_{ee}[\rho] \, . \tag{12}$$

The universal functional $F[\rho]$ is so-called because it has the same dependence on electron density for *any* system, regardless of the external potential. $F[\rho]$ is minimised over all antisymmetric wave functions to yield a functional at density ρ.

In the second step, the universal functional is added to the external (material dependent) energy term, and the total functional is minimised in density, as per the second HK theorem

$$E[\rho] = \min_{\rho} \{F[\rho] + V_{\text{ext}}(\rho)\} = T_s[\rho] + V_{ee}[\rho] + V_{\text{ext}}(\rho) \, . \tag{13}$$

In KS DFT, variational minimisation of $E[\rho]$ yields a ground state density satisfying the Euler-Lagrange equation

$$\frac{\delta F[\rho]}{\delta \rho} = -v_{\text{ext}} \, , \tag{14}$$

where particle number is conserved and $v_{\text{ext}} (= \frac{\partial V_{\text{ext}}}{\partial \rho})$ is the external potential as in Equation 11. In Equation 14, if the functional dependence on density is known for each term in $F[\rho]$, a closed set of equations exists and the ground state density can be solved for any material.

The kinetic term $T_s[\rho]$ in $F[\rho]$ is expressed in terms of KS orbitals unlike orbital-free or TF DFT. This dramatically improves the energies from TF DFT,[168] where $T_{\text{TF}}[\rho]$ is a functional of the HEG density. In KS DFT $T_s[\rho]$ is given by the expectation

$$T_s[\rho] = -\frac{1}{2} \sum_{i=1}^{N} \left\langle \varphi_i^{\text{KS}} | \triangle | \varphi_i^{\text{KS}} \right\rangle \, .$$

Note the eigen-bra-kets are not states of the electron but rather of a 'KS fermion'. However the KS orbitals are not mentioned in the HK theorems - this is resolved as the KS states equate with the ground state density *via*

$$\rho(\mathbf{r}) = \sum_{i=1}^{N} |\varphi_i^{\mathrm{KS}}(\mathbf{r})|^2 \,. \tag{15}$$

The electron-electron functional $V_{ee}[\rho]$ from $F[\rho]$ in Equation 14 has two parts - first a Hartree density-density interaction, which is the same as defined previously in TF DFT in Equation 10, and a second XC term

$$V_{ee}[\rho] = V_{\mathrm{Har}}[\rho] + E_{xc}[\rho] \,.$$

The functional derivative of the Hartree energy gives the Hartree potential

$$v_{\mathrm{Har}}(\mathbf{r}) = \frac{\delta V_{\mathrm{Har}}}{\delta \rho(\mathbf{r})} = \int d^3r' \frac{\rho(\mathbf{r}')}{|\mathbf{r} - \mathbf{r}'|} \,,$$

and the XC potential is

$$v_{xc}(\mathbf{r}) = \frac{\delta E_{xc}}{\delta \rho(\mathbf{r})} \,.$$

By summing each of the potentials from the derivative $\frac{\delta F[\rho]}{\delta \rho}$ in the Euler-Lagrange equation, and external one-body potential v_{ext}, we can write the total KS potential

$$v_{\mathrm{KS}}(\mathbf{r}) = v_{\mathrm{Har}}(\mathbf{r}) + v_{xc}(\mathbf{r}) + v_{\mathrm{ext}}\,(\mathbf{r}).$$

Adding v_{KS} to the kinetic energy, we find the the Euler-Lagrange equation is equivalent to N of the single-particle Schrödinger equations, *i.e.*,

$$\{-\frac{1}{2}\triangle + v_{\mathrm{KS}}(\mathbf{r})\}\, \varphi_i^{\mathrm{KS}}(\mathbf{r}) = \epsilon_i^{\mathrm{KS}}\, \varphi_i^{\mathrm{KS}}(\mathbf{r}) \,. \tag{16}$$

This has the same intuitive *ab initio* form as for example, Hartree-type equations, but the KS potential v_{KS} is a 'fictitious' effective potential. KS fermions with eigenstates $\varphi_i^{\mathrm{KS}}(\mathbf{r})$ move in the v_{KS} effective potential and have the spectrum of energy values ϵ_i^{KS}. The single-particle Schrödinger equation is equivalent to the Euler-Lagrange KS picture in Equation 14, which shows explicitly how the KS formulation maps the N-body problem to N single-body problems.

3.2.3 *Magnetism in DFT*

A common extension to DFT is the inclusion of spin polarisation in the XC functional. The spin extension to the local density approximation (LDA) was historically dubbed LSDA, but is now standard - spin dependence is typically now assumed in the basic LDA acronym. In collinear 'spin-DFT', $\rho(\mathbf{r})$ is decomposed into two spin channels, $\rho_\uparrow(\mathbf{r}) + \rho_\downarrow(\mathbf{r})$, for which the KS equations are solved separately. Spin exchange dependence in DFT enters solely through the $E_{xc}[\rho_\uparrow, \rho_\downarrow]$ term. The functional form of every other term remains unchanged.

In the DFT description of exchange interactions and magnetism, several approximations exist. The exchange interaction implemented in LDA or generalised gradient approximation (GGA) DFT is based on the exact but HEG exchange, which differs significantly from real materials. Poor cancellation between self-Hartree and HEG exchange results in the well-known self-interaction cancellation error, for which varieties of self-interaction corrections exist.[169] One effect of electrons interacting with themselves, includes reduced local magnetic moments, amongst other errors characteristic of self-interaction that usually also exist.

In another common approximation, we neglect the possibility of non-collinear magnetic interactions, which can arise from thermal excitation, geometric frustration, or spin-orbit coupling ($\hat{J} = \hat{L} + \hat{S}$).[170] In the materials we examine in this thesis such as VO_2, any non-collinear coupling in trial calculations was found to be weak, so in balance we avoid the added complication of non-collinear magnetic terms. In addition we also completely neglect magnetostatics, such as dipole-dipole interactions. Magnetic dipole interactions typically have a characteristic temperature of ~ 1 K,[171] usually orders of magnitude smaller than Pauli/Coulomb exchange 'interactions'.

In this thesis DFT calculations are performed in the limit of zero temperature (so temperature dependencies are only available implicitly). Complications arise in the DFT description of magnetism, when the spin structure of interest is not the low temperature magnetic ground state. An important and problematic example is if the paramagnetic state of interest exists above the Curie or Néel temperature. In theory we might question whether the paramagnetism is best described

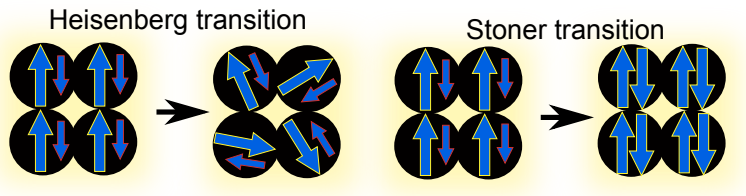

Figure 14: Traditional Stoner and Heisenberg paradigms, for transition between spin polarised (FM) ground state, and a thermally disordered paramagnetic and a non-magnetic paramagnetic states.

within itinerant Stoner or local moment Heisenberg paradigms[172] (see Figure 14). In DFT we must decide whether a static spin polarised or non-magnetic (NM) approximation best captures the material properties of interest. Admittedly, neither a fixed spin polarisation nor NM ordering are ideal descriptions of paramagnetic materials. This is further complicated in materials such as VO_2, where question marks exist over the fundamental origin of the paramagnetic susceptibilities observed experimentally.

3.3 BEYOND DENSITY FUNCTIONAL THEORY

In many materials electrons experience a strong tendency to avoid each other.[65] This tendency occurs in order to reduce Coulomb interaction between the like-charged electrons. Despite the apparent elementary nature of this interaction, the underlying many-body problem is one of the most difficult and general problems in physics. Insomuch, finding acceptable solutions to the Coulomb problem is often rate limiting in the progress of computational materials science.

Approximations used to reduce computational cost must be carefully considered and balanced against averaging out critical physics and chemistry. For example in materials science, Coulomb effects underly the origins of many of the interesting material properties, such as switchable character, magnetism and superconductivity.[65] In this regard, the importance of a Coulomb description beyond the local approximation was pointed out by Hartree and Hartree in the earliest days of modern electronic structure theory.[167] Also apparent unfortunately was the difficulty in dispensing with correlation, compared to

remedying other initial problems such as neglect of relativistic and exchange effects.[167]

In this section we introduce some basic theory relevant to the thesis but not directly covered under the KS DFT heading. This includes an introduction to concepts important to the materials science of strongly correlated oxides, such as electron localisation and Coulomb correlation, the Mott-Hubbard phase transition, and Hubbard corrected DFT methodologies.

3.3.1 *Strongly correlated materials*

Correlation nomenclatures

The term correlation is used commonly and can describe a number of different concepts. These are often related and can be somewhat confusing. Some clarifications on the most common usages are given.

- Strongly correlated is a terminology used in many-body, DFT+DMFT and DFT+U fields. It describes the tendency of electrons to avoid each other, due to strong short-range on-site Coulomb interaction. Typical effects attributed to strong correlation include polarisation of orbital occupation and orbital ordering, magnetism and charge ordering.

- Correlation energy is a concept used in *ab initio* approaches such as HF and DFT. This indicates an unknown energy error, arising from the difference in single-particle (kinetic and electrostatic) interactions, and the many-body counterparts. The correlation energy is therefore,

$$E_c = \{T_m - T_s\} + \{U_m - U_s - J_s\}.$$

- Sometimes the correlation energy, in the sense given above, is sub-divided further. *Static correlation* is due to insufficient multi-reference character in the wave-function. *Dynamic correlation* is the error due to mean-field approximations in the Coulomb operator. Occasionally *Fermi correlation* is referred to, in that a Fermionic wave function fails to obey Pauli antisymmetry.[173]

- Correlation can also be used in the general statistical sense in materials science. In this context, correlation indicates electron

states must be considered individually, so a mean-field approach would be insufficient. In terms of the expectation of observables,

$$\langle \hat{O}_i \hat{O}_j \rangle \neq \langle \hat{O}_i \rangle \langle \hat{O}_j \rangle .$$

This statistical correlation definition is closely related to the preceding correlation references above.

3.3.1.1 *Localised electrons and Coulomb correlation*

DFT successfully describes many materials and is the mainstay theoretical framework in this thesis. However DFT provides an inherently mean-field Coulomb description (*e.g.* using the LDA), and it is important to highlight that the averaged treatment of e-e interaction is often insufficient, particularly in strongly correlated TMO systems with localised electrons.

Within the Hubbard paradigm, localisation is characterised by the ratio between bandwidth W and on-site Coulomb term U,

$$\begin{aligned} U/W &\gg 1 \quad \text{Localised} \\ U/W &\ll 1 \quad \text{Delocalised} . \end{aligned} \tag{17}$$

An extreme example of localisation due to strong correlation is the crystallisation of electrons, predicted in the limit of strong e-e interaction by Wigner[174] in 1934. For an electron gas at low density, Coulomb effects dominate over kinetic interactions due to screening, resulting in the electron crystallisation. This is a limiting example, and the materials of practical interest here have more balanced Coulombic and kinetic interactions. Nonetheless Wigner crystallisation serves to illustrate that Coulomb interaction cannot always be treated as a small perturbation, or by mean-field approximation.

Systems with electrons localised due to strong correlation are poorly described by DFT, and are traditionally examined using many-body Hamiltonians - the paradigmatic Hubbard Hamiltonian is briefly introduced next.

3.3.1.2 *The Hubbard Hamiltonian*

In practice DFT is a mean-field *ab initio* theory, while the Hubbard Hamiltonian is a model to construct a tractable many-body picture.

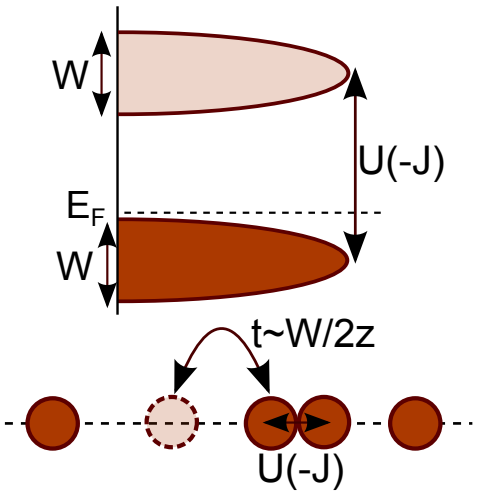

Figure 15: 1-dimensional Hubbard model, in terms of bandwidth W, on-site direct U and exchange J, intra-site hopping t, and nearest-neighbour coordination number z.

Though we use DFT in this thesis, the concept for on-site Coulomb term (Hubbard-U) is borrowed in the DFT+U schemes employed extensively. In addition, the Hubbard Hamiltonian often provides a useful paradigm for the discussion of localisation and ordering phenomena, such as anti-ferromagnetism and the Mott-Hubbard transition important to this thesis.

The Hubbard model was a first attempt to address the description of strongly correlated electrons.[66] By examining the limit of narrow bands, Hubbard was able to draw an analogy with the atomic case[66] to provide insight and useful approximations. The Hubbard Hamiltonian, which balances kinetic (inter-site hopping) and electrostatic (on-site Coulomb repulsion), can be written in simplest form as

$$\hat{H}_{\mathrm{Hub}} = -t \sum_{\langle i \neq j \rangle, \sigma} \hat{c}^{\dagger}_{i\sigma} \hat{c}_{j\sigma} + U \sum_{i} \hat{\rho}_{i\uparrow} \hat{\rho}_{i\downarrow} \,. \tag{18}$$

$t_{\langle i \neq j \rangle}$ is the hopping matrix element for nearest neighbours. $\hat{c}^{\dagger}_{i\sigma}(\hat{c}_{i\sigma})$ is a creation (annihilation) operator, and $\hat{c}^{\dagger}_{i\sigma}\hat{c}_{i\sigma} = \hat{\rho}_{i\sigma}$ is the particle number operator which counts electrons for $\downarrow$ or $\uparrow$ spin. On-site term U, which is pictured in Figure 15, is a measure of the Coulomb interaction between on-site electrons, and is defined (most nicely) by Anderson as the energy to put two electrons on the same site,[68,70]

$$U = E(2) + E(0) - 2E(1) \,,$$

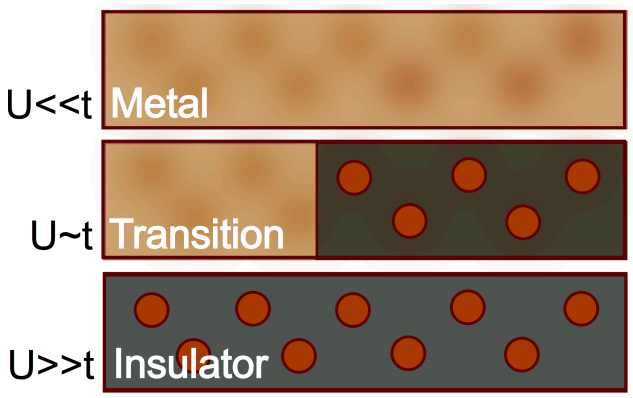

Figure 16: Mott-Hubbard metal-insulator transition limits.

and can also be thought of as the local difference between electron affinity and ionisation energy.

In the 'atomic' limit of large positive U (negative U models have been employed to describe fermion pairing, *e.g.* in superconductors[175]), electrons form localised states separated by energy gaps, akin to the Wigner crystal.[174] The low-U 'band' limit corresponds to weak correlation - this is typical of simple metals. Variation in the ratio between electron hopping amongst z sites and on-site Coulombic localisation provides an electronic phase transition mechanism (Mott) shown in Figure 16 characterised by

$$\text{Transition to} \begin{cases} \text{Metal if} & U/2zt \ll 1 \\ \text{Insulator if} & U/2zt \gg 1 \end{cases} .$$

Note the insulating and metallic regimes are equivalent to the localised and delocalised limits in Equation 17 ($W \sim 2zt$).

Although we rely on DFT for calculation, the Hubbard phenomenology has been highlighted here because of the relevance to strongly correlated materials (*e.g.* VO_2), fundamental importance to DFT+U which is discussed next, and as a tool to understand the limits of hopping exchange phenomena in simple models.

3.3.2 *On-site and hybrid corrections*

3.3.2.1 *DFT+U*

In order for DFT to account for the strong correlation physics and chemistry introduced above, a Hubbard-U correction can be added to the density functional.[59,176,177,178,179,180,181] The method known as DFT+U allows the occupancy of a set of localised orbitals to be tuned to a more physical description than provided by DFT alone, by explicit inclusion of an on-site atomic-like Coulomb interaction.

In DFT+U, the corrected DFT functional is written

$$\begin{aligned} E_{\mathrm{DFT}+U} &= E_{\mathrm{DFT}} + E_{\mathrm{corr}} \\ &= E_{\mathrm{DFT}} + E_U - E_{\mathrm{dc}} \,. \end{aligned}$$

The on-site correction is the difference between a Hubbard term added to account for localisation phenomena and correct self-interaction, and a double counting term subtracted to remove interaction already accounted for in DFT. In the following Chapter 4, a form of interaction in E_U is derived starting from a general Coulomb description. Depending on the approximations applied to E_U, two flavours of DFT+U are available in DFT+U_{eff} and DFT+$U|J$. Details and the relative merits of each scheme are discussed in Chapter 4.2.2.

3.3.2.2 *Hybrid DFT*

In a related technique, hybrid functional DFT provides access to the self-interaction-free character of HF, correcting the Coulomb-exchange cancellation error that is often problematic in standard DFT approaches. Hybrid schemes admix a percentage (usually around 25 %) of 'exact' Fock exchange, while retaining the usual local (or semi-local) DFT correlation description. A typical hybrid functional might be formulated as[160]

$$E_{xc}^{\mathrm{hybrid}}[\rho] = E_{xc}^{\mathrm{LDA/GGA}}[\rho] - \alpha \cdot \left(E_{x}^{\mathrm{LDA/GGA}}[\rho] - E_{x}^{\mathrm{HF}}[\rho_{ij}] \right) . \qquad (19)$$

If the GGA functional used is Perdew-Burke-Erzenhof (PBE) and the Fock exchange mixing is set to $\alpha = 25$ %, Equation 19 yields the 'PBE0' functional. The effect of introducing the orbitally-dependent (or non-local) Fock exchange is to improve the total and excitation energies.

In this work we use a further specialised variety of functional in the screened hybrid functional HSE.[18] In HSE, PBE GGA is corrected at the $\alpha = 25$ % level of mixing, but with the Fock Coulomb kernel range separated by using error functions. The long-range (LR) and short-range (SR) interactions are separated by μ as

$$\frac{1}{|\mathbf{r}-\mathbf{r}'|} = \mathrm{SR}_\mu(\mathbf{r},\,\mathbf{r}') + \mathrm{LR}_\mu(\mathbf{r},\,\mathbf{r}') = \frac{\mathrm{erfc}(\mu\cdot|\mathbf{r}-\mathbf{r}'|)}{|\mathbf{r}-\mathbf{r}'|} + \frac{\mathrm{erf}(\mu\cdot|\mathbf{r}-\mathbf{r}'|)}{|\mathbf{r}-\mathbf{r}'|}\,.$$

Range separation is set to the typical value of $\mu \approx 0.2$ Å^{-1}. This corresponds to a short-range domain within $|\mathbf{r}-\mathbf{r}'| \lessapprox 2$ Å.

The HSE functional relies on the approximation that the α scaled Fock and PBE exchange interactions can equate and cancel in the long-range:

$$\begin{aligned} E_{xc}^{\mathrm{HSE}}[\rho] &= \alpha\cdot\left\{E_x^{\mathrm{HF,SR}}[\rho_{ij}](\mu) + E_x^{\mathrm{HF,LR}}[\rho_{ij}](\mu)\right\} \\ &\quad +(1-\alpha)\cdot\left\{E_x^{\mathrm{PBE,SR}}[\rho](\mu) + E_x^{\mathrm{PBE,LR}}[\rho](\mu)\right\} + E_c^{\mathrm{PBE}}[\rho] \\ &= \alpha\cdot E_x^{\mathrm{HF,SR}}[\rho_{ij}](\mu) + (1-\alpha)\cdot E_x^{\mathrm{PBE,SR}}[\rho](\mu) + E_x^{\mathrm{PBE,LR}}[\rho](\mu) + E_c^{\mathrm{PBE}}[\rho]. \end{aligned}$$

In addition to the added flexibility of a screened range-separated XC description, the functional is less expensive than traditional hybrids because only short-range Fock exchange need be calculated.

Mixing exact-exchange into DFT can be shown to be closely related theoretically to the DFT+U method introduced above. Although a number of differences do exist, for example in DFT+U corrections can be applied selectively to the most error prone orbital sub-space, and, in hybrid functional methods Fock integrals are actually calculated explicitly rather than at some level of parameterisation. On-site Hartree-Fock-type corrections are discussed in more detail next in Chapter 4.2.2.

4

TECHNICAL CALCULATION DETAILS

In this chapter of the methodology we discuss XC functionals, plane wave representation and reciprocal sampling, which are important to calculation results throughout this work. We introduce orbital occupancy density matrices, giving particular heed to the Coulomb potential formulations, which are especially important topics for Chapters 6 & 10. Natural atomic units are employed again.

4.1 THE XC FUNCTIONAL

The kinetic and electrostatic energies in the single-particle approximation account for much of the true total energy, albeit with some fortuitous cancellations.[166,182] In DFT, beyond single-particle effects are ideally accounted for by the XC term, $E_{xc}[\rho]$. For analysis or calculation purposes, $E_{xc}[\rho]$ can be decomposed into electrostatic and kinetic contributions as[166]

$$E_{xc}[\rho] = U_{xc}[\rho] + T_c[\rho]\,. \tag{20}$$

The potential term $U_{xc}[\rho]$ is the difference in the many-body Coulomb and the classical Hartree interactions

$$U_{xc}[\rho] = V_{ee}[\rho] - V_{\mathrm{Har}}[\rho]\,,$$

and therefore contains both correlation and exchange contributions. Kinetic correlation term $T_c[\rho]$ in Equation 21 is the difference between the kinetic energy operator acting on the true many-body ground state density (T_m) and the single-particle non-interacting density (T_s),

$$T_c[\rho] = T_m[\rho] - T_s[\rho]\,.$$

Alternatively $E_{xc}[\rho]$ can be partitioned into exchange and correlation energy parts

$$E_{xc}[\rho] = E_x[\rho] + E_c[\rho]\,. \tag{21}$$

$E_x[\rho]$ is the electrostatic exchange term, and $E_c[\rho]$ is the correlation term containing both electrostatic *and* kinetic contributions

$$E_c[\rho] = V_{ee}[\rho] - V_{\mathrm{Har}}[\rho] - E_x[\rho] + T_c[\rho]\,.$$

Irrespective of how we partition $E_{xc}[\rho]$, into electrostatic-kinetic or exchange-correlation parts, a precise form is not available analytically or numerically in general. Although HK 1 provides a map between interacting and non-interacting pictures, $E_{xc}[\rho]$ is unknown in practice, so the many-body and non-interacting ground state densities differ in practice. This is a very basic theoretical challenge to DFT, however progress is possible in the weak and strong correlation limits, for which $E_{xc}[\rho]$ expressions exist for only the simplest electronic systems. For example, analytic and numerical expressions are known for the HEG $E_c[\rho]$ term,[183,184,185] which provides a starting point to extrapolate to real materials.

4.1.1 *Exact limits and practical XC functionals*

Previously the XC term $E_{xc}[\rho]$ was expressed as a linear sum of exchange and correlation contributions. In LDA DFT, the exchange part is

$$E_x^{\mathrm{LDA}}[\rho(\mathbf{r})] = -\frac{3}{4}(\frac{3}{\pi})^{1/3}\int dr\,\rho(\mathbf{r})^{4/3},$$

and the correlation part is given implicitly as an integral over the correlation energy eigenvalue ϵ_c and the material electronic density,

$$E_c^{\mathrm{LDA}}[\rho(\mathbf{r})] = \int dr\ \rho(\mathbf{r})\,\epsilon_c[\rho(\mathbf{r})]\,.$$

ϵ_c in E_c^{LDA} is unknown generally, but analytic expressions have been derived for very weak and very strong screening limits (for long and short screening length, r_s).

For a low density HEG, Coulomb interaction is weakly screened, so screening length tends to be long. In this limit Coulomb interaction dominates over kinetic interaction, as Coulomb interaction scales as

$U \sim 1/r_s$, compared to kinetic energy which scales as $t \sim 1/r_s^2$. This is effectively the Wigner crystallisation limit, which has the known correlation energy[174]

$$\begin{aligned} \epsilon_c &= \frac{1}{2}\left(\frac{g_0}{r_s} + \frac{g_1}{r_s^{3/2}}\right) \\ &\text{for} \quad \left\{r_s \to \infty; \frac{t}{U} \to 0; \rho \to 0\right\}. \end{aligned}$$

$r_s = \left(\frac{3}{4\pi\rho}\right)^{1/3}$ *i.e.* the Wigner-Seitz radius,[186] and g_i are numerical coefficients.

In a dense HEG, long-range Coulomb interaction is truncated by the short screening length r_s. By screening arguments,[65] Coulomb correlation can be treated as a perturbative expansion with respect to r_s. The 1957 Gell-man and Brueckner[183] calculation of ϵ_c for a dense HEG, sums terms from 2$^{\text{nd}}$ order (in the perturbative expansion of Coulomb interaction, direct interaction is o$^{\text{th}}$ order and the indirect exchange is 1$^{\text{st}}$) to give the correlation energy

$$\begin{aligned} \epsilon_c &= 0.311\ln|r_s| - 0.048 + r_s(A\ln|r_s| + C) + ... \\ &\text{for} \quad \left\{r_s \to 0; \frac{t}{U} \to \infty; \rho \to \infty\right\}. \end{aligned}$$

A and C are numerical coefficients.

The LDA[184] and semi-local GGA,[187] both parameterisations of the HEG XC from QMC,[185] are the best known practical approximations to $E_{xc}[\rho]$. In the popular LDA by Perdew and Zunger,[169] Perdew-Zunger 81 (PZ81), the XC energy is an integral over HEG XC energy eigenvalues $\epsilon_{xc}^{\text{HEG}}$, and the local material electron density $\rho(\mathbf{r})$:

$$E_{xc}^{\text{LDA}}[\rho(\mathbf{r})] = \int dr\, \rho(\mathbf{r})\, \epsilon_{xc}^{\text{HEG}}[\rho(\mathbf{r})]\,. \tag{22}$$

This expression is local - the LDA requires only the electron density at $\mathbf{r}$ to calculate an XC energy at $\mathbf{r}$. This differs from Coulomb interaction generally, but especially in ordinary materials where the charge density is inhomogenous, making the success of the LDA all the more remarkable.[166]

GGA functionals contain a local density (LDA-type) dependence, in addition to a second-order gradient dependence in the XC eigenvalue, $\epsilon_{xc}^{\mathrm{HEG}}[\rho(\mathbf{r}), \nabla\rho(\mathbf{r})]$. Usually the $\nabla\rho(\mathbf{r})$ dependence in the GGA improves on LDA exchange and kinetic energies,[166] but improvements are tempered by an ill-behaved correlation energy, for example, in the GGA the correlation hole doesn't integrate to zero breaking the correlation sum rule.

In this work two variants of the GGA are used: PBE,[187] which is the most common GGA implementation, and a re-parameterisation of PBE called Perdew-Burke-Erzenhof for solids (PBEsol),[188] which improves structural geometries in solid-state calculations.

4.2 ON-SITE COULOMB POTENTIAL

Building on the DFT+U introduction in the Theoretical Background (Chapter 3.3.2), Technical Details are presented for on-site Coulomb corrections. Some initial context is provided by an introduction to the *ab initio* and model approaches to Coulomb interaction, followed by a sketched derivation, which shows the steps to the two important practical forms of on-site Coulomb correction.

4.2.1 *Theoretical details*

Coulomb interaction in DFT

The formulation of Coulomb interaction in DFT is formally exact, and has two distinct parts - Hartree interaction, and exchange and correlation interactions:

$$E_{ee}[\rho] = \frac{1}{2}\iint drdr' \, \frac{\rho(\mathbf{r})\rho(\mathbf{r}')}{|\mathbf{r}-\mathbf{r}'|} + E_{xc}[\rho]\,. \tag{23}$$

The Hartree component is the density-density term shown explicitly, which is the simplest to calculate and also has the largest energetic contribution. The 'higher-order' Coulomb (exchange and correlation) interactions are much more difficult to calculate resulting in a reliance on approximate $E_{xc}[\rho]$ forms - typically local mean-field approxim-

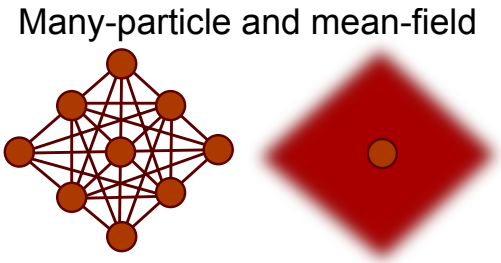

Figure 17: Figurative interpretation of many-body and single-particle pictures.

ations to $E_{xc}[\rho]$ suffice, as the quantum mechanical interactions are usually much smaller than the classical Hartree interactions.

For certain materials, such as the strongly correlated materials in this thesis, the usual approximations[169,187] to $E_{xc}[\rho]$ are insufficient. In the following section, we begin with a Coulomb description at a high level of generality. We work toward highlighting the form of interaction in the two DFT+U methods used to improve the Coulomb description of strongly correlated materials in this thesis.

From general principles to practical on-site Coulomb forms

For N electron systems, the Hamiltonian under standard assumptions requires at most pairwise two-body interactions.[189] The N electron Hamiltonian can be written $\hat{H} = \hat{h} + \hat{W}$,[190] where $\hat{h}$ accounts for interactions that can be described by one-body operators (kinetic and external interactions), and $\hat{W}$ is the two-body Coulomb operator.

Assuming on-site interactions are significantly larger than inter-site, $\hat{W}$ can be expressed as a sum over all strongly correlated single sites,

$$\begin{aligned} \hat{W} &= \sum_C \hat{U}_C \\ \hat{U}_C &= \frac{1}{2} \sum_{\alpha\beta\gamma\delta \in C} U_{\alpha\beta\gamma\delta} \rho_{\alpha\beta\gamma\delta} \,, \end{aligned} \tag{24}$$

with a familiar Hubbard-type form of interaction in $\hat{U}_C$. The $\hat{U}_C$ term contains the $2(2l+1)$-dimensional reduced two-body density matrix (2-RDM), $\rho_{\alpha\beta\gamma\delta}$, and $U_{\alpha\beta\gamma\delta} = \langle \alpha\beta \,|V|\, \gamma\delta \rangle$, the Coulomb kernel matrix elements. Generalised quantum number indices $\alpha\beta\gamma\delta$ label particle

states in a complete orthonormal basis. This description is quite general, assuming at most two-body interactions in the N particle system.

For practical applications though, we convert Equation 24 into something less abstract with explicit quantum numbers. Summing over sites (at), spin channels ($\sigma\sigma'$) and magnetic orbital angular momentum projections ($mm'm''m'''$), the e-e Coulomb potential can be expressed as

$$\hat{V}_{ee} = \sum_{at} \frac{1}{2} \sum_{\sigma,\sigma'} \sum_{mm'm''m'''} \langle m\sigma m''\sigma'|V|m'\sigma m'''\sigma'\rangle \times \hat{c}^{\dagger}_{m\sigma}\hat{c}^{\dagger}_{m''\sigma'}\hat{c}_{m'\sigma}\hat{c}_{m'''\sigma'} \,. \tag{25}$$

Here the two-body density matrix is written as four-operator of fermionic field-operators where $\hat{c}^{\dagger}_{m\sigma}$ (or $\hat{c}_{m\sigma}$) generates (or annihilates) a particle in the state $|m\sigma\rangle$. V is the form of interaction, which is manifestly spin-independent for the bare Coulomb form $V(\mathbf{r},\mathbf{r}') = 1/|\mathbf{r}-\mathbf{r}'|$.[171] The Coulomb matrix elements as integrals are

$$\langle m\sigma m''\sigma'|V|m'\sigma m'''\sigma'\rangle = \int dr \int dr' \, \varphi^{*}_{m\sigma}(\mathbf{r})\varphi_{m'\sigma}(\mathbf{r}) \frac{1}{|\mathbf{r}-\mathbf{r}'|} \varphi^{*}_{m''\sigma'}(\mathbf{r}')\varphi_{m'''\sigma'}(\mathbf{r}') \,.$$

Unfortunately the four-operator term in Equation 25 which enforces antisymmetry in the particle statistics is more of an *impasse* to practical calculations. Using commutation relations (Wick's theorem), we can rewrite the expectation of the two-body four operator as a product of one-body averages, $\langle \hat{c}^{\dagger}_{m\sigma}\hat{c}^{\dagger}_{m''\sigma'}\hat{c}_{m'\sigma'}\hat{c}_{m'''\sigma}\rangle \approx \langle \hat{c}^{\dagger}_{m\sigma}\hat{c}_{m'''\sigma}\rangle \langle \hat{c}^{\dagger}_{m''\sigma'}\hat{c}_{m'\sigma'}\rangle - \langle \hat{c}^{\dagger}_{m\sigma}\hat{c}_{m'\sigma'}\rangle \langle \hat{c}^{\dagger}_{m''\sigma'}\hat{c}_{m'''\sigma}\rangle$, where $\langle \hat{c}^{\dagger}_{m\sigma}\hat{c}_{m'\sigma'}\rangle = \rho^{\sigma}_{m'm}\delta_{\sigma,\sigma'}$. After this averaging or mean-field implementation, Equation 25 can be expressed in terms of one-body density matrices

$$\begin{aligned} \langle \hat{V}_{ee}\rangle \;=\; & \sum_{at} \frac{1}{2} \sum_{\sigma,\sigma'} \sum_{mm'm''m'''} \langle m\sigma m''\sigma'|V|m'\sigma m'''\sigma'\rangle \\ & \times (\rho^{\sigma}_{mm'''}\rho^{\sigma'}_{m'm''} - \rho^{\sigma}_{mm'}\rho^{\sigma}_{m'''m''}\delta_{\sigma,\sigma'}) \,. \end{aligned}$$

For the convenience of analysis we can rotate to a diagonal representation - finding the eigenvectors of $\rho^{\sigma}_{mm'''}$ we can work directly with the expectations, *i.e.* occupancy eigenvalues f^{σ}_{i} and $f^{\sigma'}_{j}$,

$$\rho^{\sigma}_{mm'''} = \sum_{i} \mathrm{V}^{\sigma}_{mi} f^{\sigma}_{i} (\mathrm{V}^{\sigma})^{\dagger}_{im'''} \implies \langle \rho^{\sigma}_{mm'''} \rangle = f^{\sigma}_{i} \,.$$

Note the terms V^{σ}_{mi} denote eigenvectors of $\rho^{\sigma}_{mm'''}$, and are unrelated to the italicised 'V' forms in Equation 25 (*i.e.*, the $V(\mathbf{r}, \mathbf{r}')$ bare Coulomb potential and $\hat{V}_{ee}$ on-site interaction operator).

With $\langle \hat{V}_{ee} \rangle$ written in terms of occupancies in the diagonal form

$$\langle \hat{V}_{ee} \rangle = \sum_{at} \frac{1}{2} \sum_{i,j,\sigma} (\sum_{\sigma'} \langle i\sigma j\sigma' | V | i\sigma j\sigma' \rangle f_{i\sigma} f_{j\sigma'} - \langle i\sigma j\sigma | V | j\sigma i\sigma \rangle \, f_{i\sigma} f_{j\sigma}) \,, \quad (26)$$

the lack of self-interaction is self-evident, with self-Coulomb consumed by self-exchange for $\delta_{ij}\delta_{\sigma\sigma'}$. In addition the interaction in Equation 26, derived from general principles, now bares some relationship to HF. In Equation 26 the Coulomb-exchange mean-field is made up of the left-hand term, which is summed over all spins providing a direct Hartree-type interaction, and of the left-hand term, which subtracts a like-spin Fock-type exchange interaction.

To separate like and opposite-spin terms, we expand the Hartree sum $\sum_{\sigma'}$ and factorise the spins into like-spin pairs ($f_{i\sigma} f_{j\sigma}$) and opposite-spin pairs ($f_{i\sigma} f_{j\bar{\sigma}}$)

$$\begin{aligned}
\langle \hat{V}_{ee} \rangle_{U|J} &= \frac{1}{2} \sum_{at,\sigma} \sum_{ij} \Big\{ \Big[\langle i\sigma j\sigma | V | i\sigma j\sigma \rangle - \langle i\sigma j\sigma | V | j\sigma i\sigma \rangle \Big] f_{i\sigma} f_{j\sigma} & (27) \\
&\quad + \langle i\sigma j\bar{\sigma} | V | i\sigma j\bar{\sigma} \rangle \, f_{i\sigma} f_{j\bar{\sigma}} \Big\} \,, & (28) \\
&= \frac{1}{2} \sum_{at,\sigma} \Big\{ \sum_{i \neq j} \Big[\langle i\sigma j\sigma | V | i\sigma j\sigma \rangle - \langle i\sigma j\sigma | V | j\sigma i\sigma \rangle \Big] f_{i\sigma} f_{j\sigma} & (29) \\
&\quad + \sum_{i,j} \langle i\sigma j\bar{\sigma} | V | i\sigma j\bar{\sigma} \rangle \, f_{i\sigma} f_{j\bar{\sigma}} \Big\} \,. & (30)
\end{aligned}$$

The second part of Equation 27 contains a trivial re-writing of the sum in ij to pull out the large diagonal 'Fock' contributions. This in effect manually removes self-interaction at $\delta_{ij}\delta_{\sigma\sigma'}$, explicitly making the sum over $\sum_{i \neq j}$ where self-Coulomb and self-exchange cancel. Note Equation 27 is now denoted '$\langle \hat{V}_{ee} \rangle_{U|J}$' for reasons apparent in the following paragraph.

If the 'Hartree' $\langle i\sigma j\sigma'|V|i\sigma j\sigma'\rangle$ and 'Fock' $\langle i\sigma j\sigma|V|j\sigma i\sigma\rangle$ integrals are replaced by simple U and J parameters under some further averaging, we have an even more simplified form of interaction in

$$\langle \hat{V}_{ee}\rangle_{U_{\text{eff}}} = \frac{1}{2}\sum_{at}\sum_{\sigma}\left((U-J)\sum_{i\neq j} f_{i\sigma}f_{j\sigma} + U\sum_{i,j} f_{i\sigma}f_{j\bar{\sigma}}\right). \qquad (31)$$

Note this simplified expression is labelled '$\langle \hat{V}_{ee}\rangle_{U_{\text{eff}}}$'. Incorporating either the '$\langle \hat{V}_{ee}\rangle_{U|J}$' or '$\langle \hat{V}_{ee}\rangle_{U_{\text{eff}}}$' interaction leads to the two types of DFT+U, which add effectively screened HF-type corrections to our DFT calculations. To add either correction to DFT, two further 'atomic-limit' approximations are employed: i) in the form of double-counting correction - see Chapter 4.2.2, and ii) in the use of spherically symmetric Slater's integrals[176,191] to calculate $\langle \hat{V}_{ee}\rangle_{U|J}$ matrix elements - see Appendix A.1.

4.2.2 *Practical forms of DFT+U*

In Chapter 3.3.2, the DFT+U method was briefly introduced as a correction scheme inspired by the Hubbard-U term. The scheme corrects DFT as $E_{\text{DFT}+U} = E_{\text{DFT}} + E_{\text{corr}}$, where the correction E_{corr} is given as the difference between an added on-site interaction and a double-counting term,

$$E_{\text{corr}} = E_U - E_{\text{dc}}\,.$$

By equating on-site interaction E_U with either Equation 31 or Equation 27, two types of DFT+U are available. The simpler DFT+U_{eff} approach is discussed first.

4.2.2.1 *DFT+U_{eff}*

In the 'spherically averaged' DFT+U_{eff} approach by Dudarev *et al.*,[177] $\langle \hat{V}_{ee}\rangle_{U_{\text{eff}}}$ in Equation 31 is substituted for E_U to yield

$$E_{\text{corr}} = \langle \hat{V}_{ee}\rangle_{U_{\text{eff}}} - E_{\text{dc}}\,.$$

Here the E_{dc} term is the most problematic, as the form is unknown generally. We simply note that under conditions of polarised occupation (binary f_i^σ occupancy eigenvalues), the correction should be turned off ($E_{\mathrm{corr}} \to 0$) since self-interaction errors should be minimal. Choosing E_{dc} to cancel $\langle \hat{V}_{ee} \rangle_{U_{\mathrm{eff}}}$ (see Equation 31) under conditions of integer occupation ($f_{i\sigma} = f_{i\sigma}^2$), with $N_\sigma = \sum_i f_{i\sigma}$ and $N = \sum_\sigma N_\sigma$, we get

$$\begin{aligned} E_{\mathrm{dc}} &= \frac{U-J}{2} \sum_\sigma N_\sigma (N_\sigma - 1) + U N_\sigma N_{\bar{\sigma}} \\ &= \frac{U}{2} N(N-1) - \frac{J}{2} \sum_\sigma N_\sigma (N_\sigma - 1)\,. \end{aligned} \tag{32}$$

With some algebraic manipulation we can obtain second line of Equation 32. This effectively equates the E_{dc} derived from $\langle \hat{V}_{ee} \rangle_{U_{\mathrm{eff}}}$ under limiting idempotency conditions, given on the first line in Equation 32, to the so-called fully localised limit (FLL) double-counting expression commonly found in the literature,[59,176,192] and presented on the second line of Equation 32. The FLL double-counting correction can be interpreted as an average interaction energy of each electron interacting with $(N-1)$ others in the atomic limit. For completeness we note that a second common double-counting expression is available in the so-called around mean-field (AMF) implementation.[192,193,194,195] However this is more suited to correcting local density fluctuations, for example in a metal, whereas the FLL (used throughout) is best suited to the strongly correlated limit, in for example Mott insulators.[51,59,196,177] For comparison of FLL, AMF, and theoretical origins of DFT+U, the reader is referred to the excellent review by Himmetoglu *et al.*[176] and perspective by Kulik.[197]

Cancelling common terms in E_{dc} and $\langle \hat{V}_{ee} \rangle_{U_{\mathrm{eff}}}$ gives the form of correction used in the DFT+U_{eff} scheme

$$E_{\mathrm{corr}} = \frac{U_{\mathrm{eff}}}{2} \sum_{at,i,\sigma} (f_{i\sigma} - f_{i\sigma}^2)\,, \tag{33}$$

$$E_{\mathrm{DFT}+U} = E_{\mathrm{DFT}} + \frac{U_{\mathrm{eff}}}{2} \sum_{at,i,\sigma} (f_{i\sigma} - f_{i\sigma}^2) \tag{34}$$

where $U_{\mathrm{eff}} = U - J$. By Janak's theorem, the energy eigenvalues of the corrected DFT functional are

$$\begin{aligned}\frac{\partial E_{\mathrm{DFT}+U}}{\partial f_{n\mathbf{k}\sigma}} &= \epsilon^{\mathrm{DFT}+U}_{n\mathbf{k}\sigma} = \epsilon^{\mathrm{DFT}}_{n\mathbf{k}\sigma} + \Delta\epsilon^{+U_{\mathrm{eff}}}_{n\mathbf{k}\sigma}\,. \\ &= \epsilon^{\mathrm{DFT}}_{n\mathbf{k}\sigma} + U_{\mathrm{eff}} \sum_{at,i\sigma} (\frac{1}{2} - f_{i\sigma}) \cdot \frac{\partial f_{i\sigma}}{\partial f_{n\mathbf{k}\sigma}}\end{aligned}$$

where $\frac{\partial f_{i\sigma}}{\partial f_{n\mathbf{k}\sigma}}$ is the derivative of local and total Bloch states. From the definition of occupancy matrix, $\rho^{\sigma}_{ij} = \langle \varphi_{i\sigma} | \hat{\rho}^{\sigma}_{n\mathbf{k}} | \varphi_{j\sigma} \rangle = \sum_{n\mathbf{k}} \langle \varphi_{i\sigma} | \psi_{n\mathbf{k}\sigma} \rangle f_{n\mathbf{k}\sigma} \langle \psi_{n\mathbf{k}\sigma} | \varphi_{j\sigma} \rangle$, the derivative $\frac{\partial f_{i\sigma}}{\partial f_{n\mathbf{k}\sigma}}$ is just the squared modulus of total Bloch band $\psi_{n\mathbf{k}\sigma}$ and local state $\varphi_{i\sigma}$ overlap, $\frac{\partial f_{i\sigma}}{\partial f_{n\mathbf{k}\sigma}} = |\langle \varphi_{i\sigma} | \psi_{n\mathbf{k}\sigma} \rangle|^2$, resulting in

$$\Delta\epsilon^{U_{\mathrm{eff}}}_{n\mathbf{k}\sigma} = U_{\mathrm{eff}} \sum_{at,i\sigma} (\frac{1}{2} - f_{i\sigma}) \cdot |\langle \varphi_{i\sigma} | \psi_{n\mathbf{k}\sigma} \rangle|^2\,. \tag{35}$$

The characteristic failure of DFT XC functionals generally is the excessive delocalisation of valence electrons - for the paradigmatic example of Mott insulators this is particularly problematic.[176] The correction in Equation 33 can be applied to a selected correlated subspace, on which fractional occupations are penalised by Equation 35, effectively correcting the self-interaction problem. In material terms this corresponds to the re-opening of the DFT band gap, favourable stabilisation of magnetic moments, and modification of the structure, for example, enhancing occupancy polarisation mediated Jahn-Teller distortion modes underestimated by DFT.[70]

Aside from the overlap term in Equation 35, the on-site correction can be understood intuitively from Figure 18. The 'concave' energy dependence of the correction on occupation (Figure 18) effectively cancels the erroneous smooth convex parabolic energy dependence that DFT wrongly gives for the addition and subtraction of electrons, yielding the correct particle addition/subtraction 'curve' with linear piecewise convexity. In this sense DFT+U is a linearisation scheme for the DFT electron addition/subtraction curve. By correcting the addition and subtraction gradients, the ionisation potentials ($\frac{dE(N)}{dN}|_{+} = -I$) and electron affinities ($\frac{dE(N)}{dN}|_{-} = -A$) are close to recovered, along with by extension the fundamental band gap, $E_{\mathrm{gap}} = I - A$.

The typical size of the on-site Hubbard correction set in practical DFT+U calculations usually varies between $U_{\mathrm{eff}} = 0$ and $U_{\mathrm{eff}} = 10$ eV.

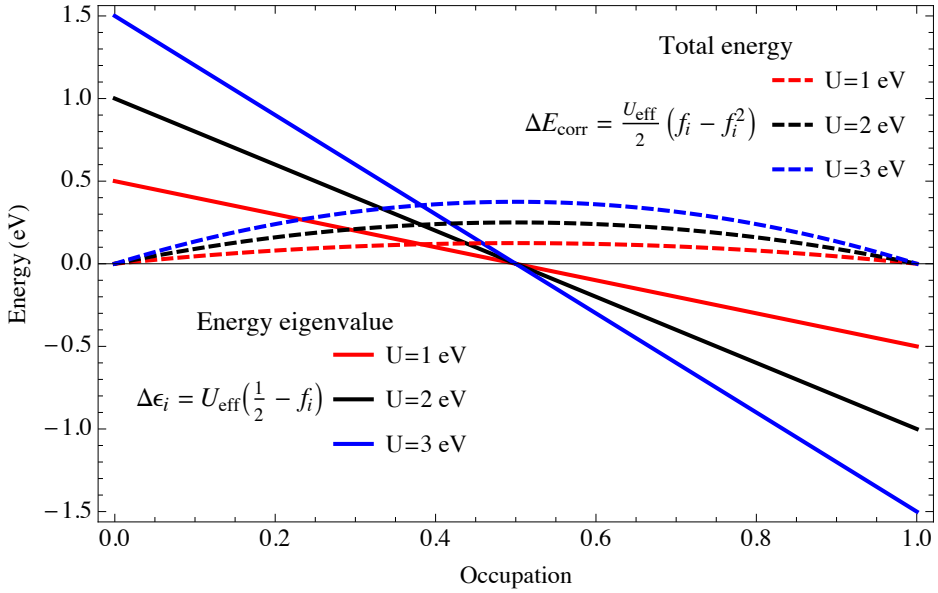

Figure 18: On-site correction total energy per atomic orbital (E_{corr}) and energy eigenvalues (ϵ_i) as a function of orbital occupation (f_i) and on-site Coulomb parameter $U_{\text{eff}} = 1, 2\,\&\,3$ eV.

Note this is much smaller than the bare atomic Coulomb repulsion due to solid state screening and breathing renormalisation effects.[191,198]

4.2.2.2 *DFT*+$U|J$

If the $\langle \hat{V}_{ee} \rangle_{U|J}$ in Equation 27 is used to define E_U rather than $\langle \hat{V}_{ee} \rangle_{U_{\text{eff}}}$ from Equation 31, it is possible to derive the 'rotationally invariant' DFT+$U|J$ approach by Liechtenstein *et al.*[59] The DFT+$U|J$ approach is particularly important to this thesis, but as the derivation of expressions in the special form we require is unwieldy (involving explicit calculation of matrix elements, and manipulations to partition different correction terms) - the reader is referred to Appendix A.1 for an outline.

For the DFT+$U|J$ scheme we skip straight to the affect of $U|J$, which tunes the relative energetics of the localised sub-space, according to the vector-matrix expression

$$\Delta\epsilon_\sigma^{U|J} = \frac{\partial(\langle V_{ee} \rangle_{U|J} - E_{\text{dc}}[\rho])}{\partial f_\sigma} \approx U_{\text{eff}} \cdot (\frac{1}{2} - f_\sigma) + J \cdot [\mathrm{A}^\sigma f_\sigma + \mathrm{B}^\sigma f_{\bar{\sigma}}]\,. \tag{36}$$

In Equation 36, $\Delta\epsilon_\sigma^{U|J}$ is the column vector of energy-splitting eigenvalues, f_σ is the column vector of occupancies, and A^σ and $\mathrm{B}^{\bar{\sigma}}$ are the

like-spin and opposite-spin matrices that account for multipole intra-orbital exchange (F_2 and F_4 Slater terms - see Appendix A.1). Although the $+U$ schemes are often said to introduce HF-type corrections, it is important to note as pointed out by Cococcioni[199] and Himmetoglu,[176] the $U|J$ scheme in particular includes an 'orbital exchange' interaction between *opposite* spin states that is inherently two-body, while HF only includes a non-local Fock interaction between same-spin states. In practice the orbital interaction between opposite states is specified by the $B^{\sigma} f_{\bar{\sigma}}$ term in Equation 36 - for an explicit expression see Appendix A.1 Equation 90.

From Equations 36 & 35, the relationship between the $U|J$ and U_{eff}-type corrections is easy to identify. The $U|J$ scheme incorporates explicit orbital exchange dependence as an additional layer of sophistication on top of the basic occupancy polarisation from U_{eff}. The U_{eff} correction can be seen as 'isotropic', stemming from only the F_0 Slater monopole (no angular dependence), and can order orbital energetics based solely on occupation. The $U|J$ scheme whereas is somewhat less mean-field, specifying pair-wise interactions between orbitals with different shapes and sizes (angular momentum), and with different spin polarisations.

The more advanced treatment of intra-orbital exchange in the $U|J$ scheme is typically inconsequential and unnecessary for most materials. However for materials with a critical dependence on Hund's coupling effects, magnetism and orbital ordering, as in many strongly correlated materials, $U|J$ can produce qualitative improvements on a DFT description.[200,201,202,203] As happens to be the case in this thesis - the spatial/orbital symmetry dependence of the $U|J$ method is necessary to reproduce magnetic and electronic ground state in materials such as $LaMnO_3$ - see Chapter 10.

4.3 BASIS AND SAMPLING

All calculations in the thesis are performed using plane waves. Errors can arise from the basis representation, for example due to basis set incompleteness, poor core augmentation, and low density of **k**-points in the reciprocal space sampling meshes. Plane waves are discussed

below, along with the measures taken to minimise controllable sources of error.

4.3.1 *Plane wave basis*

Practical calculations for this thesis were performed using the Vienna Ab Initio Simulation Program (VASP).[204,205,206,207,208] In VASP eigenfunctions are expressed in a plane wave basis.[204,205,206] According to Bloch's theorem, eigenstates of a periodic system can can be written

$$\phi_{n\mathbf{k}}(\mathbf{r}) = \mathrm{e}^{i\mathbf{k}\cdot\mathbf{r}} u_{n\mathbf{k}}(\mathbf{r}) \,, \tag{37}$$

where $u_{n\mathbf{k}}(\mathbf{r})$ is a function with the same periodicity as the lattice, such that the $\phi_{n\mathbf{k}}(\mathbf{r})$ modulus reflects a charge density with the translational invariance of the lattice. The periodic function written as a Fourier series is

$$u_{n\mathbf{k}}(\mathbf{r}) = \sum_{\mathbf{G}} c_{\mathbf{G}}^{n\mathbf{k}} \mathrm{e}^{i\mathbf{G}\cdot\mathbf{r}} \,, \tag{38}$$

where $\mathbf{G}$ are reciprocal space lattice vectors. Combining Equations 37 & 38 yields,

$$\phi_{n\mathbf{k}}(\mathbf{r}) = \sum_{\mathbf{G}} c_{\mathbf{G}}^{n\mathbf{k}} \mathrm{e}^{i(\mathbf{G}+\mathbf{k})\cdot\mathbf{r}} \,. \tag{39}$$

Although the sum in Equation 39 is unbounded, in practice only a finite number of plane waves is used. The largest value of $\mathbf{G}$ determines a cut-off energy,

$$E_{\mathrm{cut}} = \frac{\mathbf{G}_{\mathrm{max}}^2}{2} \,.$$

Incomplete basis set due to finite $\mathbf{G}_{\mathrm{max}}$ value can result in Pulay stresses. Pulay stresses are errors in the stress tensor diagonals that occur when the lattice vectors are changed (*e.g.* geometry optimisation), but the basis set ($\mathbf{G}_{\mathrm{max}}$) is kept fixed, which for example can result in discontinuities in energy. This can be mitigated by increasing $\mathbf{G}_{\mathrm{max}}$ - we have increased on the VASP recommendation throughout, consistently by $1.3 \times \mathbf{G}_{\mathrm{max}}^{\mathrm{standard}}$.

Unlike local orbital methods, the accuracy of the plane wave approach can systematically be improved by increasing E_{cut}. In practice the number of plane waves required for an adequate description of a typical material is large, and must be traded against the computational expense of increasing E_{cut}.

4.3.2 *Reciprocal-space sampling*

The eigenfunctions $\phi_{n\mathbf{k}}(\mathbf{r})$, introduced in Equation 39, are indexed in terms of each band n, and vary continuously in terms of wavevector $\mathbf{k}$. In practice calculations employ grids, *e.g.* Monkhorst-Pack,[209] to sample a representative range of $\mathbf{k}$ values, called $\mathbf{k}$-points which are spaced at finite intervals. $\mathbf{k}$-points are sampled within a parallelepiped $W = w_1 w_2 w_3$, with units of incremental volume defined by w_i and m_i, and reciprocal lattice vector $\mathbf{b}_i^{\mathbf{k}}$

$$\mathbf{k} = \sum_{i=1}^{3} \frac{m_i}{w_i} \mathbf{b}_i^{\mathbf{k}} \ .$$

Reciprocal lattice vector $\mathbf{b}_i^{\mathbf{k}}$ is conjugated to a real-space lattice vector $\mathbf{a}_i^{\mathbf{r}}$ by the Born-Von Karman boundary condition,

$$\mathbf{b}_i^{\mathbf{k}} \cdot \mathbf{a}_j^{\mathbf{r}} = 2\pi\delta_{ij} \ .$$

Solving for $\mathbf{b}_i^{\mathbf{k}}$, the reciprocal lattice vectors are

$$\mathbf{b}_1^{\mathbf{k}} = 2\pi \frac{\mathbf{a}_2^{\mathbf{r}} \times \mathbf{a}_3^{\mathbf{r}}}{\mathbf{a}_1^{\mathbf{r}} \cdot \mathbf{a}_2^{\mathbf{r}} \times \mathbf{a}_3^{\mathbf{r}}}, \quad \mathbf{b}_2^{\mathbf{k}} = 2\pi \frac{\mathbf{a}_3^{\mathbf{r}} \times \mathbf{a}_1^{\mathbf{r}}}{\mathbf{a}_1^{\mathbf{r}} \cdot \mathbf{a}_2^{\mathbf{r}} \times \mathbf{a}_3^{\mathbf{r}}}, \quad \mathbf{b}_3^{\mathbf{k}} = 2\pi \frac{\mathbf{a}_1^{\mathbf{r}} \times \mathbf{a}_2^{\mathbf{r}}}{\mathbf{a}_1^{\mathbf{r}} \cdot \mathbf{a}_2^{\mathbf{r}} \times \mathbf{a}_3^{\mathbf{r}}} \ .$$

A detailed account of $\mathbf{k}$-point sampling can be found in the original development by Monkhorst and Pack,[209] and elsewhere such as in the thesis of Smith.[210]

4.4 DENSITY MATRIX REPRESENTATION

Density matrices have long played a role in probabilistic structure of quantum mechanics,[211] and in DFT density matrices have several different uses. One example is large systems, where the reduced

single-body density matrix (1-RDM) is an essential ingredient in linear scaling *ab initio* approaches.[157,212]

In addition the density matrix (DM) formalism provides a natural representation of any electronic structure that can be represented by a discrete set of quantum numbers, *e.g.*, $|nlm_l m_s\rangle$. This is useful for analysis[1,4,40,176,180] especially in strongly correlated metal oxides, where cations can often exist close to the limit of embedded single atoms, allowing resolution of spin and orbitally-projected sub-spaces using density matrices.[70,156] In this work we use density matrices to resolve orbital sub-spaces for explicit modelling of on-site exchange interactions, and to interpret orbital effects in DFT+U electronic structure calculations - see Chapter 10.

4.4.1 *General formalism*

The DM operator formalism is used to describe an ensemble of states, where the mixture is statistical *and* quantum mechanical. The general DM operator has the following representation

$$\hat{\rho} = \sum_i |\psi_i\rangle p_i \langle\psi_i|, \tag{40}$$

where $\hat{\rho}$ is the density operator, p_i are probabilities and ψ_i are state vectors. $\hat{\rho}$ has four characteristic properties. It is

- Hermitian $\hat{\rho} = \hat{\rho}^\dagger$
- Idempotent $\hat{\rho} = \hat{\rho}^2$
- Normal $\mathrm{tr}[\hat{\rho}] = 1$
- Positive semi-definite $\hat{\rho} \geq 0$.

In an orthonormal basis $\{|\phi_m\rangle\}$ the DM is formed by taking the DM operator inside the bras and kets

$$\rho_{mm'} = \sum_i \langle\phi_m|\psi_i\rangle p_i \langle\psi_i|\phi_{m'}\rangle = \langle\phi_m|\hat{\rho}|\phi_{m'}\rangle .$$

Inversely the DM operator can be formed from the DM inside the kets and bras, $\hat{\rho} = \sum_{mm'} |\phi_m\rangle \rho_{mm'} \langle\phi_{m'}|$.

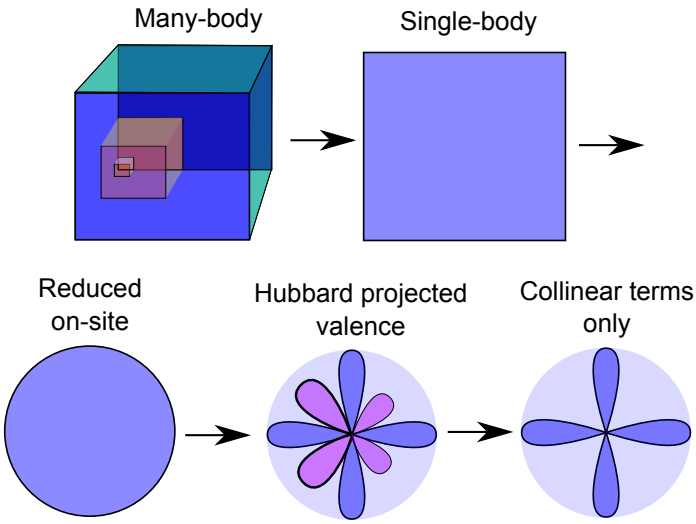

Figure 19: Artistic interpretation of transformations (tracing, projection and diagonalisation) reducing the 'full' most general density matrix to the orbital occupancy density matrix of interest.

Although we draw a distinction between the DM operator and the DM, this is often not observed in practice. This is because the DM and DM operator share the most important basic properties listed above. The final note on the general DM is on the calculation of expectation values. For an arbitrary observable O, the expectation value of the associated operator $\hat{O}$, can be re-cast in terms of a trace over the operator and DM,

$$\begin{aligned} \langle O \rangle_\rho &= \textstyle\sum_i p_i \langle \psi_i | \hat{O} | \psi_i \rangle \\ &= \textstyle\sum_{mm'} \langle \phi_{m'} | \hat{\rho} | \phi_m \rangle \langle \phi_m | \hat{O} | \phi_{m'} \rangle \\ &= \textstyle\sum_{mm'} \rho_{mm'} O_{m'm} = \mathrm{tr}[\rho O] \,. \end{aligned} \tag{41}$$

4.4.2 *Reduced orbital occupancy density matrix*

Rather than the general many-body DM, ρ^n, the object of interest here is the reduced single-body DM ρ^1, subject to constraints of N-representability.[189,213] An illustration of the reduction from many-body to single-body DM is shown in Figure 19. The zero-temperature reduced orbital occupancy density matrix relevant to this thesis,

$$\hat{\rho} = \sum_i |\psi_i\rangle f_i \langle \psi_i| \,,$$

is expressed in terms of occupation numbers f_i, such that the $\hat{\rho}$ trace gives the total electron count. Furthermore, idempotency is relaxed locally, for example to enable parameterisation of hybridisation between a 'crystal bath' and correlated sub-space in DFT+U.

Even with the reduced single-body DM we are not interested in the whole Hilbert space, but rather usually one electronic manifold from only a single specified atomic site. Localised basis projector functions (formally Hubbard $\hat{P}$ projectors) are used to identify the sub-space (e.g. d-shell states) of interest

$$\sum_{\sigma,mm'} \left\langle \varphi^{\sigma}_{m} | \hat{P}^{\dagger} \hat{\rho} \hat{P} | \varphi^{\sigma}_{m'} \right\rangle = n^{\sigma\sigma'}_{mm'} \delta_{\sigma\sigma'} = \begin{pmatrix} n^{\uparrow}_{mm'} & \\ & n^{\downarrow}_{mm'} \end{pmatrix} = n^{\sigma}_{mm'} \,,$$

with the selected sub-space DM denoted $n^{\sigma}_{mm'}$. Here the DM in orbital quantum numbers mm' has been diagonalised to decouple spin channels σ, to highlight the DM form used in analysis throughout.

4.5 VASP technical details, input and parameters

First-principles calculations in this thesis are performed using VASP,[204,205,206,207,208] the popular quantum-mechanical electronic structure and molecular dynamics code. We use VASP to perform single-point or fixed geometry electronic calculations, and for optimisation of crystal and molecular structures by energy minimisation.

Several theoretical aspects of the DFT implemented in VASP have already been introduced generally. Types of XC functional in Chapter 4.1, basis in Chapter 4.3, on-site corrections in Chapter 3.3.2 and Chapter 4.2.2, and treatment of magnetism in Chapter 3.2.3. Furthermore, the precise parameters used in each calculation are specified immediately preceding each result, in Chapters (6-10). Here we provide a brief overview of technical knowledge and files required for a typical calculation.

Operation of the VASP code requires four input files:

1. INCAR - logical and numerical parameters,

2. POSCAR - initial unit cell vectors and ionic positions,

3. POTCAR - concatenation of elemental pseudo-potentials,

4. KPOINTS - sets the method and density of **k**-point sampling.

In our calculations the geometric structure is given in the POSCAR by representing ionic positions in fractional coordinates. The KPOINTS file is set to automatically generate the Monkhorst-Pack **k**-point sampling mesh,[209] at an approximate density of $lattice\ vector \times sampling\ density \approx 30$, which we have found to provide convergence of total energies with respect to the number of **k**-points in our semiconducting systems. The pseudo-potentials employed in the POTCAR file are the standard VASP projected augmented wave (PAW) variety,[206,214] with the energy cut-off set 30 % above the advised value to minimise 'aliasing' errors.

The INCAR file is the primary VASP input file changed by the code user, and is shown below for a typical calculation. The INCAR file describes a calculation relaxing ionic positions in stoichiometric MnO_2, using the PBEsol[188] functional with on-site Coulomb corrections.[177] Magnetic moments are initialised for cations, crystal symmetry is exploited for efficiency, and cut-off parameters are defined to break the electronic and lattice geometry self-consistency routines.

The VASP output returns the optimised lattice geometry, the electronic density of states, on-site density matrices, energy eigenvalue bands, charge density and wave function. For examples of the material properties that can be produced from the basic VASP output - see Chapter 5.

Custom codes 4.1: VASP 'INCAR' input file

```
SYSTEM = MnO2

#Spin
ISPIN = 2 ! Spin polarisation turned on
MAGMOM = 8*3 8*-3 32*0 ! Atomic magnetic moments

#Symmetry
ISYM = 2 ! Efficient symmetrisation of charge density

#Electronic
ISMEAR = 0 ! Guassian smearing for semi-conductor
SIGMA = 0.1 ! Smearing width in eV
PREC = Accu ! Minimum  FFT grid and cut-off standards
ENCUT = 500 ! Planewave cut-off (standard + 30%)
LREAL = Auto ! Autiomatic real-space projectors
EDIFF = 0.0001 ! Electronic SC criterion
NELMIN = 4 ! Minmum number of electronic steps
LASPH = .TRUE. ! Non-spherical gradient corrections
GGA = PS ! PBEsol XC functional

#DFT+U settings
LDAU = .TRUE. ! On-site Coulomb corrections
LDAUL = 2 -1 ! Applied to l=2 sub-space for Mn only
LDAUU = 4.2 0.0 ! U = 4.2 eV for Mn only
LDAUTYPE = 1 ! U_effective 'Dudarev' on-site correction
LDAUPRINT = 2 !Print orbital occupancy density matrix

# Mixing parameters
MAXMIX = 40 ! Number of steps stored in Broyden mixer
LMAXMIX = 4 ! PAW charge mixing for d electrons

#Geometry relaxation
NSW = 99 ! Maximum number of geometry steps
EDIFFG = -0.01 ! Lattice geometry SC criterion
IBRION = 2 ! Conjugate-gradient minimisation
ISIF = 0 ! Relax ionic positions only

#Paralellisation
NPAR = 8 ! Parallelisation over bands

#Output
LWAVE = .TRUE. ! Print wave function output
LCHARG = .TRUE. ! Print charge density output

#Projections and DOS
NEDOS = 5000 ! DOS sampling grid points
EMIN = -10 ! DOS energy minimum
EMAX = 10 ! DOS energy maximum
LORBIT=10 ! DOS resolve into angular momentum numbers
```

5

CALCULATED MATERIAL PROPERTIES

In this final section of the methodology, we briefly outline the relationship between the DFT ground state and the calculation of material properties. Practical calculations of characteristic material properties are broadly classed as electronic, structural or thermodynamic, with each theme discussed below. Again natural atomic units ($e^2 = \hbar = m_e = 1$) are assumed throughout unless noted otherwise.

5.1 ELECTRONIC PROPERTIES

Many analytical techniques in computational materials science attempt to resolve local regional details from an encompassing global electronic structure. For a crystal observable, such as electronic density ρ, often only a projection is chemically relevant. In the example of ρ, a valence sub-space may be identified then sub-divided further into partitions that can be assigned a chemical or physical meaning. The decomposition of an observable for analysis could be in real-space such as Bader charges, or in momentum-space with the dispersion of energy bands, or the resolution of spin and orbital quantum numbers in density matrices. Some of these techniques are now outlined.

5.1.1 *The Bader atom*

Bader analysis is an intuitive way to break down the continuous charge in a solid or molecule into separate local parts for each atom. The rigorous theory to identify the charge of an ion from the charge topology of an extended system was developed in Bader's *Theory of Atoms in Molecules*.[155,215,216,217,218,219] For a local atomic charge density ρ^{at}, an atomic zero flux surface S defines an enclosed region of charge density

$$\nabla \rho^{\text{at}}(\mathbf{r}) \cdot \mathbf{n} = 0 \quad \forall\, \mathbf{r} \in S\,,$$

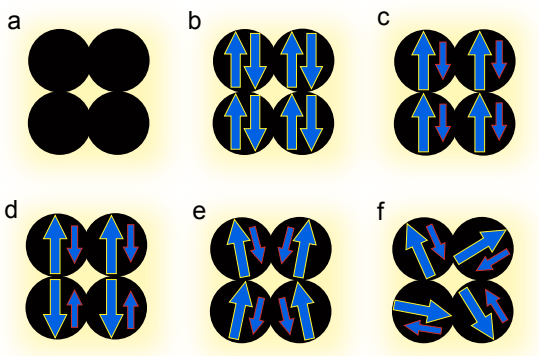

Figure 20: a) NM (no valence electrons), b) NM ($\alpha = \beta$), c) FM, d) AFM, e) non-collinear ordering and f) non-collinear PM disorder.

in terms of the charge density gradient $\nabla\rho(\mathbf{r})$ and normal surface vector $\mathbf{n}$. Bader's recognition of a single atom as an open quantum system solidified aspects of the foundations of theoretical chemistry, and provided a practical basis to calculate observables from the charge density of atomic sub-systems.

The difference in formal number of valence electrons N_e^{V}, and integrated valence charge within the closed zero flux surface S, provides a practical oxidation state

$$O_{\mathrm{ox}} = N_e^{\mathrm{V}} - \int_S dV\ \rho^{\mathrm{at}}(\mathbf{r})\,. \tag{42}$$

The integration of ρ^{at} is a difficult practical problem - many schemes have been developed, including using Tchebyshev polynomials,[220] the divergence theorem[221] and fictitious particles methods.[222] Calculation of oxidation states and other Bader analyses is central to several chapters of this thesis, and made possible by using the grid-based scripts of Henkleman *et al.*.[223]

Many other observables can also be calculated, for example, for atomic magnetisation is given by the difference in integration over the spin resolved densities, $\rho^{\mathrm{mag}} = \rho_\uparrow(\mathbf{r}) - \rho_\downarrow(\mathbf{r})$. This magnetisation formulation can be used to describe the collinear magnetic systems as in Figure 20 (a - d). Non-collinear magnetism, Figure 20 (e - f), has not been employed in this thesis.

5.1.2 *Dispersion, eigenvalues and DOS*

In the free-electron model of non-interacting electrons, delocalised electrons form energy bands that are dispersed with the quadratic dependence in **k**-space, $\epsilon(\mathbf{k}) = \frac{\hbar^2\mathbf{k}^2}{2m}$. Similarly, an energy band structure is produced by DFT, but for 'KS-particles' moving in an effective KS potential. The energy eigenvalues from solution of the N independent-particle equations in DFT, however result in non-trivial **k**-space dispersion relations.

The energy bands, from solution of KS equations, are formally related to occupation through the total energy in Janak's theorem as

$$\epsilon_{n\mathbf{k}\sigma} = \frac{\partial E[\rho]}{\partial f_{n\mathbf{k}\sigma}}, \tag{43}$$

where occupation and energy eigenvalues $f_{n\mathbf{k}\sigma}$ and $\epsilon_{n\mathbf{k}\sigma}$ are indexed for bands n at reciprocal point **k** in spin channel σ. In practice we use Janak's theorem to understand the origin of different effects, for example calculating eigenvalue splitting from the 'model' parts of the DFT+U Hamiltonian in Chapters 6 and 10.

The density of states (DOS), $g(E)$, can be expressed as a derivative

$$g(E) = \frac{dN(E)}{dE} = \frac{1}{N_k}\sum_{n\mathbf{k}}\delta(E - \epsilon_{n\mathbf{k}}), \tag{44}$$

where dN is the number of states in a small energy interval dE, or equivalently in Dirac-delta form.[160] Note N_k weights the number of **k**-points per Brillouin zone. To calculate spin or orbitally projected DOS, $g(E)$ can be 'sifted' by projection with eigenstate coefficients $\left|c^i_{n\mathbf{k}\sigma}\right|^2$. The coefficient $c^i_{n\mathbf{k}\sigma} = \langle\varphi_i|\psi_{n\mathbf{k}\sigma}\rangle$, is the overlap between total Bloch and desired local state (projection).

The DOS is important for many applications, for example, to find out if a material is metallic or if a gap exists at the Fermi level ϵ_F. The fundamental band gap (opposed to the optical gap which includes excitonic gap narrowing) is the difference in ionisation potential and electron affinity, $E_\mathrm{gap} = I - A$, or in terms of DOS $g(E)$, the difference between lowest unoccupied and highest occupied 'molecular' orbitals,

$$
\begin{aligned}
E_{\text{gap}} &= g_{\text{LUMO}} - g_{\text{HOMO}} \\
&\approx g^{\text{KS}}_{\text{LUMO}} - g^{\text{KS}}_{\text{HOMO}} + \delta_{xc} \,.
\end{aligned}
$$

In practice the KS gap is equal to the fundamental material gap, up to errors in the XC functional and lack of derivative discontinuity. The errors can be minimised to an extent with a correction, δ_{xc}.[160] In this thesis a practical partial correction δ_{xc} is provided by on-site Hubbard-U or Fock mixing - see Section 3.3.1.2.

5.1.3 *Density matrix properties and rotation*

To resolve the occupancy of local orbitals in terms of spin and angular momentum projections, we employ the reduced single-particle collinear orbital occupancy DM for the valence sub-space. This has been introduced as $n^{\sigma}_{mm'} = \langle \varphi^{\sigma}_{m'} | \psi_i \rangle \, f_i \, \langle \psi_i | \varphi^{\sigma}_{m} \rangle$, where f_i is an occupancy eigenvalue, $|\psi_i\rangle$ is a Bloch state, and $|\varphi^{\sigma}_{m}\rangle$ is a local basis state. Although the reduced one-body DM representation has many advantages[213,224] for DFT calculations, we primarily use the DM for analysis.

Complementing the Bader picture, counting diagonal DM elements trivially gives an estimation of the oxidation state. Formally, inserting the 'valence identity' into the DM expectation formula, $\langle O \rangle_{\rho}$=tr[ρO], gives the oxidation state

$$
O_{\text{ox}} = N_e^V - \text{tr}[n^{\sigma}_{mm'}] \,,
$$

where N_e^V is the formal number of valence electrons. By extension magnetisation is

$$
O_{\text{mag}} = \text{tr}[n^{\uparrow}_{mm'} - n^{\downarrow}_{mm'}] \,.
$$

Density matrix rotation

The DM used for analysis of DFT electronic structure calculations, can be expressed in terms of orbital occupancies f_i^{σ}, and its eigenvectors $\mathrm{V}^{\sigma}_{m,i}$ (and Hermitian conjugate),

$$n^{\sigma}_{mm'} = \sum_i \mathrm{V}^{\sigma}_{m,i}\, f^{\sigma}_i\, (\mathrm{V}^{\sigma})^{\dagger}_{i,m'}\,.$$

Unfortunately the eigenvectors $\mathrm{V}^{\sigma}_{m,i}$ are normally given in the global axial basis, rather than a local basis representation ideal for density matrix occupancy analysis. The basis vectors of the $2(2l+1)$ spin-orbitals form large matrices - 10-dimensional for d-shell and 14 for f-shell - which can be rotated in 3-dimensional space, using for example Wigner D-matrices, amongst other simpler methods. Here the chosen method of diagonalisation is by 'polynomial transformation'.

To illustrate the *polynomial transformation* method, consider the perovskite unit cell shown in Figure 21, which is relevant to the manganite in Chapter 10. The aim of the transformation is to rotate the density matrix for each Mn d manifold into a basis diagonal with respect to each local octahedron frame. Three Mn-O bonds are chosen that point in approximately orthogonal directions. The bonds are indexed $i = 1, 2, 3$, and we compute the difference vectors from the Mn to O positions: $\mathbf{u}_i = \mathbf{r}(O_i) - \mathbf{r}(Mn)$. These vectors are then normalised and define the local axes for the Mn. We create a 3×3 rotation matrix R connecting the global primed and local unprimed systems

$$\begin{pmatrix} x' \\ y' \\ z' \end{pmatrix} = \mathrm{R} \begin{pmatrix} x \\ y \\ z \end{pmatrix} = \begin{pmatrix} R_{11} & R_{12} & R_{13} \\ R_{21} & R_{22} & R_{23} \\ R_{31} & R_{32} & R_{33} \end{pmatrix} \begin{pmatrix} x \\ y \\ z \end{pmatrix},$$

defined by placing the unit vectors $\mathbf{u_i}$ in the columns of R. It is at this point that we choose the ordering of the unit vectors to reflect the physical questions at hand: *e.g.*, a traditional choice is to align z with 'apical' bond, but the choice is problem specific.

This rotation represents a linear polynomial transformation relating x', y', z' to x, y, z. The angular behaviour of d orbitals are quadratic in the coordinates: $3z'^2 - r'^2$, $x'^2 - y'^2$, $x'y'$, $y'z'$, $x'z'$ so that it is straightforward to plug and algebraically transform these polynomials to the unprimed (local) coordinate system. Performing the substitutions, using the orthogonal nature of the R matrix, and collecting terms, we find

$$\begin{pmatrix} 3z^2 - r^2 \\ x^2 - y^2 \\ xy \\ yz \\ xz \end{pmatrix} = \mathrm{C} \begin{pmatrix} 3z'^2 - r'^2 \\ x'^2 - y'^2 \\ x'y' \\ y'z' \\ x'z' \end{pmatrix}$$

where the matrix C is

$$\mathrm{C} = \begin{pmatrix} \frac{1}{2}(3R_{33}^2 - 1) & \frac{1}{2}(R_{13}^2 - R_{23}^2) & \frac{1}{2}R_{13}R_{23} \\ \frac{3}{2}(R_{31}^2 - R_{32}^2) & \frac{1}{2}(R_{11}^2 - R_{12}^2 + R_{22}^2 - R_{21}^2) & \frac{1}{2}(R_{11}R_{21} - R_{12}R_{22}) \\ 6R_{31}R_{32} & 2(R_{11}R_{12} - R_{21}R_{22}) & R_{11}R_{22} + R_{12}R_{21} \\ 6R_{32}R_{33} & 2(R_{12}R_{13} - R_{22}R_{23}) & R_{12}R_{23} + R_{13}R_{22} \\ 6R_{31}R_{33} & 2(R_{11}R_{13} - R_{21}R_{23}) & R_{11}R_{23} + R_{13}R_{21} \end{pmatrix} \quad \ldots$$

$$\ldots \quad \begin{pmatrix} \frac{1}{2}R_{23}R_{33} & \frac{1}{2}R_{13}R_{33} \\ \frac{1}{2}(R_{21}R_{31} - R_{22}R_{32}) & \frac{1}{2}(R_{11}R_{31} - R_{12}R_{32}) \\ R_{21}R_{32} + R_{22}R_{31} & R_{11}R_{32} + R_{12}R_{31} \\ R_{22}R_{33} + R_{23}R_{32} & R_{12}R_{33} + R_{13}R_{32} \\ R_{21}R_{33} + R_{23}R_{31} & R_{11}R_{33} + R_{13}R_{31} \end{pmatrix}.$$

The matrix C is not unitary due to the fact that the bare polynomials $3z'^2 - r'^2, x'^2 - y'^2, x'y', y'z', x'z'$ while orthogonal, are not normalised. The normalisation is done by averaging the squares of the functions $(3z'^2 - r'^2)/r'^2, (x'^2 - y'^2)/r'^2, x'y'/r'^2, y'z'/r'^2, x'z'/r'^2$ over the surface of the unit sphere. We place these averages, which are $4/5, 4/15, 1/15, 1/15, 1/15$, respectively, on the elements of a diagonal scaling matrix S and then form the scaled and unitary transformation matrix $\mathrm{D} = \mathrm{S}^{1/2}\mathrm{C}\mathrm{S}^{-1/2}$. D is our final matrix relating the *d* orbitals in primed global and unprimed local coordinates. Application of D should diagonalise the matrix of eigenvectors.

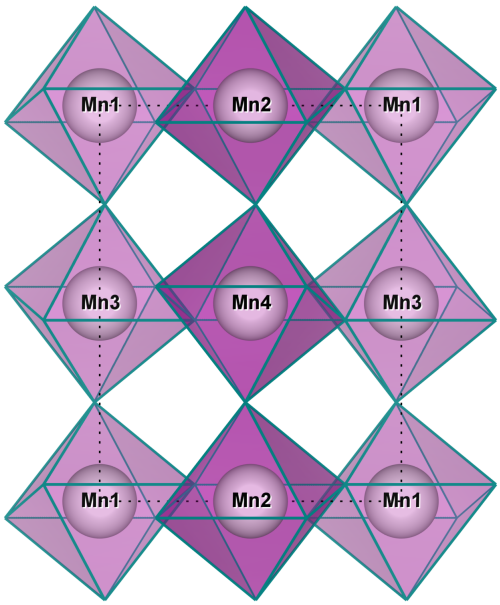

Figure 21: *Pnma* manganite perovskite unit cell, showing tilted Mn-centred octahedra.

5.2 STRUCTURAL PROPERTIES

5.2.1 *Phonons*

In this thesis the ground state phonon spectrum is calculated in the harmonic approximation, as a perturbation to the equilibrium potential

$$U_{\text{tot}} = U_{\text{equi}} + U_{\text{harm}}[u\{j_n l_m\}]\,. \tag{45}$$

The harmonic potential U_{harm} is a function of the displacements u, of the j^{th} of n atoms in the l^{th} of m unit cells. The harmonic perturbation has the quadratic form $U_{\text{harm}} = \frac{1}{2}\sum \Phi_{\alpha\beta} u_\alpha u_\beta$, in Cartesian displacements. Elements of the matrix $\Phi_{\alpha\beta}$ are known as *force constant*s, defined by potential or force derivative as

$$\Phi_{\alpha\beta}(jl, j'l') = -\frac{\partial F_\beta(j'l')}{\partial u_\alpha(jl)} = \frac{\partial^2 U}{\partial u_\alpha(jl)\,\partial u_\beta(j'l')}\,. \tag{46}$$

In practice force constants are calculated using the *frozen phonon method* by finite difference in $\Delta\mathbf{r}_\alpha(jl)$,

$$\Phi_{\alpha\beta}(jl, j'l') \approx -\frac{F_\beta(j'l'; \Delta\mathbf{r}_\alpha(jl)) - F_\beta(j'l')}{\Delta\mathbf{r}_\alpha(jl)},$$

which tends to the exact derivative in Equation 46 as $\Delta\mathbf{r}_\alpha \to 0$. Alternatively force constants can be calculated by *linear response* using the Hellman-Feynman theorem,[225] which states generally that the first-order change in energy due to a perturbation is the expectation of the perturbing potential.

A *dynamical matrix* is given by reciprocal space representation of the force constant matrix,[226]

$$\mathrm{D}_{\alpha\beta}(jj', \mathbf{q}) = \frac{1}{\sqrt{m_j m_{j'}}} \sum_{l'} \Phi_{\alpha\beta}(j0, j'l')\, \mathrm{e}^{i(\mathbf{q}\cdot[\mathbf{r}(j'l') - \mathbf{r}(j0)])},$$

where $\mathbf{q}$ is the wave vector and m_j is an atomic mass. Using the dynamical matrix, the classical equations of motion ($F = -k \cdot u = m \cdot \ddot{u}$) can be written

$$\sum_{j'\beta} \mathrm{D}_{\alpha\beta}(jj', \mathbf{q})\ \mathbf{e}_\beta(j', \mathbf{q}) = m_j\ \omega(\mathbf{q})^2\ \mathbf{e}_\alpha(j, \mathbf{q}), \tag{47}$$

where eigenvectors $\mathbf{e}_\alpha(j, \mathbf{q})$ indicate phonon displacement direction and size. Equation 47 defines an eigenvalue problem that is solved by diagonalisation.[226] For more details see the PHONOPY manual.[226]

In practice a reciprocal-space sampling scheme, such as Monkhorst-Pack,[209] can be employed to sample phonon DOS or dispersion band structure. Once the phonon spectrum is known numerically, the thermodynamics of the crystal structures phonon response can be calculated using expressions in Section 5.3.

5.3 THERMODYNAMIC PROPERTIES

To examine the temperature and pressure dependent properties of the materials in this work, we use the electronic and phonon energy eigenvalue spectra and DOS to define the thermodynamic functions of state. Expressions for particle number, spectrum energies and entropies are given in the harmonic approximation.

Calculations of phonon number from Bose-Einstein 'statistics' use the following expression for the average number of phonons of a particular frequency at a given temperature:

$$n_{\text{phon}}(\omega, T) = 1/(\mathrm{e}^{\frac{\omega}{k_{\text{B}}T}} - 1) \ .$$

The harmonic phonon energy in terms of phonon DOS $G(\omega)$ and particle number $n_{\text{phon}}(\omega, T)$ is

$$E_{\text{phon}}(\omega, T) = \int d\omega \ \omega \cdot G(\omega) \cdot (n(\omega, T) + \frac{1}{2}) \ .$$

The phonon entropy within the harmonic approximation is

$$S_{\text{phon}}(\omega, T) = -k_{\text{B}} \int d\omega \ G(\omega) \Big\{ \ln(1 - \mathrm{e}^{-\frac{\omega}{k_{\text{B}}T}}) - \frac{\omega}{k_{\text{B}}T} \frac{\mathrm{e}^{-\frac{\omega}{k_{\text{B}}T}}}{(1 - \mathrm{e}^{-\frac{\omega}{k_{\text{B}}T}})} \Big\} . \tag{48}$$

The electron number expectation in Fermi-Dirac 'statistics', where energy is transformed by the Fermi energy, $\bar{\epsilon} = \epsilon - \epsilon_{\text{F}}$, is

$$\bar{n}_{\text{el}}(\epsilon, T) = 1/(\mathrm{e}^{\frac{\bar{\epsilon}}{k_{\text{B}}T}} + 1) \ .$$

The electron energy in terms of the electronic DOS $g(\omega)$ and particle number $n_{\text{el}}(\epsilon, T)$ is

$$E_{\text{el}}(\epsilon, T) = \int d\epsilon \ \bar{\epsilon} \cdot g(\epsilon) \cdot \bar{n}(\epsilon, T) \ .$$

And the electronic entropy is[227]

$$S_{\text{el}}(\epsilon, T) = -k_{\text{B}} \int d\epsilon \ g(\epsilon) \Big\{ \bar{n}(\epsilon) \ln \bar{n}(\epsilon) + (1 - \bar{n}(\epsilon)) \ln(1 - \bar{n}(\epsilon)) \Big\} . \tag{49}$$

Part III

Results

6

DFT ELECTRONIC STRUCTURE OF VANADIUM DIOXIDE

This results chapter does not contain any compelling materials science. Instead this chapter provides some initial commentary on the capacity of 'plain' DFT, DFT+U and hybrid functional calculation frameworks to describe VO_2. This is a necessary precursor to the materials science chapters on VO_2 that follow, as a reliable description of the vanadium dioxide (VO_2) phase transition is a major challenge to DFT and *ab initio* methodologies more generally. We begin by looking at the failure of plain GGA DFT to provide the expected metallic rutile (R) phase and insulating monoclinic (M1) phase within a spin polarised description of VO_2. On-site Hubbard-U corrections ($+U$) are found to give qualitative improvements by stabilising insulating M1 and metallic R phases, but only for spin compensated NM solutions. Analyses of the orbital populations highlight the role of NM constraints in tempering the action of $+U$, such that a metallic R phase and an insulating M1 phase can both be stabilised at a single U value. The change in $x^2 - y^2$ orbital occupancy polarisation across the electronic transition is visualised. The effect of Hund's coupling on a model vanadium d^1 shell suggests that in a spin polarised M1 system, intra-orbital exchange should provide some degree of energetic re-ordering of orbitals towards an 'anisotropic' spin compensated solution, increasing the partial occupation of the vanadium minority-spin $3z^2 - r^2$ orbital. HSE calculations also suffer from a number of failings if spin polarisation is imposed, but varying the exchange parameter α can lead to the stabilisation of the correct insulating M1 and metallic R phases. The metallic spin polarised R phase is meta-stable.

6.1 INTRODUCTION

A reliable DFT description of VO_2 is important to resolve the physics and chemistry that will enable VO_2 materials design. There has been

much progress in this regard,[2,4,6,63,89,90,122,228,229,230,231] but the DFT description of VO_2 is still at best partially satisfactory, and at worst qualitatively wrong.

Of the most well-known VO_2 properties, which are listed in Table 1, the biggest challenges to a DFT description include achieving:

1. insulating M1 and metallic R phases,
2. the correct magnetic character above and below the experimental transition temperature T_c^{exp},
3. the appropriate orbital structure of both phases,
4. a total energy difference $\Delta E(\mathrm{M1}-\mathrm{R})$ commensurate with T_c^{exp},
5. potential energy surface minimum at the M1 structure and imaginary phonon modes in the R phase.

Points 1. – 3. are now briefly discussed in relation to the basic aspects of the experimental and theoretical VO_2 literature, while points 4. – 5., more related to thermodynamics and structure, are addressed in depth as part of Chapter 7.

Band gap

In rutile crystal field theory, small orthorhombic distortion of the partially filled d bands in VO_2 (R) is expected to result in close to degenerate t_{2g} states with metallic character. In VO_2 (M1), octahedra are much more strongly distorted due to V-V pairing. The structural distortion acts to polarise occupation, filling the x^2-y^2 t_{2g} state and energetically splitting it from the rest of the d shell. Enhanced by strong on-site Coulomb interaction, a band gap of approximately 0.7 eV is known to open in the VO_2 (M1) band structure at E_F.

LDA and GGA DFT both can both provide a metallic R phase,[6] but not the insulating solution required for the M1 phase. The M1 occupancy polarisation can be increased by applying an on-site Coulomb correction or by admixing HF exchange.[62,118,228,230] Both of these extensions to plain DFT open the M1 band gap, but retaining the metallic character of the R phase, simultaneously, within a single computational framework is more challenging. The band gap challenge is considered here in results in Chapter 6.3.1 & 6.3.3.

Observable	M1 phase	R phase
Region of stability[12]	$T \lessapprox 340$ K	$T \gtrapprox 340$ K
Space group[232]	$P2_1/c$	$P4_2/mnm$
Fundamental band gap at E_F[7,233]	$0.6 - 0.7$ eV	0
Conductivity[8,234,235]	semi-conductor	metal
Magnetic coupling[91,236]	strong intra-dimer AFM	paramagnetic (PM)
Magnetic susceptibility[12,83,237]	very small or NM	PM
Orbital character[63,230,238]	filled $x^2 - y^2$	partial t_{2g} filling

Table 1: Physical characteristics of M1 and R phase VO_2.

Magnetism

Magnetism in VO_2 is particularly intriguing. The M1 phase has a small almost NM susceptibility, of the order 10^{-6}, which is largely temperature independent (see Figure 3). The origin of this susceptibility is commonly attributed to a strong intra-dimer AFM coupling, forming singlet spin states in the quasi-molecular V-V units.[229,239]

In metallic VO_2 (R) a Pauli or free electron paramagnetic susceptibility might reasonably be expected, but instead a larger susceptibility closer in form to Curie-Weiss is observed. For example Maurer *et al.* indicate that in a band model of itinerant Pauli paramagnetism, some $\approx$ 20 states/eV/VO_2 at E_F are required to reproduce the experimental susceptibility of VO_2 (R).[128] A purely itinerant model is therefore unreliable as the VO_2 (R) DOS is known to be approximately $\approx$ 4 states/eV/VO_2, indicating some degree of contribution from Curie-Weiss-type disordered local moments.

The notion of any Curie-Weiss paramagnetism in VO_2 (R) is however equivocal. Curie-Weiss paramagnetism in the high temperature metallic phase implies a ferromagnetic (FM) ground state, but no Curie temperature has been experimentally observed for VO_2 (R) to our knowledge. Conventionally a FM ground state is expected in VO_2 (R) at zero temperature, but this relies on the assumption (and associated uncertainty) that T_{Curie} must be less than the the usual structural and electronic phase transition at $T_c \approx 340$ K.[83,229,235] In practice many VO_2 (R) calculations are simply NM (with $\sigma = \bar{\sigma}$), in disaccord with the Curie-Weiss paradigm at zero temperature.

In the analysis of experimental heat capacity measurements by McWhan *et al.*,[240] enhancement of the VO_2 (R) susceptibility is attributed to correlation effects, such as those suggested in the Brinkman-Rice[241] strongly correlated electron gas theory. Other model treatments, for example by Zylbersztejn and Mott,[83] prefer an alternative explanation with Stoner exchange-enhancement of the Pauli susceptibility by an effective intra-orbital Coulomb repulsion. Similarly Paquet and Leroux-Hugon[84] interpolate between free-electron Pauli and localised Curie-Weiss paramagnetic limits, with an exchange-enhanced Pauli susceptibility. Along related lines we question whether on-site Hund's coupling (intra-orbital exchange) can act to enhance the DFT magnetic ground state of either phase. Through model analysis we examine how *d* shell anisotropic exchange interactions can affect the development of M1 or R phase local magnetic moments in Chapter 6.3.2.

Orbitals

The *d* shell transition from polarised to shared orbital occupation is intimately related to magnetism and insulating character in VO_2. Several authors have emphasised the importance of orbital and localisation effects in determining the chemistry in both formal d^1 and V *d* shell systems generally.[52,55,62,101,230,231,238,242,243] For the VO_2 phase transition we are most interested in the change in $x^2 - y^2$ occupation from polarised (insulating) to partially filled (metallic).[238]

The change in $x^2 - y^2$ orbital filling from M1 and R can broadly be reproduced with DFT+U calculations,[62,229,230,238] but is strongly dependent on the calculation details - *e.g.* treatment of magnetism, lattice relaxation and choice of XC functional. The DFT+U description of the orbital transition is considered in the results in Chapter 6.3.1, with the change in orbital populations across the transition compared for DFT and DFT+U calculations.

Screened hybrid functional results are shown to improve when the intra-orbital exchange parameter is decreased below the standard HSE level. The hybrid functional ground state in VO_2 is examined and found to produce meta-stable states which are fragile with respect to the precise exchange treatment.

6.2.1 *Technical parameters*

Periodic DFT calculations were performed with VASP,[204,205] using the PBE GGA.[187] The PAW method was used to describe the interaction between the valence electrons and the core,[206,214] with the core states (up to 3*p* in V and 1*s* in O) kept frozen at the atomic reference states.

DFT and DFT+U calculations for VO_2 (M1) used a relaxed twelve atom monoclinic unit cell. VO_2 (R) calculations employed a relaxed twelve atom unit cell in a monoclinic basis for direct comparison between the phases. The number of plane waves was determined by a kinetic energy cut-off of 520 eV. A **k**-point mesh was generated by Monkhorst-Pack scheme, using a $6 \times 6 \times 6$ point sampling mesh.

Hybrid functional calculations for the M1 phase employed a twelve atom monoclinic unit cell, and six atom tetragonal unit cell for the R phase, both fixed at the experimental structures. A Monkhorst-Pack **k**-point mesh was sampled with $5 \times 5 \times 5$ points for the M1 phase, and $6 \times 6 \times 9$ for the R phase. The energy cut-offs for PAW pseudopotentials were all set to 400 eV. The fraction of HF exchange mixed into to plain PBE exchange was determined by the parameter α, which was varied between $\alpha = 0$ % (plain DFT) and $\alpha = 25$ % (HSE). The screening parameter μ was held fixed at $\mu = 0.207$ Å^{-1}.

6.2.2 *On-site Hubbard corrections*

On-site Coulomb corrections for vanadium *d* states were applied using the Dudarev 'U_{eff}' scheme[177] - for methodological details see Chapter 4.2.2.

On-site exchange corrections were calculated analytically using the Liechtenstein '$U|J$' Coulomb formalism,[59] with the on-site splitting[178]

$$\Delta\epsilon_{\sigma}^{U|J} = U_{\text{eff}}\left(\frac{1}{2} - f_{\sigma}\right) + J\,\mathrm{A}^{\sigma}\,f_{\sigma} + J\,\mathrm{B}^{\sigma}\,f_{\bar{\sigma}}\,. \tag{50}$$

Anisotropic exchange interaction is described by the matrix A^{σ} acting on the column vector of *like-spin* occupancies (f_{σ}) and B^{σ} acting on *opposite-spin* ($f_{\bar{\sigma}}$) occupancies, with both terms scaled by J. We con-

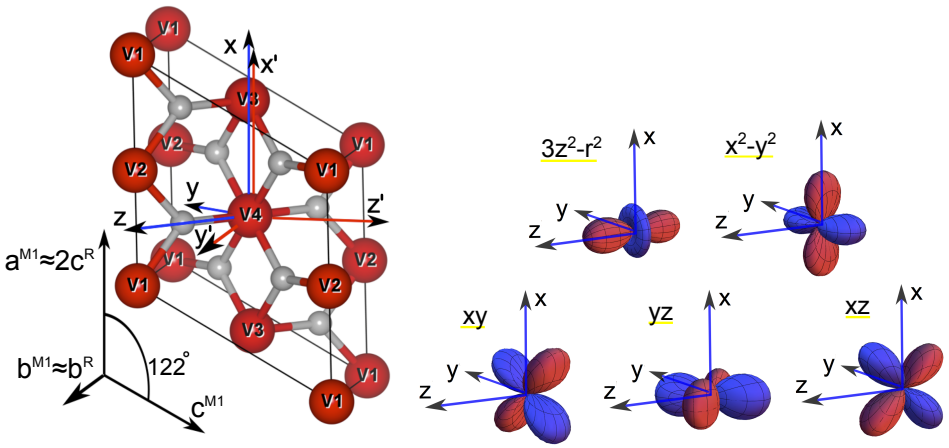

Figure 22: R phase in $P2_1/c$ unit cell, with global axial Cartesian coordinates denoted $x'y'z'$ and our local choice of basis xyz. V atoms in red, and small grey O atoms. Atomic-like d states, oriented in the local xyz basis.

sider a simple model of the VO_2 vanadium d shell. For a formal V^{4+} oxidation state, *i.e.*, d^1 configuration, only one spin channel is occupied. In this case the exchange splitting eigenvalues from the exchange part of Equation 50 is simplified for each spin channel (σ and $\bar{\sigma}$) to

$$\left(\Delta\epsilon^J_\sigma | \Delta\epsilon^J_{\bar{\sigma}}\right) = J\left(\mathrm{A}^\sigma f_\sigma | \mathrm{B}^{\bar{\sigma}} f_\sigma\right) . \tag{51}$$

Technical details on the exchange part of the '$U|J$' method and numerical matrix expressions for A^σ and B^σ are provided in Chapter 4 and Appendix A.1.

6.2.3 *Local basis*

To analyse density matrix occupancies we rotate between the primed global axial calculation basis and a more convenient unprimed local basis of our choice:

$$\begin{pmatrix} x \\ y \\ z \end{pmatrix} = \mathrm{T} \begin{pmatrix} x' \\ y' \\ z' \end{pmatrix} = \begin{pmatrix} T_{11} & T_{12} & T_{13} \\ T_{21} & T_{22} & T_{23} \\ T_{31} & T_{32} & T_{33} \end{pmatrix} \begin{pmatrix} x' \\ y' \\ z' \end{pmatrix} .$$

To rotate the R phase octahedra to a diagonal local basis, for example the VO_6 group centred about 'V4' in Figure 22, the unitary rotation matrix for $\frac{\pi}{4}$ anti-clockwise rotation about the x ($\sim c^{\mathrm{R}} \sim a^{\mathrm{M1}}$) axis is

$$\mathrm{T} = \begin{pmatrix} 1 & 0 & 0 \\ 0 & +\frac{1}{\sqrt{2}} & -\frac{1}{\sqrt{2}} \\ 0 & +\frac{1}{\sqrt{2}} & +\frac{1}{\sqrt{2}} \end{pmatrix}, \tag{52}$$

Equivalently a clockwise $\frac{3\pi}{4}$ rotation also yields a valid local basis, which just flips signs on the $y - z$ terms in Equation 52.

To directly rotate the five-dimensional d manifold, into for example the local 'V4' octahedron basis, the scaled and unitary matrix diagonalising d shell eigenvectors is

$$\mathrm{D} = \begin{pmatrix} 0 & -\sqrt{3/4} & 1/4 & 0 & -\sqrt{3}/4 \\ 0 & -1/2 & -\sqrt{3}/4 & 0 & 3/4 \\ \sqrt{2}/2 & 0 & 0 & \sqrt{2}/2 & 0 \\ 0 & 0 & \sqrt{3/4} & 0 & 1/2 \\ -\sqrt{2}/2 & 0 & 0 & \sqrt{2}/2 & 0 \end{pmatrix}. \tag{53}$$

The theory and practice of diagonalisation are described in Chapter 5 and Appendix B.4.

6.3 RESULTS

6.3.1 *DFT+U*

Results on the VO_2 electronic structure are presented and discussed for different spin polarisations (NM, FM and AFM), and for different on-site Coulomb schemes ($U_{\mathrm{eff}} = 0$ and $U_{\mathrm{eff}} = 3$ eV).

To compare orbital occupancies in compact form, it is useful to consider the *occupancy polarisation* with respect to the V $d_{||}$ ($x^2 - y^2$) state, which we define as

$$\pi^{d_{||}} = \frac{4 \cdot f_{d_{||}} - (f_{\pi^*} + f_{\sigma^*})}{\sum_i f_i}. \tag{54}$$

$\pi^{d||}$ measures how much the $d_{||}$ (x^2- y^2) site is filled compared to the π^* (yz & xz) and σ^* ($3z^2$- r^2 & xy) states.

U_{eff}	Observable	R^{NM}	R^{FM}	$M1^{NM}$	$M1^{AFM}$
0 eV	$\pi^{d\|\|}$	-0.1	0.1	0.4	-
	N_e	3.6	3.5	3.7	-
	$N_e^{\sigma} - N_e^{\bar{\sigma}}$	0	1.1	0	-
	Band gap	0	0	0	-
	Lattice stability	*yes*	*yes*	*yes*	*no*
3 eV	$\pi^{d\|\|}$	0.1	1.2	0.6	1.2
	N_e	3.4	3.3	3.5	3.4
	$N_e^{\sigma} - N_e^{\bar{\sigma}}$	0	1.1	0	1.0
	Band gap	0	0.7	0.7	1.5
	Lattice stability	*no*	*yes*	*yes*	*no*

Table 2: $\pi^{d||}$ occupancy polarisation within the majority-spin channel, along with d shell electron count per V, magnetic moment per V, band gap, and stability of lattice against distortion.

6.3.1.1 $U = 0$

For the NM VO_2 (R) calculation, the low $\pi^{d_{||}}$ value shown in Table 2 corresponds as expected to a metallic d shell. Whereas near-degenerate t_{2g} ($d_{||}$ & π^*) filling is expected experimentally, the calculation excessively spreads occupation, also partially filling σ^* (e_g) states. For FM VO_2 (R), the $\pi^{d_{||}}$ value is marginally larger, but stills yields a metallic band structure.

For the M1 phase, only NM calculations are possible - with AFM spin polarisation, the M1 phase cannot maintain local magnetic moments. The increased distortion from R to M1 modifies the electronic structure, increasing the d-d hybridisation associated with V-V pairing along a^{M1} ($\sim c^{R}$), and increasing the d-p hybridisation in the apical V-O that tilts the V-V dimer pairs. The effect on orbital occupancies, is the transfer of charge into the $d_{||}$ $x^2 - y^2$ orbital, increasing $\pi^{d_{||}}$. However due to the NM constraints, the increase in $\pi^{d_{||}}$ is small and the M1 phase remains metallic in qualitative disagreement with experiment.

Overall, the $U_{\text{eff}} = 0$ eV methodology is capable of describing VO_2 (R) as a metal with 'spread-out' occupancy, but struggles to reproduce

the precise orbital character, and is of severely limited use to describe both M1 and R phases simultaneously.

6.3.1.2 $U = 3$

For $U_{\text{eff}} = 3$ eV the NM R phase is unstable with respect to distortion - this is at least acceptable physically as the R phase is only stable at high temperature experimentally. With spin polarisation, the R phase is stable, but the M1 phase is unstable with respect to distortion. This is precisely opposite to conventional experimental expectation, indicating a spin polarised description may not be compatible with an accurate $U_{\text{eff}} = 3$ eV description of VO_2.

For the NM R phase, the $\pi^{d_{||}}$ value remains low in qualitative agreement with experiment.[238] On the other hand, for spin polarised FM calculations, $U_{\text{eff}} = 3$ eV acts to dramatically polarise occupation into the majority-spin $d_{||}$ state, leading to a substantial and erroneous band gap. In short *only* a NM R phase calculation 'works' - the reason for this appears to be the constrained partial band filling in the NM V d shell, which damps the action of the Hubbard term. The Hubbard splitting occurs as $\Delta\epsilon_{i\sigma} \approx U_{\text{eff}}(\frac{1}{2} - f_{i\sigma})$, which must be small for NM states which are necessarily partially occupied due to magnetic constraints, whereas the filling and resulting splitting of spin polarised states is unconstrained and therefore potentially much larger.

In NM calculations of the M1 phase, crystal field and on-site Coulomb effects cooperate to increase occupancy polarisation $\pi^{d_{||}}$ and also anisotropy in orbital occupations. This includes emptying π^* and filling $d_{||}$, which together produce a large $\pi^{d_{||}}$ value and band gap for the NM M1 phase.

6.3.1.3 *Details on the electronic transition*

As a reminder, we seek a computational framework can simultaneously describe the M1 and R phases. This includes $P2_1/c$ lattice symmetry, a band gap and large $\pi^{d_{||}}$ occupancy polarisation for M1, and $P4_2/mnm$ lattice symmetry, filled states at E_F, and a small value of $\pi^{d_{||}}$ for the R phase. In this regard, reasonable results have only been produced by NM $U_{\text{eff}} = 3$ eV calculations.

A qualitative picture of the change in charge density across the transition is shown in Figure 23. For a closer examination of the *orbital*

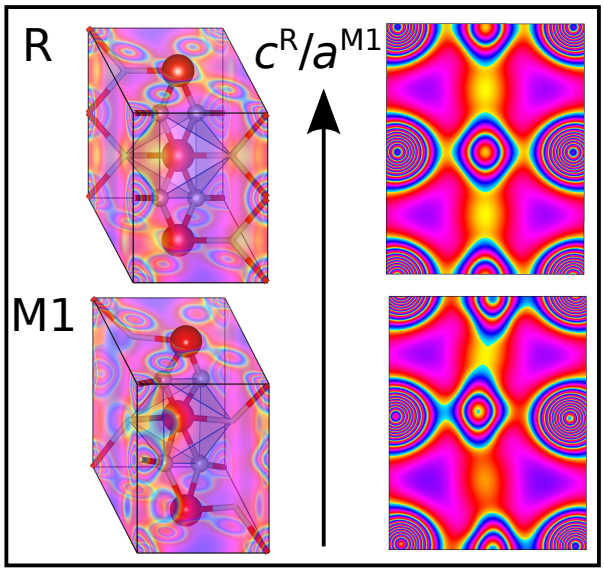

Figure 23: Figurative illustration showing redistribution of electronic charge density (2-dimensional slice) in response to distortion in the local lattice geometry (V-V dimerisation).

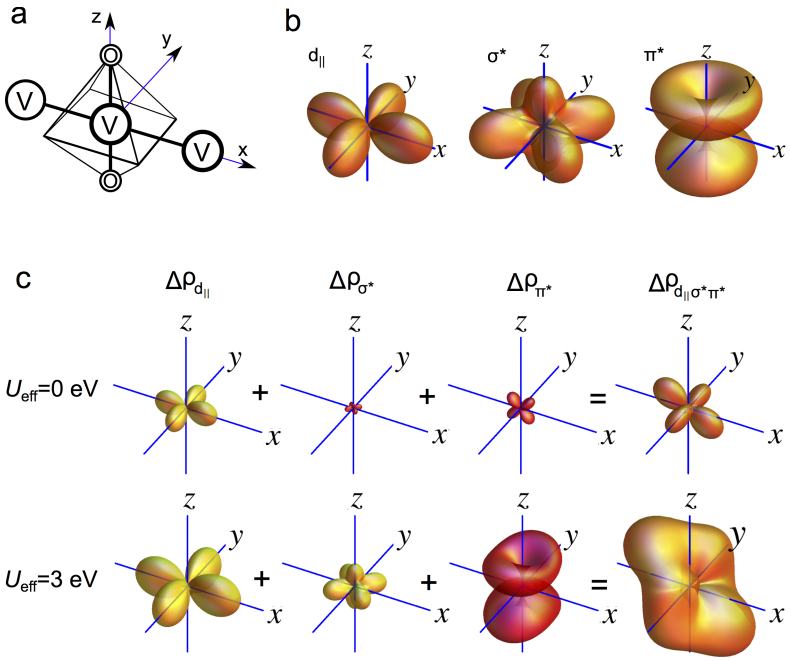

Figure 24: a) VO_6 octahedron in the local xyz basis, with apical O along z, and V chain along $c^R \sim a^{M1} \sim x$. b) Conventional VO_2 d shell states with unit occupation: $\rho_{d_{||}} = 1 \cdot x^2 - y^2$, $\rho_{\sigma^*} = 1 \cdot 3z^2 - r^2 + 1 \cdot xy$, $\rho_{\pi^*} = 1 \cdot yz + 1 \cdot xz$ c) Change in d shell density matrix from R to M1, $\Delta\rho = \rho^{M1} - \rho^R$. Positive occupancy change is shown in yellow and negative change in red, for $d_{||}$, π^*, and σ^* sub-spaces. Resultant total d shell change in orange.

transition within the NM $U_{\text{eff}} = 3$ eV picture, we briefly consider how the d shell orbital occupancy density matrix changes as the lattice structure is modified from the M1 to R phase geometry. The density matrix is considered in terms of the traditional[6,83,85,101] VO_2 d state orbital symmetry group terms and corresponding atomic-like orbitals: $d_{||}$ (x^2- y^2), π^* (yz, xz) and σ^* ($3z^2 - r^2$, xy).

The change in NM density matrix, $\Delta\rho_{d_{||}\sigma^*\pi^*}(\text{M1} - \text{R}) = \rho^{\text{M1}}_{d_{||}\sigma^*\pi^*} - \rho^{\text{R}}_{d_{||}\sigma^*\pi^*}$, is shown in Figure 24. Numerically the change in orbital filling for $U_{\text{eff}} = 0$ eV is

$$\begin{aligned}
\Delta\rho^{U=0}_{d_{||}\sigma^*\pi^*}(\text{M1} - \text{R}) &= \Delta\rho_{d_{||}} + \Delta\rho_{\sigma^*} + \Delta\rho_{\pi^*} \\
&= 0.32 \cdot x^2 - y^2 + 0.06 \cdot 3z^2 - r^2 - 0.08 \cdot xy - 0.18 \cdot yz - 0.04 \cdot xz \\
&= 0.26 \cdot x^2 - 0.38 \cdot y^2 + 0.12 \cdot z^2 - 0.08 \cdot xy - 0.18 \cdot yz - 0.04 \cdot xz \quad (55)
\end{aligned}$$

For $U_{\text{eff}} = 3$ eV, the orbital structure changes as

$$\begin{aligned}
\Delta\rho^{U=3}_{d_{||}\sigma^*\pi^*}(\text{M1} - \text{R}) &= \Delta\rho_{d_{||}} + \Delta\rho_{\sigma^*} + \Delta\rho_{\pi^*} \\
&= 0.52 \cdot x^2 - y^2 + 0.28 \cdot 3z^2 - r^2 + 0.28 \cdot xy - 0.44 \cdot yz - 0.54 \cdot xz \\
&= 0.24 \cdot x^2 - 0.80 \cdot y^2 + 0.56 \cdot z^2 + 0.28 \cdot xy - 0.44 \cdot yz - 0.54 \cdot xz \quad (56)
\end{aligned}$$

Equations 55 & 56 and Figure 24 show how increasing U_{eff} redistributes occupation to change the shape (and magnitude) of $\Delta\rho_{d_{||}\sigma^*\pi^*}(\text{M1} - \text{R})$. In particular charge is taken from π^* and placed into $d_{||}$ and σ^*, much more strongly for $U_{\text{eff}} = 3$ eV than $U_{\text{eff}} = 0$ eV. The orbitally selective removal of charge density from π^* and placement into $d_{||}$ and σ^* makes the R phase unstable in addition to increasing M1 stability. The R phase is the high temperature ($T_c \gtrapprox 340$ K) phase of VO_2, so the VO_2 (R) lattice instability to the M1 structure makes sense for a ground state DFT calculation.

The shape of $\Delta\rho_{d_{||}\sigma^*\pi^*}$, shown in Figure 24, is expected to reflect some of the distortions in VO_6 octahedra from R to M1. The change in the $d_{||}$ component corresponds to an increase in M1 d shell occupation along the local x direction, making possible the d-d hybridisation that is essential for V-V dimerisation.

A spin polarised description of the transition is reasonably expected in the zero temperature limit of DFT, however this fails on two counts: i) *magnetic moments* for M1 are unstable and cannot be maintained for $U_{\text{eff}} = 0$ eV, and ii) the M1 *lattice structure* is not stable for $U_{\text{eff}} = 3$ eV. For spin polarised calculations $\Delta\rho_{d_{||}\sigma^*\pi^*}$ could not be plotted because the magnitude is so small, as $\rho_{d_{||}\sigma^*\pi^*}$ is effectively the same for the M1 and R phases. The insufficient change in $\rho_{d_{||}\sigma^*\pi^*}$ topology gives a only a superficial reason to why spin polarised calculations fail to stabilise VO_2 (M1) and describe the transition. Next we consider one potential physical origin to the problem, by examining a range of effects due to on-site exchange.

6.3.2 *d-shell intra-orbital exchange (Hund's coupling)*

In TMO materials with formal d^4 oxidation states, intra-orbital exchange effects are known to be important to inter-site exchange and band gap formation. For example in $LaMnO_3$[†], Hund's coupling is important in the single-hole d^4 majority-spin shell of Mn^{3+}. Due to the symmetry between x hole and x electron shells (with respect to the intra-orbital exchange, see Appendix A.1.0.4), Hund's coupling effects should therefore also be important in the single electron V d^1 shell in VO_2.

[†] *On-site exchange effects are discussed for $LaMnO_3$ in Chapter 10.*

Through model analysis of the on-site anisotropic exchange term J, we investigate the range of intra-exchange effects possible in the VO_2 d shell. The explicit model calculations are important, for example to predict any enhancement or reduction of the magnetic moments expected through Hund's coupling or intra-orbital exchange effects, which are typically unaccounted for by plain DFT.

In the VO_2 model we assume a formal V^{4+} oxidation state. The form of the on-site exchange interaction is $J\,A^{\sigma}\,f_{\sigma} + J\,B^{\sigma}\,f_{\bar{\sigma}}$ (see Equation 50). The majority-spin channel denoted σ, has five m_l magnetic angular

momentum states in the V d^1 shell, and the column vector f_σ of occupancies ($f_{i\sigma}$) is

$$f_\sigma = \begin{pmatrix} 3z^2 - r^2 \\ x^2 - y^2 \\ xy \\ yz \\ xz \end{pmatrix}.$$

Anisotropic exchange is calculated for each d^1 electron configuration, testing each permutation of a single occupied site one-by-one. This shows the possible exchange effects, albeit in the limit of the extreme ionic V^{4+} d manifold.

Polarising occupation into the $3z^2 - r^2$ state produces the following exchange splittings

$$(f_\sigma | f_{\bar{\sigma}}) = \left(\begin{array}{c|c} 1 & 0 \\ 0 & 0 \\ 0 & 0 \\ 0 & 0 \\ 0 & 0 \end{array}\right) \text{ with } (\triangle\epsilon^J_\sigma | \triangle\epsilon^J_{\bar{\sigma}}) = J \cdot \left(\begin{array}{c|c} 0.00 & 1.14 \\ -0.52 & -0.63 \\ -0.52 & -0.63 \\ 0.52 & 0.06 \\ 0.52 & 0.06 \end{array}\right). \tag{57}$$

$x^2 - y^2$ polarised occupation produces the splitting

$$(f_\sigma | f_{\bar{\sigma}}) = \left(\begin{array}{c|c} 0 & 0 \\ 1 & 0 \\ 0 & 0 \\ 0 & 0 \\ 0 & 0 \end{array}\right) \text{ with } (\triangle\epsilon^J_\sigma | \triangle\epsilon^J_{\bar{\sigma}}) = J \cdot \left(\begin{array}{c|c} -0.52 & -0.63 \\ 0.00 & 1.14 \\ 0.86 & 0.29 \\ -0.17 & -0.40 \\ -0.17 & -0.40 \end{array}\right). \tag{58}$$

xy polarised occupation produces the splitting

$$(f_\sigma|f_{\bar{\sigma}}) = \left(\begin{array}{c|c} 0 & 0 \\ 0 & 0 \\ 1 & 0 \\ 0 & 0 \\ 0 & 0 \end{array}\right) \text{ with } (\triangle\epsilon^J_\sigma|\triangle\epsilon^J_{\bar{\sigma}}) = J \cdot \left(\begin{array}{c|c} -0.52 & -0.63 \\ 0.86 & 0.29 \\ 0.00 & 1.14 \\ -0.17 & -0.40 \\ -0.17 & -0.40 \end{array}\right). \tag{59}$$

yz polarised occupation produces the splitting

$$(f_\sigma|f_{\bar{\sigma}}) = \left(\begin{array}{c|c} 0 & 0 \\ 0 & 0 \\ 0 & 0 \\ 1 & 0 \\ 0 & 0 \end{array}\right) \text{ with } (\triangle\epsilon^J_\sigma|\triangle\epsilon^J_{\bar{\sigma}}) = J \cdot \left(\begin{array}{c|c} 0.52 & 0.06 \\ -0.17 & -0.40 \\ -0.17 & -0.40 \\ 0.00 & 1.14 \\ -0.17 & -0.40 \end{array}\right). \tag{60}$$

xz polarised occupation produces the splitting

$$(f_\sigma|f_{\bar{\sigma}}) = \left(\begin{array}{c|c} 0 & 0 \\ 0 & 0 \\ 0 & 0 \\ 0 & 0 \\ 1 & 0 \end{array}\right) \text{ with } (\triangle\epsilon^J_\sigma|\triangle\epsilon^J_{\bar{\sigma}}) = J \cdot \left(\begin{array}{c|c} 0.52 & 0.06 \\ -0.17 & -0.40 \\ -0.17 & -0.40 \\ -0.17 & -0.40 \\ 0 & 1.14 \end{array}\right). \tag{61}$$

The site occupied by the single electron generates an exchange splitting across all states in the shell, apart from the one state the electron itself occupies - the single electron in the formal V^{4+} shell does not interact with itself. Overall, intra-orbital term J has *no effect* on total energy, because the description is self-interaction-correct and there's only one electron, so $\sum_{i\sigma} f_{i\sigma}\Delta\epsilon_{i\sigma} = 0$.

From the results in Equations 57-61, splitting magnitudes range from $\Delta\epsilon^J_\sigma = +0.86J$ to $-0.52J$ eV for majority-spin splitting, and $\Delta\epsilon^J_{\bar{\sigma}} = +1.14J$ to $-0.63J$ eV for minority-spin splitting, with the splitting unique to each particular occupied site. The occupied site that is most

relevant to VO_2 experimentally is $d_{||}$ $(x^2 - y^2)$, which is shown in Equation 58. For $x^2 - y^2\sigma$ occupation, $3z^2 - r^2\bar{\sigma}$ is the most stabilised, by a value of $-0.63J$ eV. This result is interesting, because it indicates that a typical exchange value of $J = 1$ eV, the $3z^2 - r^2\bar{\sigma}$ orbital is likely to undergo stabilisation to within close range of the VO_2 $x^2 - y^2\sigma$ ground state occupied orbital.

The exchange splittings due to the $d_{||}$ $(x^2 - y^2)$ occupation imply some degree of spin compensation *via* Hund's coupling could be an important mechanism in VO_2, with local magnetic moments partially reduced due to intra-orbital exchange effects. This may provide some hint of why only forced NM DFT+U calculations were capable of providing reasonable results previously in Section 6.3.1.

Now we can develop the analysis to consider a NM model V^{4+} d^1 shell, examining the spin degenerate $x^2 - y^2$ occupied state,

$$(f_\sigma | f_{\bar{\sigma}}) = \left(\begin{array}{c|c} 0 & 0 \\ 0.5 & 0.5 \\ 0 & 0 \\ 0 & 0 \\ 0 & 0 \end{array}\right) \text{ with } (\Delta\epsilon^J_\sigma | \triangle\epsilon^J_{\bar{\sigma}}) = J \cdot \left(\begin{array}{c|c} -0.57 & -0.57 \\ 0.57 & 0.57 \\ 0.57 & 0.57 \\ -0.28 & -0.28 \\ -0.28 & -0.28 \end{array}\right). \tag{62}$$

The NM degeneracy in $\sigma/\bar{\sigma}$ occupation in Equation 62 is not lifted by the exchange interaction, which only splits orbital states within each spin channel. Due to the small partial occupancies, the magnitude of exchange splitting is smaller than in the previous spin polarised results in Equations 57 - 59. Interestingly the total energy shift is a destabilisation of $\sum_{i\sigma} f_{i\sigma}\Delta\epsilon_{i\sigma} = +0.57J$ eV, indicating the NM $x^2 - y^2\sigma/x^2 - y^2\bar{\sigma}$ configuration is not favoured by Hund's coupling at all. This is unexpected considering the previous results, where the spin polarised model shell was broadly re-ordered toward NM through the action of intra-orbital exchange.

However we can further consider a different configuration of the non-spin polarised d shell: in particular Equation 58 hints that an 'anisotropic' NM $x^2 - y^2\sigma/3z^2 - r^2\bar{\sigma}$ configuration could be most stable, rather than the simple degenerate NM $x^2 - y^2\sigma/x^2 - y^2\bar{\sigma}$. The splitting for the 'anisotropic' $x^2 - y^2\sigma/3z^2 - r^2\bar{\sigma}$ NM occupation is

$$(f_\sigma|f_{\bar{\sigma}}) = \left(\begin{array}{c|c} 0 & 0.5 \\ 0.5 & 0 \\ 0 & 0 \\ 0 & 0 \\ 0 & 0 \end{array}\right) \text{ with } (\Delta\epsilon^J_\sigma|\triangle\epsilon^J_{\bar{\sigma}}) = J \cdot \left(\begin{array}{c|c} 0.31 & -0.32 \\ -0.32 & 0.31 \\ 0.12 & -0.11 \\ -0.06 & 0.06 \\ -0.06 & 0.06 \end{array}\right). \tag{63}$$

For Equation 63 the total energy stabilisation is $\sum_{i\sigma} f_{i\sigma}\Delta\epsilon_{i\sigma} = -0.32\ J$ eV, with both spin channels stabilised each by $\sum_i f_{i\sigma}\Delta\epsilon_{i\sigma} = \sum_i f_{i\bar{\sigma}}\Delta\epsilon_{i\bar{\sigma}} = -0.16\ J$ eV. Therefore the anisotropic $x^2-y^2\sigma/3z^2-r^2\bar{\sigma}$ NM configuration is the most stable model configuration so far, at least in terms of the Hund's energy due to intra-orbital exchange interactions.

In summary the results for polarised occupation indicated that Hund's coupling could be an important effect that acts to significantly dampen the presence of local magnetic moments, by lowering $3z^2-r^2\bar{\sigma}$ with respect to an occupied $x^2-y^2\sigma$. This is reinforced by total energies, for which Hund's coupling favoured an 'anisotropic' NM $x^2-y^2\sigma/3z^2-r^2\bar{\sigma}$ configuration. Conversely the $x^2-y^2\sigma/x^2-y^2\bar{\sigma}$ NM solution is destabilised, and the spin polarised solution (solely $x^2-y^2\sigma$ occupation) is neutral in terms of total energy shift.

The analysis indicates that intra-orbital exchange corrections could provide an improved DFT description of VO_2, similar to that obtained in calculations with NM constraints. However any NM spin compensation provided would be physical in origin through orbital splitting due to Hund's coupling, rather than simply through NM constraints imposed *a priori* without physical justification.

The next logical step in this analysis is to switch from model *d* shell occupancies to *ab initio* occupancies provided by DFT+U_{eff}. We are somewhat limited in this capacity as the *ab initio* code used in this work, VASP, is not capable of fixing initial orbital occupancies arbitrarily to initialise the suggested anisotropic $x^2-y^2\sigma/x^2-y^2\bar{\sigma}$ NM solution. In recent advances Allen and Watson[180] have produced a methodology to modify the orbital occupancy density matrix input to VASP. For future calculations this would appear to provide the level of orbital occupancy control desired to examine the $x^2-y^2\sigma/x^2-y^2\bar{\sigma}$ configuration and other magnetic and orbital orderings in detail.

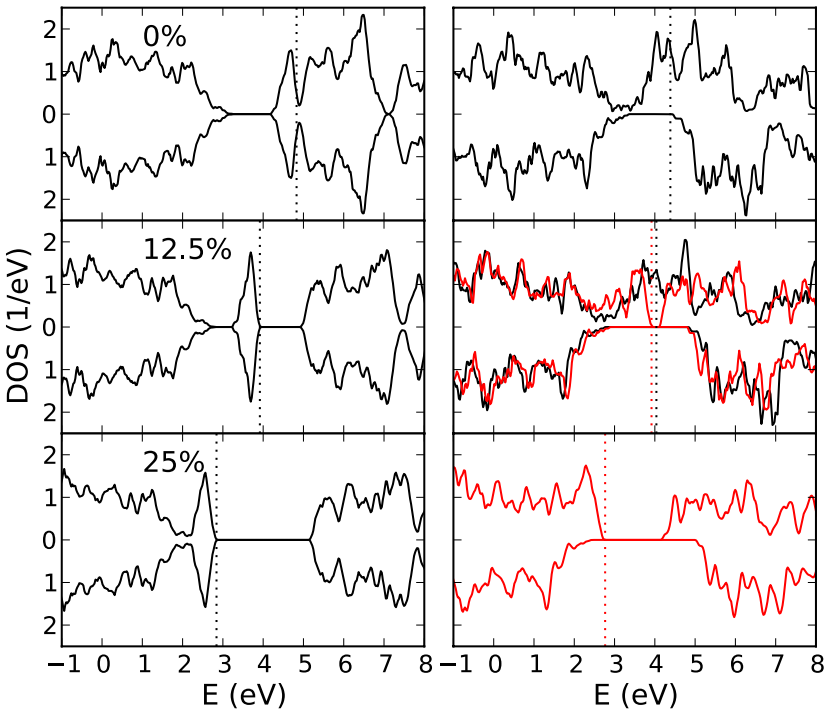

Figure 25: DOS (states/eV/VO_2) for AFM M1 (left) and FM R phase, for Hartree-Fock mixing level at $\alpha = 0$, 12.5 & 25 %. Fermi levels are marked by the dotted vertical lines. R phase density of states with insulator solutions are highlighted in red.

6.3.3 *The HSE electronic structure of VO_2*

In this final section, we examine the *ab initio* description of FM R and AFM M1 VO_2. A screened hybrid functional approach is employed, where we modify α from 0 % (PBE DFT) to 25 % (HSE). We begin discussing the M1 and R DOS shown in Figure 25.

6.3.3.1 *Spin polarisation*

At $\alpha = 0$ % (PBE), spin degenerate calculations produce metallic solutions that are correct for the R phase, but incorrect for the M1 phase. Including spin polarisation at the PBE level, M1 remains metallic but the R phase becomes half-metallic.

By mixing in HF exchange at $\alpha = 25$ %, the NM HSE calculations appear to improve the electronic description, with a metallic R phase and insulating M1 phase. On the other hand, a spin polarised HSE description produces an insulating M1 phase where the gap is too

α	Gap M1		Gap R	
(% HF)	NM	AFM	NM	FM
0(PBE)	0.0	0.0(0.4)	0.0	0.0(1.1)
5	0.0	0.3(0.7)	0.0	0.0(1.1)
10	0.3	0.8(0.8)	0.0	0.0(1.2)
12.5	0.4	1.0	0.0	0.2(1.1)
15	0.5	1.3	0.0	0.5(1.1)
20	0.8	1.8	0.0	1.0(1.1)
25(HSE)	1.1	2.3	0.0	1.5(1.1)

Table 3: Band gap (eV) and magnetic moment (μ_B /V) in brackets, listed for M1 and R VO_2. The screened hybrid calculation results are given for non-magnetic and spin polarised solutions as a function of Hartree-Fock mixing parameter α.

large (2.3 eV compared to $\sim$ 0.7 eV in experiment), in addition to a strongly insulating R phase.

To find physically reasonable spin polarised solutions for both M1 and R phases, we alter the HF mixing parameter α to values intermediate compared to the PBE (0 %) and HSE (25 %) approaches. Note the results are obtained by first converging the PBE wave function, then beginning the hybrid calculation from the PBE optimised wave function.

The results in Table 3 show that a physically reasonable spin polarised electronic structure is provided by intermediate HF mixing at $\alpha \approx 10$ %. These results show promise because they provide the first indication that a spin polarised *ab initio* description of VO_2 is possible, and can be achieved by using an α value smaller than the standard HSE.

6.3.3.2 *Meta-stable R FM solutions with orbital occupancy hysteresis*

Interestingly we find that when the input wave function for the hybrid calculation is pre-conditioned to use an initial HSE ($\alpha = 25$ %) wave function, rather then PBE ($\alpha = 0$ %) wave function, another solution appears. The second solution for the FM R phase, which occurs when $\alpha \geq 12.5$ %, is shown as the red branch in Figure 26. The second FM R solution is more stable than the original, and results in an insulating FM R phase opposed to metallic for $\alpha \geq 12.5$ %.

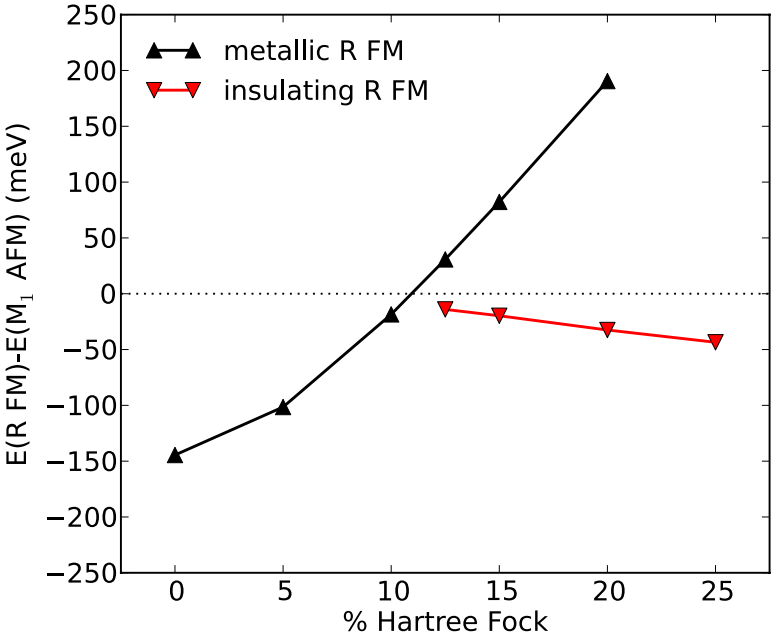

Figure 26: Total hybrid functional energy difference between FM R and AFM M1 phases per formula unit. Black triangles indicate the R FM phase is metallic, while red upside-down triangles represent insulating solutions for R FM.

For the insulating R FM phase, the band gap values for $\alpha \geq 12.5$ % are recorded in Table 3, and shown in Figure 25. The bifurcation in FM R solution for $\alpha \geq 12.5$ % indicates that a value of $\alpha = 10$ % and no larger provides the most appropriate description of both phases.

Leaving any conclusions about experimental agreement to one side, the bifurcation of FM R solutions in α is an interesting feature from a computational/theoretical perspective. The fragility of the R FM solution indicates that the characteristic localisation/delocalisation of VO_2 orbitals is highly dependent on the Coulomb exchange treatment. The existence of meta-stable solutions so close to the $\alpha = 10$ % solution (which has best experimental agreement), serves to highlight how delicate the electronic ground state is with respect to exchange.

The two different FM R VO_2 solutions can be rationalised by looking at the polarisation of orbital occupation into a ground $d_{||}$ $(x^2 - y^2)$ state. When occupation is polarised into $d_{||}$, as happens for calculations with $\alpha \geq 12.5$ % and HSE pre-conditioned wave function, R FM is insulating. Conversely when the d manifold is delocalised and the $d_{||}$ state is around half-occupation, as happens for calculations with $\alpha \leq 20$ % and a PBE pre-conditioned wave function, R FM VO_2 is

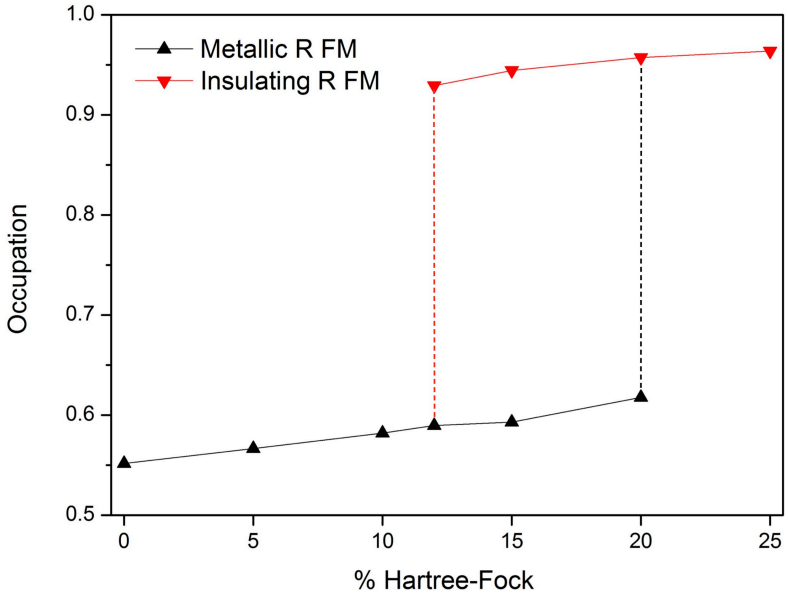

Figure 27: Occupation in the d shell ground state orbital. Black triangles indicate the R FM phase is metallic, while red upside-down triangles represent insulating solutions for R FM.

metallic. This effectively forms a hysteresis loop for metallic/insulating character in VO_2 depending on how the wave function is primed - this can be observed in Figure 27.

In our computational study we are able to control the orbital occupancy *via* α. However the orbital instability in Figure 27 may potentially be physically accessible through experimental means if some parameter exists to modify orbital polarisation and $d_{||}$ filling. Although beyond the scope of this work, progress in this regard has been made in multi-ferroic perovskite hetero-structures. For example recent advances have shown that by changing the ferroelectric polarisation, it is possible to modify orbital occupancy polarisation, which acts generally as a powerful lever to affect change over electron and spin density.[149] Due to the orbital instability in VO_2, small changes in occupancy polarisation could provide a route to access large changes in material characteristics and tuneable properties.

6.4 CONCLUSIONS

For plain DFT and DFT+U calculations, the NM $U_{\text{eff}} = 3$ eV regime provided best agreement with the experimental band gap, structural

stability and orbital character of both phases. As VO_2 M1 and R are conventionally understood to be spin polarised at 0 K, the capacity of *only* NM calculations to describe both phases simultaneously somewhat defied expectations.

Qualitatively it appears that NM spin compensation in effect places constraints on partial band filling, reigning in occupancy polarisation due to $U_{\text{eff}} = 3$ eV such that the electronic transition from delocalised to localised character can exist, and is available upon structural distortion from R to M1 symmetry. Without $+U$, occupancy polarisation from structural distortion alone in M1 will not open the band gap, and equally without NM constraints the action of $+U$ is excessive and results in an erroneous band gap in the R phase. Together $+U$ and NM constraints on occupancy appear to find a balance that ensures metallic character is retained for the high temperature R phase, and produce d state occupancy polarisation such that filling of $d_{||}$ and σ^* symmetry states occurs upon M1-type geometry distortion, opening the band gap and stabilising the M1 structure.

Model anisotropic exchange analysis of the formal d^1 shell showed that the Hund's coupling acts to reorder energy levels toward a partially spin compensated solution for VO_2. This may provide some physical indication of why only NM constraints are successful for DFT+U calculations.

Hybrid functional calculations showed that the optimum exchange mixing parameter value is $\alpha = 10$ %. This stabilised a spin polarised R phase ground state, and the correct M1 and R phase band gaps. The calculations also showed the emergence of a set of meta-stable solutions that depend on how the initial wave function was primed. This illustrated the fragility of VO_2 ground state, which can flip between insulating and metallic character, depending on the exchange parameter value which tunes occupancy polarisation.

In this chapter the objective was not to present results on the materials science of VO_2 *per se*. Nonetheless the results were essential to inform an effective choice of calculation set-up (magnetism and on-site corrections) for the following VO_2 materials science in Chapters 7 & 8.

7

VANADIUM DIOXIDE PHASE TRANSITION AND POTENTIAL ENERGY SURFACES

Potential energy surfaces for the VO_2 phase transition have been calculated in terms of V-V dimerisation using DFT+U. Surfaces are considered for different levels of electron localisation, which is modified *via* an on-site Hubbard term (+U), and for different spin ordered solutions. Spin polarisation fails to stabilise the low temperature monoclinic (M1) structure, and also erroneously produces a band gap in the metallic rutile (R) phase. NM calculations provide a more physically reasonable potential energy surface (PES), with an energy surface minimum at the M1 level of dimerisation, and a maximum at the R phase local geometry. In addition to agreement with the Peierls-like instability observed experimentally, the NM calculations also give insulating M1 and metallic R phases. Based on this we use the NM DFT+U methodology to investigate the origin of the transition entropy. Electronic entropy is calculated for the metallic R phase, and the phonon entropy in the harmonic approximation is calculated for both phases. To apply the harmonic approximation to the high temperature R phase, the squared frequency of the soft modes is extrapolated linearly in temperature. R phase phonons that are imaginary at zero temperature and in the DFT+U ground state, are extrapolated to the real-frequencies and positive phonon energies at the transition temperature. The total entropy obtained using this method is reasonably close to the experimental value: $T_c\Delta S = 56$ meV/VO_2 from DFT+U compared to 44 meV from experiment. 86 % of the transition entropy is due to phonons, and the remaining 14 % is electronic in origin. Although most of the transition entropy comes from the lattice, e-e interaction in the localised d shell facilitates this. Strong Coulombic localisation of d electrons is shown to be absolutely critical to the VO_2 transition, as the existence of low-energy phonons that yield the lattice instability depend on having a large enough on-site Coulomb interaction.

A first-order temperature-dependent phase transition in VO_2 gives rise to the characteristic Janus-natured or transitional 'two-sided' material properties. Pristine VO_2 exists in a dimerised M1 form below the phase transition temperature of $T_c \approx 340$ K, and as a tetragonal R form with raised symmetry above T_c. Change in structure is accompanied by sharp discontinuities in resistivity and magnetic susceptibility. Control of the dielectric, magnetic and structural properties in VO_2 present a potential opportunity for technological advance, with ideas ranging from thin-film thermochromic window coatings to piezoelectric transducers for high-speed electronics.[13,26,29,39,94,244]

The VO_2 phase transition has been studied since the 1950's,[9] but questions on the nature of the transition remain a perennial source of intrigue and disagreement. In the Mott-Hubbard predominantly e-e interaction picture,[83,84,123] strong intra-orbital Coulomb interaction between localised valence electrons is the central theme. In the alternative e-l picture, the transition origin is due to Peierls-type instability.[122] In this case perturbation of the quasi-one-dimensional V-V chain produces strong temperature-dependent phonon softening. Recent evidence appears to suggest that both e-l and e-e interactions together produce the transition,[63,71,124] and that a singly Mott-Hubbard or Peierls picture is not necessarily accurate. The relative influence of Mott-Hubbard or Peierls interactions in the transition is difficult to estimate quantitatively, however the calculation of separate phase transition entropies from electronic and lattice contributions *is* possible. The total latent heat of transition is experimentally known to be 44 meV/VO_2, but the precise electronic to phonon entropy ratio is widely disagreed upon historically. For example, suggestions for the electronic to phonon entropy ratio range from 2 : 3 at one extreme,[125] to 100 : 1 at the other,[127] along with a gamut of intermediate value estimates.[12,83,125,126,127,128] In this work, modern *ab initio* techniques are used to identify the origin of the VO_2 transition entropy.

Early work by Kawakubo,[245] and by Adler and Brooks,[246] qualitatively examined how localised narrow bands change to delocalised metallic states as dimerisation is modified. Here we extend the principle of their works, by quantitatively mapping PES in terms of a

structural and electronic localisation parameters (dimerisation and Hubbard U). Our detailed *ab initio* PES complement energy surfaces from experimental work on lattice softening by Hada *et al.*,[247] and classical inter-atomic potential PES by Woodley.[248] Our results are also discussed in the context of the model Hamiltonian mapping of VO_2 PES in terms of local magnetic moment and dimerisation by Paquet and Leroux-Hugon.[84] *Ab initio* PES using ordinary DFT do not provide a temperature dependence explicitly, as it is the $T = 0$ K ground state energy surfaces that are typically available.[249,250] As the VO_2 transition occurs in temperature and the PES is strongly temperature dependent, this poses a challenge to interpretation. To determine the PES in the high T limit we employ a 'structural mean-field' approach, which provides a sketch of the high T PES.

Two instability modes were predicted in early theoretical work by Brews,[82] and have recently been observed in DFT calculations and IR spectroscopy.[63,251] The imaginary phonons are problematic to an *ab initio* thermodynamic investigation of high T VO_2, as ferroelectric and anti-ferroelectric modes of distortion destabilise the rutile phase and lower its symmetry. To take into account the temperature dependence of the soft modes, imaginary phonons are transformed in temperature to yield the frequencies at $T = T_c$. This approach is based on the well-known linear dependence of the order parameter and square root of temperature on soft mode frequency in VO_2.[78,82,252] Our method to access transition-temperature vibrational thermodynamics avoids alternative complicated sampling of microscopic degrees of freedom, or computationally expensive molecular dynamics simulations.[253,254,255,256,257]

7.2 COMPUTATIONAL DETAILS

7.2.1 *Density functional theory*

Periodic DFT calculations were performed with VASP,[204,205] using the GGA in the form of the PBE XC functional.[187] The PAW method was used to describe the interaction between the valence electrons and the core,[206,214] and the core states (up to $3p$ in V, $1s$ in O, and $5p$ in W), which were kept frozen at the atomic reference states.

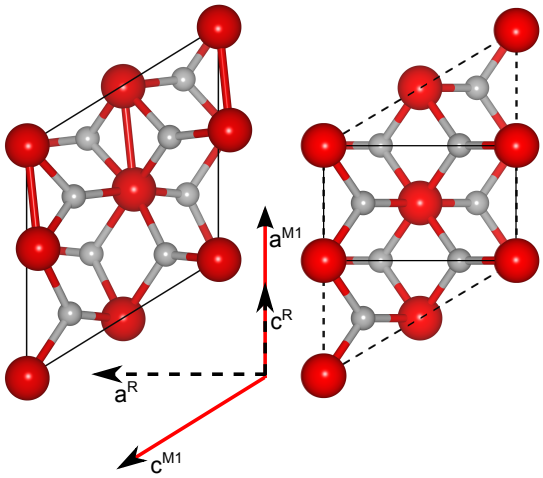

Figure 28: VO_2 M1 and R phase structures represented in a monoclinic unit cell basis. V cations large in red, O small in grey.

For the PES calculations which involved a 12 atom M1 unit cell, the number of plane waves was determined by a kinetic energy cut-off of 520 eV. A **k**-point mesh was generated by Monkhorst-Pack scheme, using a sampling mesh of $6 \times 6 \times 6$. Doped VO_2 calculations used a $2 \times 2 \times 2$ supercell for the M1 phase, and $2 \times 2 \times 4$ supercell for the R phase, each with 32 formula units. For the large doped-VO_2 supercell calculations, a smaller kinetic energy cut-off of 400 eV was used, along with a $3 \times 3 \times 3$ **k**-point sampling mesh. These parameters were checked with respect to convergence of the bulk total energy.

A Hubbard-like on-site Coulomb term was employed *via* the U_{eff} 'Dudarev' correction scheme[177] - for theoretical details on DFT+U see Chapters 3 & 4.

7.2.2 *Thermodynamics*

Phonon DOS were calculated using the displacement method and the PHONOPY program,[258] and electronic DOS directly using VASP. Phonon and electronic thermodynamics - particle expectations, spectrum energies and entropies - were calculated by numerical integration using the harmonic approximation expressions introduced in Chapter 5 on page 102.

For the R phase, the unit cell is a six atom structure with $P4_2/nmn$ symmetry and for the M1 phase, a twelve atom $P2_1/c$ unit cell is used. Transition state calculations between the phases are made possible

by expressing each phase in the M1 structural basis, as in Figure 28. In these calculations dimerisation was employed as a parameter to distinguish and systematically modify distortion between the M1 and R phases. The microscopic dimerisation,

$$\delta_j = d_j[\text{V-V}] - d_{j+1}[\text{V-V}]\,, \tag{64}$$

is the difference in V-V bond length between consecutive pairs along the dimerisation axis, c^{R} (a^{M1}). The dimerisation parameter is zero for the high T R phase, but finite for the low T M1 phase. The microscopic dimerisation is related to the macroscopic dimerisation used elsewhere[82,84]

$$\eta = \frac{1}{n}\sum_{j}^{n} \delta_j \cdot \phi_j\,. \tag{65}$$

η is the typical anti-ferroelectric order parameter,[259] ϕ_j is an alternating phase (to ensure non-zero sum for anti-ferroelectric order), and n is the number of V-V pairs. A 'structural correlation length' is defined to refer to a domain of radius ξ within which the distortion of V-V pairs is correlated - *i.e.* allowed to relax and respond, rather than for example being fixed at rutile positions to produce a high T mean-field. In the low-T limit the monoclinic structure is fully structurally correlated, such that $\delta_j = -\delta_{j+1}$ and therefore $\eta \equiv \delta$. The concept of the structural correlation length has been introduced because it is helpful to discuss the transition PES at finite T .

7.3 RESULTS

7.3.1 *Potential energy surfaces*

We begin by discussing the PES of VO_2 shown in Figure 29, which are important to the active debate on the DFT description of VO_2,[4,118,229] and to understand the disparate transition energy surfaces obtained for VO_2 from different groups.[83,84,247,248]

In Figure 29 the band gap, local magnetic moment and PES are plotted as a function of dimerisation and on-site Coulomb potential ($U_{\text{eff}} = 0$ to 3 eV), for NM, AFM and FM spin ordered solutions.

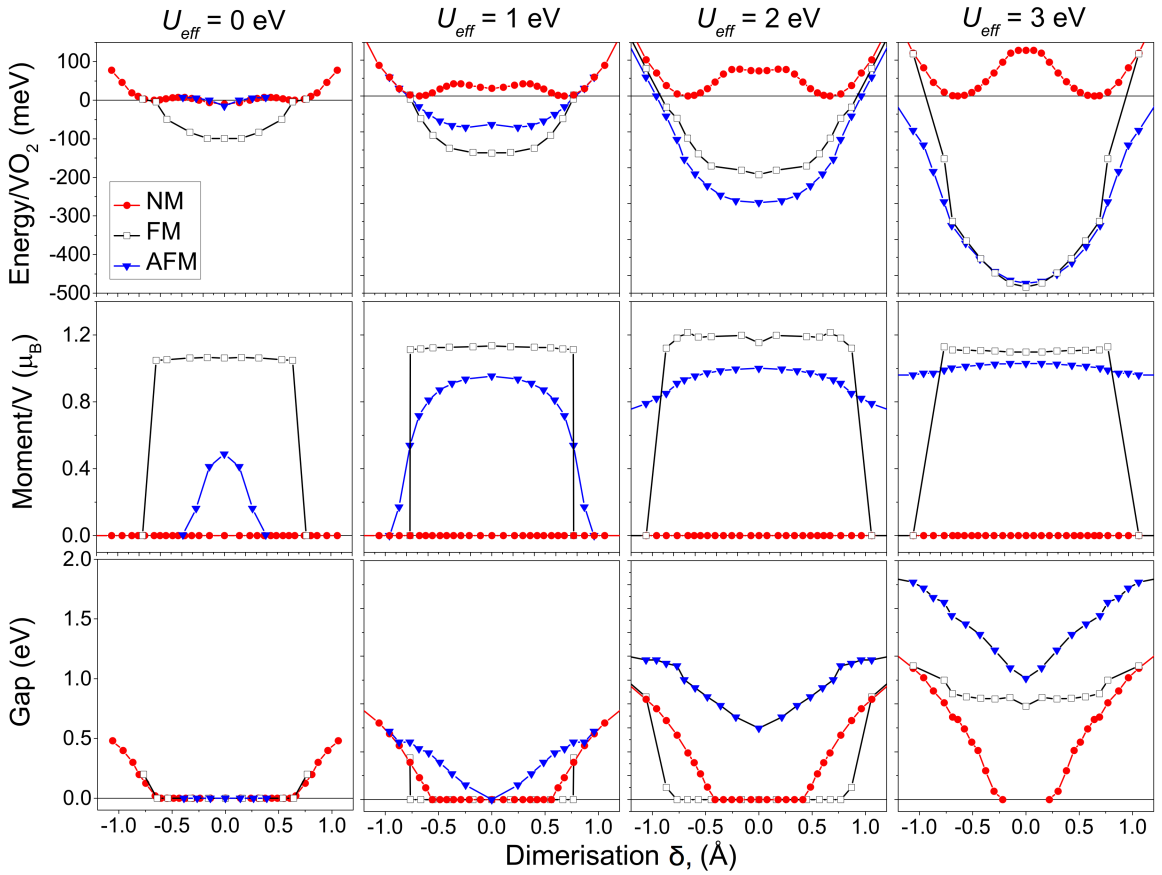

Figure 29: Total energy relative to the non-magnetic M1, local magnetic moment on vanadium cations, and band gap, each *versus* VO_2 dimerisation, defined as per Equation 64. $U_{\text{eff}} = 0$, 1, 2 and 3 eV, for columns left to right respectively.

Although both M1 and R phases have well-known paramagnetic susceptibilities experimentally, the relative roles of thermal fluctuation, inter-site spin-pairing, and Hund's coupling in VO_2 are active research questions.

Figure 29 shows imposing spin polarisation (either AFM or FM) produces an unphysical PES for the zero temperature limit. The main problem is the failure to stabilise the M1 structure, which is the low temperature ground state. In addition, for $U_{\text{eff}} = 3$ eV both spin polarised (AFM or FM) solutions erroneously open a band gap gap in the R phase.

NM calculations appear to provide the best practical description, in particular the $U_{\text{eff}} = 3$ eV NM configuration provides the results that are most physically agreeable. The $U_{\text{eff}} = 3$ eV NM surface is preferred as $U_{\text{eff}} < 3$ eV fails to produce the necessary rutile lattice instability. In terms of gap, $U_{\text{eff}} = 3$ eV NM opens smoothly with dimerisation from 0 eV in the R phase to 0.7 eV in the M1 phase. This is in accord with the $0.6 - 0.7$ eV gap observed experimentally.[260,261] From the pragmatic perspective of employing a methodology that satisfactorily reproduces experiment, NM constraints provide the most reasonable description of the various physical observables. However the choice is somewhat problematic theoretically as QMC calculations[239] have explicitly confirmed both VO_2 structural phases should be spin polarised at $T = 0$ K.

Evidence of phonon softening in the high T R phase has previously led to suggestions of an e-l transition origin.[84,262] Based on the PES results, our perspective is that dimerisation of e-l origin and e-e interactions (parameterised through U_{eff} in Figure 29) are equally important to the PES shape and phase transition. In early work by Goodenough,[263] the phase transition is proposed to be due to "homopolar bonding" of the V-V pairs, or in other words, entirely structural. Conversely, Zylbersztejn and Mott have claimed that no quantitative model of VO_2 is complete without the Hubbard U (whilst acknowledging VO_2 may not be a conventional Mott-Hubbard transition).[83] The PES reported here reinforce the predictions of Zylbersztejn and Mott, in that electron localisation is essential in addition to Peierls dimerisation.

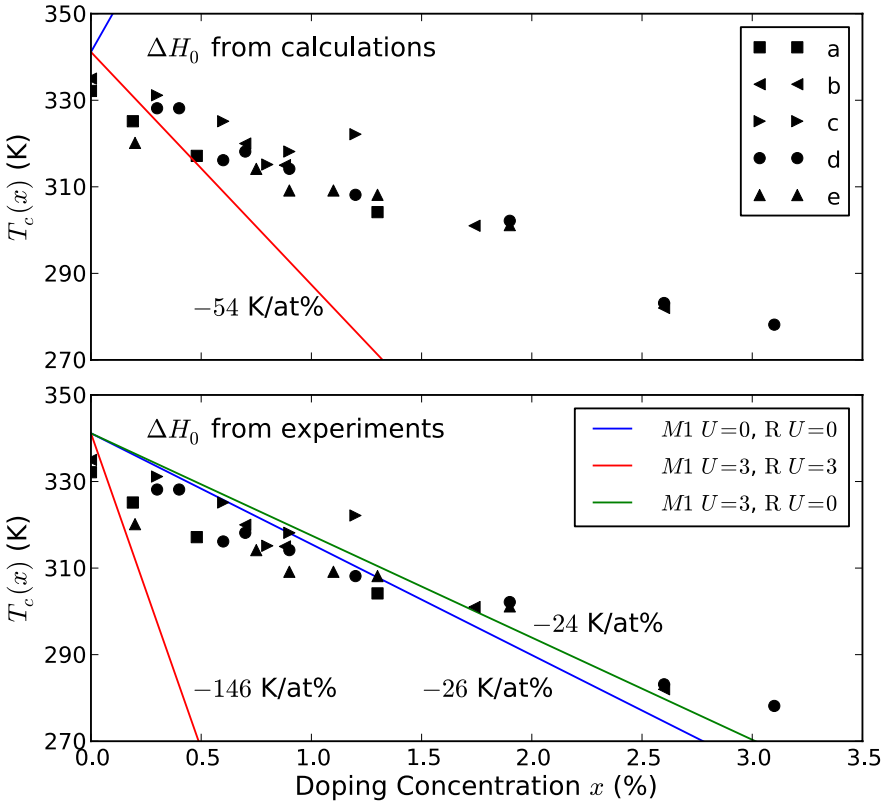

Figure 30: Transition temperature of VO_2 as a function of W doping concentration. Experimental transition temperature data marked *'a-e'*.

In the work of Paquet, the balance of Peierls pairing and electron correlation is accounted for *via* a Hubbard mechanism.[84] To study VO_2 in this work we use the same principles as Paquet, varying electronic and structural parameters, but use an *ab initio* DFT+U formalism rather than a model Hubbard Hamiltonian approach.[84] Paquet suggests Peierls dimerisation alone can distort the density of states, but is insufficient to fully open the experimental gap. Figure 29 confirms that without the presence on strong on-site Coulomb interaction, dimerising e-l interactions alone are insufficient to fully open the band gap. The VO_2 band gap only opens fully under cooperation between Peierls distortion and a minimum level of the Hubbard on-site repulsion (at $U_{\text{eff}} = 3$ eV) working to enhance the polarisation of V d state occupancies.

7.3.2 *Doping VO_2*

Building upon the DFT+U description of VO_2, we investigate how tungsten (W) doping changes the phase transition temperature, and also how the physical picture relies on appropriate U_{eff} values. Based on the discussion above, this analysis is preformed using spin restricted NM calculations.

Tungsten doping provides an effective means to reduce the transition temperature at a rate of $20 - 26$ K per atom% [80,94,264,265,266] (for example compared to niobium doping at 11 K per atom% [267]). The *ab initio* model, used to predict changes in transition temperature under doping, is based on the classical interatomic potential calculations by Netsianda *et al.*.[268] A reduction of 48.4 K per atom% of W doping has been obtained, which is about twice the measured rates. Employing the same relation between the transition temperature and the enthalpy difference between the doped R and M1 phases, recent theoretical work based on DFT has demonstrated that beryllium (Be) doping results in a reduction rate of 58 K per atom% Be .

At the temperature of transition, T_c, the Gibbs free energies of the M1 and R phase of W doped VO_2 are equal, such that

$$T_c = \frac{\Delta H}{\Delta S}\,, \tag{66}$$

where $\Delta H = H_W^R - H_W^{M1}$ and $\Delta S = S_W^R - S_W^{M1}$. At low dopant concentration, we assume that ΔS is equal to the entropy difference between R and M1 phases of pristine VO_2. The transition temperature of the doped system is therefore

$$T_c = T_{c,0}\frac{\Delta H}{\Delta H_0}\,, \tag{67}$$

where ΔH is the enthalpy difference between the two phases of $W_xV_{1-x}O_2$.

The enthalpy difference ΔH can be written as

$$\Delta H = (1 - x) \cdot \Delta H_0 + x\Delta E_{\text{sol}}, \tag{68}$$

where ΔE_{sol} is the solution energy difference per W atom between the doped R and M1 phases. For $x \to 0$, where one V atom in an infinitely

large supercell is substituted by W, ΔH coincides with definition of Netsianda *et al.*[268] However, practically the supercell cannot be infinitely large, which is why we instead use the expression in Equation 68.

Equations 67 & 68 together give the transition temperature expression

$$T_c = T_{c,0}\left[1 + x \cdot \left(\frac{\Delta E_{sol}}{\Delta H_0} - 1\right)\right]. \tag{69}$$

For ΔH_0 we can use either the experimental latent heat of the phase transition or the enthalpy difference calculated by DFT. While we can expect inaccuracies for the ΔH_0 value obtained from DFT, the calculated value should give good results for ΔE_{sol} for reasons which are discussed later in detail.

To calculate ΔE_{sol}, 96-atom supercells are employed for the M1 and R phases, where one V atom is substituted by W. This supercell size is large, to ensure we remain in the limit of low doping concentration, essential in this formulation. The DFT total energies provide a numerical value for

$$\Delta E_{sol} = H^{R}_{WV_{31}O_{64}} - H^{M1}_{WV_{31}O_{64}} - \frac{31}{32}\left(H^{R}_{V_{32}O_{64}} - H^{M1}_{V_{32}O_{64}}\right), \tag{70}$$

allowing T_c to be calculated from Equation 69.

In Figure 30 three cases are addressed: a) no on-site interaction, b) $U_{eff} = 3$ eV on the V $3d$ orbitals for both phases and c) $U_{eff} = 3$ eV on the V $3d$ orbitals only for the M1 phase. A large U_{eff} leads an antiferromagnetic insulating ground state for the R phase.[231] The on-site Coulomb interaction in the R phase should not be larger than that in the M1 phase.[269] Thus the combination of $U_{eff} = 0$ eV in the M1 phase with $U_{eff} = 3$ eV in the R phase are not considered. In the case that ΔH_0 from the DFT calculations is used in Equation 69, only results for $U_{eff} = 0$ eV or $U_{eff} = 3$ eV in both phases are calculated because different U values. For $U_{eff} = 0$ eV it turns out that the slope is opposite to the experimental findings, we attribute to the incorrect prediction of the energetic order of the two phases. For $U_{eff} = 3$ eV, we obtain $\Delta H_0 = 124$ meV which is much larger than the experimental latent heat of 44 meV.[125] Consequently the transition temperature reduces much faster upon doping than in experiment. When the experimental

latent heat is used, the theoretical $T_c(x)$ functions obtained for $U_{eff} = 0$ eV in the R phase agree with the experiment. The results for $U_{eff} = 3$ eV in the R phase strongly deviate from the experimental data points in Figure 30.

Interestingly the calculation without U_{eff} for the R phase appears to mimic the situation of R phase at high temperature, in that a low on-site Coulomb interaction value has the same affect as a high temperature, stabilising the R phase. Phonon dispersion results (discussed in the following section, and by Kim *et al.*[63]) indicate that R phase phonon softening instabilities to the M1 structure, can only be described correctly by DFT if on-site Coulomb corrections are applied. In the case of W doped R phase, the U_{eff} parameter and W doping together drive the R phase structure toward local geometry distortions in which V atoms along the c-axis dimerise. This structure is close to that of M1 phase, therefore a giant T_c reduction is achieved in the simulation as shown in Figure 30. The giant T_c reduction for Be doped VO_2 predicted by DFT+U may be due to the same effect, in that Coulomb interaction stabilises excessive distortion in the doped R phase. On the other hand, the value of the U parameter for the M1 phase has no significant effect on the results.

7.3.3 *Structural instability and phonons*

Figure 29 shows the VO_2 PES in the limit of $T = 0$ K, but gives little indication of the PES shape at temperatures characteristic of a stable R phase. To explore how the R phase is stabilised by thermal disorder, we introduce a mean-field picture of the transition. For regions outside the domain defined by a correlation length ξ, the structure is fixed to the high-symmetry high-T R phase. This represents a mean-field of the high-T structure for which V-V pairs are *structurally uncorrelated*. Inside the domain defined by ξ, V-V pairs are *structurally correlated*, and the dimerisation (η) is varied continuously to produce an energy surface using constrained relaxation (as previously in Figure 29).

Two energy surfaces are shown in Figure 31, both within the $U_{eff} = 3$ eV NM framework. Two different values of ξ are employed, corresponding to the different temperature regimes. For the completely correlated structure ($\xi \to \infty$ and $T \to 0$), the PES in Figure 31 is

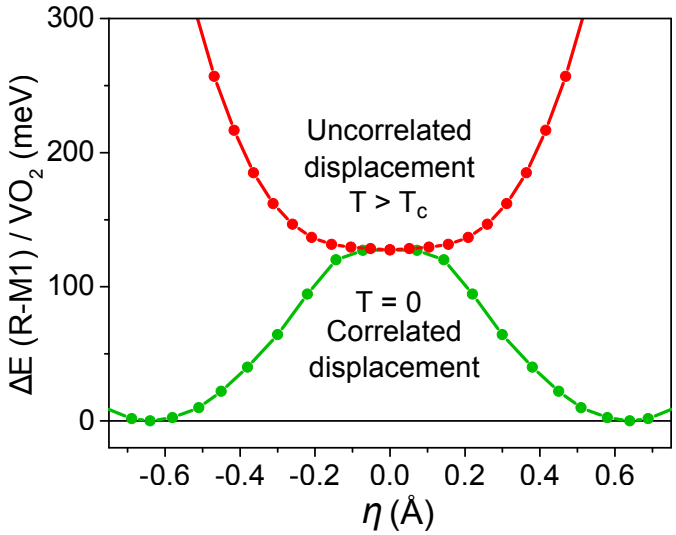

Figure 31: Potential energy surfaces in the high and low temperature limits *versus* V-V dimerisation (η), from a $U_{\text{eff}} = 3$ eV non-magnetic calculation.

green. This is equivalent to the zero-T PES shown previously in Figure 29, with all V-V pairs undergoing constrained dimerisation. In the opposite limit, the red surface represents the high temperature regime where V-V pairs are not structurally correlated at all ($\xi \to 0$ and $T \to \infty$). Here only one pair in the supercell undergoes constrained dimerisation, and the rest of the V atoms in the supercell are fixed to R positions to produce a high-T mean-field.

The green PES in Figure 31 shows the rutile instability at low temperature, however, the red high-T PES is interesting, as it shows the M1 is destabilised, and the R phase stabilised as ξ is reduced.

The low-T M1 and high-T R phonon dispersion band structures are shown in Figure 32. In 1970 Brews predicted two instability modes in the R phase. NM $U_{\text{eff}} = 3$ eV calculations provide an anti-ferroelectric instability, which is dominant over a secondary ferroelectric mode. The anti-ferroelectric instability highlighted by the imaginary modes in Figure 32 corresponds to the dimerisation and tilt of V-V pairs about $c^{\text{R}} \sim a^{\text{M1}}$.

Imaginary phonon DOS is shown in green in Figure 34. The imaginary dimerisation modes present at zero temperature for the R phase are reproduced by DFT with on-site corrections, while at the characteristic R phase temperature ($T \gtrapprox 340$ K), the imaginary phonon modes should become real. If the number of real phonons depends

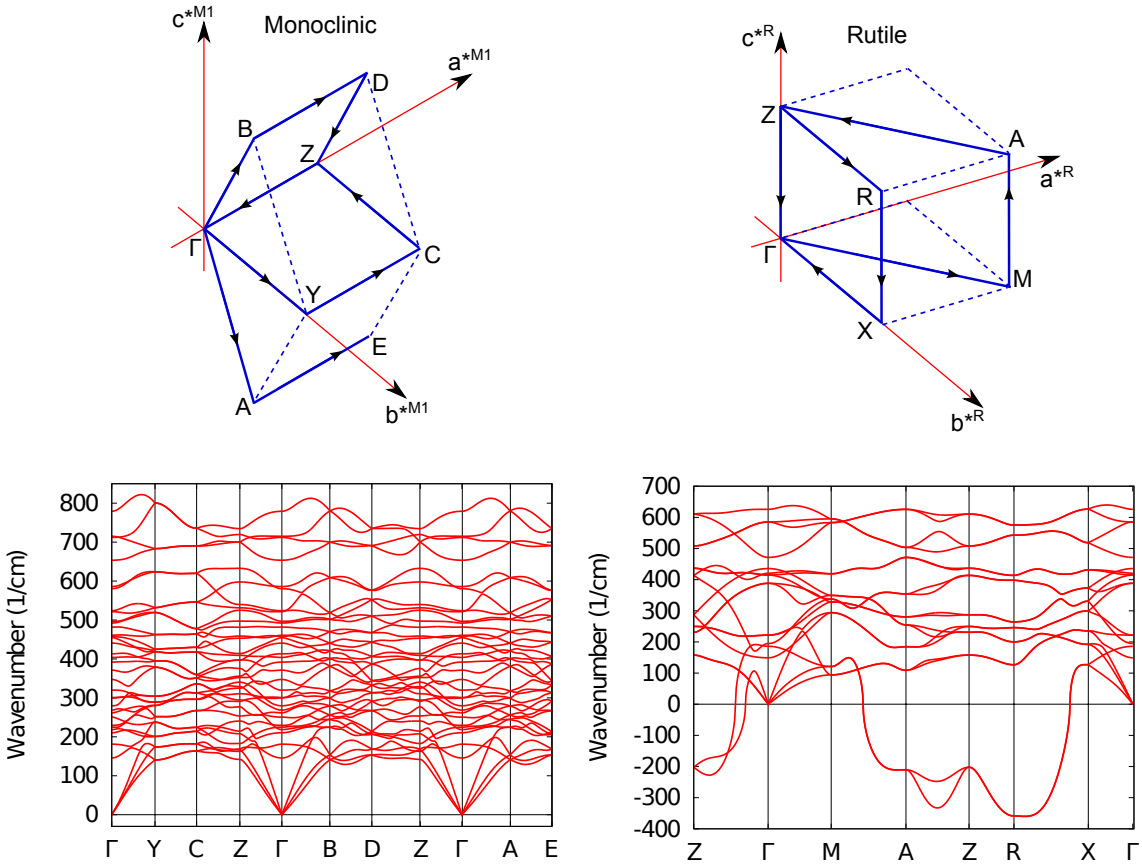

Figure 32: Twelve atom M1 unit cell and six atom R phase unit cell phonon dispersion curves (1/cm), *versus* reciprocal space sampling path around each Brillouin zone. Results are shown for a $U_{\text{eff}} = 3$ eV non-magnetic calculation.

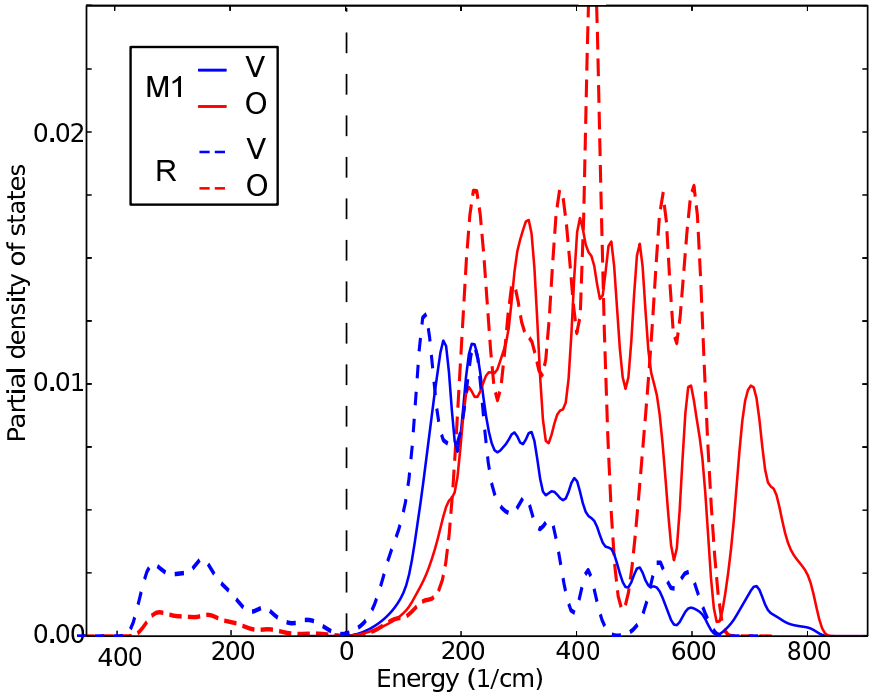

Figure 33: M1 and R phase phonon partial V and O density of states per VO_2. $U_{eff} = 3$ eV non-magnetic calculation.

on temperature (with fewer in the zero temperature DFT description of VO_2 (R) than experimentally), this presents a serious obstacle to accurate thermodynamic analysis within the unavoidable constraints of the zero temperature DFT framework. Although rigorous methods exist to account for soft mode temperature dependence,[253,254,257] a much simpler method is described below.

Cohen and Terauchi's experimental observation of the VO_2 soft mode temperature dependence identified the relationship $\omega^2 = \omega_0^2(\frac{T_c - T_0}{T_0})$,[252] where T_c is the phase transition temperature, T_0 is the classical phase transition temperature, and ω_0 is the soft mode frequency at low temperature. Using this relation, the zero-temperature imaginary modes can be shifted to the real frequencies expected at T_c. In DOS language, the imaginary phonons are transformed as

$$g_{T_c}(\omega(T)) = g_0^{\text{hard}}(\omega) + \frac{1}{\alpha(T)} \cdot g_0^{\text{soft}}(\frac{-1}{\alpha(T)} \cdot \omega(T)),$$

where α is a constant depending on T_0 and T_c: $\alpha = \sqrt{(T_c - T_0)/T_0}$. The negative argument in g_0^{soft} represents the imaginary frequencies at 0 K. The effect of the transformation with α (< 1) is to squeeze the energy (frequency) scale of the soft modes, as the temperature is

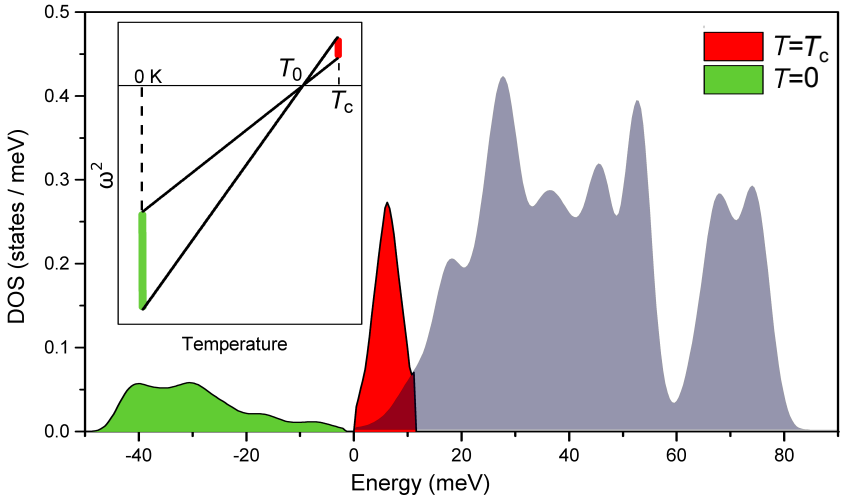

Figure 34: R phase phonon density of states per V_2O_4 rutile unit cell: low-temperature imaginary states in green are shifted to the real axis by linear extrapolation to finite temperature, to reproduce the temperature dependence of soft transition dimerisation modes.

increased and the imaginary modes become real. Commensurately the DOS is scaled-up to ensure to the sum of the soft and hard modes always remains normalised to $3n$ modes in total at any temperature.

For $\alpha = \sqrt{(T_c - T_0)/T_0}$ with $T_c = 340$ K and $T_0 = 329.5$ K, Figure 34 shows the transformation of imaginary states in green to real states in red. The new R phase phonon spectrum at $T = T_c$ with no imaginary modes relates to the locally stable red PES in Figure 31 rather than the green curve which shows a lattice instability at 0 K. After the transformation the total number of real modes in our phonon spectrum is renormalised from less than $3n$ (approximately $3n - 2$) to $3n$, as expected for the six atom R phase unit cell.

An important effect of the imaginary mode transformation is to increase the density of real low energy modes, as shown by the red peak in Figure 34. Phonon entropy weights low frequency modes more than high frequency modes, so the transformation to account for soft modes substantially increases the R phase phonon entropy.

The phonon entropy is calculated using Equation 48 in Chapter 5.3, and gives an entropy contribution for VO_2 (R) of $T_c S^{R}_{phon} = 249$ meV/VO_2, and $T_c S^{M1}_{phon} = 200$ meV/VO_2 for VO_2 (M1). These numerical values together provide an estimated lattice contribution to the latent heat of transition of $T_c \Delta S_{phon} = 49$ meV/VO_2.

In terms of other latent heat contributions, in this pristine model there is no vacancy or defect entropy difference. A further plausible source of latent heat could arise from changes in spin ordering across the transition. In such a Heisenberg picture of the magnetic transition, local magnetic moments are ordered in the M1 phase due to strong intra-dimer AFM coupling, but will become thermally disordered in the high-T R phase. The entropy change per V d^1 site of this type of contribution is approximately $\Delta S_{\text{mag}} = k_{\text{B}} \ln(2)$. This potential magnetic component of the latent heat of transition has a value of $T_{\text{c}} \Delta S_{\text{mag}} = 20\,\text{meV/VO}_2$.

While recent QMC results indicate both M1 and R phases do have local spin moments at zero temperature, it is uncertain whether a Heisenberg interpretation with local moments in the R phase is appropriate at the temperatures above T_{c} which are relevant to the R phase. Rather we believe an itinerant Stoner picture of the R phase emerges at finite temperature, wherein electronic excitations act to symmetrise the spin channels. This prevents the generation of a magnetic entropy difference between the M1 and R phases, and is supported experimentally by the measurements of Maurer *et al.*.[128] Maurer *et al.*[128] have shown that entropy from lattice modes will account for almost 90 % of the 44 meV/VO_2 transition latent heat. We therefore interpret, that for the remaining $\sim$ 10 % of the latent heat, such a large value as the 20 meV/VO_2 provided by disordered local moments in a Heisenberg picture, is highly unlikely.

The only remaining transition entropy contribution arises from the metallic R phase, which has a computed DOS of around $\sim$ 5 states/eV at the Fermi level. The VO_2 (R) electronic entropy was calculated within the $U_{\text{eff}} = 3$ eV NM framework, using Equation 49 from Chapter 5.3. The VO_2 (R) electronic entropy increases the transition entropy difference by 1.95×10^{-5} eVK^{-1}, adding $T_{\text{c}} \Delta S_{\text{el}} = 7$ meV/VO_2 to the latent heat of transition.

In Table 4 the total transition latent heat is overestimated somewhat, with a value of 56 meV/VO_2 computationally, compared to 44 meV/VO_2 experimentally. Of the calculated latent heat, 49 meV/VO_2 comes from the lattice and 7 meV/VO_2 from the electronic entropy. In percentage terms, 14 % of the transition entropy is attributed to

Table 4: Comparison of M1 and R phase entropic contributions, per VO_2 formula unit, to the transition thermodynamics at $T = T_c$.

Entropic contribution	R (meV)	M1 (meV)	$\Delta^{\text{R-M1}}$ (meV)
$T_c\Delta S_{el}$	7	0	7
$T_c\Delta S_{phon}$	249	200	49
$T_c\Delta S_{total}$	256	200	56
$T_c\Delta S_{exp}$	-	-	44

electronic states, whereas the majority at 86 % originates from lattice or phonon states.

Since the lattice entropy comes in majority from the two soft temperature dependent phonon modes, and the lattice entropy is dominant by 7 : 1 over electronic entropy, it is tempting to say the transition is e-l mediated and Peierls in nature. However both the magnitude and frequency of the displacive low energy modes, which dominate the lattice entropy in the R phase, are strongly tuned by Coulombic localisation. As well as *d* electron localisation determining the PES gradient for the R structure (which is the origin of imaginary modes), the role of e-e interaction is further emphasised by the strong dependence of $\Delta E(\text{R} - \text{M1})$ on the Hubbard U.

Interestingly the electronic DOS at the Fermi level, and therefore electronic entropy, is only weakly dependent on the Hubbard U. Unlike the phonon entropy, the electronic entropy changes only by a few percent from the delocalised $U_{\text{eff}} = 0$ eV picture to localised $U_{\text{eff}} = 3$ eV. Nonetheless, e-e Coulomb interaction facilitates phonon softening, which provides the majority of transition entropy. Although the entropies can be partitioned, the actual roles of e-e and e-l interaction to the latent heat of transition are inseparable. The transition is dominantly Peierls in character, but the phonon softening is only made possible through cooperation with strong on-site Coulomb localisation enhancing dimerisation phonon modes.

In Table 4, our result is presented in the context of other transition entropy ratios from a number of works. The various results are now briefly discussed. Berglund and Guggenheim estimate a total latent heat of 3 Cal/mol°C, based on experimental observation of the heat capacity.[12] By estimating a discontinuity of 0.5 Cal/mol°C, they de-

duce an approximate electronic entropy contribution. Together these values equate to a ratio of phonon to electron entropy of 83 % to 17 %. This estimate is actually in very close agreement with our results in Table 5.

Another early prediction by Paul[126] reports the transition is driven by latent heat due the excess entropy of soft phonon modes in the metal phase. We strongly agree with this statement, and transition origin ratio agrees well with the prediction by Paul.[126] Zylberstejn and Mott[83] argued that Paul's predictions on soft phonon importance to transition entropy are correct only to an extent, and that electron correlation is also critically important. We agree that e-e correlation *via* the Hubbard U is essential, but not because of any strong enhancement of the magnetic susceptibility and therefore electronic heat capacity as claimed. Rather, the Hubbard U is essential because the frequency and magnitude of the soft transition modes depend on it, and these low frequency modes dominate phonon entropy. We believe this disagreement reflects the Zylberstejn and Mott overestimation of electronic entropy by a factor of $\sim 2-3$, both with respect to the value we present and the most recent experimental results shown in Table 5.

Using a model approach to e-l coupling, Hearn concluded that the electronic contribution to the transition entropy is negligible. While we agree phonon entropy is dominant, we disagree with Hearn's approximations and conclusion that electronic entropy is entirely negligible. Calorimetric measurements by Pintchovski *et al.*[125] detail the variation in entropy with doping concentration, and conclude the pristine VO_2 electronic entropy is as much as 40 % of the total transition entropy, which we believe is an overestimate. Recently Maurer *et al.*[128] have reported from experiment that the phonon contribution to transition entropy using a Debye model. Employing Rayleigh-type surface acoustic waves, Maurer *et al.* measured the mean sound velocity and used this to calculate the Debye temperature. This most recent experimental entropy report provides verification of our theoretical estimate, with agreement to within 1 %.

Table 5: Historical context: lattice *versus* electronic entropy at the VO_2 phase transition.

Authors	Year	Methodology	Entropy ratio $\Delta S_{phon} : \Delta S_{el}$
Berglund *et al.*[12]	1969	*Exp.* (heat capacity)	83 % : 17 %
Paul[126]	1970	*Calc.* (band theory)	90 % : 10 %
Hearn[127]	1972	*Calc.* (model Hamiltonians)	99 % : 1 %
Mott *et al.*[83]	1975	*Calc.* ($\chi^{magnetic}$)	64 % : 36 %
Pintchovski *et al.*[125]	1978	*Exp.* (doping)	40 % : 60 %
Maurer *et al.*[128]	1999	*Exp.* (sound velocity)	87 % : 13 %
This work	2015	*Calc.* (DFT+U)	86 % : 14 %

7.4 CONCLUSIONS

The NM $U_{eff} = 3$ eV methodology was shown to give a description of both VO_2 phases with plausible electronic and structural aspects - correct qualitative insulating (M1) and metallic (R) band gap values, and PES turning points with minima at M1 geometry (stable) and a maximum at the R phase. The PES show that Coulombic electron localisation and Peierls lattice distortion are both instrumental in determining the character of each phase and the transition between them. The DFT description was used as an *ab initio* basis to estimate different transition entropy contributions. R phase phonon modes, which are as expected imaginary in the zero temperature DFT description, were transformed to their real frequencies at the transition temperature, providing means to estimate R phase phonon entropy at the transition temperature. The phonon entropy was found to outweigh the electronic contribution by almost an order of magnitude (seven to one). The majority of the phonon entropy comes from two temperature dependent modes, which at the point of transition form a sharp low energy peak to be transferred *via* displacive transition to the imaginary energy axis. The two imaginary modes can only be produced computationally if significant Coulombic localisation is applied *via* a Hubbard correction of $U_{eff} = 3$ eV. The transition is driven in most part by phonon entropy, the majority of which originates from the states associated with the low energy displacive Peierls phonon modes, which are in turn strongly dependent on cooperation with

Mott-Hubbard-like on-site electron localisation effects of the rutile phase V *d* electrons. The calculated electronic and phonon entropies more than account for the total experimental latent heat, providing support for a transition with no magnetic entropy difference, due to coupled spins in an intra-dimer AFM M1 phase and a NM Stoner-type R phase.

8

THERMODYNAMICS OF VANADIUM DIOXIDE SURFACES

This chapter investigates the thermodynamics of VO_2, in particular the tetragonal rutile (R) phase of VO_2. Five unique low Miller index planes are identified, and the (110) plane is shown to be the most stable and therefore equilibrium surface. The equilibrium morphology is identified as an acicular particle, bounded laterally by (110) planes, and completed by (011) planes. The redox properties of the most stable (110) surface are investigated further, to examine stoichiometry as a function of an oxygen chemical potential. The (110) surface is strongly oxidised under ambient and typical experimental conditions. Even at the high temperature when VO_2 bulk is preferentially stabilised with respect to V_2O_5, the (110) surface still favours non-stoichiometric oxidation in the form surface vanadyl species.

8.1 INTRODUCTION

Understanding the properties of VO_2 surfaces is important in the context of thermochromic applications. Experimental research has shown that the morphology and preferred crystallographic orientation of VO_2 particles in thin films can have significant effects on both the hysteresis width and the critical temperature of the transition.[81] Furthermore, the study of the free surfaces is a necessary first step for many more advanced investigations, such as interactions of VO_2 with metal nanoparticles, which are able to modify the optical properties of the thermochromic films,[95,270] and of the interfaces of VO_2 with the glass substrate and other coating layers, such as antireflective TiO_2.

The rutile phase of VO_2 is chosen for our study because it is the one stable under typical growth/synthesis conditions, *e.g.*, synthesis of VO_2 by chemical vapour deposition typically requires temperatures above 700 K,[27,271] thus VO_2 (R) thermodynamics are considered as the monoclinic (M1) phase is not stable above $T_c \approx 340$ K. Since the

VO_2 (R) phase does not exhibit a band gap, the local DFT approach is not as problematic here as in the description of the M1 VO_2 phase (see Chapters 6 & 7). We also discuss the redox behaviour of the most stable surface of R VO_2 as a function of temperature and oxygen partial pressure.

8.2 COMPUTATIONAL DETAILS

8.2.1 *Density functional theory*

8.2.1.1 *Technical details*

Periodic DFT calculations were performed with the VASP program,[204,205] using the GGA approximation in the form of the PBE exchange- correlation functional.[187] The projected augmented wave method was used to describe the interaction between the valence electrons and the core,[206,214] and the core states (up to $3p$ in V and $1s$ in O) were kept frozen at the atomic reference states. The kinetic energy cut-off was set to 500 eV, and the mesh of **k**-points $6 \times 6 \times 9$ divisions.

All surface geometries are fully relaxed. As DFT+U yields an unstable R phase with imaginary phonon modes, DFT is preferable to DFT+U to reproduce the high temperature thermodynamics- see Chapter 6 & 7 for discussion.

8.2.1.2 *Magnetic ordering*

Here, as in previous DFT investigations of VO_2 (R),[6,122,228] our calculations are not spin polarised. However, contrasting with M1 VO_2, where V^{4+}-V^{4+} dimerisation leads to spin pairing,[272] in R phase V^{4+} cations are expected to have a single unpaired $3d$ electron, and there is experimental evidence of paramagnetic behaviour of the high-temperature phase.[83] Although a non-magnetic calculation is not a good representation of a paramagnetic phase, a spin-polarised calculation with ordered magnetic moments is not generally adequate either. We have tried NM, FM and AFM calculations of the VO_2 (R) bulk using the GGA PBE functional, and found that the FM ground state exhibits a gap at the Fermi level in the minority spin channel (see Figure 35), and metallic behaviour of the majority spin electrons. This strong spin

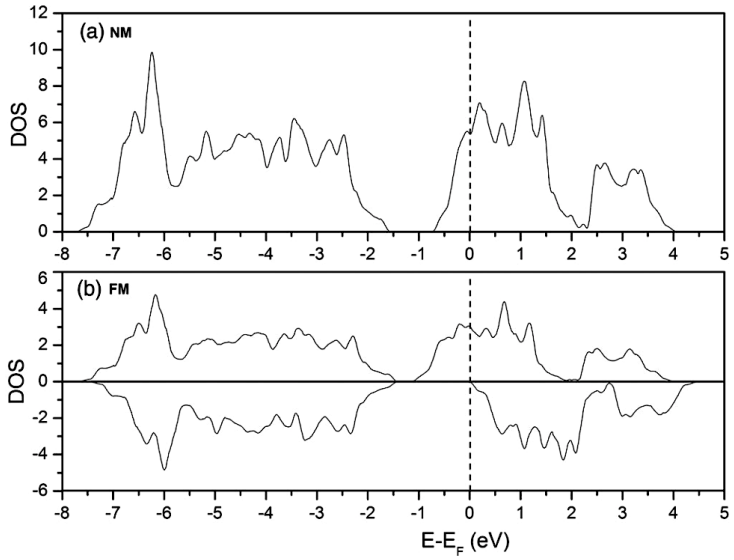

Figure 35: Density of states (states/eV/V_2O_4 unit cell) for bulk VO_2 (R), for spin-restricted NM and FM spin-polarisation.

asymmetry means that the FM ground state is a poor representation of the paramagnetic state of VO_2 (R). On the other hand, while an AFM solution can lead in principle to a more realistic symmetric behaviour of majority and minority spin electrons, our GGA calculation with initial AFM ordering of the moments converged to a solution very close to the NM ground state, with nearly zero final magnetic moments. Spin-polarised solutions with different orientation of the magnetic moments can be stabilised for VO_2 (R) using the screened hybrid functional HSE, but as mentioned above, this leads to solutions with artificial gaps at the Fermi level (in both the majority and minority spin channels),[228] which is in conflict with the well-established metallic character of VO_2 (R).[234,273] Therefore, in the present work we use the plain GGA functional, without any HF exchange contribution, which gives the correct metallic character.

8.2.2 *Surface thermodynamics*

8.2.2.1 *Surface model*

Bulk VO_2 (R) was cut along high symmetry planes to form slabs with the five low Miller index planes: (110), (010), (100), (111) and (011), as in Figure 36. In the periodic model used, each slab has two

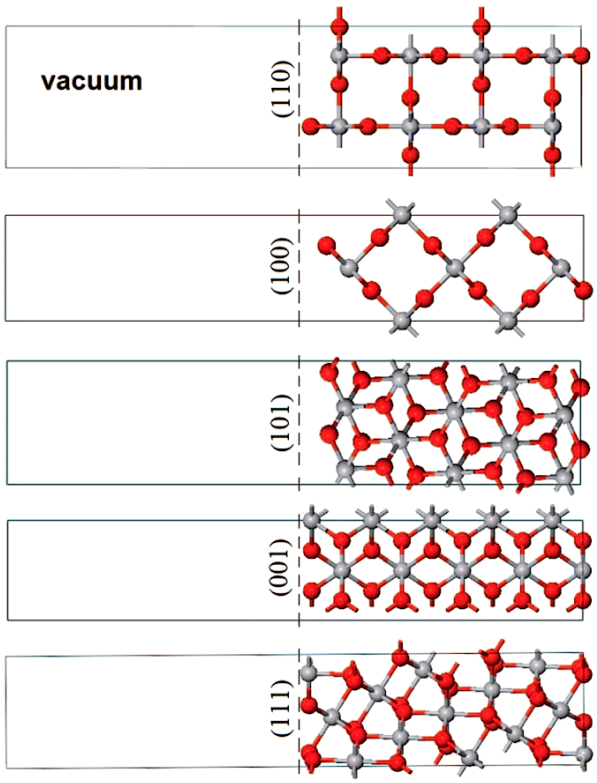

Figure 36: Slab models for the five unique low Miller index surfaces of VO_2 (R). V in red, and O in grey.

stoichiometric surfaces. Inversion symmetry of the slab surfaces was enforced to prevent to formation of electric dipole moments associated with slab asymmetry. Slab thicknesses range from 11 to 14 Å, with a vacuum gap of $\sim$ 14 Å (see Figure 36).

Each slab is built from the relaxed bulk unit cell, which has the relaxed lattice parameters, $a = 4.617$ Å and $c = 2.774$ Å. This deviates from the experimental lattice parameter $a_{\text{exp}} = 4.554$ Å by $+1.4$ % and from $c_{\text{exp}} = 2.857$ Å by -2.9 %, producing an overall cell volume error of -0.1 %.[274] The surface energy γ is given with respect to the relaxed bulk unit cell as,

$$\gamma = \frac{E_{\text{slab}} - E_{\text{bulk}}}{2A},$$

where E_{slab} is the relaxed slab energy per surface unit cell, E_{bulk} is the relaxed energy of the equivalent number of bulk formula units, and A is the slab surface area. The equilibrium morphology of a VO_2 (R) particle is constructed from the low Miller index planes using Wulff's method. In the Wulff particle construction, the distance from

the particle centre to a given surface is proportional to the surface energy γ.[275]

8.2.2.2 *Redox thermodynamics*

Redox thermodynamics are investigated for the most stable of the low Miller index surface planes. Surface oxygen atoms are removed and added to vary slab stoichiometry. As with the stoichiometric slabs, inversion symmetry is maintained for the non-stoichiometric compositions, again to prevent formation of electric dipole moments.

The *ab initio* redox thermodynamics formalism used is due to Reuter and Scheffler,[276]. The surface free energy is given in terms of surface energy γ, with temperature and pressure dependence introduced *via* chemical potential μ_O,

$$\sigma(T,p) = \gamma - \frac{\Gamma}{A}\mu_O(T,p)\,. \tag{71}$$

Here Γ is the excess oxygen per slab surface,

$$\Gamma = \frac{1}{2}(N_O - 2N_V)\,, \tag{72}$$

and μ_O is an oxygen gas phase chemical potential,

$$\mu_O = \frac{1}{2}(E[O_2] + \Delta g_{O_2}(T,p_0) + k_B T \ln(\frac{p}{p_0})\,. \tag{73}$$

This redox potential takes into account the DFT zero point energy of oxygen $E[O_2]$, the Gibbs temperature/pressure dependence g_{O_2}, and ideal gas law temperature/pressure dependence. Δg_{O_2} is the difference between Gibbs energies at 0 K and T for O_2 gas at $p_0 = 1$, and can be calculated,[276,277] however we use tabulated experimental data.[278]

The zero point energy is an additive constant, so can be dropped, and is by convention,

$$\mu_O(T,p) - \frac{1}{2}E[O_2] \rightarrow \mu_O(T,p).$$

The last term in μ_O is $k_B T \ln(\frac{p}{p_0})$, which gives ideal gas law pressure dependence for a given temperature. This allows the free surface energy to be plotted as a function of T and p.

Surface	γ (J/m^2)
(110)	0.29
(100)	0.42
(101)	0.75
(001)	0.96
(111)	1.25

Table 6: Low Miller index surface energies for VO_2 (R).

8.3 RESULTS

In VO_2 the metal to insulator and structural (M1 to R) phase transitions occur at $T_c \approx 340$ K. As the R structure is the stable VO_2 phase at typical synthesis temperatures (assuming standard pressure, zero external strain, *etc.*), results related to the redox and surface properties of the rutile phase are given.

In Section 8.3.1 we consider the order of surface stability for low index planes, the equilibrium particle morphology defined by this set of low index planes, and local surface relaxation for the most stable surface.

In Section 8.3.2 the redox behaviour of the most stable rutile surface is given at zero temperature and pressure. This picture is extended by using the surface free energy, to considered the effect of temperature and pressure through an oxygen chemical potential on surface oxidation and reduction.

8.3.1 *Stoichiometric surfaces*

Table 6 shows the surface energy for each of the five low Miller index planes. As a point of reference, the VO_2 surface results are compared throughout to the iso-structural and very well known TiO_2.[279]

In Table 6 the (110) VO_2 (R) surface energy is $\gamma = 0.29$ J/m^2, preferentially stabilising (110) above any other low Miller index surface. This is analogous to rutile TiO_2 which also stabilises the (110) surface under equilibrium.[280]

In (110) VO_2 the surface terminates in bridging oxygen, which form rows along the [110] direction, as in Figure 37. In-plane surface species

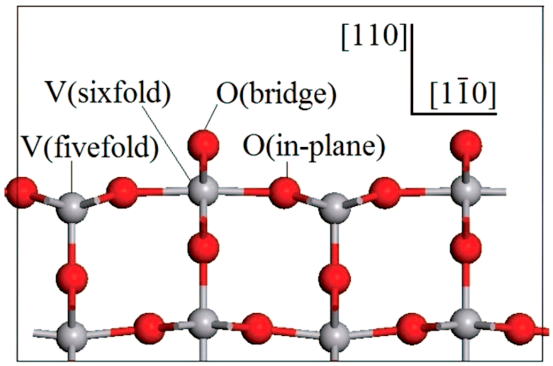

Figure 37: Relaxed (110) stoichiometric surface for R VO_2.

in Figure 37 include triple coordinated oxygen, and five and six fold coordinated vanadium atoms. The most significant local relaxation is rumpling due to the 5-fold coordinated V atoms. As a result of the partial coordination, the 5-fold V atoms relax ~ 0.42 Å inwards with respect to the relaxed surface plane (see Figure 37). Again this relaxation is very similar to that observed in TiO_2.[280] In TiO_2, under coordinated surface cations relax by a similar ~ 0.44 Å, according to low-energy electron diffraction measurements, and between $0.39 - 0.42$ Å according to theoretical techniques.[281]

In Table 6 the order of the (110) surfaces is ranked in terms of surface stability is: $(110) > (100) > (101) > (001) > (111)$. Once again this echoes results from investigation of rutile TiO_2, which produces the same surface stability ordering (although (111) was not considered).[282]

When the surface energies in Table 6 are used to construct the equilibrium morphology of VO_2 (R), the acicular shape shown in Figure 38 is obtained. As might be expected from Table 6, the predominant morphology facets are (110) planes. Interestingly the (100) surface which is second in terms of stability is does not appear in the equilibrium particle morphology. This peculiarity occurs simply because the equilibrium particle is a strong function of the relative geometry of different surfaces, as well as their surface energy. More precisely, the (100) phase does not appear because the ratio $\frac{\gamma(100)}{\gamma(110)} = 1.45$, is marginally greater than the critical value of $\sqrt{2}$. Above this critical value, the (100) planes are cut out by the very stable (110) planes in the Wulff's construction. In order for the (100) face to be present in the equilibrium particle morphology, the (100) surface would need to be $\gamma(100) < \sqrt{2}\gamma(110)$. This geometric argument is shown more

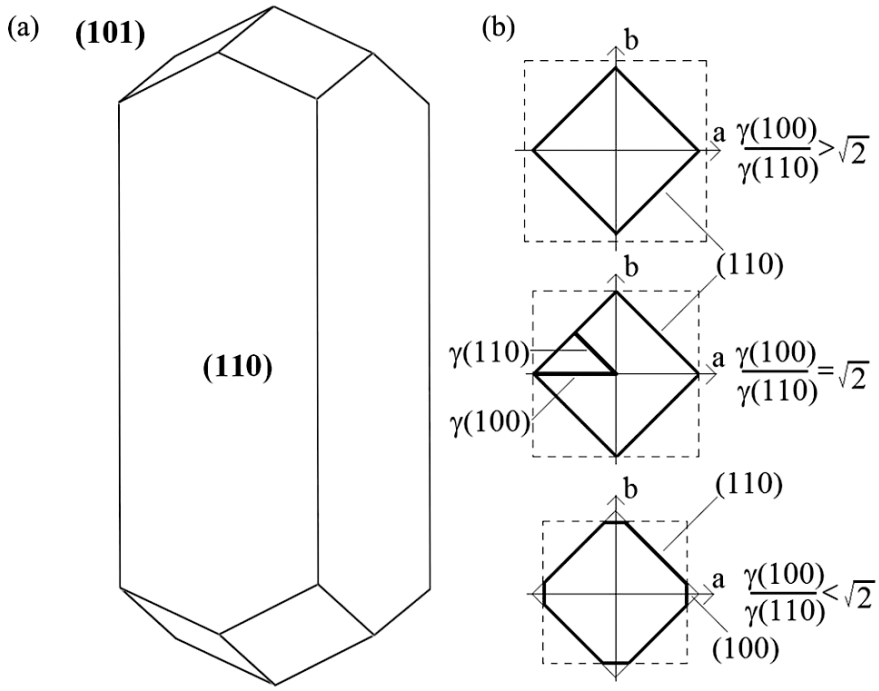

Figure 38: Equilibrium morphology of a VO_2 (R) particle. Morphology depends on the ratio of $\gamma(110)$ and $\gamma(100)$ surface energies.

intuitively in Figure 38. In addition to the (110) surface, the (101) surface shown in Figure 38 'tops' the equilibrium morphology.

A number of recent experimental works have investigated VO_2 micro and nanoparticles, which provide practical reference point for comparison. Experimental VO_2 crystal habits reported by Misra *et al.*,[272] show two crystal habits dominantly featuring the (110) surface, although in one, elongation along [001] is more prominent. As in our calculations, the experimental particles exhibit a square cross section limited by the (110) surfaces. We theoretically predict an acicular particle bounded by (101) on the top and bottom, however this has not observed (reported) experimentally. Sohn *et al.*,[283] have described VO_2 nanowires. These structures exhibit again the characteristic (110) predicted theoretically, along with massive extension along [001]. The nano structures of Sohn *et al.*,[283] are grown at high temperature, but they are characterised at low temperature, when the VO_2 is monoclinic rather than rutile. Despite the abrupt change in symmetry group and unit cell at the point of MIT, the local structural distortion is only a small dimerisation, so the comparison between low temperature experimental M1 and theoretical R should be valid. For commensurate

comparison between the structural phases, we took into account that the R and M1 phases have different labelling conventions: the rutile [001] direction corresponds to the monoclinic [100] direction, while the rutile (110) surface corresponds to the monoclinic (011) surface.

8.3.2 *Redox behaviour of the stable* (110) *surface*

The (110) surface stability at zero temperature and pressure was identified in Sub-Section 8.3.1. Here we now consider the corresponding free surface energy, varying the ratio of terminating oxygen and vanadium at the (110) surface.

The number of vanadium atoms in the slab is kept the same as in the stoichiometric surface, but the number of oxygen atoms at each surface is changed by Γ (see Equation 72). In the limit of large surface supercell, Γ becomes continuous function between $\Gamma = \pm 2$. Limited by our surface supercell (see Figure 36) size, and assuming a single mono-layer (ML) of surface defects that take only bulk-like positions, Γ is limited to only five values. $\Gamma = 0$ corresponds to the stoichiometric surface, $\Gamma = +1, +2$ are the partially and totally oxidised surfaces, and $\Gamma = -1, -2$ are the partially and totally reduced surfaces (see Figure 39). Although a finer distribution of Γ values is preferable to investigate intermediate degrees of oxidation and reduction quantitatively, the present course-grained pictures is illustrative and still provides a very useful model picture.

8.3.2.1 *Oxidation correction*

In the following redox analysis, a satisfactory description of the O_2 molecule (in terms of structure but primarily energy) is essential. DFT calculations of the O_2 triplet ground state yield a binding energy of -6.08 eV with respect to triplet oxygen atoms, and an equilibrium bond length of 1.23 Å. This compares favourably with previous computational values,[284,285] however the computational binding energy at absolute zero is considerably different (-5.12 eV).[286] The overbinding of small molecules is typical of GGA,[187] and the effect of overbinding (0.96 eV in our calculations) in the O_2 molecule is known. Wang *et al.*[287], have argued that besides O_2 molecule overbinding (and the

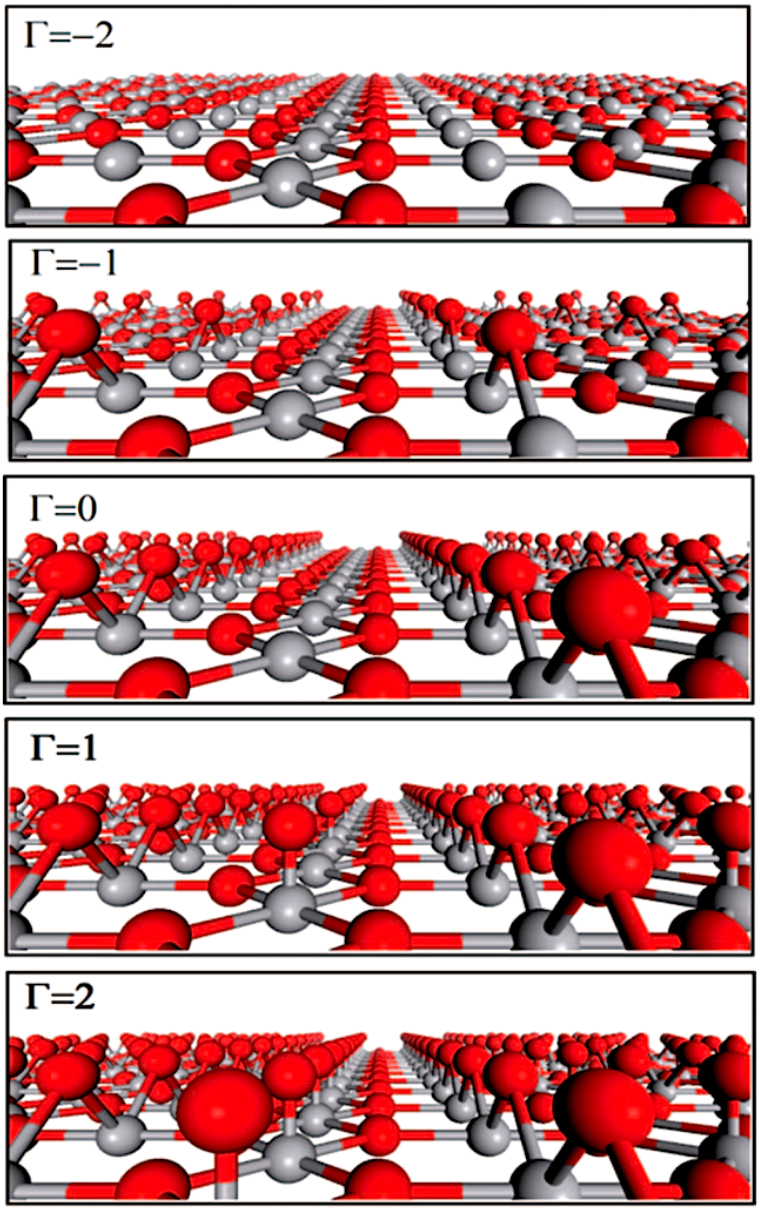

Figure 39: (110) surface of VO_2 (R), with $\Gamma = 0$ stoichiometric, $\Gamma = -1, -2$ partially and totally reduced, and $\Gamma = +1, +2$ partially and totally oxidised.

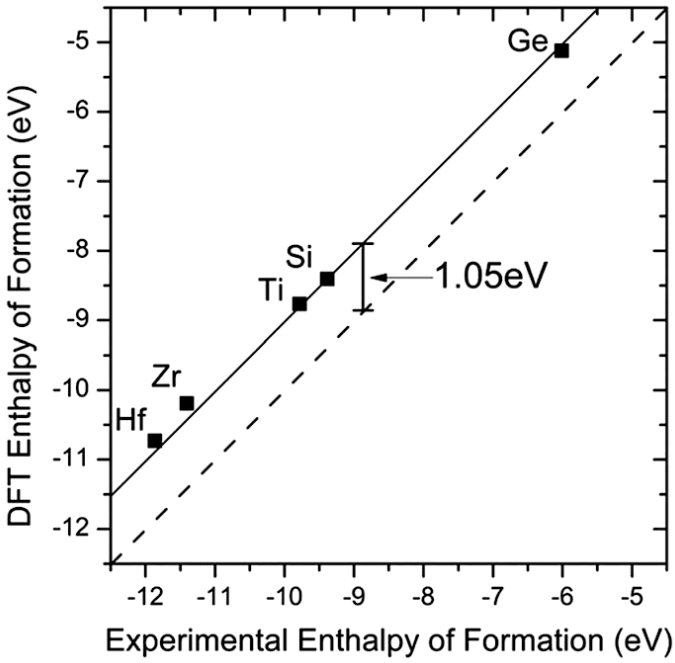

Figure 40: O_2 overbinding correction estimated to be $+1.05$ eV from GGA oxidation enthalpies.

correlation errors associated with description of *d* orbitals in transition metal cations), there is an additional error in the calculation of redox reactions involving oxides. The additional error is associated with adding electrons to the O 2*p* orbitals upon the formation of the O^{2-} lattice species. Wang *et al.*[287], have proposed a empirical correction based on shifting the energy of an oxygen molecule in order to reproduce the experimental formation energy of several typical metal oxides. We follow a similar procedure.

Figure 40 shows the formation energy of five simple tetravalent metal oxides: HfO_2, ZrO_2, TiO_2, SiO_2, and GeO_2. In Figure 40 an upward shift of $+1.05$ eV in the O_2 energy, decreases the DFT enthalpy of formation. This simple single number correction brings the calculated enthalpy of formation into excellent agreement with experimental values, and remarkably is approximately constant over the wide range of 7 eV, from the formation enthalpy of HfO_2 at -11 eV to GeO_2 at -5 eV.

Unlike previous work which employed a similar correction,[287] the magnitude of the oxidation correction here (Figure 40) accounts for the majority of the error in the oxygen binding energy. The systematic and constant error in formation enthalpy, further suggests that O_2

over-binding accounts for most of the error in formation enthalpy. Conversely the error associated with the filling of the O $2p$ orbitals in the oxides is very small. This difference in the character and size of the formation enthalpy correction between this work and Wang *et al.*,[287] most probably is due to the consideration here only of tetravalent oxides in our analysis, while Wang *et al.* considered mainly alkaline and alkaline earth metal oxide formations. Results will be presented throughout with both the O_2 binding energy corrected and uncorrected, for clarity, impartiality and discussion.

8.3.2.2 *Vacancy defects*

The reduction of the (110) VO_2 (R) surface is now discussed. Removing one oxygen atom per slab surface (see Figure 36) yields an surface excess oxygen (as defined in Equation 72) of $\Gamma = -1$, or 0.5 ML of oxygen vacancies. The vacancy formation energy,

$$E_{\text{vac}} = \frac{1}{2}(E[O_2] + E[\Gamma = -1] - E[\Gamma = 0]),$$

is $E_{\text{vac}} = 3.33$ eV (3.85 eV after correction) for the bridging oxygen vacancies and $E_{\text{vac}} = 4.30$ eV (4.83 eV after correction) for the in-plane oxygen vacancies. The higher stability of the bridging vacancy is not unique to this particular rutile-like oxide, having also been reported for rutile TiO_2 (110).[288,289,290]

As a point of comparison, the vacancy formation energy in bulk VO_2 is $E_{\text{vac}} = 3.00$ eV (3.53 eV after correction), significantly lower than at the surface irrespective of correction. The difference in bulk and surface vacancy formation energy strongly suggests vacant surface defects will migrate to towards the bulk in the thermodynamic limit. Interestingly this is where characteristics of VO_2 (R), which are otherwise so far in-line with rutile TiO_2, depart from agreement. In TiO_2 it is much easier to introduce surfaces vacancies, particularly on the bridging oxygen of the (110) face, than equivalently reduce the bulk.[290]

Reduction of the $\Gamma = -1$ VO_2 (110) surface to form $\Gamma = -2$, yields $E_{\text{vac}} = 4.07$ eV (or 4.60 eV after correction). This is much more energy than removing the first bridging oxygen atoms (reduction from $\Gamma = 0$ to $\Gamma = -1$), but still less than removing in-plane oxygen atoms. This

provides an insight into the nature of pristine surface degradation in a highly reducing environment: in-plane oxygen vacancies are created only after all the bridging oxygen atoms have already been removed.

Bader analysis of surface ions indicates the change in charge concentration before and after reduction. After the creation of a bridging oxygen vacancy, the oxidation state of surface cations is reduced in magnitude. Here the majority of reduction is localised on the two V ions that were bridged by the removed oxygen, which show a decrease in Bader charge from $+1.88\ |e|$ in the stoichiometric surface to $+1.71\ |e|$ in the partially reduced surface. The charge of the other surface V cations decreased by less than $0.05\ |e|$ each. Normally this suggests the formation of local surface V^{3+} cations upon the formation of oxygen vacancies. Although the formal picture is topologically correct, the formal oxidation states are strongly exaggerated compared to the *ab initio* picture, due to the delocalised nature of charge in this metallic system.

8.3.2.3 *Adatom defects*

The adsorption of one oxygen atom per slab surface, results in 0.5 ML adatom coverage, and $\Gamma = +1$. The energy of adsorption is defined here as

$$E_{\text{ads}} = \frac{1}{2}(E[\Gamma = +1] - E[\Gamma = 0] - E[O_2]),$$

per surface adatom.

Formation of surface vanadyl species through adsorption energy of an oxygen adatom on top of a 5-fold coordinated V atom (see Figure 37), requires $E_{\text{vac}} = -1.58$ eV (-2.10 eV after correction). Oxygen adsorption from the gas phase is strongly exothermic suggesting surface oxidation will be thermodynamically favourable, but a complete analysis requires consideration of the gas partial pressure in equilibrium with the surface. Oxidation from $\Gamma = +1$ to $\Gamma = +2$ (0.5 to 1 ML) is also exothermic with $E_{\text{vac}} = -1.03$ eV (-1.56 eV after correction) per surface adatom.

The calculated vanadyl V=O equilibrium bond length is 1.61 Å, which is typical of surface vanadyl species reported elsewhere (1.55 – 1.70 Å).[291] The formation of a double bond here is much shorter than

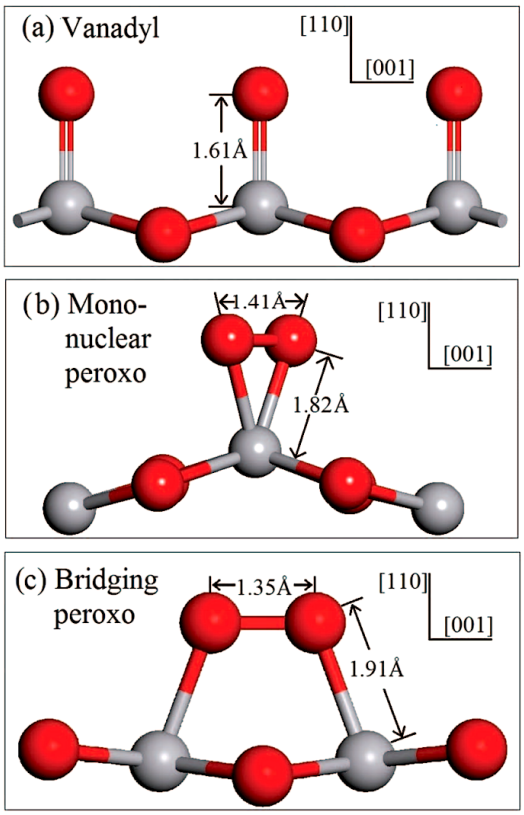

Figure 41: Fully oxidised ($\Gamma = +2$) terminations for the (110) surface of VO_2 (R).

the single V-O distance, which is 1.95 Å in these calculations. Bader analysis indicates that the vanadyl oxygen charge (-0.51 $|e|$) is less negative than the bridging oxygen, whose charge goes from -0.76 $|e|$ in the stoichiometric surface to -0.71 $|e|$ in the oxidised surface. After oxidation the charges on all surface cations increases by a similar small amount (≈ 0.05 $|e|$).

In addition to surface vanadyl species (single oxygen adatoms on bulk-like sites) for $\Gamma = +2$, two other stable configurations are shown in Figure 41. Oxygen adsorbed as a peroxo species $(O_2)^{2-}$, should require less electron transfer between anion adatom and surface cation, than with the vanadyl. The presence of peroxo species has been investigated for other oxide surfaces, *e.g.*, in the surfaces of alkaline-earth oxides,[292] in MoO_3 (010),[293] in V_2O_3 (0001),[294] and in $FeSbO_4$ (100).[285] The first type of peroxo shown in Figure 41, corresponds to the flat peroxo species coordinated to a single V atom, and is nominally referred to as 'mono-peroxo'. The second type shown is the shared peroxo species coordinated to two V atoms, nominally the 'bridging-peroxo'. Both

types of peroxo correspond to local potential energy surface minima. The O-O distances of 1.41 Å and 1.35 Å are very similar to theoretical results presented elsewhere for peroxo surface groups,[285,292,293,294] and slightly less than the experimental O-O distance of the peroxo ion in hydrogen peroxide (1.475 Å).[286] Bader analysis shows that the charge of the oxygen atoms forming the peroxo groups ($\approx -0.3\ |e|$) is significantly less negative than the lattice oxygen species at the surface, as expected. The mono-coordinated peroxo species is slightly more stable than the bridging species (by ≈ 24 meV per peroxo), but it is much higher in energy than the vanadyl-terminated surface discussed earlier (by 1.72 eV per peroxo). For this reason most of the excess oxygen at the VO_2 (110) surface is expected to form vanadyl species.

8.3.2.4 *Finite temperature and pressure thermodynamics*

Finally, the surface thermodynamics of oxidation and reduction is considered as a function of temperature and gas phase oxygen partial pressure, using the oxygen chemical potential from Equations 71 & 73.

In Figure 42 *top* the variation of surface free energy energy is given as a function of chemical potential for the stable (110) surface. The chemical potential is plotted in terms of temperature and oxygen partial pressure (see also Figure 42 *bottom*) to allow conversion between a particular chemical potential and temperature and pressure range. The chemical potential is put in context by referencing the value at which bulk VO_2 becomes stable with respect to bulk V_2O_5 (see the vertical line in Figure 42 *bottom*). This corresponds approximately to the enthalpy of the reaction,

$$2VO_2 + \frac{1}{2}O_2 \rightarrow V_2O_5\,,$$

with $\Delta H = -1.36$ eV, which is obtained from experimental formation energies of the two oxides.[295] At the chemical potential $\mu_O = \Delta H$, the free energy of the above reaction changes sign (we are neglecting here the small contributions from the variation of enthalpies with temperature and from the difference in entropy between the two oxides). The area to the left of the vertical line in the chemical potential plot thus corresponds to the conditions under which bulk VO_2 is thermodynamically stable with respect to bulk V_2O_5. At ambient

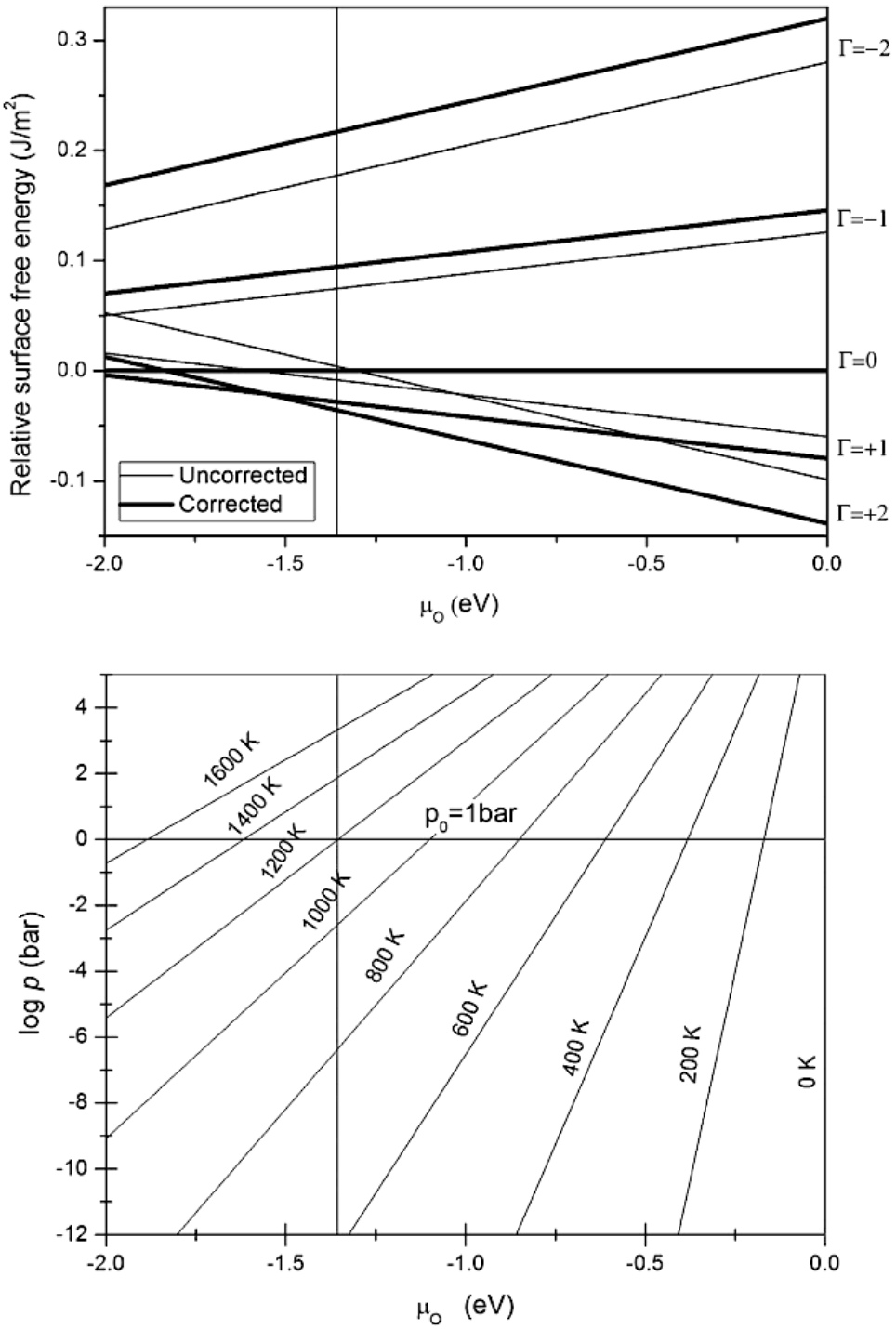

Figure 42: VO_2 (110) surface phase diagram. Surface free energy as a function of chemical potential (*top*), and temperature and pressure *versus* chemical potential (*below*).

conditions V_2O_5 is the stable bulk phase, while the synthesis of VO_2 requires high temperature or a controlled oxygen atmosphere.

The correction to the O_2 energy does not change the gradient of the lines plotted in Figure 42 *top*, but does affect the relative positions of the lines (whereas the lines in the bottom of Figure 42 are determined only by experimental information and are independent from the calculations). Regardless of whether the correction is applied or not, the fully oxidised surface is the most stable at ambient conditions. Surface oxidation of VO_2 can be expected for all the conditions under which V_2O_5 is the most stable bulk phase, including most temperatures and oxygen partial pressure of practical interest for applications. On the other hand, the predicted behaviour at the very reducing conditions (below $\mu_O \approx -1.36$ eV) under which bulk VO_2 is stable with respect to V_2O_5 depends somewhat on whether the oxygen correction is introduced, as the uncorrected DFT calculations underestimate the level of oxidation. The corrected results suggest that there is surface oxidation even at these very reducing conditions. At ambient pressure, the excess surface oxygen forming vanadyl species becomes thermodynamically unstable with respect to a stoichiometric surface only at temperature ~ 1600 K.

The trend towards oxidation of the VO_2 surface seems consistent with the presence of V^{5+} ions at the surface of VO_2 films, which was suggested on the basis of x-ray photoelectron spectroscopy (XPS) measurements by Manning *et al.*.[94] However, according to these authors, a very thin film ($10 - 20$ nm) of V_2O_5 develops at the surface VO_2 samples which are exposed to atmospheric conditions, and it is probably this surface film which leads to the V^{5+} XPS signal. This experimental observation means that surface oxidation of VO_2 samples occurs at a level much deeper than what we have considered in our models. Our calculations therefore only describe the first stage of surface oxidation, after the formation of VO_2 crystals.[295]

8.4 CONCLUSIONS

As in rutile TiO_2, the oxygen-terminated (110) surface is the most stable in rutile VO_2. The surface relaxation patterns are also very similar in both oxides. The equilibrium morphology of VO_2 (R) has

been shown to be acicular, laterally confined by the (110) planes; therefore, the formation of VO_2 nano wires growing along the rutile [001] direction is energetically favourable. Because the (110) surface is by far the most prominent surface in the VO_2 morphology, which is in agreement with experimental observations, future theoretical and experimental studies of the VO_2 surface behaviour will probably focus on this surface.

The VO_2 (R) (110) surface can be expected to be oxidised even at strongly reducing conditions; it would then be very difficult to grow VO_2 samples that maintain the bulk stoichiometry at the surface. In the initial state of oxidation, the excess oxygen forms surface vanadyl groups, while peroxo species are comparatively much less stable. On the other hand, reduction of the surfaces is thermodynamically very unfavourable, and oxygen vacancies are in fact easier to form in the bulk than in the surface.

The application of a correction to the overbinding of the oxygen molecule within the GGA approximation is found to have a non-negligible effect on the prediction of the surface composition under reducing conditions. The uncorrected results indicate that the VO_2 surface will be stable against oxidation for chemical potentials in the region where bulk VO_2 is stable. However, after applying a correction to the oxygen molecule energy, it is found that much of the surface excess oxygen can actually survive these very reducing conditions.

9

THERMODYNAMICS OF LITHIUM DOPED MANGANESE DIOXIDE SURFACES

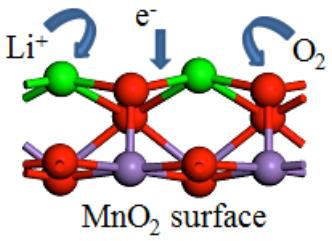

In this chapter, the adsorption and co-adsorption of lithium and oxygen at the surface of rutile-like manganese dioxide (β-MnO_2), which are important in the context of Li–air batteries, are investigated using density functional theory. In the absence of lithium, the most stable surface of β-MnO_2, the (110), adsorbs oxygen in the form of peroxo groups bridging between two manganese cations. Conversely, in the absence of excess oxygen, lithium atoms adsorb on the (110) surface at two different sites, which are both tri-coordinated to surface oxygen anions, and the adsorption always involves the transfer of one electron from the adatom to one of the 5-fold coordinated manganese cations at the surface, creating formal Li^+ and Mn^{3+} species. The co-adsorption of lithium and oxygen leads to the formation of a surface oxide, involving the dissociation of the O_2 molecule, where the O adatoms saturate the coordination of surface Mn cations and also bind to the Li adatoms. This process is energetically more favourable than the formation of gas-phase lithium peroxide (Li_2O_2) monomers, but less favourable than the formation of Li_2O_2 bulk. These results suggest that the presence of β-MnO_2 in the cathode of a non-aqueous Li–O_2 battery lowers the energy for the initial reduction of oxygen during cell discharge.

Manganese dioxide (MnO_2) has been widely investigated as a cathode material in lithium-ion batteries, due to their Li intercalation capacity (forming Li_xMnO_2 phases), low toxicity, and relative low cost compared to oxides of other metals like Co or Ni.[129,130,131,132] Several MnO_2 polymorphs have been investigated in the context of Li-ion cells, including α-MnO_2 (hollandite), β-MnO_2 (pyrolusite), γ-MnO_2 (nsutite) and R-MnO_2 (ramsdellite).[129] Contrasting with other polymorphs, the rutile-structured phase (β-MnO_2) does not seem to be able to intercalate Li in the bulk, while mesoporous samples of the same polymorph do exhibit high Li uptake.[43] A recent computer simulation study by Tompsett *et al*.[40] has shown that there is an energy barrier ($\gtrapprox 0.6$ eV) for diffusion of Li from the surface to the bulk of β-MnO_2, which they demonstrate to be due to the much higher electrostatic potential (and therefore higher insertion energy) within the bulk. It thus seems plausible that most of the Li incorporated in β-MnO_2 lies at the surface (that is, in the walls of the pores), which would explain why mesoporous samples are able to accommodate much more Li than highly crystalline samples.

The Li–air system is a novel battery technology which promises higher specific energy than Li-ion batteries. In this battery the cathode reaction is not the formation of an intercalation compound but the reduction of oxygen gas in the presence of Li^+ ions forming lithium peroxide Li_2O_2 (or LiOH in the aqueous version).[16,133,134,135,136] Manganese oxides may also play an important role here: it has been shown that nanostructured MnO_2 in different polymorphic states are able to catalyse the formation and decomposition of Li_2O_2 in the cathode, thus decreasing the over-potentials required for the operation of the Li–air cell.[137] In this case it is the surface rather than the bulk of the manganese oxide which controls its function in the cathode, and therefore the lack of Li intercalation in bulk β-MnO_2 should not limit its utilisation. Understanding the behaviour of the cathode catalysts is the key for improving the function of Li–air batteries.[31]

In order to gain insight into the molecular processes occurring at the Li–air battery cathode reaction in the presence of β-MnO_2, the simultaneous adsorption of lithium and oxygen has been investigated

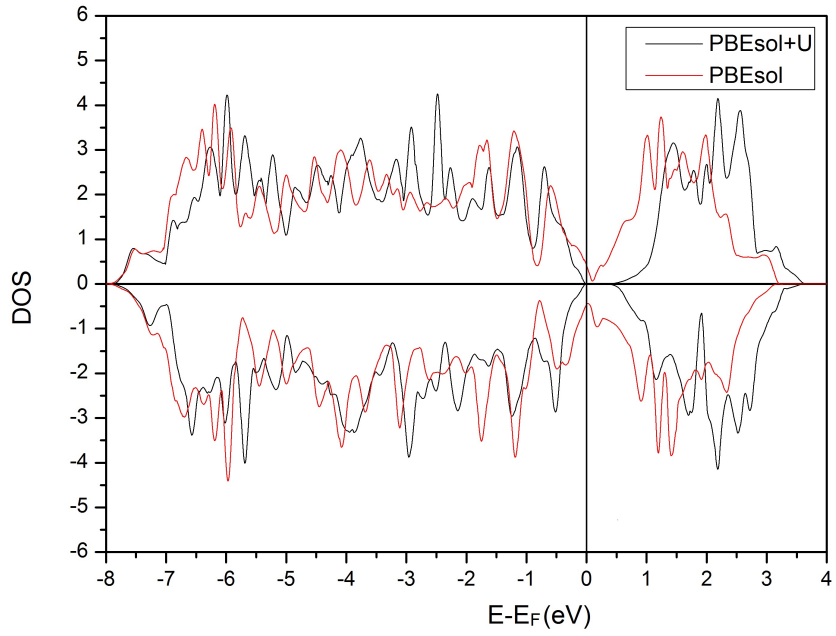

Figure 43: Electronic density of states (states/eV/V_2O_4 unit cell) for AFM MnO_2 bulk with (black) and without (red) the on-site Coulomb correction ($U|J = 2.8|1.2$ eV) applied.

at the most stable surface of this oxide, the (110). First considered are the pure β-MnO_2 surfaces and their redox behaviour as a function of oxygen chemical potential, then the Li adsorption in the absence of excess oxygen and the transfer of electrons between the Li adatoms and the surface, and finally oxygen adsorption at the lithiated surface. In the subsequent sections, MnO_2 refers to the β polymorph, unless otherwise stated.

9.2 COMPUTATIONAL DETAILS

9.2.1 *Density functional theory*

Periodic DFT calculations were performed with the VASP program,[204,205] using the GGA in the form of the PBEsol.[188] In order to correct for the poor description of d orbitals in GGA functionals, the GGA+U approach was used. Cockayne and Li have shown that a Hubbard-corrected PBEsol+$U|J$ functional with $U = 2.8$ eV and $J = 1.2$ eV

(following the approach of Liechtenstein *et al.*,[59] where the two parameters enter independently in the corrected functional) produces electronic properties in good agreement with experiment.[296] In contrast to the uncorrected PBEsol functional, the PBEsol+$U|J$ functional produces a gap at the Fermi level, thus reproducing the experimentally observed semiconducting character of MnO_2 (see Figure 43). The reasons why the description of MnO_2 requires the use of the two-parameter approach ($U|J = 2.8|1.2$ eV) with explicit exchange have been discussed in detail in a recent paper.[40]

The PAW method,[206,214] was used to describe the interaction between the valence electrons and the core, and the core states (up to $3p$ in Mn, and $1s$ in O) were kept frozen at the atomic reference states. The number of plane waves was determined by a kinetic energy cutoff of 500 eV, and a $6 \times 6 \times 9$ mesh of **k**-points was employed for the bulk unit cell calculations. These parameters were checked with respect to convergence of the bulk total energy. For surface calculations, the number of **k**-points was adapted to achieve a similar sampling density in the reciprocal space.

A collinear AFM ordering, shown in Figure 44, is imposed in all our calculations, as justified in the previous work of Kresse *et al.*.[41] This is the lowest-energy magnetic configuration within the rutile unit cell, but not the magnetic ground state of this oxide: there is a complex non-collinear screw-type magnetic structure below 92 K.[42] The low value of the transition temperature to paramagnetism is indicative of very weak coupling, which means that the calculated total energies will be practically unaffected by the chosen spin arrangement.

9.2.2 *Surface thermodynamics*

The stabilities of five low-index surface orientations ((110), (010), (001), (111) and (011)) were considered by performing periodic calculations of slabs with stoichiometric composition, thicknesses between 11 and 14 Å (depending on the orientation), and vacuum gaps of ~ 14 Å (see Figure 45). The two surfaces of each slab are symmetrically equivalent, and this equivalence is kept during all of the calculations to prevent the formation of an electric dipole that can be associated with asymmetric slabs. The cell parameters of the slab are kept con-

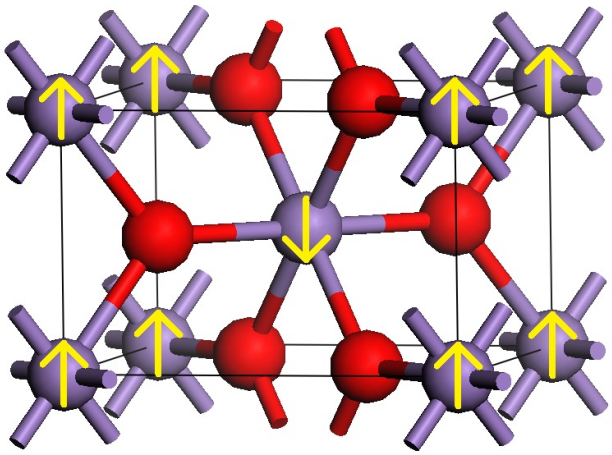

Figure 44: Rutile unit cell of MnO_2 showing the AFM spin ordering. O sites in red, and Mn in grey.

stant during the calculations, based on the relaxed cell parameters of the bulk. For MnO_2, the calculated unit cell parameters are $a = 4.366$ Å and $c = 2.961$ Å, which gives an acceptable agreement with experimental values $a_{exp} = 4.399$ Å and $c_{exp} = 2.872$ Å (deviations of -0.8 % and $+3.1$ % for a and c, respectively, and of -1.6 % in the cell volume).[274]

In our surface simulations, all atoms in the slabs are fully relaxed, and the surface energies γ and surface free energies $\sigma(T, p)$ are obtained using the standard expressions,

$$\gamma = \frac{E_{slab} - E_{bulk}}{2A},$$

and

$$\sigma(T, p) = \gamma - \frac{\Gamma}{A}\mu_O(T, p).$$

Following the *ab initio* redox thermodynamics methodology of Scheffler *et al.*,[276] the surface free energy is given using a oxygen gas phase chemical potential (μ_O), where Γ is the excess surface oxygen, and A is the slab surface area.

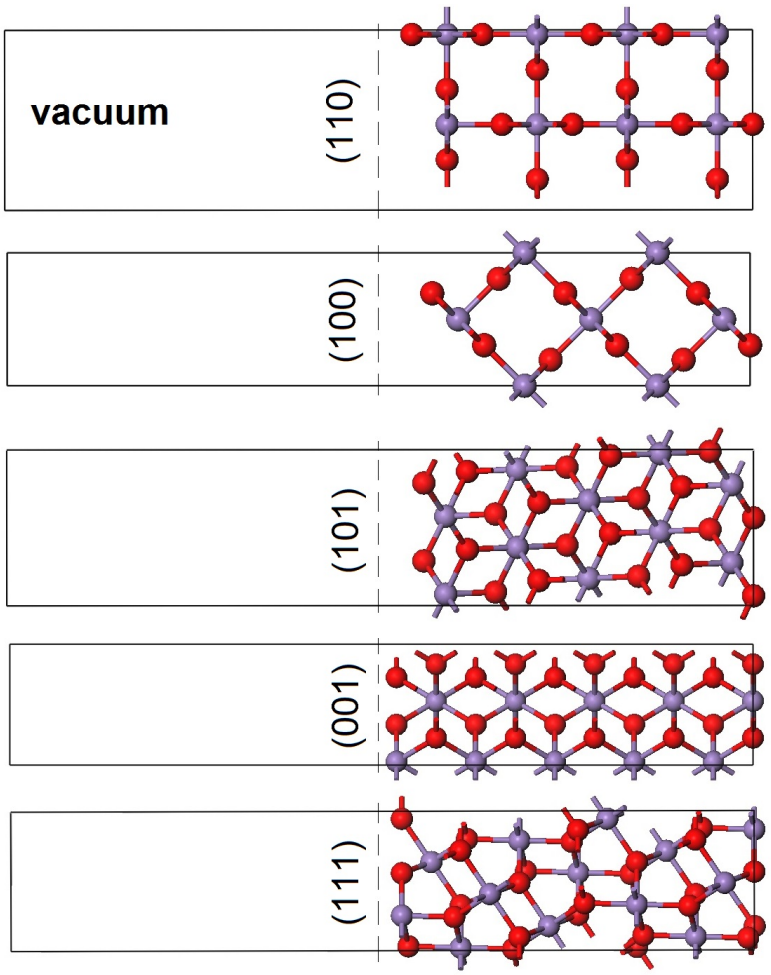

Figure 45: Slab unit cells used for modelling the low Miller index surfaces of rutile MnO_2.

Surface plane	γ (J/m^2)
(110)	1.15
(100)	1.43
(101)	2.03
(001)	2.20
(111)	3.61

Table 7: Surface energy for low Miller index MnO_2 surfaces.

9.3 RESULTS

9.3.1 *Surfaces and morphology*

The surface energies for each of the five low Miller index crystallographic planes are given in Table 7. As with other isostructural transition metal oxides such as TiO_2 and VO_2, the most stable surface is the (110).[2,280] These surface energies were used to calculate the planes exposed to the equilibrium morphology of an MnO_2 particle (see Figure 46). The particle volume is largely bounded by the (110) and (101) planes. Calculations performed using classical pair-wise interatomic potentials have produced a similar though more rounded morphology due to a higher (110) surface energy.[297] Experimentally, the morphology of MnO_2 particles is strongly dependent on synthesis conditions, but the observed tendency to form particles with large aspect ratio is consistent with our results.[298]

As in TiO_2 (110) and VO_2 (110), the main relaxations in MnO_2 (110) occur normal to the surface, with the 5-fold coordinated manganese atoms relaxing inward and the 6-fold coordinated manganese atoms and the in-plane oxygen atoms relaxing outward (see Figure 47).

9.3.2 *Redox properties of pristine* (110)

In order to discuss the redox properties of the (110) surface of MnO_2, surface free energies are calculated for different stoichiometries. Only variations in the oxygen content is considered (the number of manganese atoms is fixed). Five values of Γ are possible if only bulk-like oxygen positions are considered: $\Gamma = 0$ (stoichiometric surface),

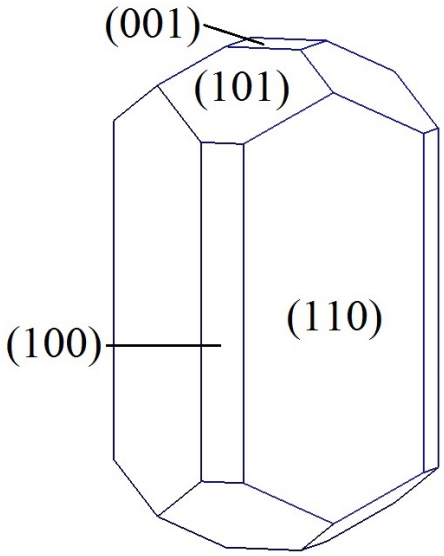

Figure 46: Wulff's construction of the equilibrium morphology for a MnO_2 particle.

$\Gamma = +1$ & $+2$ (partially and totally oxidised surfaces), and $\Gamma = -1$ & -2 (partially and totally reduced surfaces). Here, total reduction means the removal of the full top layer of bridging oxygen ions, while total oxidation means the addition of a full layer of oxygen ions forming manganyl-like terminations on top of the previously unsaturated Mn sites. "Mono-peroxo" and "bridging-peroxo" modes of O_2 adsorption (shown in Figure 48), where the molecule remains undissociated, are also considered, and these situations will be compared to the $\Gamma = +2$ manganyl bulk-like termination.

To correct for the poor PBEsol description of redox enthalpies, an adjusted value for the O_2 energy is used, similar to the correction proposed by Wang *et al.*.[287] The value is determined such that the PBEsol calculated energies of formation are corrected to agree with the experimental enthalpies (see Figure 49). The correction, in the case of MnO_2, should also improve the poorer description of molecules by the PBEsol functional compared to standard PBE, as the former is designed to model extended systems.

Here, thermodynamics are discussed of reduction and oxidation on the surface as a function of temperature and partial pressure of oxygen. Figure 50 shows the variation of the surface free energies for different surface terminations as a function of chemical potential. In the bottom graph a vertical line is included that marks the boundary

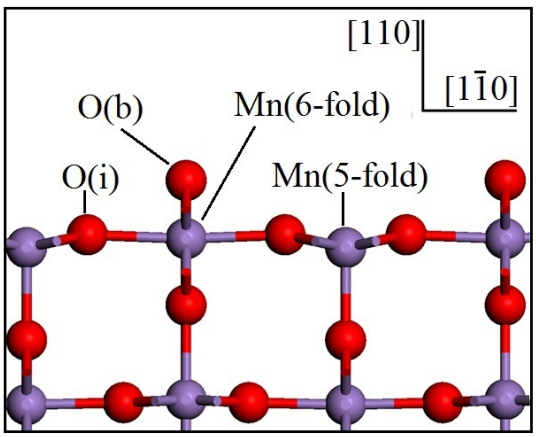

Figure 47: Lateral view of the MnO_2 (110) relaxed surface.

between the regions of stability of MnO_2 and Mn_2O_3 in their bulk forms. This is estimated from the change in enthalpy of the reaction,

$$2Mn_2O_3 + O_2 \rightarrow 4MnO_2,$$

$\Delta H = -1.68$ eV, which was obtained from the experimental formation energies of the two oxides. At the chemical potential $\mu_O = \Delta H$, the free energy of the above reaction changes sign (again, small contributions are neglected from the variation of enthalpies with temperature and from the difference in entropy between the two oxides). The area to the left of the vertical line in the chemical potential plot thus corresponds to the conditions under which bulk Mn_2O_3 is thermodynamically stable with respect to bulk MnO_2. Under ambient conditions, for example, MnO_2 is in the stable bulk phase.

Figure 50 shows that the two reduced terminations considered ($\Gamma = -1$ & $\Gamma = -2$) are not stable at moderate T and p conditions. Complete reduction of the MnO_2 surface cannot be expected, except for extremely reducing conditions where bulk Mn_2O_3 is more stable than bulk MnO_2 (*i.e.* left of the vertical line in Figure 50). Under mildly reducing conditions (approximately -1.7 eV $\lessapprox \mu_O \lessapprox -0.6$ eV) the $\Gamma = 0$ stoichiometry is always the most stable. Under oxidising conditions (lower temperatures and/or high oxygen partial pressures), although $\Gamma = +1$ oxidation is unfavourable, the specific bridging-peroxo $\Gamma = +2$ mode of oxidation is stable. The stoichiometric composition, moreover, becomes unstable with respect to the bridging-peroxo mode of $\Gamma = +2$ oxidation at approximately ambient temperature and pres-

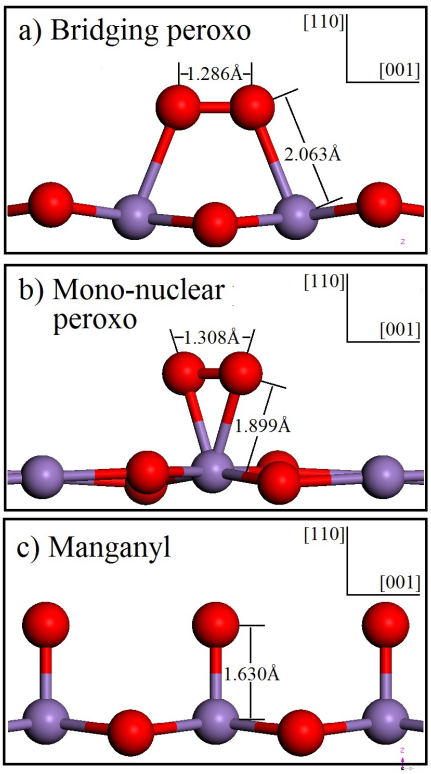

Figure 48: Fully oxidised ($\Gamma = +2$) MnO_2 (110) surface terminations.

sure. The general trend towards a stoichiometric surface, or a surface with adsorbed oxygen, is consistent with the presence of some Mn^{5+} ions at the surface of MnO_2 films. XPS of MnO_2 microstructures gives a Mn to O ratio of 1 : 2.12, which is evidence for a moderate oxidation of the oxide surfaces.[299] Other recent theoretical investigations present similar trends in oxidation/reduction, although with less stabilisation of surface oxidation.[300] This result may be due to not considering the adsorption of bridging-type oxygen, where the adsorbate maintains its molecular character.

Vacancy formation energies were calculated from the energies of the $\Gamma = -1$ and $\Gamma = -2$ slabs. Bridging O vacancies have a formation energy of 1.87 eV, while it costs 4.25 eV to remove both bridging oxygen atoms, that is, reduction becomes more difficult with the removal of each bridging O (4.25/2 eV $>$ 1.87 eV).

Adsorption energies were calculated for the four oxidised configurations (one with $\Gamma = +1$, and three with $\Gamma = +2$, with respect to oxygen in an isolated O_2 molecule. Adsorption of an oxygen atom on a 5-fold coordinated Mn site yields an adsorption energy of $+0.53$ eV.

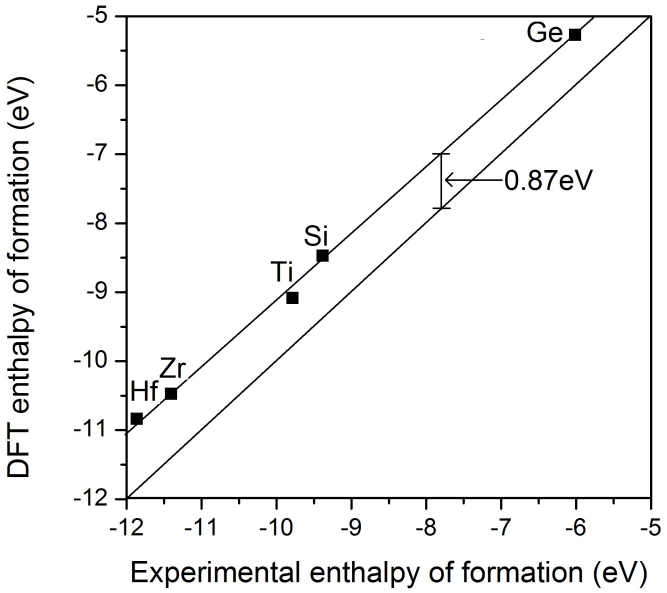

Figure 49: O_2 overbinding correction (+0.87 eV), to correct the GGA (PBEsol) oxidation enthalpies.

$\Gamma = +2$ surfaces were calculated with manganyl, mono-peroxo and bridging-peroxo configurations, which yield adsorption energies of $+1.16$ eV, -0.02 eV, and -1.15 eV respectively. These figures show that adsorption of oxygen can be both endo and exothermic, depending on whether or not oxygen maintains its molecular character on the surface. The formation of manganyl species from adsorbed oxygen is a local minimum in the adsorption energy landscape, but is the least favourable configuration and is indeed thermodynamically unfavourable with respect to desorption. The bridging peroxo unit is probably the most favoured because it is shared between two Mn surface cations and requires the least charge transfer per Mn cation of all possible oxidised species. Minimal charge transfer from Mn to O occurs as the Mn cations have already a formal oxidation state of $+4$ in MnO_2.

9.3.3 *Charge transfer*

Understanding the surface behaviour of Li-doped MnO_2 is important in the context of MnO_2 based Li–air batteries. The mode of the transfer is considered for an electron from a Li adatom to a surface Mn cation.

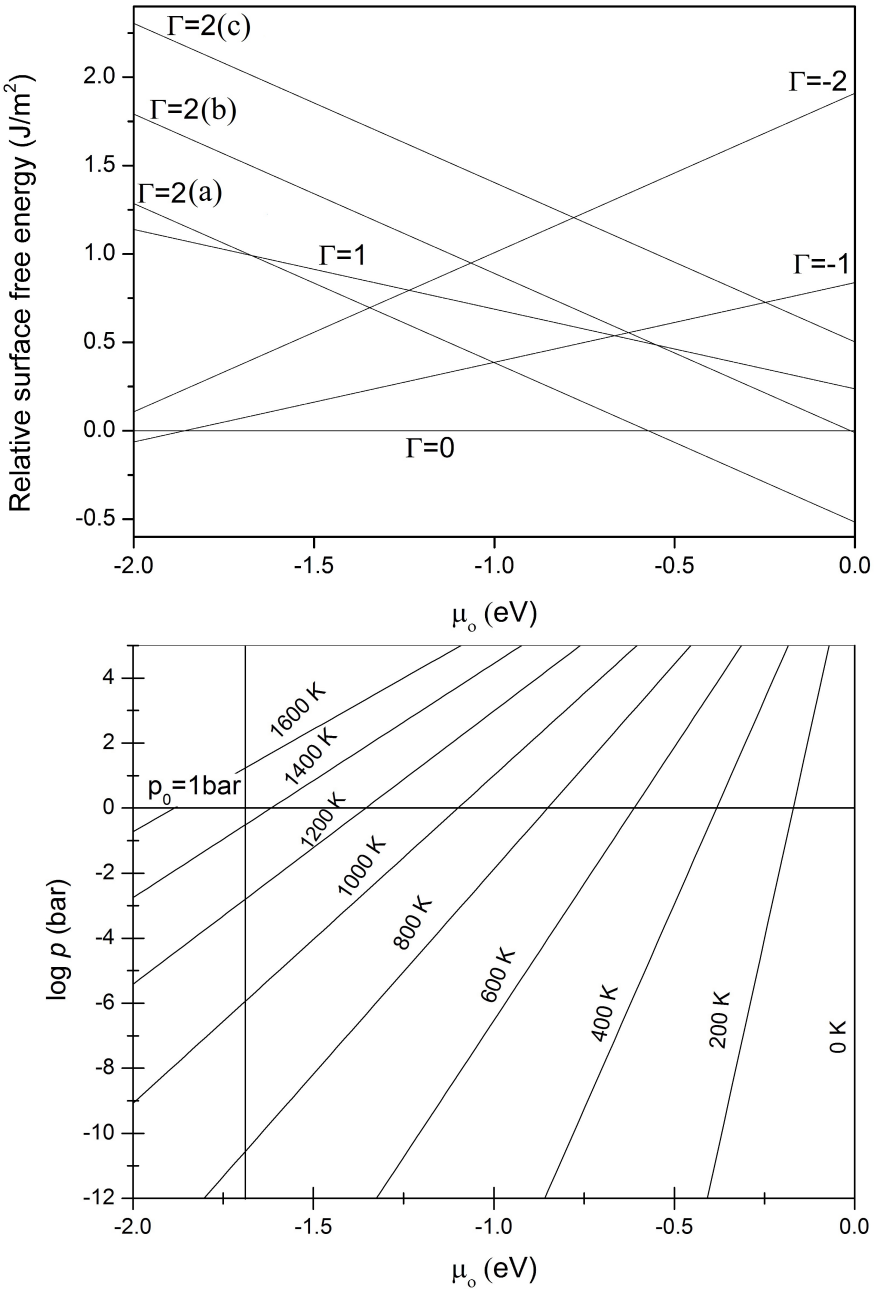

Figure 50: MnO_2 (110) surface phase diagram. Surface free energy γ as a function of O chemical potential μ_O, and temperature T and pressure p.

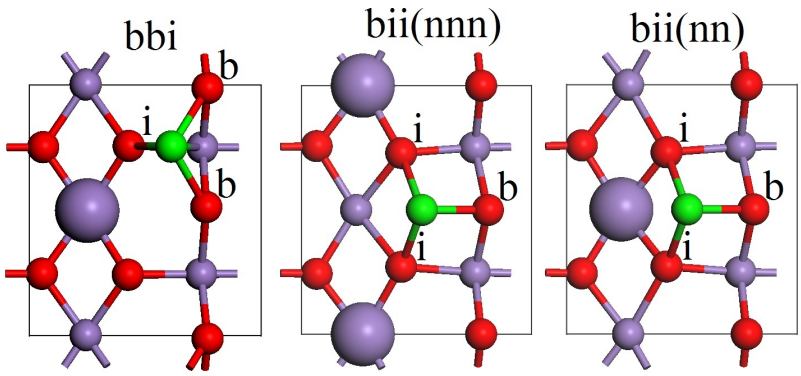

Figure 51: Top view of the MnO_2 (110) surface with Li adsorbed with bridging-bridging-inplane O coordination (bbi), next-nearest-neighbour bridging-inplane-inplane coordination (bii (nnn)), and nearest-neighbour bridging-inplane-inplane coordination (bii (nn)). Mn^{4+} site small in grey, Mn^{3+} site large in grey, O^{2-} in red and Li^{+} in green.

The first step is to determine onto which surface site Li preferentially adsorbs.

Different possible adsorption sites on the surface were systematically tested and the results are reported in Table 8. Li adatoms are more stable in sites of high oxygen coordination. The site with lowest adsorption energy (-1.80 eV) is that where Li is triply coordinated, bonded to two bridging and one in-plane oxygen atoms (bridging-bridging-inplane O coordination (bbi)). Another adsorption site, with almost the same adsorption energy, has Li coordinated to one bridging and two in-plane oxygen atoms (bridging-inplane-inplane O coordination (bii)). Sites with Li bonded to only two bridging oxygen (bridging-bridging O coordination (bb)), or to one bridging oxygen (bridging O coordination (b)) do not correspond to local minima of the potential energy landscape and can only be stabilised by symmetry constraints. When the initial symmetry is broken the Li adatoms move away from these sites.

Electron transfer from Li adatoms, in the bbi and bii sites, to the surface cations is now examined. A Bader analysis shows that in all cases the adsorbed Li adopts a positive charge ($\approx +0.9\ |e|$), which indicates that an electron has been donated to the surface. This electron should go to the manganese cations, because the oxygen anions formally have a complete electron shell. In order to identify which Mn cations were reduced, the integration of the spin density is

examined over the Mn Bader volumes, which generally gives a better indication of cation reduction than the charge density.[301,302] For the reduced Mn cation a clear increase is found in the spin moment of $+0.99\ \mu_B$ within the Bader volume.

For the bbi site, there are three symmetrically distinct possibilities for where the electron localises on the surface cations: one 5-fold Mn and two 6-fold Mn cations. Each of these is tested in turn, initially localising the electron on each site and then relaxing the electronic and geometric structure. The initial localisation was forced by using a computational "trick": Mn are temporarily substituted by Fe in the site for which localisation is forced. Because Fe is more stable in the 3+ oxidation state than in the 4+, the geometry relaxation leads to a structural distortion favourable to the presence of a 3+ cation in that lattice site. When Mn are put back in that position, it tends to reduce preferably over those in other lattice positions. Following this procedure, it is found that the Mn (6-fold) cations are not stable for localisation of the extra electron, that is, the transferred electron always goes to the Mn (5-fold) cation at the surface, regardless of the initial localisation.

For a bii lithium adatom, again there are three distinct possibilities for the localisation of the transferred electron. The localisation on the Mn (6-fold) cation is again found to be unstable. Electron localisation on the two different Mn (5-fold) cations (relative to the Li position) leads to different adsorption energies: the electron localises on the Mn (5-fold) cation that is the next-nearest neighbour (nnn) to the Li adatom, where it is 0.14 eV more stable than in the nearest neighbour (nn) position. This behaviour, which arises from the higher elastic energy in accommodating the distortions produced by both the adatom and the reduced cation in very close positions, is the opposite of what is expected in terms of pure electrostatics: if the Coulomb effect was dominant, the nn Mn cation would be reduced, in order to decrease the Mn–Li repulsion. The non-Coulombic charge localisation effect has been found in other cases of charge transfer between adatoms and oxide surfaces.[302] The three discussed adsorption sites and charge localisation configurations are shown in Figure 51, and their energies are summarised in Table 8.

Li adsorption site	Adsorption energy	d(Li-O_i)	d(Li-O_b)
bbi	-1.80	2.00	1.94, 1.97
bii (nnn)	-1.76	2.03×2	1.80
bii (nn)	-1.62	2.10×2	1.79

Table 8: Energies (eV/O_2) and bond lengths (in-plane and bridging d(Li-O) in Å) for the three different stable modes of adsorption.

9.3.4 *Oxygen adsorption*

Finally, adsorption is considered of oxygen (two O atoms per surface cell, $\Gamma = +2$) on the Li/MnO_2 (110) surface. In order to investigate the stability of Li–O–O–Li species, which are known to be important in the Li–air battery, we also consider two Li atoms per surface cell, assuming that they both occupy the most stable bbi sites. It should be noted that since there are only two bbi sites at each surface in our simulation cell, this structure corresponds to full coverage of the bbi sites at the surface, that is, a monolayer of Li adatoms. Therefore, based on the results discussed above, all the Mn (5-fold) surface cations can be expected to be reduced before oxygen adsorption, which has been confirmed using Bader analysis.

Here a number of oxygen adsorption configurations are investigated, in some cases keeping the molecular bond between the two oxygen atoms, and in others assuming dissociative adsorption. Four different stable configurations are found, which are shown in Figure 52. Some of the configurations initially considered were found to be unstable (in the sense of not being a minimum in the adsorption energy landscape). For example, although a configuration with one oxygen atom directly on top of each Li is a stationary point, it is in fact unstable and relaxes (if the symmetry of the initial configuration is broken) to a peroxo configuration bridging between two Li atoms, as in Figure 52. The oxygen adsorption energy in this Li-peroxo configuration is -1.81 eV/O_2.

The Li-peroxo is not the only stable peroxo adsorption configuration: a peroxo group bridging directly between the two previously unsaturated Mn cations, as in Figure 52 ($E_{ads} = -2.00$ eV/O_2), and a peroxo group perpendicular to the surface and binding to Li on one end and to Mn on the other end ($E_{ads} = -1.27$ eV/O_2), are also stable.

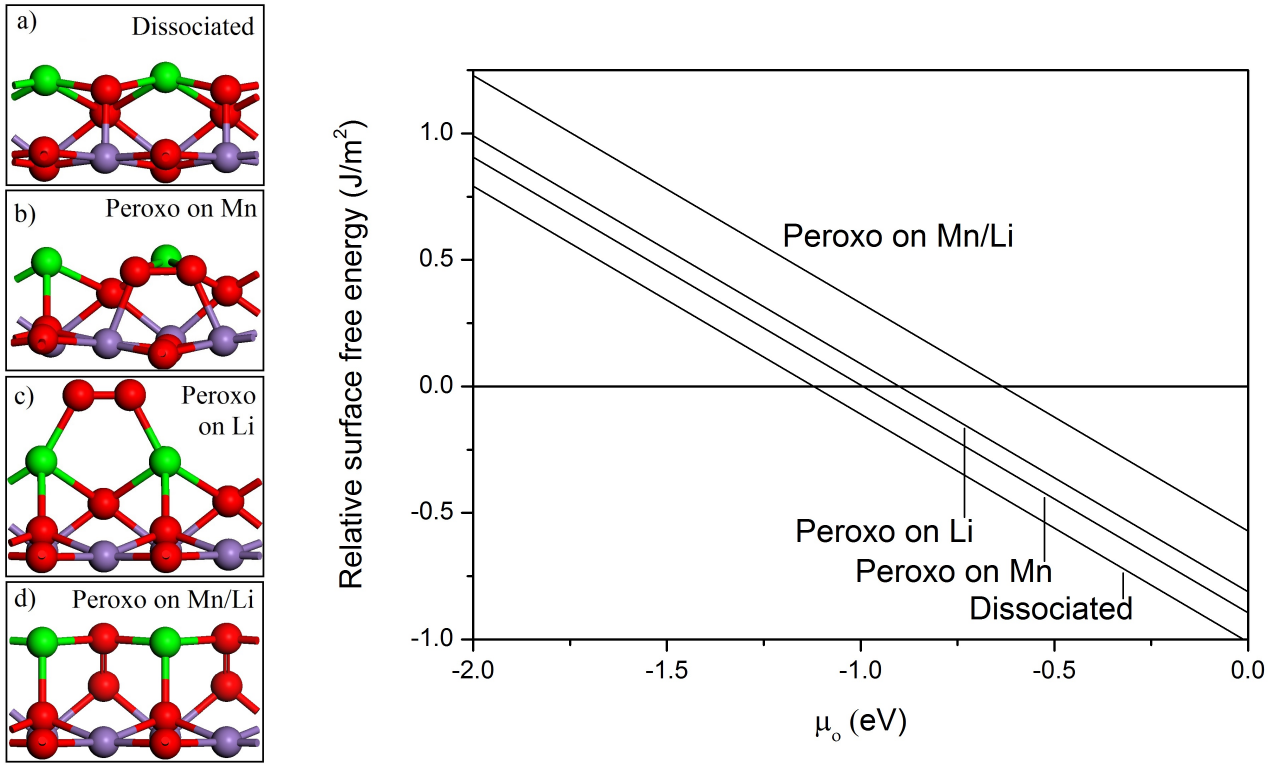

Figure 52: Stable adsorption configurations and surface free energy (with respect to the non-oxidised termination) for two O atoms at the Li/MnO_2 (110) surface.

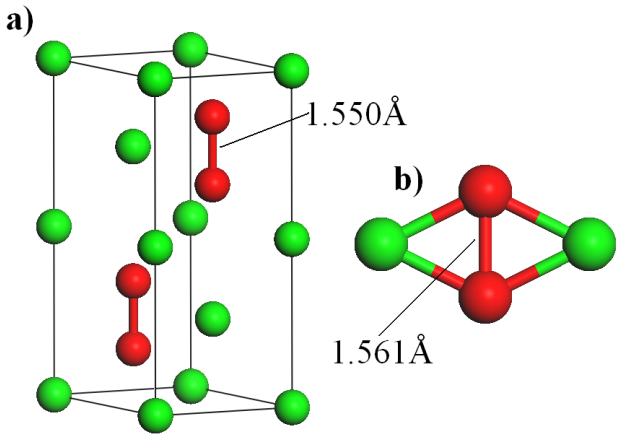

Figure 53: Structure of Li_2O_2 in the bulk form (hexagonal $P6_3/mmc$ space group) and as a monomer.

However, the most stable configuration found was the dissociative adsorption where there is an oxygen atom on the "bulk-like" positions on top of each of the Mn cations, but with additional bonds formed with the Li adatoms. This preferred configuration is shown in Figure 52 and has the adsorption energy $E_{ads} = -2.25$ eV/O_2.

These results show that, due to the presence of cation sites amenable to oxidation, oxygen adsorption on the Li/MnO_2 (110) surface is much more favourable than on the pure MnO_2 (110) surface. In Figure 52 we show that the range of chemical potentials at which oxygen adsorption is stable with respect to the non-oxidised surface (at a coverage of two O atoms per cell), extends beyond -1 eV. This is ~ 0.5 eV below the threshold in the Li-free surface, meaning that the Li/MnO_2 (110) surface will remain oxidised up to temperatures of ~ 1000 K at ambient oxygen pressure.

9.3.5 *Lithium-air battery*

The results presented above can help us understand better the cathode reaction in a Li–air battery, in the presence of MnO_2. During the battery discharge process, molecular oxygen is reduced in the cathode, in the presence of Li cations and electrons, forming lithium peroxide (Li_2O_2) particles:

$$O_2 + 2Li^+ + 2e^- \rightarrow Li_2O_2\,.$$

Comparing the energy of formation of bulk Li_2O_2 (a hexagonal crystal,[303] shown in Figure 53) with the energy of formation of the surface lithium oxide at MnO_2 (110) (Figure 52), the former is lower by 1.25 eV/Li. This agrees with the experimental observation that Li_2O_2 is the main product of the cathode reaction in Li–air batteries (both in the presence and in the absence of MnO_2).[137] However, in the initial stage of growth of Li_2O_2 in the cathode, the small Li_2O_2 clusters have a high energy per formula unit relative to the bulk. For example, calculations have shown that the Li_2O_2 monomer (Figure 53, initial geometry from Lau *et al.*[304]) is 3.55 eV per formula unit (or 1.78 eV/Li) higher in energy than the Li_2O_2 bulk, and therefore also higher in energy than the surface lithium oxide. This implies that the initial reduction of oxygen in the cathode occurs more favourably *via* the dissociative adsorption of the oxygen molecule at the lithiated MnO_2 surface, forming the structures described above (Figure 52), than *via* the formation of small unsupported Li_2O_2 clusters. If it is possible for the Li_2O_2 particles to grow in contact with these LiO/MnO_2 surfaces, then the barrier for the formation of the lithium peroxide particles at the cathodes would be reduced.

9.4 CONCLUSIONS

The main conclusions of our study of the redox behaviour of the pure and lithiated (110) surface of rutile-structured MnO_2 are as follows:

(a) The stoichiometric MnO_2 (110) surface is very stable under reducing conditions, and can be expected to resist significant reduction under most temperatures and oxygen partial pressures of interest. The adsorption of oxygen, on the other hand, is relatively favourable at low to ambient temperatures and high partial pressures of oxygen. This adsorption mainly occurs in the form of peroxo species bridging between two surface Mn cations.

(b) The preferred site for the Li adatom is one where the adatom is tri-coordinated to one in-plane and two bridging oxygen atoms. Charge transferred from the Li always localises on the coordinatively unsaturated (5-fold) Mn surface cations, irrespective of the Li adsorption site.

(c) Oxygen adsorption is stabilised by the presence of Li at the surface. The most stable adsorption mode is dissociative, where oxygen atoms saturate the coordination of Mn surface cations, and at the same time bind to the Li adatoms.

(d) The formation of the surface lithium oxide is energetically more favourable than the formation of gas-phase lithium peroxide (Li_2O_2) monomers, but less favourable than the formation of Li_2O_2 bulk, which suggest that the presence of β-MnO_2 in the cathode of a Li air battery lowers the energy for the initial reduction of oxygen. An experimental verification of this conclusion from electrochemical studies would be welcome.

10

ANISOTROPIC COULOMB INTERACTION IN LANTHANUM MANGANITE

In low-temperature anti-ferromagnetic $LaMnO_3$ (LMO), strong electronic interactions among localised Mn $3d$ electrons prevent a satisfactory description from standard local density and generalised gradient approximations in density functional theory calculations. Here we show that the strong on-site electronic interactions are described well only by using direct *and* exchange corrections to the intra-orbital Coulomb potential. Only DFT+U calculations with explicit exchange corrections produce a balanced picture of electronic, magnetic and structural observables in agreement with experiment. To understand the reason, a rewriting of the functional form of the +U corrections is presented that leads to a more physical and transparent understanding of the effect of these correction terms. The approach highlights the importance of Hund's coupling (intra-orbital exchange) in providing anisotropy across the occupation and energy eigenvalues of the Mn d states. This intra-orbital exchange is the key to fully activating the Jahn-Teller distortion, reproducing the experimental band gap and stabilising the correct magnetic ground state in LMO.

10.1 INTRODUCTION

LMO exhibits many fascinating characteristics, from octahedral and JT distortions,[138,139,140,141] to orbital ordering and on-site Coulombic localisation effects.[45,46,53,142,143,144,145] The wide range of symmetry breaking and ordering phenomena in LMO provides fertile grounds for materials science to design functional applicability. In this regard a reliable *ab initio* description is desirable, but also a significant technical challenge.

In this work we show the limitations and successes of two different DFT+U methods. The "spherically averaged" Dudarev *et al*. Coulomb correction,[177] here called U_{eff}, averages out exchange effects of the

Mn d shell, and we show that it cannot simultaneously reproduce the bulk band gap, structure and magnetism. The dedicated anisotropic exchange term in the "rotationally invariant" Liechtenstein *et al.* Coulomb correction,[59] here called $U|J$, dramatically improves the description of LMO. The $U|J$ method answers the specific call[305] for a practical DFT-based methodology capable of reproducing the gap, structure and magnetism simultaneously in LMO. This is useful as understanding the coupling between electronic, magnetic and lattice degrees of freedom in LMO has been a matter of persistent interest.[139,305,306]

Using the $U|J$ method we show the importance of Hund's coupling in LMO. Intra-orbital exchange can energetically order the orbitals of the Mn ${t_{2g}}^3{e_g}^1$ ion, which in turn strongly affects *inter-orbital* magnetism and the size of the LMO band gap. The Mn ${e_g}^1$ occupancy polarisation[149,307]

$$\pi^{e_g\sigma} = \frac{f_{x^2-y^2\sigma} - f_{3z^2-r^2\sigma}}{f_{x^2-y^2\sigma} + f_{3z^2-r^2\sigma}}\,, \tag{74}$$

where σ labels spin, is highly sensitive to intra-orbital exchange term J in the $U|J$ scheme. By modifying the sign and value of $\pi^{e_g\sigma}$, we correct the DFT description of both JT distortion, and the electronic and magnetic structures of LMO. Beyond an improved *ab initio* description, the $U|J$ calculations also provide insight into the origin of magnetic, electronic and structural ordering in LMO.

10.2 COMPUTATIONAL DETAILS

Periodic plane wave DFT calculations were performed using the VASP software,[204,205] the LDA (PZ81),[169] and the GGA in the form of PBEsol.[187,188] Valence electrons are described using the PAW method[206,214] with core states (up to 4d in La, 2p in Mn, and 2s in O) frozen at their atomic reference states. Plane waves were cutoff above a kinetic energy of 520 eV, and a $5 \times 4 \times 5$ **k**-point mesh was employed for the LMO unit cells. All relaxed structures fulfil a convergence criterion of less than 0.01 eV/Å, for both ionic forces and volume-normalised stresses (as standard in VASP).

DFT has known shortcomings in the prediction of the electronic structure of materials with localised electronic states.[51,59,70] A typical example are the bands derived from Mn d orbitals in $LaMnO_3$: the errors can be corrected to various extents by employing Hubbard-U-type corrections to account for intra-atomic Coulomb interactions in the DFT+U approach.[51,59,177]

Both U_{eff} and $U|J$ DFT+U methodologies add HF-type corrections to the DFT total energy that act on a local sub-space of atomic-like orbitals. For DFT+U_{eff}, the total energy with occupation ($f_{i\sigma}$) correction is given by

$$E_{\text{DFT}+U_{\text{eff}}} = E_{\text{DFT}} + \frac{U_{\text{eff}}}{2} \sum_{at} \sum_{i\sigma} (f_{i\sigma} - f_{i\sigma}^2) \,, \tag{75}$$

and for DFT+$U|J$ by

$$\begin{aligned} E_{\text{DFT}+U|J} &= E_{\text{DFT}} + E_{\text{corr}} \\ &= E_{\text{DFT}} + \frac{U_{\text{eff}}}{2} \sum_{at} \sum_{i\sigma} (f_{i\sigma} - f_{i\sigma}^2) \; + \\ &\quad \frac{1}{2} \sum_{\sigma\sigma',ij} \mathrm{C}_{ij}^{\sigma\sigma'} f_{i\sigma} f_{j\sigma'} - \Delta \mathrm{X}_{ij}^{\sigma} f_{i\sigma} f_{j\sigma} \delta_{\sigma\sigma'} \,. \end{aligned} \tag{76}$$

The energy eigenvalue splitting in the U_{eff} scheme is solely occupation dependent, while the $U|J$ scheme includes two additional terms proportional to J

$$\Delta\epsilon_{\sigma}^{\text{corr}} = U_{\text{eff}} \cdot \left(\frac{1}{2} - f_{\sigma} \right) + J \cdot \mathrm{A}^{\sigma} f_{\sigma} + J \cdot \mathrm{B}^{\sigma} f_{\bar{\sigma}} \,, \tag{77}$$

where $\bar{\sigma}$ represents the opposite spin to σ. In the unitless intra-orbital exchange matrices, A^{σ} and B^{σ}, the multipole Coulomb and exchange interactions inside $\mathrm{C}_{ij}^{\sigma\sigma'}$ and $\Delta\mathrm{X}_{ij}^{\sigma}$ are factorised into same and opposite-spin interactions - for explicit definition of these matrices, and numerical matrix elements in an e_g-t_{2g} basis, see Appendix A.1.

The U_{eff} and $U|J$ formulations are discussed in detail in Chapter 4 and Appendix A.1, but in short the DFT+U methodology permits the description of electron localisation phenomena. This stems from HF-type physics and the related removal of self-interaction error which is essential to enable long-range ordering (of orbital, spin, charge, *etc.*

degrees of freedom).[70] For Mn in LMO, delocalised s and p orbitals typify the weakly correlated electronic states successfully described by DFT, while the localised Mn d states require the $+U$ correction. In the DFT+U_{eff} approach, U_{eff} provides occupation-dependent corrections to DFT, while the DFT+$U|J$ approach adds further degrees of explicit spatial/orbital dependent corrections.

In particular on-site exchange corrections of the $U|J$ variety in Equation 77 are most relevant to materials with strongly interacting electrons with an explicit spatial or orbital symmetry dependence,[176] for example, Fe-based superconductors,[200] heavy fermion metals,[201] non-collinear magnetic materials,[40,202] and orbitally ordered materials in which Hund's coupling is critical to establishing the correct insulating or metallic character.[203] The $U|J$ corrections to the LDA/GGA density functionals provide a basis for further energy splitting of d orbitals (and related symmetry breaking and orbital polarisation) on top of splittings due to spin exchange and/or crystalline geometrical distortions already present at the LDA or GGA level. Although the anisotropic Hubbard corrections to DFT have successfully been used to describe manganese oxides in the past,[3,40,296] our work is the first explicit calculation of the $U|J$ exchange matrix elements and anisotropic splitting for $LaMnO_3$.

In our work, our global coordinate system is chosen to align the orthogonal $x', y,' z'$ axes along the LMO unit cell (a, b, c) vectors. A local x, y, z basis for each Mn is defined by aligning the local axes with the Mn-O bonds of each tilted MnO_6 octahedron (see Figures 54 and 58): the local x axis is chosen along the shortest Mn-O bond (strongly JT active), the local y axis along the intermediate length Mn-O bond (apical and non-JT active), and the local z axis is along the longest Mn-O bond (strongly JT active). The use of this local basis is more convenient for analysis of the electronic states and occupancies. The transformation from global to local coordinates is performed for each relaxed geometry by employing a direct polynomial-based transformation of orbitals, detailed in Chapter 5.1.3 and Appendix B.4.

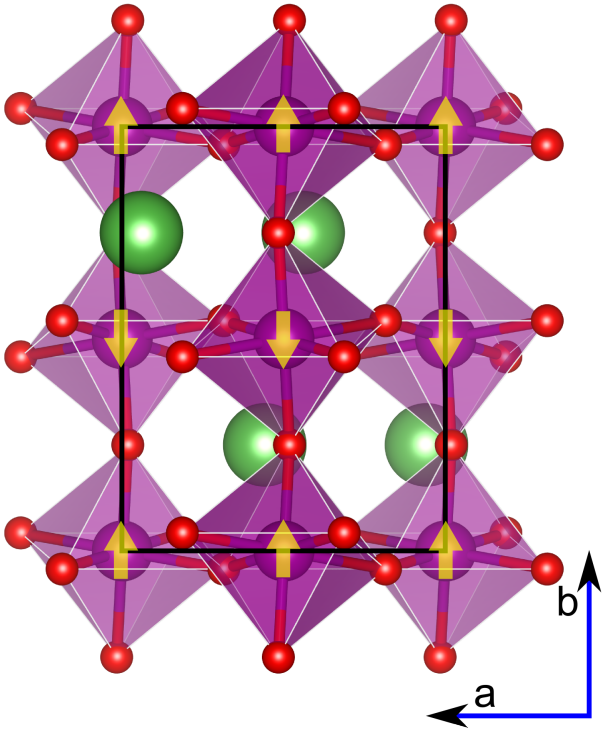

Figure 54: (001) face of the $LaMnO_3$, with A-type AFM spin ordering. Mn in purple, La in green and O in red. Arrows indicate direction of spin polarisation on Mn ions.

10.3 RESULTS

At 750 K LMO undergoes a structural phase transition, transforming from cubic to orthorhombic symmetry. Under ambient conditions the orthorhombic perovskite has a paramagnetic spin structure. Below the Néel temperature of $T_N \approx 140$ K,[308] LMO is an insulator with A-type anti-ferromagnetic (A-AFM) spin ordering.

The reported experimental band gaps in LMO cover a range of values, depending on whether the gap is determined from measurements on conductivity (0.24 eV),[48] optical absorption (1.1 eV),[309] photoemission (1.7 eV),[310] optical conductivity (1.9 eV),[20] or resonant Raman spectroscopy (2 eV).[311] As DFT provides the fundamental gap (up to XC errors), we consider as a point of reference to experiment the 1.7 eV photoemission gap measured by Saitoh *et al.*.[310] We note that recent computational work by Lee *et al.*[312] predicts a direct gap of 1.1 eV, in agreement with the optical absorption gap of 1.1 eV measured by Arima *et al.*.[309] However as LMO is an indirect insulator, and also because optical measurements include energy gap renormalisation

due to electron-hole electrostatic effects, we believe the most reliable comparisons should be made between a benchmark indirect experimental gap (e.g. the 1.7 eV Saitoh photoemission gap)[310] and the indirect DFT gap.

Calculations here concern the low T orthorhombic *Pnma* structure of LMO shown in Figure 54. In the experimental literature, the lattice parameters measured by neutron powder and X-ray diffraction have been reported as $a = 5.736$ Å, $b = 7.703$ Å and $c = 5.540$ Å.[19] To support the A-AFM ordering in LMO, the Mn d^4 electrons exchange anisotropically: FM coupling exists between Mn in $\{010\}$ planes while AFM coupling exists between successive planes along $[010]$. One of our main practical considerations here is to reproduce the above experimental description. To do this, DFT calculations are first performed with different levels of Coulombic localisation.

10.3.1 *Description of $LaMnO_3$ using DFT+U*

Previous work has applied the single-term U_{eff} approach to calculations on bulk $LaMnO_3$.[36,138,305,313] The failure of this approach to *simultaneously* describe the energy gap, structure and magnetism drive us to systematically examine the U_{eff} method. These initial results also provide context for the more sophisticated $U|J$ method and analysis of its merits and behaviour below.

10.3.1.1 *Experimental $LaMnO_3$ structure via* DFT+U_{eff}

Standard LDA (PZ81) and GGA (PBEsol) without on-site corrections ($U_{\text{eff}} = 0$ eV) both successfully stabilise the low temperature experimental A-AFM ordering as shown in Table 9. However this is essentially where the success ends. As noted previously, both LDA and GGA are often unable to produce significant orbital splitting (beyond some aspects due to spin exchange and structural distortion) and also exaggerate electron delocalisation due to inexact exchange (or equivalently lack of self-interaction correction). This inevitably results in a qualitatively incorrect electronic structure with a seriously underestimated band gap: both LDA and GGA with $U_{\text{eff}} = 0$ eV yield band gaps that are far too small compared to experiment.

Table 9: LDA+U_{eff} and GGA+U_{eff} results for the band gap Δ^{Gap} (in eV), for the A-AFM and FM phases, and the total energy difference $\Delta E = E^{\text{A-AFM}} - E^{\text{FM}}$ per formula unit of $LaMnO_3$. The crystal structure is held fixed at the experimental geometry.

U_{eff} (eV)	LDA (PZ81)			GGA (PBEsol)		
	$\Delta^{\text{Gap}}_{\text{AFM}}$	$\Delta^{\text{Gap}}_{\text{FM}}$	ΔE (meV)	$\Delta^{\text{Gap}}_{\text{AFM}}$	$\Delta^{\text{Gap}}_{\text{FM}}$	ΔE (meV)
0	0.0	0.0	−22	0.2	0.0	−13
2	0.5	0.0	−5	0.6	0.0	1
4	1.0	0.0	4	1.0	0.0	8
6	1.3	0.1	10	1.3	0.1	14
8	1.4	0.2	14	1.4	0.2	17

Increasing U_{eff} stabilises the occupied ($f_{i\sigma} \gtrapprox \frac{1}{2}$) eigenstates and drives orbital occupations toward binary polarisation: filled states become more filled and empty states more empty. For example, increasing U_{eff} from 0 to 8 eV in GGA calculations results in the following change in occupancies in the Mn d manifold:

$$(f_\sigma | f_{\bar{\sigma}}) = \left(\begin{array}{c|c} 0.65 & 0.22 \\ 0.73 & 0.26 \\ 0.93 & 0.11 \\ 0.93 & 0.10 \\ 0.93 & 0.09 \end{array}\right) \rightarrow \left(\begin{array}{c|c} 1.00 & 0.10 \\ 0.57 & 0.17 \\ 0.98 & 0.04 \\ 0.97 & 0.03 \\ 0.97 & 0.04 \end{array}\right), \tag{78}$$

where the ordering of orbitals in the local basis is $\begin{pmatrix} 3z^2 - r^2 \\ x^2 - y^2 \\ xy \\ yz \\ xz \end{pmatrix}$.

The Hubbard limit of very large U_{eff} typically favours FM coupling in LMO,[53] and Table 9 confirms this. The primary reason is that increasing U_{eff} kills the superexchange mechanism, which scales as $\sim t^2/U_{\text{eff}}$ where t is the effective Mn-Mn hopping, and this mechanism underlies the stability of A-AFM ordering in LMO. As a result, e_g double-exchange is relatively strengthened and we find FM ordering.

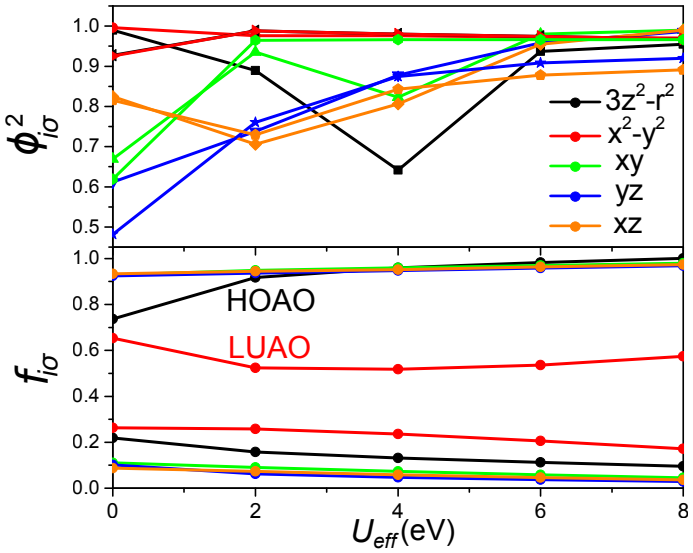

Figure 55: Occupancy polarisation increases with the value of U_{eff}, pushing the Mn d^4 eigensystem of A-AFM $LaMnO_3$ toward the atomic limit. Occupancy eigenvalues ($f_{i\sigma}$) and the squared value of the characteristic (largest) eigenvector contribution ($\phi^2_{i\sigma}$), from the diagonalised density matrix.

Critically, Table 9 shows that a large U_{eff} value is required to open a satisfactory energy gap. Unfortunately this situation results in a trade-off between having the correct gap *or* correct magnetism.

10.3.1.2 *Relaxed $LaMnO_3$ structure via* DFT+U_{eff}

When we permit the structure of LMO to fully relax during the calculation, we find the results in Table 10. We see that having a non-zero U_{eff} improves the crystal geometry and the electronic structure description for both GGA and LDA. Particular improvements are for the large erroneous distortion in a (insufficient orthorhombic character) and the opening of the band gap. Figure 56 and Table 10 show that the band gap increases roughly linearly with U_{eff} at first but then tails off at higher U_{eff}. The ineffectiveness of U_{eff} at high values (see Figure 56) occurs as a result of the partial e_g occupation, evident in Figure 55. For example, partial $x^2 - y^2$ occupation damps the impact of U_{eff} the energy eigenvalue splittings since $\Delta\epsilon_{x^2-y^2\sigma} = U_{\text{eff}}\left(\frac{1}{2} - f_{x^2-y^2\sigma}\right) \approx 0$ for $f_{x^2-y^2\sigma} \approx \frac{1}{2}$. Partial e_g occupation occurs due to the partial covalency of the Mn-O bond - the d manifold is not isolated but connected to the rest of the system *via* hybridisation to the O $2p$ orbitals.

Table 10: Band gap Δ^{Gap}, total energy difference $\Delta E = E^{\text{A-AFM}} - E^{\text{FM}}$ per formula unit, and percentage errors with respect to experiment for lattice parameters and unit cell volume of fully relaxed A-AFM bulk $LaMnO_3$.

	U_{eff} (eV)	Δ^{Gap} (eV)	Δ^{a} (%)	Δ^{b} (%)	Δ^{c} (%)	$\Delta^{\text{Vol.}}$ (%)	ΔE (meV)
LDA	0	0.00	−5.8	−3.0	−1.2	−9.8	54
	2	0.22	−2.9	−1.6	−1.1	−5.5	52
	4	0.81	−1.8	−1.6	−1.1	−4.4	25
	6	1.13	−1.5	−1.0	−1.0	−3.5	13
	8	1.23	−1.4	−0.6	−1.0	−3.0	19
GGA	0	0.00	−3.5	−0.6	−0.3	−4.4	34
	2	0.48	−0.6	−0.8	−0.5	−1.9	47
	4	0.92	−0.0	−0.5	−0.3	−0.9	19
	6	1.10	0.2	−0.1	−0.3	−0.1	19
	8	1.08	0.4	0.4	−0.2	0.6	27

Although adding U_{eff} to GGA and LDA produces similar band gaps as per Table 10, the GGA+U_{eff} geometry is preferable. Overall a high value of $U_{\text{eff}} \sim 6$ eV, correcting the GGA formalism, provides on balance the best gap/structure combination. Again, the pronounced failure of U_{eff} evident is its inability to predict the correct magnetic ordering at the U_{eff} level required to correct the structure and the band gap.

10.3.1.3 *Experimental $LaMnO_3$ structure via* DFT+$U|J$

Following the failure of the U_{eff} scheme in both single-point and relaxed geometry calculations, we turn to the DFT+$U|J$ methodology. The U_{eff} results conveniently suggest a reasonable starting point: since $U_{\text{eff}} = U - J$, a $U|J$ correction with a magnitude of approximately $U - J \approx 6$ eV is appropriate. Results in Table 11 are for bulk LMO at the experimental structure, and sample J from 0 to 3 eV in conjunction with $U = 6$ eV and 8 eV. Increasing J for a fixed value of U stabilises A-AFM ordering and enhances orbital splitting which further opens the band gap. Orbital splittings due to the U_{eff} are "isotropic" in that they are based solely on the magnitude of the occupation. The marked improvement by the $U|J$ method emphasises the importance of explicit spatial exchange anisotropy in the A-AFM Mn d manifold. The results in Table 11 are encouraging, but since distortion of the lattice is critical

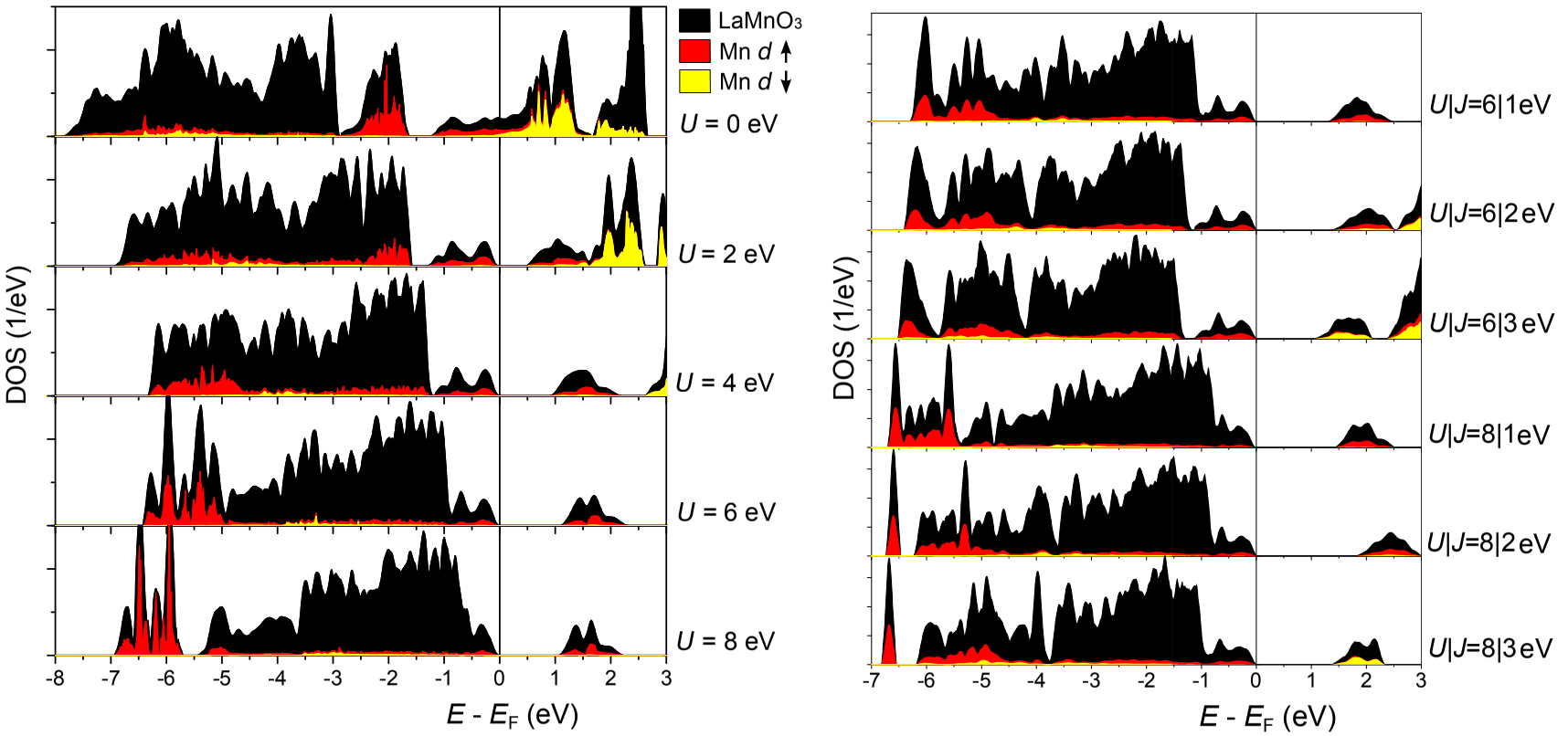

Figure 56: Density of states versus energy ($E - E_F$), corrected by U_{eff} (*left*) and $U|J$ (*right*), for fully relaxed A-AFM $LaMnO_3$. Black curves show the total $LaMnO_3$ density of states (DOS/eV), while red and yellow curves show majority and minority spin channels for Mn *d* states.

Table 11: Results from GGA+$U|J$ for the experimental geometry of bulk $LaMnO_3$. Band gaps Δ^{Gap} are in eV for each magnetic state, and $\Delta E = E^{\text{A-AFM}} - E^{\text{FM}}$ is the total energy difference per formula unit between the two magnetic phases.

$U\|J$ (eV)	$\Delta^{\text{Gap}}_{\text{A-AFM}}$ (eV)	$\Delta^{\text{Gap}}_{\text{FM}}$ (eV)	ΔE (meV)
6|0	1.3	0.1	14
6|1	1.3	0.2	6
6|2	1.2	0.4	−10
6|3	0.6	0.2	−39
8|0	1.4	0.2	17
8|1	1.5	0.4	11
8|2	1.6	0.8	−2
8|3	1.0	0.5	−32

in A-AFM,[139] the trends observed must be verified by fully relaxing ionic positions and lattice parameters, which we report on next.

10.3.1.4 *Relaxed $LaMnO_3$ structure via* DFT+$U|J$

Table 11 displays key data for fully relaxed bulk $LaMnO_3$ using the DFT + $U|J$ framework. Relaxed results largely echo the experimental structure results above indicating that, for A-AFM LMO the most appropriate $U|J$ combination is $U = 8$ eV and $J = 2$ eV, although other choices are reasonable. The $U|J = 8|2$ eV combination provides agreement, with both experimental observations, and results reported from computationally expensive many-body Green's function screened Coulomb interaction calculation (GW) calculations.[19,20,314] Volume errors below 1 % improve on previous work,[305] and the error in energy gap is small at approximately 5 % (0.07 eV). In addition the A-AFM ordering is stabilised against AFM ordering which was previously seen as a missing ingredient.[305,306] The improvements in LMO description depend on the intra-orbital exchange description - the Mn d state Hund's coupling interaction is quantified next.

Table 12: Fully relaxed $LaMnO_3$ results based on GGA+$U|J$. Band gaps Δ^{Gap}, lattice parameter errors, and total energy differences between the A-AFM and FM magnetic phases $\Delta E = E^{\text{A-AFM}} - E^{\text{FM}}$ per formula unit are listed.

$U\|J$ (eV)	A-AFM					ΔE (meV)
	Δ^{Gap} (eV)	Δ^{a} (%)	Δ^{b} (%)	Δ^{c} (%)	$\Delta^{\text{Vol.}}$ (%)	
6|0	1.1	0.4	−0.1	−0.4	0.0	19
6|0.5	1.2	0.6	−0.4	−0.4	−0.2	14
6|1	1.3	0.9	−0.7	−0.5	−0.3	7
6|1.5	1.4	1.2	−0.9	−0.6	−0.3	−1
6|2	1.4	0.8	−1.2	0.1	−0.4	−10
6|2.5	1.3	1.8	−1.3	−0.8	−0.2	−21
7|0	1.2	0.5	0.1	−0.3	0.3	23
7|0.5	1.3	0.7	−0.2	−0.4	0.2	17
7|1	1.4	0.9	−0.5	−0.5	0.0	11
7|1.5	1.5	1.2	−0.7	−0.5	−0.1	3
7|2	1.6	1.6	−1.0	−0.7	0.0	−6
7|2.5	1.5	1.9	−1.2	−0.7	−0.1	−17
8|0	1.1	0.5	0.4	−0.3	0.6	27
8|0.5	1.2	0.6	0.1	−0.3	0.4	21
8|1	1.4	1.0	−0.2	−0.5	0.3	15
8|1.5	1.6	1.2	−0.5	−0.5	0.1	7
8|2	1.8	1.5	−0.8	−0.6	0.1	−2
8|2.5	1.7	1.7	−1.0	− − 0.6	0.1	−14

10.3.2 *Explicit exchange anisotropy in Mn^{3+}*

Strong on-site Coulomb repulsion is the central theme in paradigms of "Mottness" and electron localisation. However, the importance of Hund's coupling (intra-orbital exchange) in materials with partial d and f shell occupations has recently been highlighted.[315] In this section, we attempt to understand the nature of Hund's coupling in LMO, by examining the effects of the on-site exchange terms as defined in Chapter 4. We explore why the $U|J$ methodology can provide an improved description of the LMO band gap and magnetic state. We employ a simple model where we focus only on the occupancies of the Mn^{3+} d^4 manifold in order to isolate the effect of the J exchange parameter (and related physics) on the Mn d states as per Equation 77. Majority spin ${t_{2g}}^3$ states are generally fully occupied due to the strong exchange splitting between spin channels, and as is well known, increasing U increases occupancy polarisation. However the nature of anisotropic interactions in the Mn d shell due to J is less well understood, particularly with respect to the polarisation of the ${e_g}^1$ occupation into $3z^2 - r^2$ or $x^2 - y^2$ (or some mix of the two).

We begin with three model ${e_g}^1$ occupations, $\pi^{e_g\sigma} = 0, \pm 1$, in an attempt to pinpoint what J really does and understand the nature of Hund's coupling in different limits. As a reminder, $\pi^{e_g\sigma}$ is the e_g occupancy polarisation as defined in Equation 74. After examining these model systems, we will consider the effect of J in the actual calculations where we use the calculated *ab initio* occupations together with our analytical rewriting of the $U|J$ energy function and eigenvalue corrections. As explained above, the e_g and t_{2g} group terms discussed correspond to the local octahedral basis (*i.e.*, post rotation as per Chapter 5.1.3 and Appendix B.4).

10.3.2.1 *Anisotropic exchange for model orbital occupations*

To illustrate the anisotropic effects of the J terms in the $U|J$ schema, we begin with a set of model occupancies where we fix the formal occupation of Mn^{3+} (d^4) but vary the orbital polarisation.

A $\pi^{e_g\sigma} = +1$ model polarisation corresponds to a single hole on the majority spin $3z^2 - r^2$ site (*i.e.*, $f_{x^2-y^2\sigma} = f_{t_{2g}\sigma} = 1$, $f_{3z^2-r^2\sigma} = 0$ and $f_{\bar{\sigma}} = 0$). Based on Equation 77, the added effect of the exchange J terms

is to create additional energy splittings, beyond simple occupancy polarisation proportional to U_{eff}, given by

$$\pi^{e_g\sigma} = +1 \;:\quad (\triangle\epsilon_\sigma|\triangle\epsilon_{\bar{\sigma}}) = J \cdot \left(\begin{array}{c|c} 0.00 & -1.14 \\ 0.52 & 0.63 \\ 0.52 & 0.63 \\ -0.52 & -0.06 \\ -0.52 & -0.06 \end{array}\right). \tag{79}$$

The opposite polarity, $\pi^{e_g\sigma} = -1$, corresponds to a single hole on the majority spin $x^2 - y^2$ site (that is, $f_{3z^2-r^2\sigma} = f_{t_{2g}\sigma} = 1$, $f_{x^2-y^2\sigma} = 0$ and $f_{\bar{\sigma}} = 0$). This results in the following exchange energy splittings

$$\pi^{e_g\sigma} = -1 \;:\quad (\triangle\epsilon_\sigma|\triangle\epsilon_{\bar{\sigma}}) = J \cdot \left(\begin{array}{c|c} 0.52 & 0.63 \\ 0.00 & -0.14 \\ -0.86 & 0.29 \\ 0.17 & 0.40 \\ 0.17 & 0.40 \end{array}\right). \tag{80}$$

Removing the polarisation, $\pi^{e_g\sigma} = 0$, the single hole is equally spread over the two majority spin e_g sites ($f_{e_g\sigma} = 0.5$ and $f_{t_{2g}\sigma} = 1$ and $f_{\bar{\sigma}} = 0$). This leads to the splittings

$$\pi^{e_g\sigma} = 0 \;:\quad (\triangle\epsilon_\sigma|\triangle\epsilon_{\bar{\sigma}}) = J \cdot \left(\begin{array}{c|c} 0.26 & -0.26 \\ 0.26 & -0.26 \\ -0.17 & 0.17 \\ -0.17 & 0.17 \\ -0.17 & 0.17 \end{array}\right). \tag{81}$$

To visualise these results, we display a schematic showing these splittings in these three cases of $\pi^{e_g\sigma} = 0, \pm 1$ in Figure 57 where the corrections due to both U and J are shown.

These model results together with the Figure 57 point out that the effect of the J terms is explicitly anisotropic, and its anisotropy and precise value depends on the orbital polarisation - *i.e.* is cooperative with the direct Coulomb term. The anisotropy exists across both the

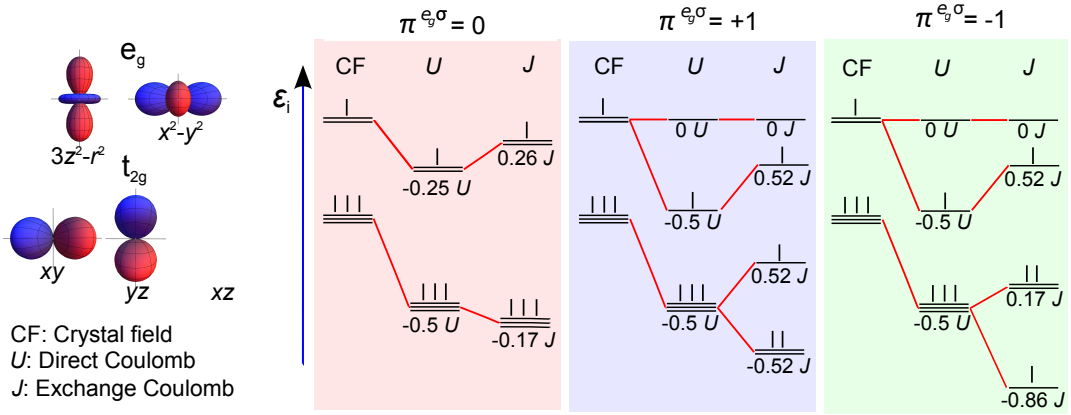

Figure 57: The occupation of states is represented in the model Mn^{3+} d^4 manifold (majority spin only). The schematic qualitatively shows how orbital degeneracy is broken by octahedral crystal field (CF), Coulomb repulsion U_{eff} (U in the figure) and exchange J following Equation 77. Each vertical bar represents one unit of electron occupation, while the energy scale is qualitative. $\pi^{e_g\sigma}$ is defined in Equation 74 for which three limits are examined: $\pi^{e_g\sigma} = 0$ ($f_{x^2-y^2\sigma} = f_{3z^2-r^2\sigma} = 0.5$), $\pi^{e_g\sigma} = +1$ ($f_{x^2-y^2\sigma} = f_{3z^2-r^2\sigma} + 1 = 1$), and $\pi^{e_g\sigma} = -1$ ($f_{x^2-y^2\sigma} + 1 = f_{3z^2-r^2\sigma} = 1$).

magnetic quantum number and spin channels (σ and $\bar{\sigma}$). We now discuss these three cases in more detail.

When we have full e_g orbital polarisation, *i.e.* $\pi^{e_g\sigma} = \pm 1$, each polarity produces a unique splitting pattern where the magnitude of anisotropy depends on the sign of $\pi^{e_g\sigma}$. This is despite the fact that $3z^2 - r^2$ and $x^2 - y^2$ states both have e_g symmetry: as we can see that occupying each one (separately) splits the t_{2g} quite differently. This difference is due to fact that the $x^2 - y^2$ state is symmetry related to the t_{2g} states (it is the xy state rotated by $\pi/4$ about the z axis). For example, when $x^2 - y^2$ is fully occupied, the splittings for $x^2 - y^2$ and xy are identical but differ from the other orbitals, but the same is not true when $3z^2 - r^2$ is filled instead. Interestingly $\sum_i \Delta\epsilon_{i\sigma} f_{i\sigma} = 0$ when $\pi^{e_g\sigma} = \pm 1$: this indicates that neither polarisation is energetically preferred by intra-orbital J terms.

With zero e_g orbital polarisation, *i.e.* $\pi^{e_g\sigma} = 0$, we find that this degeneracy inhibits anisotropy from the J terms: the splittings *within* each t_{2g} and e_g manifold is isotropic for both spin channels. The action of the J terms in this situation is to shift the energies of this manifold *en masse*. Here, $\sum_{i\sigma} \Delta\epsilon_{i\sigma} f_{i\sigma} = -0.26J$ when $\pi^{e_g\sigma} = 0$ compared to zero for $\pi^{e_g\sigma} = \pm 1$. Hence, the anisotropic exchange terms in isola-

tion actually favour degenerate occupancy. This result appears to be counter-intuitive given the importance of J to anisotropy. The resolution is that we have a much larger and dominant direct Coulomb term U that produces orbital polarisation in the first place; the weaker J terms then further enlarge the polarisation and make the system more anisotropic. Table 13 shows this behaviour numerically.

In brief, we see that J acting alone energetically *favours degeneracy*. However, with a strong U term already creating orbital polarisation, the J terms provide the enlarged anisotropic splitting that one finds in the final results of the calculation.

10.3.2.2 *Anisotropic exchange for ab initio orbital occupations*

For the *ab initio* orbital occupations we use the DFT+$U|J = 8|2$ eV calculation results, which yield an occupation-polarised e_g manifold as shown in Table 13. The e_g polarity is found to be orbitally ordered across the LMO unit cell as shown in Figure 58. We now examine this situation in more detail.

The Mn d occupancies from the $U|J = 8|2$ eV method with relaxed geometry are

$$(f_\sigma|f_{\bar{\sigma}}) = \left(\begin{array}{c|c} 0.99 & 0.10 \\ 0.41 & 0.33 \\ 0.98 & 0.06 \\ 0.96 & 0.04 \\ 0.97 & 0.05 \end{array}\right). \tag{82}$$

These occupancies correspond to $\pi^{e_g\sigma} = -0.41$ (from $f_{3z^2-r^2\sigma} = 0.99$ and $f_{x^2-y^2\sigma} = 0.41$). The Mn d shell obviously has more electrons than the model system above which was based on formal occupancies for Mn^{3+}. Again, we note that this increase is due to hybridisation of the Mn d orbitals with the neighbouring O $2p$ orbitals which admixes some Mn d into the low-energy occupied valence states and increases the electron count. Put differently, itineracy due to the kinetic energy minimisation competes with Hubbard-esque Coulomb repulsion and we reach a balance. Numerically, for $U|J = 8|2$ eV, the oxidation state based on the above Mn d occupations can be calculated to be 2.12+. An

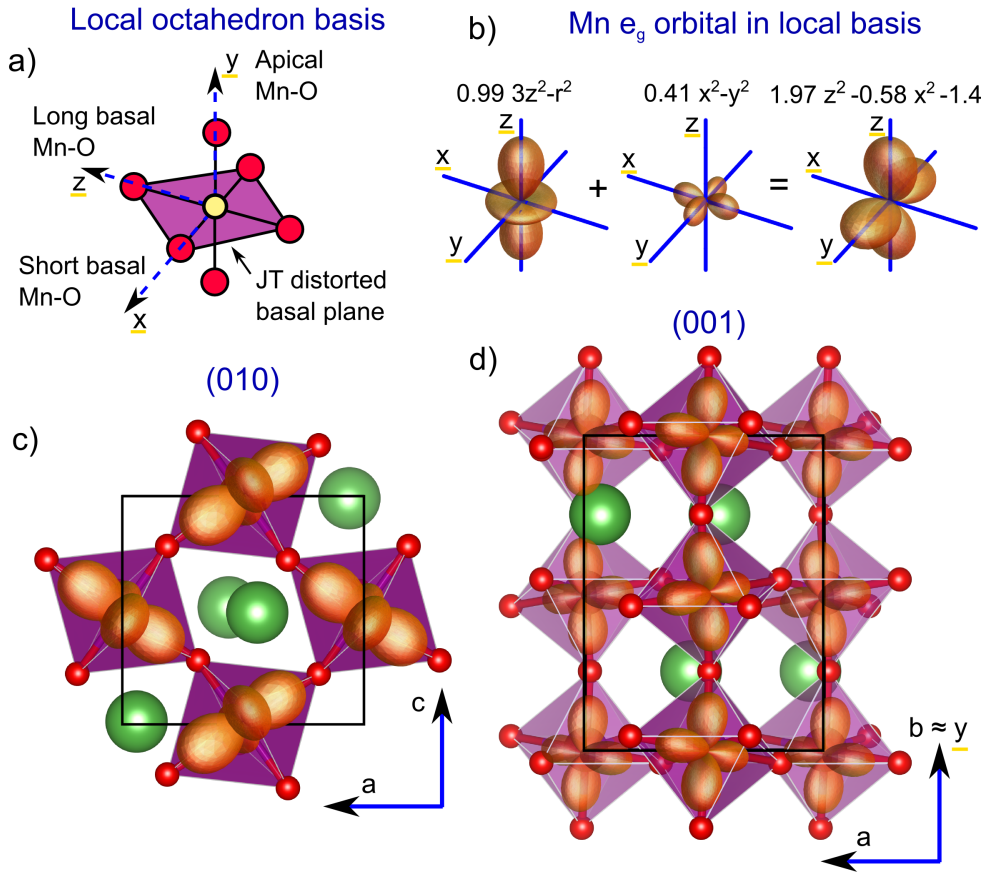

Figure 58: Orbitals in the $LaMnO_3$ unit cell from a $U|J = 8|2$ eV calculation. a) MnO_6 octahedron with Jahn-Teller distorted plane and local basis vectors labelled. b) Visualisation of the occupation of the $3z^2 - r^2$ and $x^2 - y^2$ states in the rotated basis of the density matrix as well as their superposition for the total local e_g occupancy (plotting the occupation times the orbital expressed in spherical harmonics). c) The ordering of the occupied e_g shell ($1.97z^2 - 0.58x^2 - 1.4y^2$) in the (010) Jahn-Teller distorted FM coupled plane. d) The ordering of the occupied e_g shell in the (001) plane with AFM coupling along b. Note x, y, z is the local octahedron basis, and a, b, c lattice vectors correspond to x', y', z' global (pre-rotation) calculation basis.

alternative or complementary Bader charge picture yields an oxidation state of 1.68+, still less than the formal 3+.

The $U|J = 8|2$ eV occupancies of Equation 82 result in additional energy splitting beyond splitting from U_{eff} alone:

$$(\triangle\epsilon_\sigma|\triangle\epsilon_{\bar{\sigma}}) = J \cdot \left(\begin{array}{c|c} 0.15 & 0.20 \\ 0.30 & -0.65 \\ -0.41 & -0.06 \\ -0.03 & 0.18 \\ -0.01 & 0.20 \end{array}\right) . \tag{83}$$

The e_g occupancy polarisation of the $U|J = 8|2$ eV calculation is considerably weaker than the previous model cases. Nevertheless, it is large enough to drive significant anisotropic exchange splittings present in Equation 83. For example, the splittings are anisotropic within the majority spin t_{2g} manifold: the xy state is pushed down by approximately $0.4J$ compared to the other two t_{2g} states. Within the e_g manifold, the fully occupied $3z^2 - r^2$ state is pushed up by $0.15J$ while the partially occupied $x^2 - y^2$ state is pushed up considerably more by $0.30J$.

The direct Coulomb interaction U obviously increases $\pi^{e_g\sigma}$, as expected from the standard instability condition for orbital polarisation,[69,305,316]

$$U_{\text{eff}} \times D^\sigma(E_F) \gg 1 ,$$

where $D^\sigma(E_F)$ is the density of states in the σ spin channel at the Fermi level. The origin of the monotonic relation between $\pi^{e_g\sigma}$ and J, shown in Table 13, is less obvious as J is naïvely expected to drive the electronic structure away from orbital polarisation as $U_{\text{eff}} = U - J$. However $\pi^{e_g\sigma}$ does increase with J, for the above-noted reason that J alone may favour orbital degeneracy but J is strongly anisotropic when in conjunction with a large U value, resulting in the unequal upward "push" of the two e_g orbitals with increasing J. That J and $\pi^{e_g\sigma}$ are so strongly coupled in this material is interesting, as band gap, JT distortions, and inter-site magnetic couplings all depend on $\pi^{e_g\sigma}$.

Table 13: Orbital occupation polarisation, $\pi^{e_g\sigma}$, for fully relaxed $LaMnO_3$ within the U_{eff} and $U|J$ approaches. Majority spin are labelled σ and minority spin are $\bar{\sigma}$.

Correction (eV)	Like-spin polarisation, $\pi^{e_g\sigma}$	Opposite-spin polarisation, $\pi^{e_g\bar{\sigma}}$
$U_{\text{eff}} = 0$	0.06	0.08
$U_{\text{eff}} = 8$	-0.27	0.25
$U\|J = 8\|1$	-0.33	0.41
$U\|J = 8\|2$	-0.41	0.54
$U\|J = 8\|3$	-0.52	0.65

As first examined by Kugel and Khomskiĭ,[58] $e_g{}^1$ occupation polarisation (*i.e.*, an electron-electron JT degeneracy breaking) enhances virtual superexchange interactions, relative to kinetic exchange interactions such as FM double-exchange. This competition between superexchange and double-exchange is observed in the LMO magnetic ground state, which varies according to the magnitude of $\pi^{e_g\sigma}$ (e_g occupancy polarisation). $\pi^{e_g\sigma}$ increases with J, which explains the flip in long range magnetic ordering of the ground state from FM to A-AFM as the intra-orbital parameter J is increased.

At $J = 2$ eV the value of $\pi^{e_g\sigma}$ in Table 13 is large enough to stabilise the correct A-AFM ordering (as per Table 12). The $U|J = 8|2$ eV A-AFM ground state in Figure 54 corresponds to a $0.99(3z^2 - r^2) + 0.41(x^2 - y^2)$ e_g occupation density in the local octahedral basis. The orbital ordering pattern across the unit cell is shown in Figure 58, and can be rationalised in terms of the Goodenough-Kanamori superexchange rules.[317,318]

The $0.99(3z^2 - r^2) + 0.41(x^2 - y^2)$ e_g occupation density can be rewritten as $1.97z^2 - 0.58x^2 - 1.4y^2$. This expression shows the anisotropy in the e_g state, in particular between the z and x directions in the octahedron: the z^2 contribution is much larger than x^2, as per Figure 58 b). Each octahedral frame in the ac plane is related to its neighbour by a $\pi/2$ rotation about the b lattice vector, so z^2/x^2 anisotropy forms a checker board pattern of e_g partial occupation in the ac plane. Note this corresponds to the "$(\pi, 0, \pi)$" JT long/short Mn-O pattern in the ac plane, as per Figure 58 c). According to the Goodenough-Kanamori

rules, superexchange in the *ac* plane is determined by z^2/x^2 anisotropy in the e_g partial occupation, and results in the FM coupling in the *ac* plane.

The y^2 component of the e_g partial occupation forms occupied stripes pointed along local octahedra y axes, following the b lattice direction (with a small tilt) as in Figure 58 d). The continuous stripes of y^2 character along the b lattice direction correspond to the non-Jahn-Teller Mn-O bonds in this direction. The Goodenough-Kanamori rules determine that the continuous stripe of y^2 character from the e_g partial occupation corresponds to AFM superexchange. The AFM coupling is along the b lattice parameter direction, between the FM coupled *ac* planes. Together the in-plane FM and inter-plane AFM produce the A-AFM ground state of $LaMnO_3$, so our $U|J = 8|2$ eV calculation results are in-line with experiment as well.

If instead the Hund's coupling was weaker (*i.e.*, smaller J), then $\pi^{e_g\sigma}$ would also be smaller. This alters the character of the occupied states in the e_g shell, so that orbital-ordering mediated A-AFM superexchange is reduced relative to other effects such as FM double-exchange. This explains why stabilisation of A-AFM magnetic ordering (see Table 12) is only possible when intra-orbital exchange is large enough. Too small of an intra-orbital exchange interaction is the origin of the incorrect FM ground state found in prior examinations[305,139,306] of LMO using standard DFT.

The improvements in the LMO description through applying exchange corrections reinforce hints by Sawada *et al.*,[305] Solovyev *et al.*[139] and Hashimoto *et al.*,[306] that the correct orbital and magnetic ordering in LMO requires an anisotropic intra-orbital exchange correction to the DFT ground state. In what follows, we discuss further details of the electronic and crystal structure.

10.3.3 *Electronic and structural symmetry breaking*

10.3.3.1 *Orbital order*

It was previously shown that applying Coulomb corrections, such as with $U|J = 8|2$ eV, corrected the LMO electronic, magnetic and

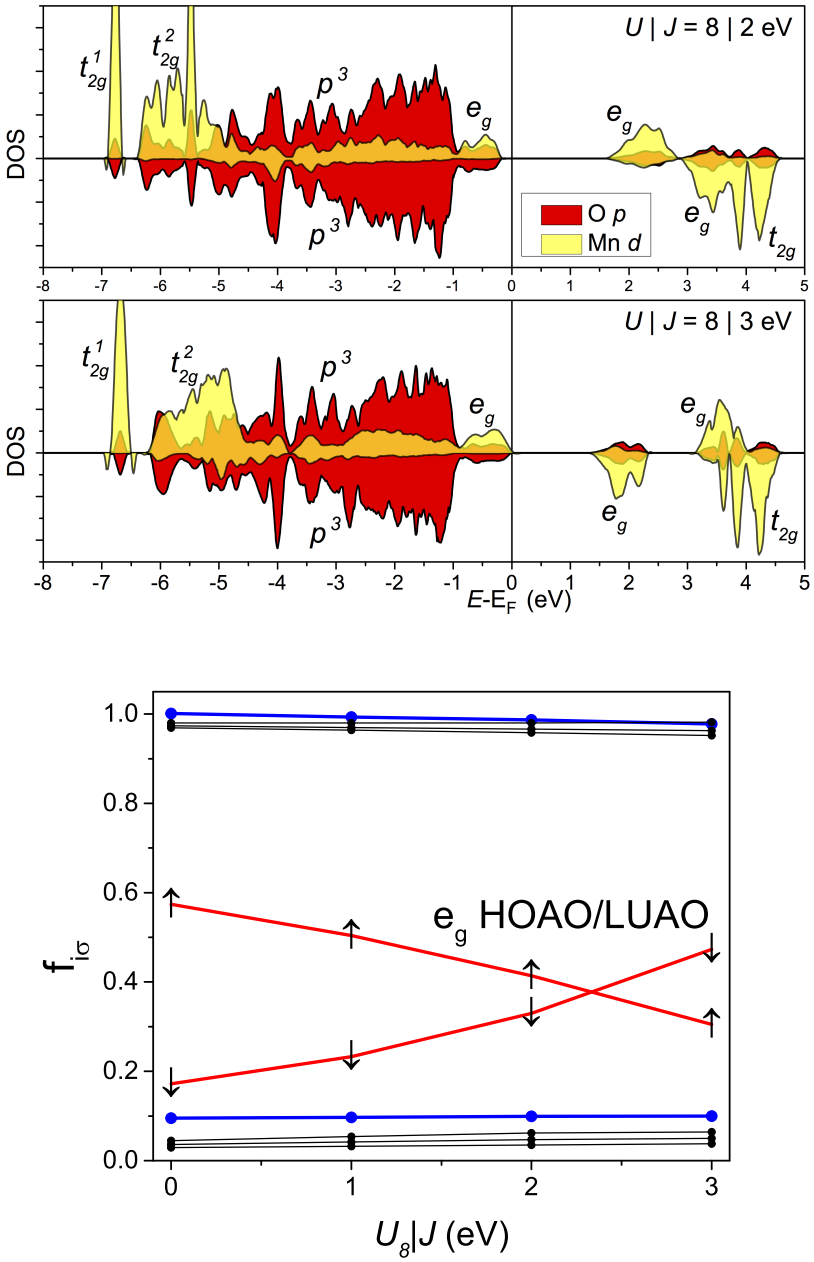

Figure 59: *Top*: Mn d and O p density of states (states/eV) for both spin channels in a single $LaMnO_3$ formula unit, from $U|J = 8|2$ eV and $U|J = 8|3$ eV calculations. *Bottom*: Occupation ($f_{i\sigma}$) for $U|J = 8|0, 1, 2, 3$ eV, showing the spin/occupation polarisation cross-over for e_g occupation at $J \approx 2.4$ eV.

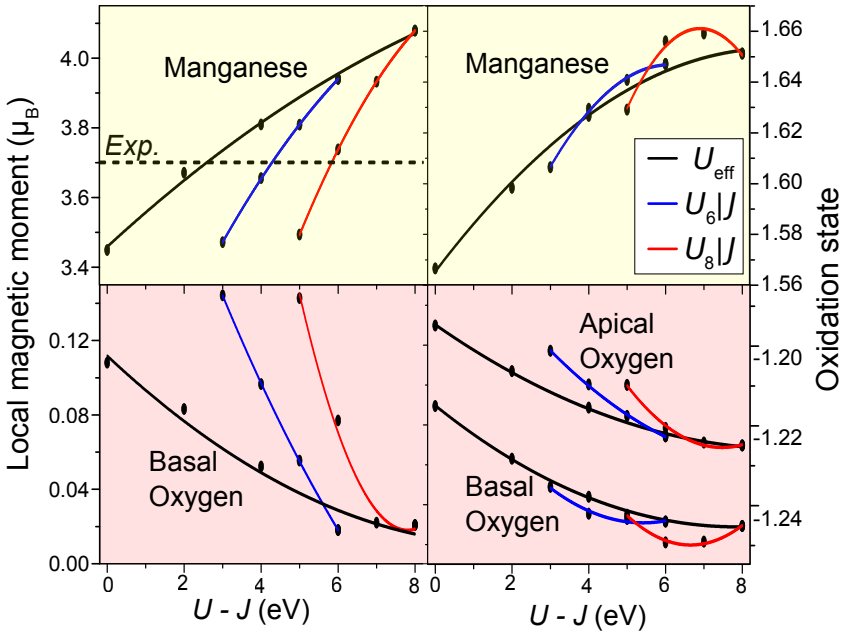

Figure 60: Local magnetic moment and oxidation state within the Bader volumes centred on single Mn cations (*top*) and O anions (*bottom*). Basal O within Jahn-Teller (JT) active (010) *ac* plane, and apical O in the non-JT [010] *b* direction. Calculations from DFT+U_{eff} and DFT+$U|J$ methods, where notation $U_6|J$ and $U_8|J$ indicates U is fixed to 6 eV and 8 eV respectively, while J is varied. The experimental reference local magnetic moment is 3.7 μ_B.[17] Note, the Mn-O-Mn AFM coupling along the 'non-JT' out-of-plane direction does not generate a local magnetic moment for the apical O.

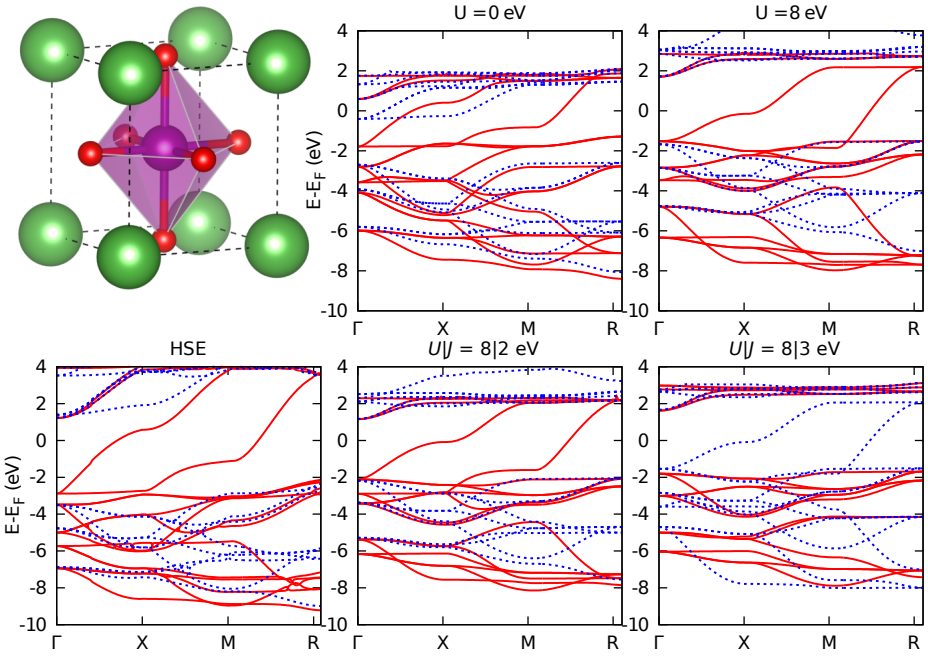

Figure 61: Simplified cubic single formula unit *Pm-3m* $La_1Mn_1O_3$ structure and dispersion compared for HSE,[18] $U_{eff} = 0$ eV and $U_{eff} = 8$ eV, and $U|J = 8|2$ eV and $U|J = 8|3$ eV calculations. Minority spin bands given by dotted blue line.

lattice structure. Further electronic structure details are shown for the LMO DOS in Figure 59 at the $U|J = 8|2$ eV level of correction. In Figure 59 the position of each band in the Mn DOS agree quantitatively with the optical conductivity measurements of Jung *et al.*.[20] Further experimental agreement comes from our $U|J = 8|2$ eV calculated local magnetic moment, which at 3.7 μ_B agrees with Eleman's measurement.[17] The U and J dependence of the local magnetic moments and oxidation states are shown in Figure 60. The high sensitivity of the electronic structure of LMO to perturbations in part underlies its complex phase diagram. This is illustrated by comparing the $U|J = 8|2$ and $U|J = 8|3$ eV DOS in Figure 59, and examining the magnetic state of DOS near the edges of the valence band maximum (VBM) and conduction band maximum (CBM). For $U|J = 8|2$ eV, Hund's rules are obeyed as both VBM and CBM have the same spin state whereas Hund's rules are broken for $U|J = 8|3$ eV. We find that the cross-over occurs at $J \approx 2.4$ eV. In short LMO is fragile in terms of exchange: above $J = 2.4$ eV we have the breakdown of Hund's rules while J below ≈ 1.8 eV incorrectly stabilises the FM rather than A-AFM ground state.

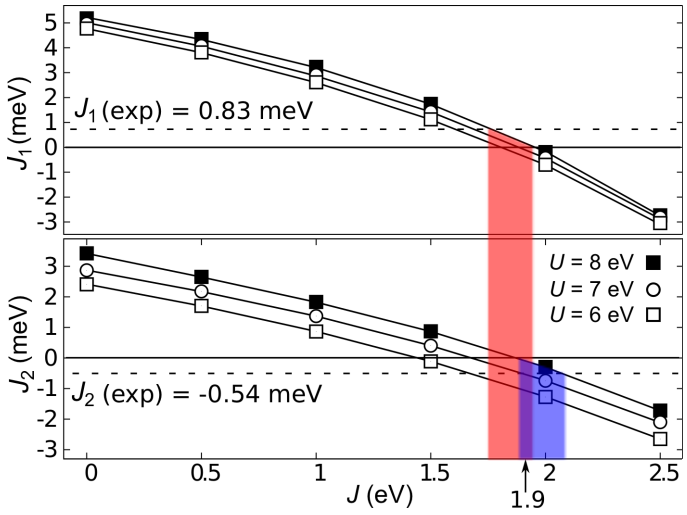

Figure 62: $LaMnO_3$ magnetic coupling constants J_1 and J_2 versus $U|J$ schema Hund's exchange parameter J, for $U = 6$ eV (white squares), $U = 7$ eV (white circles), $U = 8$ eV (black squares). J_1 and J_2 are defined in Equation 84.

In Figure 61 band structures are plotted for a simplified *Pm-3m* cubic unit cell of LMO, with five atoms compared to twenty in the usual *Pnma* unit cell. Plain DFT, DFT+U_{eff},[177] HSE,[18] and DFT+$U|J$[59] with $U|J = 2|3$ eV produce band structures that are qualitatively similar, but with differing degrees of band localisation. The HSE band structure is similar to plain DFT but with majority spin bands stretched out further about E_{F}. For DFT+$U|J$ with $J \gtrsim 3$ eV a qualitatively different band structure is produced, with reversal in the spin polarisation of E_{F}. Again at $J \gtrsim 3$ eV the breakdown in Hund's rules occurs for *Pm-3m* structure as with *Pnma*.

In the simplified *Pm-3m* cubic unit cell, octahedral tilts and rotations are not present, raising the LMO structural symmetry such that JT distortions are necessarily neglected too. Irrespective of the orbital splitting generated by local crystal field, on-site direct (U), intra-orbital anisotropic exchange (J), screened non-local exchange (Fock), and HEG spin exchange and correlation effects (*via* the XC functional), no gap is present in Figure 61. The emphasises the need for cooperation between electronic means of splitting and relaxation of structural distortion modes.

10.3.3.2 *Magnetic coupling constants*

The magnetic coupling constants in LMO have been extracted by Muñoz *et al.*[319] amongst others,[139,306,312,320] by considering an Ising model (with $S = 2$ spin moment per Mn ion) for different spin-ordered solutions. The intra-plane (ac) J_1 and inter-plane (b) J_2 coupling constants for the 20 atom LMO unit cell are

$$\begin{aligned} J_1 &= \frac{1}{64}\left[E^{\text{G-AFM}} - E^{\text{A-AFM}}\right] \\ J_2 &= \frac{1}{32}\left[E^{\text{A-AFM}} - E^{\text{FM}}\right] . \end{aligned} \tag{84}$$

The initial A-AFM/FM stability results in Table 12 hint that the coupling constants will depend strongly on the Hund's exchange parameter. In the context of previous works, J_i are well known to be highly sensitive, for example to variation in Mn-O-Mn angle through superexchange interactions,[321] and the Mn ionic charge population.[320]

On the trend of magnetic stability in U and J, the superexchange interaction which stabilises AFM ordering is expected to scale inversely with effective on-site Coulomb interaction, *i.e.* $\sim t^2/U_{\text{eff}}$. Considering first J_2 ($\sim E^{\text{A-AFM}} - E^{\text{FM}}$) in Figure 62, the stability of AFM coupling along b decreases both with increasing U or decreasing J as expected since $U_{\text{eff}} = U - J$. However, the dependence of the J_2 coupling on U and J is not equivalent: the variation in J_2 is some five-fold more sensitive to changes in J than U, *i.e.*, $\partial J_2/\partial J \approx -5\partial J_2/\partial U$. The AFM coupling in the ac plane, measured by J_1, is even more sensitive to the intra-orbital Hund's parameter, with $\partial J_1/\partial J \approx -10\partial J_1/\partial U$. The origin of coupling constant sensitivity to J, is the strongly anisotropic effect of J on the LMO Mn d shell states, with variation in J increasing $\pi^{e_g\sigma}$ in Table 13 above and beyond that accessible with U alone.

Neutron scattering experiments have determined coupling constant values of $J_1^{\text{exp}} = 0.83$ meV and $J_2^{\text{exp}} = -0.58$ meV.[22] In Figure 62 reasonable values for J_1 are produced with $J \approx 1.75$ eV, and for J_2 with $J_2 \approx 2$ eV. The discrepancy in J value for each J_i is perhaps unsurprising given the extreme sensitivity of A-AFM, G-type anti-ferromagnetic (G-AFM) and FM phases to the intra-orbital Hund's interaction. Overall the $U|J = 8|2$ eV combination previously suggested remains a good com-

promise at the level of half integer eV screening intervals considered here. Although higher resolution screening in J is beyond the scope of this work, if DFT+$U|J$ calculations are required for thermodynamics applications, results in Figure 62 indicate a small modification of J by a few percent may be advantageous to tune the magnetic transition temperatures precisely, while the magnetic couplings are relatively insensitive to the direct U term.

Due to the sensitivity of the magnetic couplings to the Coulombic J correction, precise agreement with experiment is challenging. At the $U = 8$ eV required to open the band gap, and screening in J at half integer intervals shown in Figure 62, $U|J = 8|2$ eV remains the best compromise. For $U|J = 8|2$ eV the inter-plane coupling at $J_2 = -0.30$ meV has the correct sign but in magnitude falls short of $J_2^{\text{exp}} = -0.58$ meV.[22] More problematic is the intra-plane coupling, which overestimates the tendency for electrons to couple anti-ferromagnetically in the *ac* plane, excessively stabilising G-AFM ordering at $J_2 = -0.19$ meV compared to $J_2^{\text{exp}} = 0.83$ meV.

In Figure 62 the coloured areas show the J values that correspond to coupling constants between zero and J_i^{exp}, *i.e.* the correct sign for each J_i. The overlap in coloured areas identifies the narrow range of intra-orbital exchange values, $1.88 \leq J \leq 1.95$ eV, that gives the correct signs for both J_i together, with $E(\text{A-AFM}) < E(\text{FM}) < E(\text{G-AFM})$ in agreement with experiment.[22] Based on the refinement in J value, we have performed GGA (PBEsol) calculations with $U|J = 8|1.9$ eV. The error in calculation results with respect to experimental values[17,19,20,21,22,23] is summarised in Table 14. The $U|J = 8|1.9$ eV calculations produce good experimental agreement overall, with magnetic coupling constants with signs that agree with experiment, $J_1 = +0.2$ and $J_2 = -0.1$ meV, a band gap value only a couple of percent above the experimental 1.7 eV value, and lattice parameter errors between $+1.5$ % and -0.8 % which largely cancel to give a volume error with respect to experiment of $+0.1$ %.[20,22,23]

10.3.3.3 *Jahn-Teller distortion*

We end our analysis with conclusions on the nature of JT distortion in LMO and on the origin of the LMO insulating state. JT distortion in LMO can be characterised in terms of two normal modes of the type

Table 14: $LaMnO_3$ electronic, magnetic and structural properties obtained from a $U|J = 8|1.9$ eV calculation, with comparison to experimental counter-parts.[17,19,20,21,22,23] The $J = 1.9$ eV value is based on a refinement of the Hund's exchange parameter to secure the correct sign for both magnetic coupling constants, J_1 and J_2, which are exceptionally sensitive to on-site exchange - see Figure 62.

Observable		$U\|J = 8\|1.9$ eV	*Exp.*
Electronic gap	E^{Gap} (eV)	1.75	1.7 [20]
	Character	$e^1_{g\uparrow} \rightarrow e^2_{g\uparrow}$	$e^1_{g\uparrow} \rightarrow e^2_{g\uparrow}$ [20]
Magnetic	J_1, J_2 (meV)	$+0.2$, -0.1	$+0.83$, -0.58 [23]
	M (μ_B)	3.76	3.7 [17]
Structural	$\mathbf{Q}^{\text{Ortho}}$, $\mathbf{Q}^{\text{Tetra}}$ (a.u.)	0.145, 0.856	0.14, 0.78 [19]
	a, b, c (Å)	5.823, 7.642, 5.508	5.736, 7.703, 5.540 [19]
	V (Å^3)	245	245 [19]

introduced by van Vleck[322] and by Kanamori.[323] The normal modes are shown in Figure 63 along with the crystal unit cell and the local octahedral basis. The modes are calculated as

$$\begin{aligned} \mathbf{Q}^{\text{Ortho}} &= \frac{1}{\sqrt{2}}\left[\mathbf{Y}_2 - \mathbf{Y}_5 - \mathbf{X}_1 + \mathbf{X}_4\right] \\ \mathbf{Q}^{\text{Tetra}} &= \frac{1}{\sqrt{6}}\left[2\mathbf{Z}_3 - 2\mathbf{Z}_6 - \mathbf{Y}_2 + \mathbf{Y}_5 - \mathbf{X}_1 + \mathbf{X}_4\right] . \end{aligned}$$

Each variable represents an octahedral bond length, with subscripts indexing oxygen octahedral cage sites around a given manganese centre, $i(i = 1, ...6)$. In the local basis in this work, which differs from other choices,[306,312] $\mathbf{Z}_i = \mathbf{z}^{\text{O}}_i - \mathbf{z}^{\text{Mn}}$ are the long Mn-O bonds and $\mathbf{X}_i = \mathbf{x}^{\text{O}}_i - \mathbf{x}^{\text{Mn}}$ short Mn-O bonds, with both in the FM coupled *ac* plane. $\mathbf{Y}_i = \mathbf{y}^{\text{O}}_i - \mathbf{y}^{\text{Mn}}$ are along the inter-plane AFM coupled *b* lattice direction.

We begin commenting the formation of a band gap in LMO is not solely e-e or e-l in character. Rather, it is a joint function of the lattice relaxation and development of JT distortions as well as the strong on-site Coulomb interaction. This is illustrated explicitly in Figure 63. As mentioned above, two logically distinct routes to breaking symmetry exist in order to produce a gap: (i) a purely electronic effect *via* electron-electron interactions and the formation of a sizeable orbital polarisation $\pi^{e_g\sigma}$ that breaks symmetry (also called e-e JT distortion),[58]

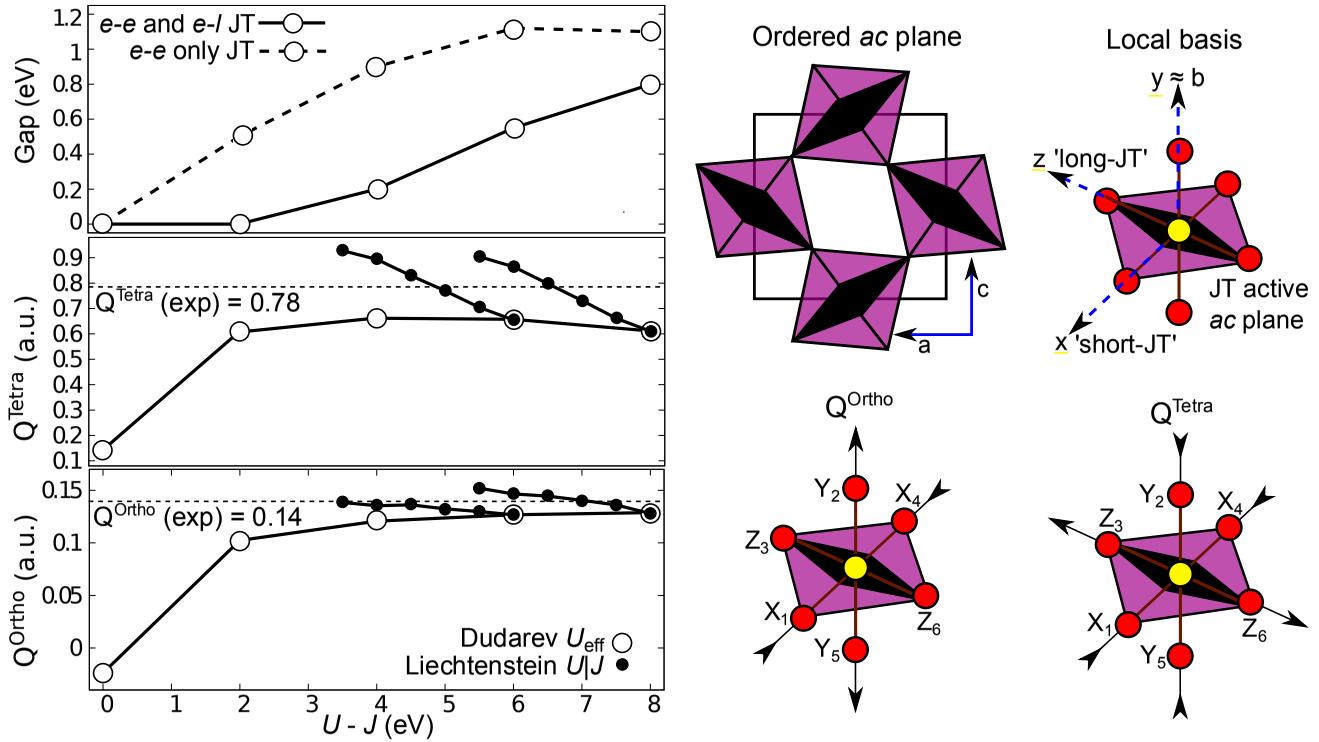

Figure 63: *Left top panel:* Band gap of $LaMnO_3$ versus $U - J$ within the U_{eff} approach for fully relaxed structures where both electron-lattice and electron-electron interactions are active (dashed line, *e-l* and *e-e*) and for structures with the Jahn-Teller distortion frozen out so only electron-electron interactions are active (solid line, *e-e* only). *Left bottom and middle panels:* Jahn-Teller normal modes versus $U - J$ within the U_{eff} (white circles) and $U|J$ (black circles) approaches. *Right panels:* Orbitally ordered and strongly Jahn-Teller active *ac* plane, the local basis convention, and $\mathbf{Q}^{\text{Ortho}}$ and $\mathbf{Q}^{\text{Tetra}}$ modes.

or (ii) e-l JT distortions where certain local octahedral phonon modes become soft, the Mn-O bond lengths become unequal, and this creates crystal field symmetry breaking. These two mechanisms are in fact mutually enhancing, and which one causes which in LMO is an open question that has been debated in the works of Khomskiĭ,[52] Yin *et al.*,[44] and Loa *et al.*.[142]

In some materials, one mechanism can clearly dominate over the other. For example, in $KCuF_3$, to which LMO is superficially similar as both are perovskites with partial e_g occupation, the symmetry lowering is truly driven by electronic interactions alone,[59] and thus $KCuF_3$ is said to exhibit e-e JT distortion. Figure 63 shows that the nature of JT is different in LMO.

Firstly, with the e-l distortion frozen out at the $U_{\text{eff}} = 0$ eV level, one can generate symmetry breaking and a gap for a Coulomb interaction strength $(U - J)$ above a critical value $\sim$ 2 eV, so that in principle, additional lattice distortion is not necessary to create a gap. However, in practice, the gap and orbital splitting remain small without lattice JT distortions. Secondly, with $U - J$ set to zero, the DFT calculations do produce weakly active e-l JT distortions of $\mathbf{Q}^{\text{Ortho}} = -0.02$ a.u. and $\mathbf{Q}^{\text{Tetra}} = 0.14$ a.u., but the gap remains essentially zero. The addition of Coulomb repulsion *via* U_{eff} greatly enhances the e-l distortion of each mode to approximately $\mathbf{Q}^{\text{Ortho}} \approx 0.12$ a.u. and $\mathbf{Q}^{\text{Tetra}} \approx 0.62$ a.u.. However even with U_{eff} applied, $\mathbf{Q}^{\text{Ortho}}$ and $\mathbf{Q}^{\text{Tetra}}$ still remain short of experiment by some 13 % and 20 % respectively. As per Table 13 and Figure 63, one can only go so far with U_{eff}: the orbital polarisation $\pi^{e_g\sigma}$ is too weak and the e-l JTdistortion remains largely unchanged with increasing U_{eff}.

The only way to bridge the deficit is through the use of a dedicated exchange term *via* the $U|J$ approach. As shown in Table 13, J increases $\pi^{e_g\sigma}$ and anisotropy throughout the d manifold significantly. By increasing J in the $U|J$ scheme, the LMO $\mathbf{Q}^{\text{Ortho}}$ and $\mathbf{Q}^{\text{Tetra}}$ modes can be tuned to agree with experiment by accessing additional e-e JT activity otherwise unavailable.

An isotropic Hubbard correction, such as the U_{eff} methodology, is unable to simultaneously reproduce the band gap and magnetic ordering of bulk $LaMnO_3$. At small U_{eff}, A-AFM magnetic ordering is correctly stabilised but the gap and structural distortions are underestimated. With increasing U_{eff} values, the gap and crystal structure are reproduced but FM ordering is incorrectly stabilised. Only the $U|J$ approach, with its explicit exchange dependence on orbital symmetry, is capable of simultaneously predicting electronic, magnetic and structural properties of LMO. The origin of the $U|J$ success is the Hund's coupling accounted for by the spatial/orbital dependence of the dedicated exchange terms that depend on J. These terms selectively polarise orbital occupation through highly anisotropic energy splitting in the Mn d manifold. Only the addition of J terms, rather than crystal field or direct Coulomb U, can provide appropriate and large enough anisotropic splitting within the t_{2g} and e_g manifolds. Orbital order due to the short-range on-site J makes possible the combination of long-range FM exchange in the (010) plane, and AFM exchange between $\{010\}$ planes, resulting in the A-AFM ordered ground state. Soft phonon modes (e-l JT) and electronic occupation polarisation (e-e JT) contribute jointly to the insulating state, with the latter predominant. The experimental JT distortion magnitude can only be achieved by adding the anisotropy J provides on top of the direct Coulomb occupancy polarisation. The best description of $LaMnO_3$ is achieved within the PBEsol+U framework when $U = 8$ eV and $J = 1.9$ eV.

Part IV

Conclusions

11

SUMMARY AND OUTLOOK

Individual conclusions on each topic have been placed at the end of each chapter, so only a short summary is given now for each material.

VANADIUM DIOXIDE

Chapter 6 confirmed that DFT at the GGA level can qualitatively describe the metallic ground state of VO_2 (R), but not the insulating ground state of VO_2 (M1). DFT+U and hybrid functional techniques also have limitations in describing both phases of VO_2 simultaneously. For example with DFT+U, calculations of VO_2 can reproduce the experimentally expected M1 and R phase stability and qualitative insulating and metallic band structures respectively, but only if we accept the approximation of non-spin polarised solutions for both phases. Spin-polarised DFT+U calculations fail to provide the correct order of stability for the M1 and R phases and produce qualitative errors in electronic features. Spin polarised screened hybrid functional calculations (HSE) report KS-HSE eigenvalue gaps at the Fermi level of 2.3 eV for VO_2 (M1) and 1.5 eV for VO_2 (R) - in context, the M1 and R phase experimental band gaps are 0.7 eV and 0 eV respectively. The KS-HSE gaps can be tuned to give experimental band gap agreement by setting the mixing parameter to an atypical value, but this introduces the additional complication of meta-stable R phase solutions. The Hund's coupling part of $U|J$-type corrections was explored *via* a model of anisotropic intra-orbital exchange acting on a formal V^{4+} d^1 shell. This indicated a degree of spin-compensation is likely to occur in the VO_2 *via* the anisotropic on-site exchange which acts to stabilise the opposite spin $3z^2 - r^2\bar{\sigma}$ state, when the ground state occupies the $x^2 - y^2\sigma$ orbital. Intra-orbital exchange effects were observed to be cooperative in the sense that anisotropic Hund's splitting only occurs if occupancy polarisation is pre-existing, for example due to localisation from strong on-site Coulomb interaction, or in the M1

phase due to lattice distortions such as V-V dimerisation. Investigation of Hund's coupling merits further testing using *ab initio* rather than model calculations.

In Chapter 7, *ab initio* calculations using NM DFT+U with $U = 3$ eV produced M1 and R phase band gaps and an order of energetic phase stability in qualitative agreement with experimental expectations. M1 to R potential energy surfaces were examined in terms of structural and electronic parameters, and lead to a description of the transition with energy minima at the M1 phase and a maximum at the R phase, as conventionally expected. A thermodynamic analysis showed a VO_2 transition mainly driven by phonons. Most of the entropy in the latent heat of transition comes from phonons, which outweigh electronic entropy by almost a factor of eight. We propose a single transformation scheme that allows us to obtain the (real) frequencies of the low-energy modes of the R phase at the phase transition, starting from their calculated imaginary values at zero temperature. Most phonon entropy was found to be supplied by two soft low-energy modes. Although the the M1 to R phase instability is driven by lattice effects, the soft-phonon transition modes and phonon entropy are enabled critically by the on-site Coulomb interaction between V d states, emphasising e-e/e-l cooperation in the transition.

In our investigation of the VO_2 (R) surfaces in Chapter 8, the (110) surface was shown to be favoured energetically over other surfaces. This underlies the stability of the (110)-bounded 'acicular' VO_2 particle morphology that is observed experimentally. Reduction of the (110) surface was very unstable thermodynamically - oxygen vacancies even preferred to form in the bulk rather than at the (110) surface. Under all typical experimental conditions, the (110) surface oxidised, with excess surface oxygen forming vanadyl groups in preference to peroxo species.

MANGANESE DIOXIDE

In Chapter 9 the stoichiometric surfaces of β-MnO_2 resisted reduction under most temperatures and pressures of interest. Oxygen was favourably adsorbed, particularly at low temperature in the form of peroxo species bridging between surface Mn sites. The preferred Li

adsorption site is tri-coordinated to one in-plane and two bridging surface oxygen, with charge transferred from the Li adatom localising onto the surface Mn site that is most coordinatively unsaturated. Li defects increase surface oxidation generally, with a dissociative mode of O_2 adsorption favoured in particular, where O bonds to surface Li^+ defects and coordinatively unsaturated Mn sites. Surface lithium oxide is more energetically favourable than gas phase lithium peroxide (Li_2O_2) monomers, but more stable than Li_2O_2 bulk, which suggests β-MnO_2 at the Li-air battery cathode lowers the energy for initial oxidation, and therefore charge cycle over-potentials.

LANTHANUM MANGANITE

Chapter 10 showed that only an on-site Coulomb description with a dedicated anisotropic exchange term could access the Hund's coupling interaction needed to *simultaneously* reproduce the lattice, electronic and magnetic structure of $LaMnO_3$. Neither plain DFT nor DFT+U with an effective on-site potential ($U_{\text{eff}} = U - J$) could adequately describe $LaMnO_3$. Hund's coupling was found to selectively polarise occupation, particularly stabilising the $x^2 - y^2\sigma$ state. Both the degree of anisotropy across the d shell and strength of the occupancy polarisation depended on cooperation between intra-orbital exchange and direct Coulomb terms. The anisotropic orbital splitting was key to stabilising both the correct long-range A-AFM magnetic ordering and full level of JT distortions. The $LaMnO_3$ insulating state, opened to the full experimental band gap value, was shown to be a joint function of e-l JT from soft crystal field lattice modes, and e-e JT distortion due to strong intra-orbital Coulomb effects. The best description of $LaMnO_3$ is achieved within the PBEsol+U framework when $U = 8$ eV and $J = 1.9$ eV.

Vanadium dioxide

- Continue exploring more sophisticated corrections to DFT in order to achieve a satisfactory description of the spin-polarised ground states.
- Understand in better detail why only a NM DFT+U description of VO_2 provides a reasonable electronic structure and thermodynamics.
- Investigate the viability of optical properties calculations for the insulating VO_2 phase using the VASP linear response routines.
- Calculate thermodynamical and optical properties of VO_2 surfaces and doped bulks.
- Map VO_2 energy surfaces in terms of different orbital occupation orderings, for example, using the *occupation matrix control* routines for VASP by Allen and Watson.[180]

Manganese dioxide

- Perform more realistic analysis of Li and O adsorption dynamics on MnO_2 surfaces, using larger supercells and a multi-scale approach.
- Extend the calculations and analysis performed for Li doped MnO_2 to isomorphic transition metal oxides such as TiO_2 and VO_2.

Lanthanum manganite

- Employ the DFT+$U|J$ parameters determined in Chapter 10, to further study $LaMnO_3$.

- Investigate the viability of more sophisticated mean-field parameterised Coulomb interaction corrections to DFT, in the style of the U_{eff} and $U|J$ schemes but to a 'higher-order' of correction.
- Investigate VASP occupation matrix control, for matrices in a local diagonal basis rather than the standard global axial unit cell basis.

Part V

Appendix

A

FURTHER TECHNICAL DETAILS

A.1 ORBITALLY DEPENDENT ON-SITE COULOMB POTENTIAL

In Chapter 4 we began with general considerations on two-body Coulomb interactions, in order to provide a theoretical origin to the two different flavours of $+U$ correction (*i.e.* the $U|J$[59] and U_{eff}[177] approaches). As several steps in the derivation were skipped over for readability, these steps are now filled in for completeness.

In Chapter 4 we obtained the mean-field form of on-site Coulomb potential in a general non-diagonal ($mm'm''m'''$) basis

$$\langle \hat{V}_{ee} \rangle = \sum_{at} \frac{1}{2} \sum_{\sigma,\sigma'} \sum_{mm'm''m'''} \langle m\sigma m''\sigma' | V | m'\sigma m'''\sigma' \rangle \times (\rho^{\sigma}_{mm'''} \rho^{\sigma'}_{m'm''} - \rho^{\sigma}_{mm'} \rho^{\sigma}_{m'''m''} \delta_{\sigma,\sigma'}) \,. \tag{85}$$

As a reminder, V is the form of interaction, m^i labels orbital angular momentum states, σ labels spin, at is atomic site, and ρ is the orbital occupancy density matrix. To re-write Equation 85 in a simpler form, first consider the standard expression for a multipole expansion around the bare Coulomb form of interaction, $V(\mathbf{r}_1, \mathbf{r}_2) = \frac{1}{|\mathbf{r}_1 - \mathbf{r}_2|}$,

$$\frac{1}{|\mathbf{r}_1 - \mathbf{r}_2|} = \sum_{k=0}^{\infty} \frac{4\pi}{2k+1} \sum_{q=-k}^{k} Y_{kq}(\mathbf{r}_1) Y_{kq}(\mathbf{r}_2)^* \frac{\min(r_1, r_2)^k}{\max(r_1, r_2)^{k+1}} \,.$$

Here the interaction $V(\mathbf{r}_1, \mathbf{r}_2)$ now depends on separate angular parts (between vectors $\mathbf{r}_1$ and $\mathbf{r}_2$), and a radial scalar distance. To digest the multipole expansion of the Coulomb kernel in an orbital setting, we express the interaction matrix elements in terms of Slater's integrals as

$$
\begin{aligned}
&\langle m\sigma m''\sigma'|V|m'\sigma m'''\sigma'\rangle \\
&\qquad = \int d^3\mathbf{r}_1 \int d^3\mathbf{r}_2 \frac{R_{nl}(r_1)^2 R_{nl}(r_2)^2 Y^*_{lm}(\mathbf{r}_1) Y_{lm'}(\mathbf{r}_1) Y^*_{lm''}(\mathbf{r}_2) Y_{lm'''}(\mathbf{r}_2)}{|\mathbf{r}_1 - \mathbf{r}_2|} \\
&\qquad = \sum_{k=0}^{\infty} \sum_{q=-k}^{k} \frac{4\pi}{2k+1} \left\langle Y_{lm}|Y_{kq}Y_{lm'}\right\rangle \left\langle Y_{lm'''}|Y_{kq}Y_{lm''}\right\rangle F^k \\
&\qquad = \delta_{m-m',m'''-m''} \sum_{k=0}^{2l} c^k(lm,lm') c^k(lm''',lm'') F^k \,. \quad (86)
\end{aligned}
$$

In this expression the Slater radial terms are

$$
F^k = \int dr \int dr' R^2_{nl}(r_1) R^2_{nl}(r_2)\, f_k(r_1, r_2)\,, \tag{87}
$$

with $f_k(r_1, r_2) = \frac{\min(r_1,r_2)^k}{\max(r_1,r_2)^{k+1}}$ for the bare form of Coulomb interaction. The angular terms in Equation 86 are given as

$$
c^k(lm, l'm') = \sqrt{\frac{4\pi}{2k+1}} \int d\Omega Y_{lm}(\theta,\phi)^* Y_{l'm'}(\theta,\phi) Y_{k,m-m'}(\theta,\phi)\,, \tag{88}
$$

for which values are widely available in tabular form. While the Slater formulation is strictly only valid in the atomic limit of spherical symmetry, we assume this is a good approximation for the localised d and f sub-spaces of cations embedded in strongly correlated materials.

As Equation 85 is written in non-diagonal form (with $mm'm''m'''$ quantum numbers), we can simplify the analysis by rotating to a diagonal frame of reference. To diagonalise the angular terms in Equations 86 & 88, we see that the Hermitian density matrices are related *via* basis eigenvectors V^{σ}_{mi} to the diagonal occupancies: $\rho^{\sigma}_{mm'} = \sum_i \mathrm{V}^{\sigma}_{mi} f^{\sigma}_i (\mathrm{V}^{\sigma})^{\dagger}_{im'}$. Expressing Equation 85 in terms of the Slater's integrals, and diagonalising using the eigenvectors of $\rho^{\sigma}_{mm'}$ leads to

$$
\begin{aligned}
\langle \hat{V}_{ee} \rangle_{U|J} &= \frac{1}{2} \sum_{at,\sigma\sigma',mm'm''m'''} \langle m\sigma m''\sigma'|V|m'\sigma m'''\sigma' \rangle \times \\
&\quad (\rho^{\sigma}_{mm'''}\rho^{\sigma'}_{m'm''} - \rho^{\sigma}_{mm'}\rho^{\sigma}_{m'''m''}\delta_{\sigma,\sigma'}) \\
&= \frac{1}{2} \sum_{at,\sigma\sigma',mm'm''m''',k} F^k \delta_{m-m',m'''-m''} c^k(lm,lm') c^k(lm''',lm'') \times \\
&\quad (\rho^{\sigma}_{mm'''}\rho^{\sigma'}_{m'm''} - \rho^{\sigma}_{mm'}\rho^{\sigma}_{m'''m''}\delta_{\sigma,\sigma'}) \\
&= \frac{1}{2} \sum_{at,\sigma,\sigma',k} F^k \sum_{ij} f_{i\sigma} f_{j\sigma'} \sum_{mm'm''m'''} \delta_{m-m',m'''-m''} \times \\
&\quad \Big[\mathrm{V}^{\sigma *}_{mi} c^k(lm,lm') \mathrm{V}^{\sigma}_{m'i} \ \mathrm{V}^{\sigma'}_{m'''j} c^k(lm''',lm'') \mathrm{V}^{\sigma' *}_{m''j} \\
&\quad - \mathrm{V}^{\sigma *}_{mi} c^k(lm,lm') \mathrm{V}^{\sigma}_{m'j} \ \mathrm{V}^{\sigma}_{m'''i} c^k(lm''',lm'') \mathrm{V}^{\sigma *}_{m''j} \delta_{\sigma\sigma'} \Big] \\
&= \frac{F^0}{2} \sum_{at,\sigma,\sigma',i,j,} f_{i\sigma} f_{j\sigma'} (1 - \delta_{ij}\delta_{\sigma\sigma'}) + \frac{1}{2} \sum_{at,\sigma\sigma',ij} f_{i\sigma} f_{j\sigma'} \sum_{k=2}^{2l} F^k \sum_{mm'm''m'''} \delta_{m-m',m'''-m''} \times \\
&\quad \Big[(\mathrm{V}^{\sigma})^{\dagger}_{im} c^k(lm,lm') \mathrm{V}^{\sigma}_{m'i} \ (\mathrm{V}^{\sigma'})^{\dagger}_{jm'''} c^k(lm''',lm'') \mathrm{V}^{\sigma'}_{m''j} \\
&\quad - (\mathrm{V}^{\sigma})^{\dagger}_{im} c(lm,lm') \mathrm{V}^{\sigma}_{m'j} \ (\mathrm{V}^{\sigma})^{\dagger}_{im'''} c^k(lm''',lm'') \mathrm{V}^{\sigma}_{m''j} \delta_{\sigma\sigma'} \Big] . \qquad (89)
\end{aligned}
$$

To obtain the second part of Equation 89, we substitute in the Slater terms, for the third equation we have used the unitary nature of density matrix eigenvectors to re-write the diagonalisation of the c^k angular terms, and in the fourth part of Equation 89, we have pulled the monopole radial term F^0 out of the k sum as $c^0(lm,lm') = \delta_{mm'}$.

To further simplify Equation 89, we collect together the mixed spin terms for $k \geq 2$ as the $\mathrm{C}^{\sigma\sigma'}_{ij}$ multipole orbitally-dependent Coulomb matrix

$$
\begin{aligned}
\mathrm{C}^{\sigma\sigma'}_{ij} = \sum_{k=2}^{2l} F^k \sum_{mm'm''m'''} &\delta_{m-m',m'''-m''} \times \\
&(\mathrm{V}^{\sigma})^{\dagger}_{im} c^k(lm,lm') \mathrm{V}^{\sigma}_{m'i} (\mathrm{V}^{\sigma'})^{\dagger}_{jm'''} c^k(lm''',lm'') \mathrm{V}^{\sigma'}_{m''j} , \qquad (90)
\end{aligned}
$$

and the degenerate spin terms ($\delta_{\sigma\sigma'}$) for $k \geq 2$ as the X^{σ}_{ij} multipole orbitally dependent spin-exchange matrix

$$X^{\sigma}_{ij} = \sum_{k=2}^{2l} F^k \sum_{mm'm''m'''} \delta_{m-m',m'''-m''} \times (\mathrm{V}^{\sigma})^{\dagger}_{im} c^k(lm,lm') \mathrm{V}^{\sigma}_{m'j} \, (\mathrm{V}^{\sigma})^{\dagger}_{im'''} c^k(lm''',lm'') \mathrm{V}^{\sigma}_{m''j} \,. \quad (91)$$

Summing over ij in Equation 90, and using the unitary nature of the V^{σ} density matrix eigenvectors, $m = m'$ and $m'' = m'''$ and the Kronecker-delta is satisfied leading to

$$\sum_{ij} \mathrm{C}^{\sigma\sigma'}_{ij} = \sum_{k=2}^{2l} \sum_{mm''} F^k c^k(lm,lm) c^k(lm'',lm'') \,.$$

Similarly summing ij in Equation 91 naturally simplifies to

$$\sum_{ij} \mathrm{X}^{\sigma}_{ij} = \sum_{k=2}^{2l} \sum_{mm''} F^k c^k(lm,lm'')^2 \,.$$

Now Equation 85 can now be expressed as

$$\langle \hat{V}_{ee} \rangle_{U|J} = \frac{1}{2} \sum_{at,\sigma\sigma',ij} f_{i\sigma} f_{j\sigma'} \{ F^0 (1 - \delta_{ij}\delta_{\sigma\sigma'}) + \mathrm{C}^{\sigma\sigma'}_{ij} - \mathrm{X}^{\sigma}_{ij} \} \,. \quad (92)$$

For a d electron system, the k sum inside $\mathrm{C}^{\sigma\sigma'}_{ij}$ and X^{σ}_{ij} has only two terms, $k = 2$ & 4, since $2l = 4$. In the $k = 0$ monopole term, there is no angular interaction, so the single radial interaction is parameterised simply as $F^0 = U$. For the higher order ($k = 2$ and $k = 4$) terms, radial and angular integrals can be parameterised using 'sum rules' to give $J = \sum_{k=2}^{2l} \frac{c^k(l0,l0)}{2l} F^k$, which for d electrons is $J = (F^2 + F^4)/14$.

After expressing Equation 92 in terms of U and J, and removing double counting terms using the standard 'FLL' double counting expression (see Chapter 4.2.2 Equation 32), the remaining expression is

$$\langle \hat{V}_{ee} \rangle_{U|J} - E_{\mathrm{dc}}[\rho] = \frac{(U-J)}{2} \sum_{at,i,\sigma} (f_{i\sigma} - f^2_{i\sigma}) + \frac{1}{2} \sum_{at,\sigma\sigma',ij} f_{i\sigma} f_{j\sigma'} \left\{ \mathrm{C}^{\sigma\sigma'}_{ij} - \Delta \mathrm{X}^{\sigma}_{ij} \delta_{\sigma\sigma'} \right\} \,. \quad (93)$$

The exchange term has been re-cast as $\Delta \mathrm{X}^{\sigma}_{ij} = \mathrm{X}^{\sigma}_{ij} - J(1 - \delta_{ij})$ in order to ensure the first term is in the same form as the Dudarev

U_{eff} correction, so that the $U|J$ scheme is transparently an additional correction to U_{eff}.

To clarify the action of correction $\langle \hat{V}_{ee} \rangle_{U|J} - E_{\text{dc}}[\rho]$ in Equation 93, we can take derivatives with respect to occupation to provide the energy splitting by Janak's theorem

$$\begin{aligned} \Delta\epsilon^{i\sigma}_{U|J} &= \frac{\partial(\langle \hat{V}_{ee} \rangle_{U|J} - E_{\text{dc}}[\rho])}{\partial f_{n\mathbf{k}\sigma}}. \\ &\approx (U-J) \cdot \left(\frac{1}{2} - f_{i\sigma}\right) + \frac{1}{2} \sum_{\sigma',j} f_{j\sigma'} \left\{ \mathrm{C}^{\sigma\sigma'}_{ij} - \Delta \mathrm{X}^{\sigma}_{ij} \delta_{\sigma\sigma'} \right\}. \end{aligned}$$

In a final simplification we collect like and opposite-spin terms into unitless 'A$^{\sigma}$' and 'B$^{\sigma}$' matrices scaled by J leading to the vector-matrix equation

$$\Delta\epsilon^{\sigma}_{U|J} \approx (U-J) \cdot \left(\frac{1}{2} - f_{\sigma}\right) + J \left[\mathrm{A}^{\sigma} f_{\sigma} + \mathrm{B}^{\sigma} f_{\bar{\sigma}}\right], \tag{94}$$

where $\mathrm{A}^{\sigma} = (\mathrm{C}^{\sigma,\sigma} - \Delta\mathrm{X}^{\sigma})/J$ and $\mathrm{B}^{\sigma} = \mathrm{C}^{\sigma,\bar{\sigma}}/J$. In the orthonormal d electron basis most convenient for high-symmetry solid-state applications, the matrices are

$$\mathrm{A}^{\sigma} = \left(\begin{array}{c|ccccc} & 3z^2-r^2 & x^2-y^2 & xy & yz & xz \\ \hline 3z^2-r^2 & 0 & -0.52 & -0.52 & 0.52 & 0.52 \\ x^2-y^2 & -0.52 & 0 & 0.86 & -0.17 & -0.17 \\ xy & -0.52 & 0.86 & 0 & -0.17 & -0.17 \\ yz & 0.52 & -0.17 & -0.17 & 0 & -0.17 \\ xz & 0.52 & -0.17 & -0.17 & -0.17 & 0 \end{array}\right)$$

and

$$
\mathrm{B}^{\sigma} = \left(\begin{array}{c|ccccc}
 & 3z^2-r^2 & x^2-y^2 & xy & yz & xz \\ \hline
3z^2-r^2 & 1.14 & -0.63 & -0.63 & 0.06 & 0.06 \\
x^2-y^2 & -0.63 & 1.14 & 0.29 & -0.40 & -0.40 \\
xy & -0.63 & 0.29 & 1.14 & -0.40 & -0.40 \\
yz & 0.06 & -0.40 & -0.40 & 1.14 & -0.40 \\
xz & 0.06 & -0.40 & -0.40 & -0.40 & 1.14
\end{array}\right).
$$

The action of Equation 94 can now be understood - the left hand term scaled by $(U - J)$ is nothing more than Dudarev U_{eff} correction.[177] This term originates in the derivation from the F^0 radial monopole interaction which is entirely blind to symmetry, hence the dependence solely on occupancy. The higher-order multipole exchange interactions, with angular dependence, are contained inside $\mathrm{C}_{ij}^{\sigma\sigma'}$ and $\Delta\mathrm{X}_{ij}^{\sigma}$, with each of the terms scaled by the 'Hund's exchange' parameter J. This interaction is entirely orbitally dependent - both $\mathrm{C}_{ij}^{\sigma\sigma'}$ and $\Delta\mathrm{X}_{ij}^{\sigma}$ average to zero unless some dependence on $i\,(m)$ is present across the occupations, *e.g.*, $\mathrm{C}_{ij}^{\sigma\sigma'}$ and $\Delta\mathrm{X}_{ij}^{\sigma}$ terms should sum to zero in an isotropic manifold.

For more details on Coulomb formulation and application, see Ismail-Beigi[178] & Mellan *et al.*.[1]

A.1.0.4 *Particle-hole exchange symmetry*

An exchange symmetry exists between systems that have commensurate numbers of electrons and holes. For example, for the form of exchange in Equation 94, $J\left[\mathrm{A}^{\sigma} f_{\sigma} + \mathrm{B}^{\sigma} f_{\bar{\sigma}}\right]$, the splitting caused by a majority-spin manifold with a single hole, and with a single electron, are equivalent up to a sign. In $LaMnO_3$, the formal Mn d shell has four electrons or one hole, while in the VO_2 d shell has one electron or four holes. Due to the symmetry in particle-hole degeneracies, the intra-orbital exchange splitting is the same for both, up to a change of sign.

To make this statement more clear, consider the occupied $x^2 - y^2$ state in VO_2 (V^{4+} d shell), and an empty $x^2 - y^2$ or hole state in $LaMnO_3$ (Mn^{3+} d shell):

$$(f^1_\sigma|^{V^{4+}}_{x^2-y^2} = \left(\begin{array}{c|} 0 \\ 1 \\ 0 \\ 0 \\ 0 \end{array}\right) \quad \& \quad (f^4_\sigma|^{Mn^{3+}}_{x^2-y^2} = \left(\begin{array}{c|} 1 \\ 0 \\ 1 \\ 1 \\ 1 \end{array}\right) \equiv (h^1_\sigma|^{Mn^{3+}}_{x^2-y^2} = \left(\begin{array}{c|} 0 \\ 1 \\ 0 \\ 0 \\ 0 \end{array}\right) .$$

The resulting intra-orbital exchange splittings due to the V state and Mn state are as mentioned equivalent up to a sign:

$$(\Delta\epsilon^J_\sigma|\triangle\epsilon^J_{\bar{\sigma}})^{V^{4+}}_{x^2-y^2} = J \left(\begin{array}{c|c} -0.52 & -0.63 \\ 0.00 & 1.14 \\ 0.86 & 0.29 \\ -0.17 & -0.40 \\ -0.17 & -0.40 \end{array}\right) \; \& \; (\Delta\epsilon^J_\sigma|\triangle\epsilon^J_{\bar{\sigma}})^{Mn^{3+}}_{x^2-y^2} = J \left(\begin{array}{c|c} 0.52 & 0.63 \\ 0.00 & -1.14 \\ -0.86 & -0.29 \\ 0.17 & 0.40 \\ 0.17 & 0.40 \end{array}\right) . \tag{95}$$

The electron-hole exchange symmetry is not limited to the $x^2 - y^2$ site of course. More generally the relationship is true for the whole group exchange splittings $\{\Delta\epsilon^J_\sigma\}$ generated by different combinations of single-hole or single-electron sites, f^1_σ and h^1_σ:

$$\{\Delta\epsilon^J_\sigma(f^1_\sigma)\} = -\{\Delta\epsilon^J_\sigma(h^1_\sigma)\} .$$

In other words, exchange splitting that can be generated by all possible occupancy configurations, $\{f^1_\sigma\}$, is equal to the splitting generated by holes $\{h^1_\sigma\}$ (or $\{f^4_\sigma\}$), where

$$\{f^1_\sigma\} = \forall f^1_\sigma \in d^1 = \left\{ \left(\begin{array}{c|} 1 \\ 0 \\ 0 \\ 0 \\ 0 \end{array}\right), \left(\begin{array}{c|} 0 \\ 1 \\ 0 \\ 0 \\ 0 \end{array}\right), \left(\begin{array}{c|} 0 \\ 0 \\ 1 \\ 0 \\ 0 \end{array}\right), \left(\begin{array}{c|} 0 \\ 0 \\ 0 \\ 1 \\ 0 \end{array}\right), \left(\begin{array}{c|} 0 \\ 0 \\ 0 \\ 0 \\ 1 \end{array}\right) \right\}_f ,$$

and

$$\{h_\sigma^1\} = \forall h_\sigma^1 \in d^4 = \left\{ \left(\begin{array}{c|c|c|c|c} 1 & 0 & 0 & 0 & 0 \\ 0 & 1 & 0 & 0 & 0 \\ 0 & 0 & 1 & 0 & 0 \\ 0 & 0 & 0 & 1 & 0 \\ 0 & 0 & 0 & 0 & 1 \end{array} \right)_h \right\}$$

$$\equiv \{f_\sigma^4\} = \forall f_\sigma^4 \in d^4 = \left\{ \left(\begin{array}{c|c|c|c|c} 0 & 1 & 1 & 1 & 1 \\ 1 & 0 & 1 & 1 & 1 \\ 1 & 1 & 0 & 1 & 1 \\ 1 & 1 & 1 & 0 & 1 \\ 1 & 1 & 1 & 1 & 0 \end{array} \right)_f \right\} .$$

In addition to the symmetry existing between the single-electron and single-hole configurations, the symmetry exists more generally between systems with x electrons and $2l + 1 - x$ holes. The expression equating the exchange splitting up to a sign for x electron and $2l + 1 - x$ hole systems is

$$\{\Delta\epsilon_\sigma^J(f_\sigma^x)\} = -\{\Delta\epsilon_\sigma^J(h_\sigma^{2l+1-x})\} .$$

The intra-orbital exchange particle-hole symmetry appears to be analogous to the particle-hole transformations employed in Hubbard-type models.[324]

B

CUSTOM CODES

B.1 ELECTRONIC ENTROPY CODE

Electronic entropy code calculates the metallic entropy contribution from states near the Fermi level for a given DOS distribution. The code was written in `FORTRAN` to help study the VO_2 phase transition in Chapter 7 - for example, to consider questions such as whether the transition is driven by electronic or phonon entropy - see Chapter 7.3.3 for answer.

B.2 DENSITY MATRIX ROTATION CODE

Density matrix rotation code was written in `Mathematica` to input orbital occupancies from VASP in the form of $2l + 1$ dimensional density matrices, and rotate from the global unit cell basis into a basis diagonal in the local octahedral coordinates. The code is an extended version of an Octave script by Sohrab Ismail-Beigi. The code was used to diagonalise the V^{4+} and Mn^{3+} d shell density matrices to make orbital analysis easier for VO_2 and $LaMnO_3$ in Chapters 6 & 10.

Custom codes B.1: Electronic entropy code.

```
!ENTROPY CODE PART I
PROGRAM CNTROPY

!DECLARATIONS
IMPLICIT NONE
INTEGER :: NEDOS1
INTEGER :: I REAL, DIMENSION(:), ALLOCATABLE :: ENERGY,
    DOS_E, INT_DOS_E
REAL :: E_MIN, E_MAX, E_FERMI, T, N
REAL, PARAMETER :: KB_EV = 8.61733E-05

!READ USER VARIABLES
WRITE(*,*) "Fermi energy?"; READ(*,*) E_FERMI
WRITE(*,*) "Temp?"; READ(*,*) T
WRITE(*,*) "N KT?"; READ(*,*) N
WRITE(*,*) "DOS MESH DIVISIONS (NEDOS)?"; READ(*,*) NEDOS1
E_MAX = E_FERMI + N*KB_EV*T; E_MIN = E_FERMI - N*KB_EV*T

!ARRAYS
ALLOCATE(ENERGY(NEDOS1));
ALLOCATE(DOS_E(NEDOS1));
ALLOCATE(INT_DOS_E(NEDOS1))

!OPEN EXTERNAL FILES
OPEN(UNIT=9, FILE="DOS.dat")
OPEN(UNIT=10, FILE="ENERGY.dat")
OPEN(UNIT=11, FILE="DOSCAR_simple")

!READ EXTERNAL FILES AND LOOP OVER DATA
DO I= 1, NEDOS1
READ (11, 110) ENERGY(I), DOS_E(I), INT_DOS_E(I)
110 FORMAT(F11.3, E12.4, E12.4)
IF (ENERGY(I) >= E_MIN) THEN
IF (ENERGY(I) < E_MAX) THEN

!PRINTING
WRITE (10,120) ENERGY(I) 120 FORMAT(F11.3)
WRITE (9, 130) DOS_E(I) 130 FORMAT(E12.4)

!GOOD NIGHT
END IF
END IF
END DO
DEALLOCATE(ENERGY)
DEALLOCATE(DOS_E)
DEALLOCATE(INT_DOS_E)
CLOSE(11); CLOSE(10); CLOSE(9)
END PROGRAM CNTROPY
```

Custom codes B.2: Electronic entropy code part II.

```
!ENTROPY CODE PART IIa
PROGRAM DNTROPY

!DECLARATIONS
IMPLICIT NONE
INTEGER :: NEDOS, NEDOS1
INTEGER :: I, J
REAL, DIMENSION(:), ALLOCATABLE :: ENERGY, DOS_E, INT_DOS_E
REAL, DIMENSION(:), ALLOCATABLE :: GAMMA, INTEGRAND, F_DIST
REAL :: E_MIN, E_MAX, E_FERMI, E, ENT_EL, T, INTEGRAL, N,
REAL :: FORM_UNIT, DEL_E, RANGE, ENT_EL_LINEAR
REAL, PARAMETER :: KB_EV = 8.6173324E-05, G = 3.28987

!READ USER VARIABLES
WRITE(*,*) "Temp?";
READ(*,*) T
WRITE(*,*) "Fermi energy?";
READ(*,*) E_FERMI
WRITE(*,*) "Number of kB*T for integration limits?"
READ(*,*) N
WRITE(*,*) "Formula units?";
READ (*,*) FORM_UNIT
WRITE(*,*) "DOS mesh divisions (NEDOS)?"
READ (*,*) NEDOS1
WRITE(*,*) "DOS Range?";
READ (*,*) RANGE
E_MAX = E_FERMI + N*KB_EV*T
E_MIN = E_FERMI - N*KB_EV*T
DEL_E = RANGE/NEDOS1
NEDOS = (E_MAX-E_MIN)/DEL_E

!ARRAYS
ALLOCATE(ENERGY(NEDOS)); ALLOCATE(DOS_E(NEDOS))
ALLOCATE(INT_DOS_E(NEDOS)); ALLOCATE(F_DIST(NEDOS))
ALLOCATE(GAMMA(NEDOS)); ALLOCATE(INTEGRAND(NEDOS))

!OPEN EXTERNAL FILES
OPEN(UNIT=9, FILE="DOS.dat")
OPEN(UNIT=10, FILE="ENERGY.dat")
OPEN(UNIT=11, FILE="ANSWERS.dat")

!READ EXTERNAL FILES AND LOOP OVER DATA
DO I= 1, NEDOS
READ (10,140) ENERGY(I)
140 FORMAT(F11.3)
READ (9,150) DOS_E(I)
150 FORMAT(E12.4)
END DO
```

Custom codes B.3: Electronic entropy code part III.

```
!ENTROPY CODE PART IIb

!CALCULATE ENTROPY
!HARMONIC APPROX
F_DIST = 1/((EXP((ENERGY - E_FERMI)/(KB_EV*T)))+1)
GAMMA = F_DIST*LOG(F_DIST)+(1-F_DIST)*LOG(1-F_DIST)
INTEGRAND = GAMMA*DOS_E
INTEGRAL = SUM(INTEGRAND*DEL_E)
ENT_EL = -KB_EV*INTEGRAL

!CALCULATE ENTROPY
!LINEAR HIGH TEMP APPROX
J=NEDOS/2
ENT_EL_LINEAR = G*(DOS_E(J))*(KB_EV**2)*T

!PRINT RESULTS
!HARMONIX APPROXIMATION
WRITE (11,*) "Electronic entropy in the Harmonic Approx is"
WRITE (11,*)  ENT_EL/FORM_UNIT, "eV/K/fu"
WRITE (11,*) "TS in the Harmonic Approx is"
WRITE (11,*)  T*ENT_EL/FORM_UNIT,"eV/fu at", T, "K."

!LINEAR (HIGH T) APPROXIMATION
WRITE (11,*) "Electronic entropy in the Harmonic Approx is"
WRITE (11,*)  ENT_EL_LINEAR/FORM_UNIT, "eV/K/fu"
WRITE (11,*) "TS in the Harmonic Approx is"
WRITE (11,*)  T*ENT_EL_LINEAR/FORM_UNIT,"eV/fu at", T, "K."

!GOODNIGHT
DEALLOCATE(ENERGY); DEALLOCATE(DOS_E)
DEALLOCATE(INT_DOS_E); DEALLOCATE(F_DIST)
DEALLOCATE(GAMMA); DEALLOCATE(INTEGRAND);
CLOSE(9); CLOSE(10); CLOSE(11)
END PROGRAM DNTROPY
```

Custom codes B.4: Density matrix rotation code.

```
"Density matrix code PART I"

"p and d orbital occupancy density matrix rotation"

"User defined d (lm=2) orbital occupancy density matrix"
updatad = {{ud11, ud12, ud13, ud14, ud15},
           {ud21, ud22, ud23, ud24, ud25},
           {ud31, ud32, ud33, ud34, ud35},
           {ud41, ud42, ud43, ud44, ud45},
           {ud51, ud52, ud53, ud54, ud55}};

"User defined p (lm=1) orbital occupancy density matrix"
updatap = {{up11, up12, up13},
           {up21, up22, up23},
            {up31, up32, up33}};

"User defined coordinate system"
atpos = {{a11, a12, a13},
         {a21, a22, a23},
         {a31, a32, a33},
         {a41, a42, a43}};

"Coordinate system axes"
u1 = (atpos[[2]] - atpos[[1]])/Norm[(atpos[[2]] - atpos
    [[1]])];
u2 = (atpos[[3]] - atpos[[1]])/Norm[(atpos[[3]] - atpos
    [[1]])];
u3 = (atpos[[4]] - atpos[[1]])/Norm[(atpos[[4]] - atpos
    [[1]])];

"Transformation matrix"
R = Transpose[{u1, u3, u2}];

"Transformation matrix 2l+1 dimension space: l=2"
d = {{d11, d12, d13, d14, d15},
     {d21, d22, d23, d24, d25},
     {d31, d32, d33, d34, d35},
     {d41, d42, d43, d44, d45},
     {d51, d52, d53, d54, d55}};

"Transformation matrix 2l+1 dimension space: l=1"
p = {{p11, p12, p13},
     {p21, p22, p23},
     {p31, p32, p33}};
```

Custom codes B.5: Density matrix rotation part code II.

```
"Density matrix code PART II"

"d polynomial matrix elements"

"2z**2-x**2-y**2"
d[[1, 3]] = (3*R[[3, 3]]^2 - 1)/2;
d[[2, 3]] = (3*R[[3, 1]]^2 - 3*R[[3, 2]]^2)/2;
d[[3, 3]] = 6*R[[3, 1]]*R[[3, 2]];
d[[4, 3]] = 6*R[[3, 2]]*R[[3, 3]];
d[[5, 3]] = 6*R[[3, 1]]*R[[3, 3]];

"x**2-y**2"
d[[1, 5]] = (R[[1, 3]]^2 - R[[2, 3]]^2)/2;
d[[2, 5]] = (R[[1, 1]]^2 + R[[2, 2]]^2 - R[[2, 1]]^2 - R
    [[1, 2]]^2)/2;
d[[3, 5]] = 2*(R[[1, 1]]*R[[1, 2]] - R[[2, 1]]*R[[2, 2]]);
d[[4, 5]] = 2*(R[[1, 2]]*R[[1, 3]] - R[[2, 2]]*R[[2, 3]]);
d[[5, 5]] = 2*(R[[1, 1]]*R[[1, 3]] - R[[2, 1]]*R[[2, 3]]);

"xy"
d[[1, 1]] = R[[1, 3]]*R[[2, 3]]/2;
d[[2, 1]] = (R[[1, 1]]*R[[2, 1]] - R[[1, 2]]*R[[2, 2]])/2;
d[[3, 1]] = R[[1, 1]]*R[[2, 2]] + R[[1, 2]]*R[[2, 1]];
d[[4, 1]] = R[[1, 2]]*R[[2, 3]] + R[[1, 3]]*R[[2, 2]];
d[[5, 1]] = R[[1, 1]]*R[[2, 3]] + R[[1, 3]]*R[[2, 1]];

"yz"
d[[1, 2]] = R[[2, 3]]*R[[3, 3]]/2;
d[[2, 2]] = (R[[2, 1]]*R[[3, 1]] - R[[2, 2]]*R[[3, 2]])/2;
d[[3, 2]] = R[[2, 1]]*R[[3, 2]] + R[[2, 2]]*R[[3, 1]];
d[[4, 2]] = R[[2, 2]]*R[[3, 3]] + R[[2, 3]]*R[[3, 2]];
d[[5, 2]] = R[[2, 1]]*R[[3, 3]] + R[[2, 3]]*R[[3, 1]];

"xz"
d[[1, 4]] = R[[1, 3]]*R[[3, 3]]/2;
d[[2, 4]] = (R[[1, 1]]*R[[3, 1]] - R[[1, 2]]*R[[3, 2]])/2;
d[[3, 4]] = R[[1, 1]]*R[[3, 2]] + R[[1, 2]]*R[[3, 1]];
d[[4, 4]] = R[[1, 2]]*R[[3, 3]] + R[[1, 3]]*R[[3, 2]];
d[[5, 4]] = R[[1, 1]]*R[[3, 3]] + R[[1, 3]]*R[[3, 1]];
```

Custom codes B.6: Density matrix rotation code part III.

```
"Density matrix code PART III"

"p polynomial matrix elements"

"px"
p[[1, 3]] = R[[1, 1]];
p[[2, 3]] = R[[1, 2]];
p[[3, 3]] = R[[1, 3]];

"py"
p[[1, 1]] = R[[2, 1]];
p[[2, 1]] = R[[2, 2]];
p[[3, 1]] = R[[2, 3]];

"pz"
p[[1, 2]] = R[[3, 1]];
p[[2, 2]] = R[[3, 2]];
p[[3, 2]] = R[[3, 3]];

"d scaling and reordering"
ID = {{1, 0, 0, 0, 0},
      {0, 1, 0, 0, 0},
      {0, 0, 1, 0, 0},
      {0, 0, 0, 1, 0},
      {0, 0, 0, 0, 1}};

scaleoutd =
Sqrt[{4/5, 4/15, 1/15, 1/15, 1/15}].ID

scaleind =
Sqrt[{1/15, 1/15, 4/5, 1/15, 4/15}].ID

dnorm = scaleoutd.d.Inverse[scaleind];

"p scaling and reordering"
IP = {{1, 0, 0},
      {0, 1, 0},
      {0, 0, 1}};

scaleoutp = Sqrt[{1, 1/2, 1}].IP

scaleinp = Sqrt[{1, 1, 1/2}].IP

pnorm = scaleoutp.p.Inverse[scaleinp];

"Print rotated p and d orbital occupancy density matrices"
dnorm.Transpose[updatad] // MatrixForm
pnorm.Transpose[updatap] // MatrixForm
```

Part VI

Bibliography

BIBLIOGRAPHY

[1] TA Mellan, F Cora, R Grau-Crespo, and S Ismail-Beigi. Importance of anisotropic Coulomb interaction in LaMnO3. *Physical Review B*, 92:085151–16, 2015.

[2] Thomas A Mellan and R Grau-Crespo. Density functional theory study of rutile VO2 surfaces. *The Journal of Chemical Physics*, 137:154706–8, 2012.

[3] TA Mellan, KP Maenetja, PE Ngoepe, SM Woodley, CRA Catlow, and R Grau-Crespo. Lithium and oxygen adsorption at the β-MnO2 (110) surface. *Journal of Materials Chemistry A*, 1(47):14779–15168, 2013.

[4] H Wang, Thomas A Mellan, R Grau-Crespo, and U Schwingenschlögl. Spin polarization, orbital occupation and band gap opening in vanadium dioxide: The effect of screened Hartree-Fock exchange. *Chemical Physics Letters*, 608:126–129, 2014.

[5] JH Park, JM Coy, TS Kasirga, C Huang, Z Fei, S Hunter, and DH Cobden. Measurement of a solid-state triple point at the metal-insulator transition in VO2. *Nature*, 500:431–4, 2013.

[6] V Eyert. The metal-insulator transitions of VO2: A band theoretical approach. *Annalen der Physik (Leipzig)*, 11(9):650–702, 2002.

[7] H Verleur, A Barker, and C Berglund. Optical Properties of VO2 between 0.25 and 5 eV. *Physical Review*, 172(3):788–798, 1968.

[8] SM Babulanam, TS Eriksson, GA Niklasson, and CG Granqvist. Thermochromic VO2 films for energy-efficient windows. *Solar Energy Materials*, 16:347–363, 1987.

[9] FJ Morin. Oxides which show a metal to insulator transition at the Neel temperature. *Physical Review Letters*, 3(1):34, 1959.

[10] W Bruckner, W Moldenhauer, and H Oppermann. Conductivity transition in Ga+Mo doped VO2. *Physica Status Solidi A*, 47:129–132, 1978.

[11] JB Macchesney, JF Potter, and HJ Guggenheim. Preparation and Properties of Vanadium Dioxide Films. *Journal of The Electrochemical Society: Solid State Science*, 115(1):3–6, 1968.

[12] CN Berglund and HJ Guggenheim. Electronic Properties of VO2 near the Semiconductor-Metal Transition. *Physical Review*, 185:1022, 1969.

[13] F Chudnovskiy, S Luryi, and B Spivak. *Switching device based on first-order metal-insulator transition induced by external electric field*. 2002.

[14] K Wang, C Cheng, E Cardona, J Guan, K Liu, and J Wu. Performance limits of microactuation with vanadium dioxide as a solid engine. *ACS Nano*, 7(3):2266–72, 2013.

[15] MEA Warwick and R Binions. Advances in thermochromic vanadium dioxide films. *Journal of Materials Chemistry A*, 2:3275–92, 2014.

[16] PG Bruce, SA Freunberger, Hardwick LJ, and J-M Terascon. Li-O2 and Li-S batteries with high energy storage. *Nature materials*, 11:19–30, 2012.

[17] JBAA Elemans. The crystallographic and magnetic structures of La(1-x)Ba(x)Mn(1-x)MexO3 (Me = Mn or Ti). *Journal of Solid State Chemistry*, 3:238–242, 1971.

[18] J Heyd, GE Scuseria, and M Ernzerhof. Hybrid functionals based on a screened Coulomb potential. *The Journal of Chemical Physics*, 118:8207, 2003.

[19] N Sakai, H Fjellvag, and B Lebech. Effect of non-stoichiometry on properties of La(1-t)Mn O(3+d). *Acta Chemica Scandinavica*, 51:904–909, 1997.

[20] JH Jung, KH Kim, DJ Eom, TW Noh, EJ Choi, Y Jaejun, YS Kwon, and Y Chung. Determination of electronic band structures

of $CaMnO_3$ and $LaMnO_3$ using optical-conductivity analyses. *Physical Review B*, 55(23):04823, 1997.

[21] JH Jung, KH Kim, TW Noh, EJ Choi, and J Yu. Midgap states of La1-xCaxMnO3: Doping-dependent optical-conductivity studies. *Physical Review B*, 57(18):43–46, 1998.

[22] J Rodríguez-Carvajal, M Hennion, F Moussa, A Moudden, L Pinsard, and A Revcolevschi. Neutron-diffraction study of the Jahn-Teller transition in stoichiometric $LaMnO_3$. *Physical Review B*, 57(6):R3189–R3192, 1998.

[23] F Moussa, M Hennion, J Rodriguez-Carvajal, H Moudden, L Pinsard, and A Revcolevschi. Spin waves in the antiferromagnet perovskite $LaMnO_3$: A neutron-scattering study. *Physical Review B*, 54(21):15149–15155, 1996.

[24] SY Li, GA Niklasson, and CG Granqvist. Nanothermochromics: Calculations for VO_2 nanoparticles in dielectric hosts show much improved luminous transmittance and solar energy transmittance modulation. *Journal of Applied Physics*, 108(6), 2010.

[25] Z Zhang, Y Gao, Z Chen, J Du, C Cao, L Kang, and H Luo. Thermochromic VO_2 thin films: solution-based processing, improved optical properties, and lowered phase transformation temperature. *Langmuir: The ACS Journal of Surfaces and Colloids*, 26(13):10738–10744, 2010.

[26] L Dai, S Chen, J Liu, Y Gao, J Zhou, Z Chen, C Cao, H Luo, and M Kanehira. F-doped VO_2 nanoparticles for thermochromic energy-saving foils with modified color and enhanced solar-heat shielding ability. *Physical Chemistry Chemical Physics*, 15(28):11723–9, 2013.

[27] CS Blackman, C Piccirillo, R Binions, and IP Parkin. Atmospheric pressure chemical vapour deposition of thermochromic tungsten doped vanadium dioxide thin films for use in architectural glazing. *Thin Solid Films*, 517:4565–4570, 2009.

[28] IP Parkin and R Binions. Thermochromic coatings for intelligent architectural glazing. *Journal of Nanomaterials*, 2:1–20, 2008.

[29] M Saeli, MEA Warwick, C Piccirllo, and R Binions. Thermochromic Thin Films: Synthesis, Properties and Energy Consumption Modelling. In *Materials and processes for energy*, pages 736–746. 2013.

[30] JM Tomczak and S Biermann. Materials design using correlated oxides: Optical properties of vanadium dioxide. *Europhysics Letters*, 86:37004, 2009.

[31] Y Shao, S Park, J Xiao, J-G Zhang, Y Wang, and J Liu. Electrocatalysts for Nonaqueous Lithium-Air Batteries: Status, Challenges, and Perspective. *ACS Catalysis*, 2:844–857, 2012.

[32] NC Bristowe, M Stengel, PB Littlewood, JM Pruneda, and E Artacho. Electrochemical ferroelectric switching: Origin of polarization reversal in ultrathin films. *Physical Review B*, 85:024106–7, 2012.

[33] V Garcia, S Fusil, K Bouzehouane, S Enouz-Vedrenne, ND Mathur, A Barthélémy, and M Bibes. Giant tunnel electroresistance for non-destructive readout of ferroelectric states. *Nature*, 460:81–84, 2009.

[34] J Hoffman, X Hong, and CH Ahn. Device performance of ferroelectric/correlated oxide heterostructures for non-volatile memory applications. *Nanotechnology*, 22:254014, 2011.

[35] M Gibert, P Zubko, R Scherwitzl, J Íñiguez, and J Triscone. Exchange bias in LaNiO3-LaMnO3 superlattices. *Nature Materials*, 11:195–198, 2012.

[36] H Chen and S Ismail-Beigi. Ferroelectric control of magnetization in Sr doped LaMnO3 manganites: A first principles study. *Physical Review B*, 86:024433, 2012.

[37] Y Tokura. Critical features of colossal magnetoresistive manganites. *Reports on Progress in Physics*, 69:797–851, 2006.

[38] JM Tomczak and S Biermann. Optical properties of correlated materials: Generalized Peierls approach and its application to VO2. *Physical Review B*, 80:085117, 2009.

[39] IP Parkin and TD Manning. Products of Chemistry Intelligent Thermochromic Windows. *Chemistry for Everyone*, 83:393–400, 2006.

[40] DA Tompsett, DS Middlemiss, and MS Islam. Importance of anisotropic Coulomb interactions and exchange to the band gap and antiferromagnetism of β-MnO2 from DFT+U. *Physical Review B*, 86:205126, 2012.

[41] C Franchini, R Podloucky, J Paier, M Marsman, and G Kresse. Ground state properties of multivalent manganese oxides: Density functional and hybrid density functional calculations. *Physical Review B*, 75:195128, 2007.

[42] A Yoshimori. A new type of antiferromagnetic structure in the rutile type crystal. *Journal of the Physical Society of Japan*, 14:807, 1959.

[43] F Jiao and PG Bruce. Mesoporous Crystalline β-MnO2 - a Reversible Positive Electrode for Rechargeable Lithium Batteries. *Advanced Materials*, 19:657–660, 2007.

[44] WG Yin, D Volja, and W Ku. Orbital Ordering in LaMnO3: Electron-Electron versus Electron-Lattice Interactions. *Physical Review Letters*, 96:116405–4, 2006.

[45] LF Feiner and AM Oleś. Electronic origin of magnetic and orbital ordering in insulating LaMnO3. *Physical Review B*, 59:3295–3298, 1999.

[46] Q Chu, X Wang, B Li, F Liu, and X Liu. High pressure flux synthesis of LaMnO(3+δ) with charge ordering. *RSC Advances*, 3(44):21311, 2013.

[47] GH Rao, JR Sun, K Bärner, and N Hamad. Crystal structure and magnetoresistance of Na-doped LaMnO3. *Journal of Physics: Condensed Matter*, 11:1523–1528, 1999.

[48] R Mahendiran, Sk Tiwary, Ak Raychaudhuri, R Mahesh, and Cn Rao. Thermopower and nature of the hole-doped states in LaMnO3 and related systems showing giant magnetoresistance. *Physical Review B*, 54:R9604–R9607, 1996.

[49] MG Blamire, JL MacManus-Driscoll, ND Mathur, and ZH Barber. The materials science of functional oxide thin films. *Advanced Materials*, 21:3827–3839, 2009.

[50] ZL Wang and ZC Kang. *Functional and smart materials: structural evolution and structure analysis*. Springer Science & Business Media, 1998.

[51] VI Anisimov, F Aryasetiawan, and AI Liechtenstein. First-principles calculations of the electronic structure and spectra of strongly correlated systems: the LDA+ U method. *Journal of Physics: Condens. Matter*, 9:767–808, 1997.

[52] DI KhomskiÄ. Role of orbitals in the physics of correlated electron systems. *Physica Scripta*, 72:8–14, 2005.

[53] AJ Millis. Orbital ordering and superexchange in manganite oxides. *Physical Review B*, 55(10):6405–6408, 1997.

[54] R Vidya. *Theoretical investigations on mixed-valence transition-metal oxides*. PhD thesis, 2005.

[55] DI KhomskiÄ. *Transition metal compounds*. Cambridge University Press, 2014.

[56] E. Pavarini. Lattice distortions in KCuF3: A paradigm shift? *Annalen der Physik (Leipzig)*, 523(10):865–866, 2011.

[57] YA Izyumov and VN Syromyatnikov. Phenomenological theory of phase transitions with quantum-mechanical order parameters. *Phase Transitions*, 66:23–79, 1998.

[58] Kl Kugel and DI KhomskiÄ. The Jahn-Teller effect and magnetism: transition metal compounds. *Soviet Physics Uspekhi*, 25:231–256, 1982.

[59] AI Liechtenstein, VI Anisimov, and J Zaanen. Density functional theory and strong interactions: Orbital ordering in Mott-Hubbard insulators. *Physical Review B*, 52:R5467–R5471, 1995.

[60] G Kotliar and D Vollhardt. Strongly correlated materials: Insights from dynamical mean-field theory. *Physics Today*, 53:53–59, 2004.

[61] JM Tomczak and S Biermann. Effective band structure of correlated materials: the case of VO2. *Journal of Physics: Condensed Matter*, 19(36):365206, 2007.

[62] A Liebsch, H Ishida, and G Bihlmayer. Coulomb correlations and orbital polarization in the metal-insulator transition of VO2. *Physical Review B*, 71:085109, 2005.

[63] S Kim, K Kim, CJ Kang, and BI Min. Correlation-assisted phonon softening and the orbital-selective Peierls transition in VO2. *Physical Review B*, 87:195106, 2013.

[64] HP Ehrke. *Dynamics of electronic order in Magnetoresistive Manganites studied with time-resolved x-ray scattering*. PhD thesis, 2010.

[65] K Yamada. Electron correlation in metals. *Cambridge University Press*, 2010.

[66] J Hubbard. Electron Correlations in Narrow Energy Bands. *Proceedings of the Royal Society*, 276:238–257, 1963.

[67] J Hubbard. Electron Correlations in Narrow Energy Bands III. An improved solution. *Proceedings of the Royal Society*, 281:401–428, 1964.

[68] PW Anderson. Localized Magnetic States in Metals. *Physical Review*, 124(1):41 53, 1961.

[69] J Kanamori. Electron Correlation and Ferromagnetism of Transition Metals. *Progress of Theoretical Physics*, 30(3):275–289, 1963.

[70] VI Anisimov and Y Izyumov. *Electronic structure of strongly correlated materials*. Springer, 2010.

[71] S Biermann, A Poteryaev, A Liechtenstein, and A Georges. Dynamical Singlets and Correlation-Assisted Peierls Transition in VO2. *Physical Review Letters*, 94:026404, 2005.

[72] F Theobold, R Cabala, and J Bernard. Essai sur la Structure de VO2 (B). *Journal of Solid State Chemistry*, 438:431–438, 1976.

[73] S Zhang, B Shang, J Yang, W Yan, S Wei, and Y Xie. From VO2 (B) to VO2 (A) nanobelts: first hydrothermal transformation, spectroscopic study and first principles calculation. *Physical Chemistry Chemical Physics*, 13:15873–81, 2011.

[74] Y Wang, Z Zhang, Y Zhu, Z Li, R Vajtai, L Ci, and PM Ajayan. Nanostructured VO2 photocatalysts for hydrogen production. *ACS Nano*, 2(7):1492–6, 2008.

[75] J Xie, C Wu, S Hu, J Dai, N Zhang, J Feng, J Yang, and Y Xie. Ambient rutile VO2(R) hollow hierarchitectures with rich grain boundaries from new-state nsutite-type VO2, displaying enhanced hydrogen adsorption behavior. *Physical Chemistry Chemical Physics*, 14:4810, 2012.

[76] SR Popuri, M Miclau, A Artemenko, C Labrugere, A Villesuzanne, and M Pollet. Rapid hydrothermal synthesis of VO2 (B) and its conversion to thermochromic VO2 (M1). *Inorganic Chemistry*, 52:4780–4785, 2013.

[77] Y Ji, Y Zhang, M Gao, Z Yuan, Y Xia, C Jin, B Tao, C Chen, Q Jia, and Y Lin. Role of microstructures on the M1-M2 phase transition in epitaxial VO2 thin films. *Scientific Reports*, 4:4854, 2014.

[78] A Tselev, IA Lukyanchuk, IN Ivanov, JD Budai, JZ Tischler, E Strelcov, A Kolmakov, and SV Kalinin. Symmetry relationship and strain induced transitions between insulating M1 and M2 and metallic R phases of vanadium dioxide. *Nano letters*, 10:4409–4416, 2010.

[79] Zhensheng Tao, Tzong-Ru Han, Subhendra Mahanti, Phillip Duxbury, Fei Yuan, Chong-Yu Ruan, Kevin Wang, and Junqiao Wu. Decoupling of Structural and Electronic Phase Transitions in VO2. *Physical Review Letters*, 109:166406, 2012.

[80] C Piccirillo, R Binions, and IP Parkin. Synthesis and characterisation of W doped VO2 by Aerosol Assisted Chemical Vapour Deposition. *Thin Solid Films*, 516:1992–7, 2008.

[81] R Binions, G Hyett, C Piccirillo, and IP Parkin. Doped and undoped vanadium dioxide thin films prepared by atmospheric

pressure chemical vapour deposition from vanadyl acetylacetonate and tungsten hexachloride: the effects of thickness and crystallographic orientation on thermochromic properties. *Journal of Materials Chemistry*, 17:4652, 2007.

[82] JR Brews. Symmetry Considerations and the Vanadium Dioxide Phase Transition. *Physical Review B*, 1(6):2557–12, 1970.

[83] A Zylbersztejn and NF Mott. Metal insulator transition in vanadium dioxide. *Physical Review B*, 11(11):4383–4395, 1975.

[84] D Paquet and P Leroux-Hugon. Electron correlations and electron-lattice interactions in the metal-insulator, ferroelastic transition in VO2: A thermodynamical study. *Physical Review B*, 22(11):5284, 1980.

[85] JB Goodenough. Metallic oxides. *Progress in Solid State Chemistry*, 5:145–399, 1971.

[86] A Tanaka. A New Scenario on the Metal Insulator Transition in VO2. *Journal of the Physical Society of Japan*, 72(10):2433–2436, 2003.

[87] M Qazilbash, K Burch, D Whisler, D Shrekenhamer, B Chae, H Kim, and D Basov. Correlated metallic state of vanadium dioxide. *Physical Review B*, 74:205118, 2006.

[88] J Tomczak, F Aryasetiawan, and S Biermann. Effective bandstructure in the insulating phase versus strong dynamical correlations in metallic VO2. *Physical Review B*, 78:115103, 2008.

[89] V Eyert. VO2: a novel view from band theory. *Physical Review Letters*, 107:016401, 2011.

[90] S Hu, SY Li, R Ahuja, CG Granqvist, K Hermansson, GA Niklasson, and RH Scheicher. Optical properties of Mg doped VO2: Absorption measurements and hybrid functional calculations. *Applied Physics Letters*, 101:201902, 2012.

[91] H Zheng and LK Wagner. The mechanism of metal-insulator transition in vanadium dioxide from a first-principles quantum Monte Carlo perspective. 2013.

[92] C Schuster, U Lueders, R Frésard, and U Schwingenschlögl. Lattice relaxation and ferromagnetic character of (LaVO3)m/SrVO3 superlattices. *Europhysics Letters*, 103(3):1–8, 2012.

[93] B Lazarovits, K Kim, K Haule, and G Kotliar. Effects of strain on the electronic structure of VO2. *Physical Review B*, 81:1–23, 2010.

[94] TD Manning, IP Parkin, ME Pemble, D Sheel, and D Vernardou. Intelligent window coatings: atmospheric pressure chemical vapor deposition of tungsten-doped vanadium dioxide. *Chemistry of Materials*, 16:744–749, 2004.

[95] R Binions, C Piccirillo, RG Palgrave, and IP Parkin. Hybrid Aerosol Assisted and Atmospheric Pressure CVD of Gold-Doped Vanadium Dioxide. *Chemical Vapor Deposition*, 14:33–39, 2008.

[96] HM Pinto, J Correia, and R Binions. Determination of the Optical Constants of VO2 and Nb doped VO2 Thin Films. *Materials Science Forum*, 587:640, 2008.

[97] JK Crow. On Hypovanadic Oxide (Vanadium Tetroxide), and its Compounds. *Journal of the Chemical Society*, 30:453, 1876.

[98] HE Roscoe. The Bakerian Lecture: Researches on Vanadium. *Proceedings of the Royal Society of London*, 16:220–228, 1867.

[99] HE Roscoe. Researches on vanadium. *Philosophical Transactions of the Royal Society of London - The Bakerian Lecture*, 11:322–350, 1868.

[100] MS Archer, DSP Roebuck, and FJ Whitby. Magnetic Susceptibility of Vanadium Dioxide. *Nature*, 174:754, 1954.

[101] T Mizokawa. Metal insulator transitions: Orbital control. *Nature Physics*, 9:612–613, 2013.

[102] JM Longo and P Kierkegaard. A refinement of the structure of VO2. *Acta Chemica Scandinavica*, 24:420–426, 1970.

[103] AS Barker Jr, HW Verleur, and HJ Guggenheim. Infrared optical properties of vanadium dioxide above and below the transition temperature. *Physical Review Letters*, 17(26):1286–1289, 1966.

[104] I Kawada, N Kimizuka, and M Nakahira. Crystallographic investigations of the phase transition of VO2. *Journal of Applied Crystallography*, 4(5):343–347, 1971.

[105] M Nakano, K Shibuya, D Okuyama, T Hatano, S Ono, M Kawasaki, Y Iwasa, and Y Tokura. Collective bulk carrier delocalization driven by electrostatic surface charge accumulation. *Nature*, 487:459–62, 2012.

[106] C Kübler, H Ehrke, R Huber, R Lopez, A Halabica, R Haglund, and A Leitenstorfer. Coherent Structural Dynamics and Electronic Correlations during an Ultrafast Insulator-to-Metal Phase Transition in VO2. *Physical Review Letters*, 99:116401, 2007.

[107] TL Cocker, LV Titova, S Fourmaux, G Holloway, HC Bandulet, D Brassard, JC Kieffer, MA El Khakani, and FA Hegmann. Phase diagram of the ultrafast photoinduced insulator-metal transition in vanadium dioxide. *Physical Review B*, 85:1–11, 2012.

[108] A Cavalleri, CS Tóth, C Siders, J Squier, F Ráksi, P Forget, and J Kieffer. Femtosecond Structural Dynamics in VO2 during an Ultrafast Solid-Solid Phase Transition. *Physical Review Letters*, 87(23):237401, 2001.

[109] E Merced, X Tan, and N Sepúlveda. Strain energy density of VO2 based microactuators. *Sensors and Actuators A: Physical*, 196:30–37, 2013.

[110] MA Kats, R Blanchard, S Zhang, P Genevet, C Ko, S Ramanathan, and F Capasso. Vanadium dioxide as a natural disordered metamaterial: Perfect thermal emission and large broadband negative differential thermal emittance. *Physical Review X*, 3:041004–7, 2014.

[111] KA Khan, GA Niklasson, and CG Granqvist. Optical properties at the metal-insulator transition in thermochromic VO2-xFx thin films. *Journal of Applied Physics*, 64:3327–3329, 1988.

[112] KA Khan and CG Granqvist. Thermochromic sputter-deposited vanadium oxyfluoride coatings with low luminous absorptance. *Applied Physics Letters*, 55:4–6, 1989.

[113] J Du, Y Gao, H Luo, L Kang, Z Zhang, Z Chen, and C Cao. Significant changes in phase-transition hysteresis for Ti-doped VO2 films prepared by polymer-assisted deposition. *Solar Energy Materials and Solar Cells*, 95:469–475, 2011.

[114] AM Tripathi, RG Nair, and SK Samdarshi. Visible active silver sensitized vanadium titanium mixed metal oxide photocatalyst nanoparticles through sol-gel technique. *Solar Energy Materials and Solar Cells*, 94:2379–2385, 2010.

[115] W Burkhardt, T Christmann, S Franke, W Kriegseis, D Meister, BK Meyer, W Niessner, D Schalch, and A Scharmann. Tungsten and fluorine co-doping of VO2 films. *Thin Solid Films*, 402:226–231, 2002.

[116] Y Jiazhen, Z Yue, H Wanxia, and T Mingjin. Effect of Mo-W Co-doping on semiconductor-metal phase transition temperature of vanadium dioxide film. *Thin Solid Films*, 516:8554–8558, 2008.

[117] Y Xu, W Huang, Q Shi, Y Zhang, L Song, and Y Zhang. Synthesis and properties of Mo and W ions co-doped porous nanostructured VO2 films by sol-gel process. *Journal of Sol-Gel Science and Technology*, 64:493–499, 2012.

[118] R Grau-Crespo, Thomas A Mellan, H Wang, and U Schwingenschlögl. Examining the density functional theory description of VO2 above and below the metal-insulator transition. In *APS Meeting*, 2013.

[119] Y Wu, L Fan, Q Liu, S Chen, W Huang, F Chen, G Liao, C Zou, and Z Wu. Decoupling the Lattice Distortion and Charge Doping Effects on the Phase Transition Behavior of VO2 by Titanium Doping. *Scientific Reports*, 5:9328, 2015.

[120] X Tan, T Yao, R Long, Z Sun, Y Feng, H Cheng, X Yuan, W Zhang, Q Liu, C Wu, Y Xie, and S Wei. Unraveling metal insulator transition mechanism of VO2 triggered by tungsten doping. *Scientific Reports*, 2:466, 2012.

[121] G Andersson. Studies on Vanadium Oxides. *Acta Chemica Scandinavica*, 10(4):623–628, 1956.

[122] RM Wentzcovitch, WW Schulz, and PB Allen. VO2: Peierls or Mott-Hubbard? A view from band theory. *Physical Review Letters*, 72(21):3389–3392, 1994.

[123] R Eguchi, M Taguchi, M Matsunami, K Horiba, K Yamamoto, Y Ishida, A Chainani, Y Takata, M Yabashi, D Miwa, Y Nishino, K Tamasaku, T Ishikawa, Y Senba, H Ohashi, Y Muraoka, Z Hiroi, and S Shin. Photoemission evidence for a Mott-Hubbard metal insulator transition in VO2. *Physical Review B*, 78:075115, 2008.

[124] K Okazaki, H Wadati, A Fujimori, M Onoda, Y Muraoka, and Z Hiroi. Photoemission study of the metal-insulator transition in VO2/TiO2 (001) : Evidence for strong electron-electron and electron-phonon interaction. *Physical Review B*, 69:165104, 2004.

[125] F Pintchovski, WS Glaunsinger, and A Navrotsky. Experimental study of the electronic and lattice contributions to the VO2 transition. *Journal of Physics and Chemistry of Solids*, 39:941–949, 1978.

[126] W Paul. The present position of theory and experiment for VO2. *Materials Research Bulletin*, 5:691–702, 1970.

[127] CJ Hearn. Phonon softening and the metal-insulator transition in VO2. *Journal of Physics C: Solid State Physics*, 5:1317, 1972.

[128] D Maurer, A Leue, R Heichele, and V Müller. Elastic behavior near the metal-insulator transition of VO2. *Physical Review B*, 60:249–252, 1999.

[129] MM Thackeray. Manganese oxides for lithium batteries. *Progress in Solid State Chemistry*, 25:1–71, 1997.

[130] Y Xia, K Tatsumi, T Fujieda, PP Prosini, and T Sakai. Solid-State Lithium-Polymer Batteries Using Lithiated MnO2 Cathodes. *Journal of The Electrochemical Society*, 147(6):2050, 2000.

[131] AR Armstrong and PG Bruce. Synthesis of layered LiMnO2 as an electrode for rechargeable lithium batteries. *Nature*, 381:499, 1996.

[132] F Cheng, J Zhao, W Song, C Li, H Ma, J Chen, and P Shen. Facile controlled synthesis of MnO2 nanostructures of novel shapes and their application in batteries. *Inorganic Chemistry*, 45(5):2038–44, 2006.

[133] M Armand and JM Tarascon. Building better batteries. *Nature*, 451:652–7, 2008.

[134] KM Abraham and Z Jiang. A Polymer Electrolyte-Based Rechargeable lithium/Oxygen Battery. *Journal of The Electrochemical Society*, 143(1):1–5, 1996.

[135] R Black, B Adams, and LF Nazar. Non-Aqueous and Hybrid Li-O2 Batteries. *Advanced Energy Materials*, 2:801–815, 2012.

[136] J Christensen, P Albertus, RS Sanchez-Carrera, T Lohmann, B Kozinsky, R Liedtke, J Ahmed, and A Kojic. A Critical Review of Li-Air Batteries. *Journal of The Electrochemical Society*, 159(2):1–30, 2012.

[137] A Débart, AJ Paterson, J Bao, and PG Bruce. α-MnO2 Nanowires: A Catalyst for the O2 Electrode in Rechargeable Lithium Batteries. *Angewandte Chemie*, 120:4597–4600, 2008.

[138] C Franchini, R Kováčik, M Marsman, SS Murthy, J He, C Ederer, and G Kresse. Maximally localized Wannier functions in LaMnO3 within PBE+U, hybrid functionals and partially self-consistent GW: an efficient route to construct ab initio tight-binding parameters for eg perovskites. *Journal of Physics: Condensed Matter*, 24:235602, 2012.

[139] I Solovyev, N Hamada, and K Terakura. Crucial Role of the Lattice Distortion in the Magnetism of LaMnO3. *Physical Review Letters*, 76(25):4825–4828, 1996.

[140] AJ Millis. Lattice effects in magnetoresistive manganese perovskites. *Nature*, 392:147–150, 1998.

[141] M Baldini, VV Struzhkin, AF Goncharov, P Postorino, and WL Mao. Persistence of Jahn-Teller Distortion up to the Insulator to Metal Transition in LaMnO3. *Physical Review Letters*, 106:066402, 2011.

[142] I Loa, P Adler, A Grzechnik, K Syassen, U Schwarz, M Hanfland, G Rozenberg, P Gorodetsky, and M Pasternak. Pressure-Induced Quenching of the Jahn-Teller Distortion and Insulator-to-Metal Transition in LaMnO3. *Physical Review Letters*, 87(12):125501, 2001.

[143] Y Tokura. Orbital Physics in Transition-Metal Oxides. *Science*, 288:462–468, 2000.

[144] M Uehara, S Mori, CH Chen, and SW Cheong. Percolative phase separation underlies colossal magnetoresistance in mixed-valent manganites. *Nature*, 399:560–563, 1999.

[145] Michael Coey. Charge ordering in oxides. *Nature*, 430:155, 2003.

[146] J He and C Franchini. Screened hybrid functional applied to 3do to 3d8 transition-metal perovskites doped LaXO3: Influence of the exchange mixing parameter on the structural. *Physical Review B*, 86:235117, 2012.

[147] ND Mathur, G Burnell, SP Isaac, TJ Jackson, BS Teo, JL MacManus-Driscoll, LF Cohen, JE Evetts, and MG Blamire. Large low-field magnetoresistance in La(0.7)Ca(0.3)MnO3 induced by artificial grain buondaries. *Nature*, 387:266, 1997.

[148] J Garcia-Barriocanal, JC Cezar, FY Bruno, P Thakur, NB Brookes, C Utfeld, A Rivera-Calzada, SR Giblin, JW Taylor, JA Duffy, SB Dugdale, T Nakamura, K Kodama, C Leon, S Okamoto, and J Santamaria. Spin and orbital Ti magnetism at LaMnO3/SrTiO3 interfaces. *Nature Communications*, 1:82–7, 2010.

[149] H Chen, Q Qiao, MSJ Marshall, AB Georgescu, A Gulec, PJ Phillips, RF Klie, FJ Walker, CH Ahn, and S Ismail-Beigi. Reversible Modulation of Orbital Occupations via an Interface- Induced Polar State in Metallic Manganites. *Nano Letters*, 14:4965–4970, 2014.

[150] WR Hamilton. Second Essay on a General Method in Dynamics, 1835.

[151] WR Hamilton. On the application to dynamics of a general mathematical method previously applied to optics. *British Association Report*, pages 513–518, 1834.

[152] W Ritz. Uber eine neue Methode zur Losung gewisser Variationsprobleme der mathematischen Physik. 1909.

[153] E Schrödinger. An undulatory theory of the mechanics of atoms and molecules. *Physical Review*, 28(6):1049, 1926.

[154] M Born and R Oppenheimer. Zur Quantentheorie der Molekln. *Annalen Der Physik*, 20(84):457, 1927.

[155] RFW Bader. Chemistry and the near-sighted nature of the one-electron density matrix. *International Journal of Quantum Chemistry*, 56(4):409–419, 1995.

[156] DD O'Regan, MC Payne, and AA Mostofi. Subspace representations in ab initio methods for strongly correlated systems. *Physical Review B*, 83:245124, 2011.

[157] PD Haynes. *Linear scaling methods in ab initio quantum mechanical calculations*. PhD thesis, 1998.

[158] JC Slater. A simplification of the Hartree-Fock method. *Physical Review*, 81(3):385, 1951.

[159] P Heenen and M R Godefroid. The Hartree-Fock method. *Scholarpedia*, 2012.

[160] M Leuders. *Electrons in Solids*. 2012.

[161] JC Slater. The theory of complex spectra. *Physical Review*, 34(10):1293, 1929.

[162] PJ Knowles and HJ Werner. An efficient method for the evaluation of coupling coefficients in configuration interaction calculations. *Chemical Physics Letters*, 145(6):514–522, 1988.

[163] W Foulkes, L Mitas, R Needs, and G Rajagopal. Quantum Monte Carlo simulations of solids. *Reviews of Modern Physics*, 73(1):33–83, 2001.

[164] ND Drummond, MD Towler, and RJ Needs. Jastrow correlation factor for atoms, molecules, and solids. *Physical Review B*, 70:235119, 2004.

[165] P Hohenberg and W Kohn. Inhomogeneous electron gas. *Physical review*, 136(3):166, 1964.

[166] K Burke. *The ABC of DFT*. 2003.

[167] DR Hartree and W Hartree. Self-Consistent Field, with Exchange, for Beryllium. *Proceedings of the Royal Society of London.*, 150(869):9–33, 1935.

[168] K Burke and LO Wagner. DFT in a nutshell. *International Journal of Quantum Chemistry*, 113:96–101, 2013.

[169] JP Perdew and A Zunger. Self-interaction correction to density-functional approximation for many-electron systems. *Physical Review B*, 23(10):5048–5079, 1981.

[170] S Lounis and P Mavropoulos. Non-collinear magnetism induced by frustration in transition-metal nano-structures deposited on surfaces. *Psi-k Scientific Highlight of the month*, 6:27–59, 2011.

[171] E Koch. Strongly Correlated Electrons: Exchange Mechanisms. In *Autumn School on Correlated Electrons, Jülich*, page 31, 2012.

[172] K Baberschke, M Donath, and W Nolting. *Springer: Lecture Notes in Physics: Band-ferromagnetism*. 2001.

[173] P Manninen. *Lecture notes on Advanced Computational Chemistry*. 2009.

[174] EP Wigner. On the Interaction of Electrons in Metals. *Physical Review*, 46:1002, 1934.

[175] RT Scalettar, EY Loh, and JE Gubernatis. Phase Diagram of the Two-Dimensional Negative-U Hubbard Model. *Physical Review B*, 62(12):1407–1410, 1989.

[176] B Himmetoglu, A Floris, S de Gironcoli, and M Cococcioni. Hubbard-corrected DFT energy functionals: the LDA+U description of correlated systems. *International Journal of Quantum Chemistry*, 114:14–49, 2014.

[177] SL Dudarev, GA Botton, SY Savrasov, CJ Humphreys, and AP Sutton. Electron-energy-loss spectra and the structural stability of nickel oxide: An LSDA+U study. *Physical Review B*, 57(3):1505–1509, 1998.

[178] S Ismail-beigi. Coulomb interaction written in terms of U and J, and DFT+U, 2013.

[179] M Freyss, B Dorado, M Bertolus, G Jomard, E Vathonne, P Garcia, and B Amadon. Scientific Highlight Of The Month. *Psi-k Newsletter*, 4:1–20, 2014.

[180] JP Allen and GW Watson. Occupation matrix control of d- and f-electron localisations using DFT+U. *Physical Chemistry Chemical Physics*, 16:21016–21031, 2014.

[181] AB Shick, AI Liechtenstein, and WE Picket. Implementation of the LDA+U method using the full-potential linearized augmented plane-wave basis'. *Physical Review B*, 60(15):7, 1999.

[182] O Gunnarsson and BI Lundqvist. Exchange and correlation in atoms, molecules, and solids by the spin-density-functional formalism. *Physical Review B*, 13(10):4274–4298, 1976.

[183] M Gell-Mann and KA Brueckner. Correlation Energy of an Electron Gas at High Density. *Physical Review*, 106(2):364–368, 1957.

[184] LJ Sham and W Kohn. One Particle Properties of an Inhomogeneous Interacting Electron Gas. *Physical Review*, 145(2), 1966.

[185] DM Ceperley and BJ Alder. Ground State of the Electron Gas by a Stochastic Method. *Physical Review Letters*, 45(7):566, 1980.

[186] EP Wigner and F Seitz. On the Constitution of Metallic Sodium. *Physical Review*, 43(15):804, 1933.

[187] JP Perdew, K Burke, and M Ernzerhof. Generalized Gradient Approximation Made Simple. *Physical Review Letters*, 77(18):3865–3868, 1996.

[188] JP Perdew, A Ruzsinszky, G Csonka, O Vydrov, G Scuseria, L Constantin, X Zhou, and K Burke. Restoring the Density

Gradient Expansion for Exchange in Solids and Surfaces. *Physical Review Letters*, 100(13):136406, April 2008.

[189] DA Mazziotti. Structure of Fermionic density matrices: Complete N-representability conditions. *Physical Review Letters*, 108:1–5, 2012.

[190] PE Blochl, CFJ Walther, and T Pruschke. Is reduced-density-matrix functional theory a suitable vehicle to import explicit correlations into density-functional calculations? 2013.

[191] L Vaugier, H Jiang, and S Biermann. Hubbard U and Hund exchange J in transition metal oxides: Screening versus localization trends from constrained random phase approximation. *Physical Review B*, 86:1–23, 2012.

[192] MT Czyzyk and GA Sawatzky. Local-density functional and on-site correlations: The electronic structure of La2CuO4 and LaCuO3. *Physical Review B*, 49(20):14211, 1993.

[193] VI Anisimov, J Zaanen, and OK Andersen. Band theory and Mott insulators: Hubbard U instead of Stoner I. *Physical Review B*, 44(3):943–954, 1991.

[194] AG Petukhov, II Mazin, L Chioncel, and AI Liechtenstein. Correlated metals and the LDA+U method. *Physical Review B*, 67(15):153106, April 2003.

[195] VI Anisimov, AV Kozhevnikov, MA Korotin, AV Lukoyanov, and DA Khafizullin. Orbital density functional as a means to restore the discontinuities in the total-energy derivative and the exchange correlation potential. *Journal of Physics: Condensed Matter*, 19:1–18, 2007.

[196] VI Anisimov, IV Solovyev, MA Korotin, MT Czyyk, and GA Sawatzky. Density-functional theory and NiO photoemission spectra. *Physical Review B*, 48(23):16929, 1993.

[197] HJ Kulik. Perspective: Treating electron over-delocalization with the DFT+U method. *The Journal of Chemical Physics*, 142(24):240901, 2015.

[198] O Gunnarsson. Strongly Correlated Electrons: Estimates of Model Parameters. In *Autumn School on Correlated Electrons, Jülich*, pages 1–27, 2012.

[199] M Cococcioni. The LDA+U Approach: A Simple Hubbard Correction for Correlated Ground States. In *Autumn School on Correlated Electrons, Jülich*, pages 1–40, 2012.

[200] H Nakamura, N Hayashi, N Nakai, M Okumura, and M Machida. First-principle electronic structure calculations for magnetic moment in iron-based superconductors: An LSDA+negative U study. *Physica C: Superconductivity*, 469:908–911, 2009.

[201] T Jeong and WE Pickett. First-principles study of the electronic structure of heavy fermion YbRh2Si2. *Journal of Physics: Condensed Matter*, 18(46):10529, 2006.

[202] E Bousquet and N Spaldin. J dependence in the LSDA+U treatment of noncollinear magnets. *Physical Review B - Condensed Matter and Materials Physics*, 82:220402, 2010.

[203] B Himmetoglu, R Wentzcovitch, and M Cococcioni. First-principles study of electronic and structural properties of CuO. *Physical Review B*, 84:115108, 2011.

[204] G Kresse and J Furthmüller. Efficiency of ab-initio total energy calculations for metals and semiconductors using a plane-wave basis set. *Computational Materials Science*, 6:15–50, 1996.

[205] G Kresse and J Furthmüller. Efficient iterative schemes for ab initio total energy calculations using a planewave basis set. *Physical Review B*, 54(16):11169–11186, 1996.

[206] G Kresse and D Joubert. From ultrasoft pseudopotentials to the projector augmented-wave method. *Physical Review B*, 59(3):1758, 1999.

[207] G Kresse and J Hafner. Ab initio molecular dynamics for liquid metals. *Physical Review B*, 47(1):558–561, 1993.

[208] G Kresse and J Hafner. Ab initio molecular-dynamics simulation of the liquid-metal amorphous-semiconductor transition in germanium. *Physical Review B*, 49(20):14251–14269, 1994.

[209] HJ Monkhorst and JD Pack. Special points for Brillouin-zone integrations. *Physical Review B*, 13(12):5188–5192, 1976.

[210] AGH Smith. *Structural and Defect Properties of Strontium Titanate*. PhD thesis, 2012.

[211] J Von Neumann. Wahrscheinlichkeitstheoretischer aufbau der quantenmechanik. *Nachrichten von der Gesellschaft der Wissenschaften*, 11:245–272, 1927.

[212] DD O'Regan. *Optimised Projections for the Ab Initio Simulation of Large and Strongly Correlated Systems*. PhD thesis, 2012.

[213] AJ Coleman. Structure of fermion density matrices. *Reviews of Modern Physics*, 35:668–686, 1963.

[214] PE Blöchl. Projector augmented-wave method. *Physical Review B*, 50(24):17953–17979, 1994.

[215] RFW Bader. Atoms in molecules. *Accounts of Chemical Research*, 18:9–15, 1985.

[216] RFW Bader, MT Carroll, JR Cheeseman, and C Chang. Properties of atoms in molecules: atomic volumes. *Journal of the American Chemical Society*, 109(26):7968–7979, 1987.

[217] RFW Bader. The zero-flux surface and the topological and quantum definitions of an atom in a molecule. *Theoretical Chemistry Accounts: Theory, Computation, and Modeling*, 105:276–283, 2001.

[218] RFW Bader. A comment on "Some fundamental problems with zero-flux partitioning of electron densities". *Theoretical Chemistry Accounts: Theory, Computation, and Modeling*, 107(6):381–382, 2002.

[219] RFW Bader. A bond path: a universal indicator of bonded interactions. *The Journal of Physical Chemistry A*, 5639(98):7314–7323, 1998.

[220] PLA Popelier. An analytical expression for interatomic surfaces in the theory of atoms in molecules. *Theoretica Chimica Acta*, 87:465–476, 1994.

[221] PLA Popelier. A fast algorithm to compute atomic charges based on the topology of the electron density. *Theoretica Chimica Acta*, 105:393–399, 2001.

[222] BP Uberuaga, ER Batista, and H Jonsson. Elastic sheet method for identifying atoms in molecules. *The Journal of Chemical Physics*, 111:10664, 1999.

[223] E Sanville, SD Kenny, R Smith, and G Henkelman. Improved Grid-Based Algorithm for Bader Charge Allocation. *Journal of Computational Chemistry*, 28(5), 2007.

[224] Y Quan, V Pardo, and WE Pickett. Formal valence, 3d-electron occupation, and charge-order transitions. *Physical Review Letters*, 109:216401, 2012.

[225] S Baroni and SD Gironcoli. Phonons and related crystal properties from density-functional perturbation theory. *Reviews of Modern Physics*, 73(2), 2001.

[226] A Togo. The Phonopy Manual, 2013.

[227] F Zhou, T Maxisch, and G Ceder. Configurational electronic entropy and the phase diagram of mixed-valence oxides: The case of LixFePO4. *Physical Review Letters*, 97:155704–4, 2006.

[228] R Grau-Crespo, H Wang, and U Schwingenschlögl. Why the Heyd Scuseria Ernzerhof hybrid functional description of VO2 phases is not correct. *Physical Review B*, 86:081101, 2012.

[229] B Xiao, J Sun, A Ruzsinszky, and JP Perdew. Testing the Jacob's ladder of density functionals for electronic structure and magnetism of rutile VO2. *Physical Review B*, 90:085134, 2014.

[230] X Yuan, Y Zhang, TA Abtew, P Zhang, and W Zhang. VO2: Orbital competition, magnetism, and phase stability. *Physical Review B*, 86(23):235103, 2012.

[231] MA Korotin, NA Skorikov, and VI Anisimov. Variation of orbital symmetry of the localized 3d1 electron of the V4+ ion upon the metal-insulator transition in VO2. *Physics of Metals and Metallurgy*, 2:4–9, 2003.

[232] R Heckingbottom and JW Linnett. Structure of Vanadium Dioxide. *Nature*, 194:678, 1962.

[233] HK Kim, H You, RP Chiarello, and HLM Chang. Finite-size effect on the first-order metal-insulator transition in VO2 films grown by metal-organic chemical-vapor deposition. *Physical Review B*, 47(19):900–907, 1993.

[234] PF Bongers. Anisotropy of the electrical conductivity of the VO2 single crystal. *Solid State Communications*, 3:275–277, 1965.

[235] GJ Hill and RH Martin. Electrical and magnetic properties of vanadium dioxide. *Physics Letters A*, 27(1):1–2, 1968.

[236] J P Pouget and H Launois. Metal-Insulator Phase Transition in VO2. *Journal De Physique*, 37:49–57, 1976.

[237] K Kosuge. The phase transition in VO2. *Journal of the Physical Society of Japan*, 22(2):552, 1967.

[238] MW Haverkort, Z Hu, A Tanaka, W Reichelt, SV Streltsov, MA Korotin, VI Anisimov, HH Hsieh, HJ Lin, CT Chen, D. I. Khomskii, and LH Tjeng. Orbital Assisted Metal Insulator Transition in VO2. *Physical Review Letters*, 95:196404, 2005.

[239] H Zheng and LK Wagner. Computation of the Correlated Metal-Insulator Transition in Vanadium Dioxide from First Principles. *Physical Review Letters*, 114(17):176401, 2015.

[240] DB McWhan, JP Remeika, JP Maita, H Okinaka, K Kosuge, and S Kachi. Heat Capacity of Vanadium Oxides at Low Temperature. *Physical Review B*, 7(1):326–331, 1973.

[241] WF Brinkman and TM Rice. Application of Gutzwiller's variational method to the metal-insulator transition. *Physical Review B*, 2(10):4302–4304, 1970.

[242] E Pavarini, A Yamasaki, J Nuss, and O K Andersen. How chemistry controls electron localization in 3d 1 perovskites: A Wannier-function study. *New Journal of Physics*, 7:1–5, 2005.

[243] NB Aetukuri, AX Gray, M Drouard, M Cossale, L Gao, AH Reid, R Kukreja, H Ohldag, CA Jenkins, E Arenholz, KP Roche, HA Dürr, MG Samant, and SSP Parkin. Control of the metal insulator transition in vanadium dioxide by modifying orbital occupancy. *Nature Physics*, 9:661–666, 2013.

[244] D Newns and BR Elmegreen. A low-voltage high-speed electronic switch based on piezoelectric transduction. *Journal of Applied Physics*, 111(8):084509, 2012.

[245] T Kawakubo. Crystal Distortion and Electric and Magnetic Transition in VO2. *Journal of the Physical Society of Japan*, 20(4):516–520, 1965.

[246] D Adler and H Brooks. Theory of Semiconductor-To-Metal Transitions. *Physical Review*, 155(3):826–840, 1967.

[247] M Hada, K Okimura, and J Matsuo. Photo-induced lattice softening of excited-state VO2. *Applied Physics Letters*, 99(5):051903, 2011.

[248] SM Woodley. The mechanism of the displacive phase transition in vanadium dioxide. *Chemical Physics Letters*, 453:167–172, 2008.

[249] G Henkelman and H Jónsson. A dimer method for finding saddle points on high dimensional potential surfaces using only first derivatives. *The Journal of Chemical Physics*, 111(15):7010, 1999.

[250] KJ Caspersen and EA Carter. Finding transition states for crystalline solid to solid phase transformations. *PNAS*, 102(19):6738–6743, 2005.

[251] TJ Huffman, P Xu, MM Qazilbash, EJ Walter, H Krakauer, J Wei, DH Cobden, HA Bechtel, MC Martin, GL Carr, and D. N. Basov. Anisotropic infrared response of vanadium dioxide microcrystals. *Physical Review B*, 87:115121, 2013.

[252] H Terauchi and J Cohen. Diffuse x-ray scattering due to the lattice instability near the metal-semiconductor transition in VO2. *Physical Review B*, 17(6):2494–2496, 1978.

[253] W Zhong, D Vanderbilt, and KM Rabe. Phase transitions in BaTiO3 from first principles. *Physical Review Letters*, 73:1861–1864, 1994.

[254] KM Rabe and JD Joannopoulos. *Ab initio statistical mechanics of phase transitions*. PhD thesis, 1992.

[255] Neil Drummond and G. J. Ackland. Ab initio quasiharmonic equations of state for dynamically stabilized soft-mode materials. *Physical Review B*, 65:184104, 2002.

[256] GJ Ackland. Calculation of free energies from ab initio calculation. *Journal of Physics: Condensed Matter*, 14:2975, 2002.

[257] J Íñiguez, S Ivantchev, J Perez-Mato, and A García. Devonshire-Landau free energy of BaTiO3 from first principles. *Physical Review B*, 63(14):144103, 2001.

[258] L Chaput, A Togo, I Tanaka, and G Hug. Phonon-phonon interactions in transition metals. *Physical Review B*, 84:094302, 2011.

[259] MT Dove and AE Phillips. *Phase Transitions Course QM*. 2013.

[260] MM Qazilbash, AA Schafgans, KS Burch, SJ Yun, BG Chae, BJ Kim, HT Kim, and DN Basov. Electrodynamics of the vanadium oxides VO2 and V2O3. *Physical Review B*, 77:115121, 2008.

[261] WT Liu, J Cao, W Fan, Z Hao, and MC Martin. Intrinsic Optical Properties of Vanadium Dioxide near the Insulator Metal Transition. *Nano Letters*, 11(2):466–470, 2010.

[262] R Srivastava and LL Chase. Raman Spectrum of Semiconducting and Metallic VO2. *Physical Review Letters*, 27(11):727, 1971.

[263] JB Goodenough. Direct Cation-Cation Interactions in Several Oxides. *Physical Review*, 117(6):1442, 1960.

[264] P Jin, S Nakao, and S Tanemura. Tungsten doping into vanadium dioxide thermochromic films by high-energy ion implantation and thermal annealing. *Thin Solid Films*, 324:151–158, 1998.

[265] W Burkhardt, T Christmann, BK Meyer, W Niessner, D Schalch, and A Scharmann. W and F doped VO2 films studied by photoelectron spectrometry. *Thin Solid Films*, 345:229–235, 1999.

[266] TD Manning and IP Parkin. Atmospheric pressure chemical vapour deposition of tungsten doped vanadium (IV) oxide from VOCl3, water and WCl6. *Journal of Materials Chemistry*, 14:2554–2559, 2004.

[267] C Tang, P Georgopoulos, M Fine, J Cohen, M Nygren, G Knapp, and A Aldred. Local atomic and electronic arrangements in W doped VO2. *Physical Review B*, 31:1000–1011, 1985.

[268] M Netsianda, PE Ngoepe, CRA Catlow, and SM Woodley. The displacive phase transition of vanadium dioxide and the effect of doping with tungsten. *Chemistry of Materials*, 20(5):1764–1772, 2008.

[269] S Shin, S Suga, M Taniguchi, M Fujisawa, H Kanzaki, A Fujimori, H Daimon, Y Ueda, K Kosuge, and S Kachi. Vacuum-ultraviolet reflectance and photoemission study of the metal-insulator phase transitions in VO2, V6O13, and V2O3. *Physical Review B*, 41(8):4993–5009, 1990.

[270] G Xu, Y Chen, M Tazawa, and P Jin. Surface plasmon resonance of silver nanoparticles on vanadium dioxide. *The Journal of Physical Chemistry B*, 110:2051–6, 2006.

[271] TD Manning and IP Parkin. Atmospheric pressure chemical vapour deposition of tungsten doped vanadium (IV) oxide from VOCl3, water and WCl6. *Journal of Materials Chemistry*, 14:2554–2559, 2004.

[272] SK Misra, SI Andronenko, and RR Andronenko. Variable-temperature EPR study of Fe3+ in VO2 single crystals. *Physical Review B*, 57(14):8203–8210, 1998.

[273] SA Corr, DP Shoemaker, BC Melot, and R Seshadri. Real-Space Investigation of Structural Changes at the Metal-Insulator Transition in VO2. *Physical Review Letters*, 105:056404, 2010.

[274] KD Rogers. An X-ray diffraction study of semiconductor and metallic vanadium dioxide. *Powder Diffraction*, 8(04):240–244, 1993.

[275] G Wulff. Zur Frage der Geschwindigkeit des Wachsthums und der Auflosung der Krystallflächen, 1901.

[276] K Reuter and M Scheffler. Composition, structure, and stability of RuO2 (110) as a function of oxygen pressure. *Physical Review B*, 65(3):035406, 2001.

[277] R Grau-Crespo, C Catlow, and N De Leuw. A computer modeling study of redox processes on the FeSbO4 (100) surface. *Journal of Catalysis*, 248:77–88, 2007.

[278] MW Chase. NIST-JANAF Thermochemical Tables. 1998.

[279] U Diebold. The surface science of titanium dioxide. *Surface Science Reports*, 48:53–229, 2003.

[280] A Kiejna, T Pabisiak, and SW Gao. The energetics and structure of rutile TiO2 (110). *Journal of Physics: Condensed Matter*, 18:4207–17, 2006.

[281] R Lindsay, A Wander, A Ernst, B Montanari, G Thornton, and N Harrison. Revisiting the Surface Structure of TiO2 (110): A Quantitative low-Energy Electron Diffraction Study. *Physical Review Letters*, 94(24):246102, 2005.

[282] H Perron, C Domain, J Roques, R Drot, E Simoni, and H Catalette. Optimisation of accurate rutile TiO2 (110), (100), (101) and (001) surface models from periodic DFT calculations. *Theoretical Chemistry Accounts*, 117(4):565–574, 2007.

[283] JI Sohn, HJ Joo, AE Porter, C-J Choi, K Kim, DJ Kang, and ME Welland. Direct observation of the structural component of the metal-insulator phase transition and growth habits of epitaxially grown VO2 nanowires. *Nano Letters*, 7(6):1570–4, 2007.

[284] XG Wang, W Weiss, and SK Shaikhutdinov. The hematite alpha-Fe2O3 (0001) surface: evidence for domains of distinct chemistry. *Physical Review Letters*, 81:3–6, 1998.

[285] R Grau-Crespo, IDPR. Moreira, F Illas, NH de Leeuw, and CRA Catlow. The effect of cation coordination on the properties of oxygen vacancies in FeSbO4. *Journal of Materials Chemistry*, 16(20):1943, 2006.

[286] DR Lide. CRC Handbook of Chemistry and Physics. 89. 2008.

[287] L Wang, T Maxisch, and G Ceder. Oxidation energies of transition metal oxides within the GGA+U framework. *Physical Review B*, 73(19):195107, 2006.

[288] A Vijay, G Mills, and H Metiu. Adsorption of gold on stoichiometric and reduced rutile TiO2 (110) surfaces. *The Journal of Chemical Physics*, 118(14):6536, 2003.

[289] J Oviedo, MA San Miguel, and JF Sanz. Oxygen vacancies on TiO2 (110) from first principles calculations. *The Journal of Chemical Physics*, 121:7427–33, 2004.

[290] T Pabisiak and A Kiejna. Energetics of oxygen vacancies at rutile TiO2 (110) surface. *Solid State Communications*, 144:324–328, 2007.

[291] M Iwamoto and H Furukawa. Photoluminescence spectra of surface vanadyl groups. Direct evidence for change of bond strength and electronic structure of metal-oxygen bond upon supporting. *Journal of the American Chemical Society*, (105):3719–3720, 1983.

[292] C Di Valentin, R Ferullo, R Binda, and G Pacchioni. Oxygen vacancies and peroxo groups on regular and low-coordinated sites of MgO, CaO, SrO, and BaO surfaces. *Surface Science*, 600:1147–1154, 2006.

[293] R Coquet and DJ Willock. The (010) surface of MoO3, a DFT+U study. *Physical Chemistry Chemical Physics*, 3(010):3819–3828, 2005.

[294] MA Haija, S Guimond, Y Romanyshyn, A Uhl, H Kuhlenbeck, TK Todorova, MV Ganduglia Pirovano, J Dobler, J Sauer, and HJ Freund. Low temperature adsorption of oxygen on reduced V2O3 (0001) surfaces. *Surface Science*, 600:1497–1503, 2006.

[295] J Stringer. The vanadium-oxygen system - a review. *Journal of the Less Common Metals*, 8:1–14, 1965.

[296] E Cockayne and L Li. First-principles DFT+U studies of the atomic, electronic, and magnetic structure of α-MnO2 (cryptomelane). *Chemical Physics Letters*, 544:53–58, 2012.

[297] RR Maphanga, SC Parker, and PE Ngoepe. Atomistic simulation of the surface structure of electrolytic manganese dioxide. *Surface Science*, 603(21):3184–3190, 2009.

[298] L Zhang, Z-H Liu, X Tang, J Wang, and K Ooi. Synthesis and characterization of β-MnO2 single crystals with novel tetragonous morphology. *Materials Research Bulletin*, 42:1432–1439, 2007.

[299] B Tang, G Wang, L Zhuo, and J Ge. Novel dandelion-like beta-manganese dioxide microstructures and their magnetic properties. *Nanotechnology*, 17:947–51, 2006.

[300] GAE Oxford and AM Chaka. First-Principles Calculations of Clean, Oxidized, and Reduced β-MnO2 Surfaces. *The Journal of Physical Chemistry C*, 115:16992–17008, 2011.

[301] MM Branda, NJ Castellani, R Grau-Crespo, NH de Leeuw, NC Hernandez, Javier F Sanz, KM Neyman, and F Illas. On the difficulties of present theoretical models to predict the oxidation state of atomic Au adsorbed on regular sites of CeO2 (111). *The Journal of Chemical Physics*, 131(9):094702, 2009.

[302] NC Hernández, R Grau-Crespo, NH de Leeuw, and JF Sanz. Electronic charge transfer between ceria surfaces and gold adatoms: a GGA+U investigation. *Physical Chemistry Chemical Physics*, 11:5246–52, 2009.

[303] LG Cota and P de la Mora. On the structure of lithium peroxide, Li2O2. *Acta Crystallographica*, 61:133–6, 2005.

[304] KC Lau, RS Assary, P Redfern, and LA Curtiss. Electronic Structure of Lithium Peroxide Clusters and Relevance to Lithium Air Batteries. *The Journal of Physical Chemistry C*, 116:23890–23896, 2012.

[305] H Sawada, Y Morikawa, K Terakura, and N Hamada. Jahn-Teller distortion and magnetic structures in LaMnO3. *Physical Review B*, 56(19):12154–12160, 1997.

[306] T Hashimoto, S Ishibashi, and K Terakura. Jahn-Teller distortion and magnetic structure in LaMnO3: A first-principles theoretical study with full structure optimizations. *Physical Review B*, 82(4):045124, 2010.

[307] M Wu, E Benckiser, MW Haverkort, A Frano, Y Lu, U Nwankwo, S Bruck, P Audehm, E Goering, S Macke, V Hinkov, P Wochner, G Christiani, S Heinze, G Logvenov, HU Habermeier, and B Keimer. Strain and composition dependence of orbital polarization in nickel oxide superlattices. *Physical Review B*, 88:125124, 2013.

[308] N Kovaleva, A Boris, C Bernhard, A Kulakov, A Pimenov, A Balbashov, G Khaliullin, and B Keimer. Spin-Controlled Mott-Hubbard Bands in LaMnO3 Probed by Optical Ellipsometry. *Physical Review Letters*, 93(14):147204, 2004.

[309] T Arima, Y Tokura, and JB Torrance. Variation of optical gaps in perovskite-type 3d transition-metal oxides. *Physical Review B*, 48(23):17006–17009, 1993.

[310] T Saitoh, AE Bocquet, T Mizokawa, H Namatame, A Fujimori, M Abbate, Y Takeda, and M Takano. Electronic structure of La1-xSrxMnO3 studied by photoemission and x-ray-absorption spectroscopy. *Physical Review B*, 51(20):13942–13951, 1995.

[311] R Krüger, B Schulz, S Naler, R Rauer, D Budelmann, J Bäckström, KH Kim, SW Cheong, V Perebeinos, and M Rübhausen. Orbital ordering in LaMnO3 investigated by resonance raman spectroscopy. *Physical Review Letters*, 92(9):097203–4, 2004.

[312] JH Lee, KT Delaney, E Bousquet, NA Spaldin, and KM Rabe. Strong coupling of Jahn-Teller distortion to oxygen-octahedron

rotation and functional properties in epitaxially strained orthorhombic LaMnO3. *Physical Review B*, 88:174426, 2013.

[313] G Trimarchi and N Binggeli. Structural and electronic properties of LaMnO3 under pressure: An ab initio LDA+U study. *Physical Review B*, 71:035101–9, 2005.

[314] Y Nohara, A Yamasaki, S Kobayashi, and T Fujiwara. Electronic structure of antiferromagnetic LaMnO3 and the effects of charge polarization. *Physical Review B*, 74:064417, 2006.

[315] A Georges, LD Medici, and J Mravlje. Strong Correlations from Hunds Coupling. *Annual Review of Condensed Matter Physics*, 4:137–178, 2013.

[316] F Lu, D-M Chen, and L-J Zou. Orbital Order Instability and Orbital Excitations in Degenerate Itinerant Electron Systems. *Chinese Physics Letters*, 26:097501–5, 2009.

[317] JB Goodenough. An interpretation of the magnetic properties of the perovskite-type mixed crystals La(1-x)Sr(x)CoO(3-λ). *Journal of Physics and Chemistry of Solids*, 6:287–297, 1958.

[318] J Kanamori. Superexchange interaction and symmetry properties of electron orbitals. *Journal of Physics and Chemistry of Solids*, 10:87–98, 1959.

[319] D Muñoz, N Harrison, and F Illas. Electronic and magnetic structure of LaMnO3 from hybrid periodic density-functional theory. *Physical Review B*, 69:085115, 2004.

[320] M Nicastro and C Patterson. Exchange coupling in CaMnO3 and LaMnO3: Configuration interaction and the coupling mechanism. *Physical Review B*, 65:205111–15, 2002.

[321] H Meskine, H König, and S Satpathy. Orbital ordering and exchange interaction in the manganites. *Physical Review B*, 64(9):1–13, 2001.

[322] J. H. van Vleck. The Jahn-Teller Effect and Crystalline Stark Splitting for Clusters of the Form XY6. *Journal of Chemical Physics*, 220:72–84, 1939.

[323] J Kanamori. Crystal Distortion in Magnetic Compounds. *Journal of Applied Physics*, 31:14–22, 1960.

[324] GS Tian. Particle-hole transformations and sum rules for the Hubbard model. *Physics Letters A*, 228:383–390, 1997.